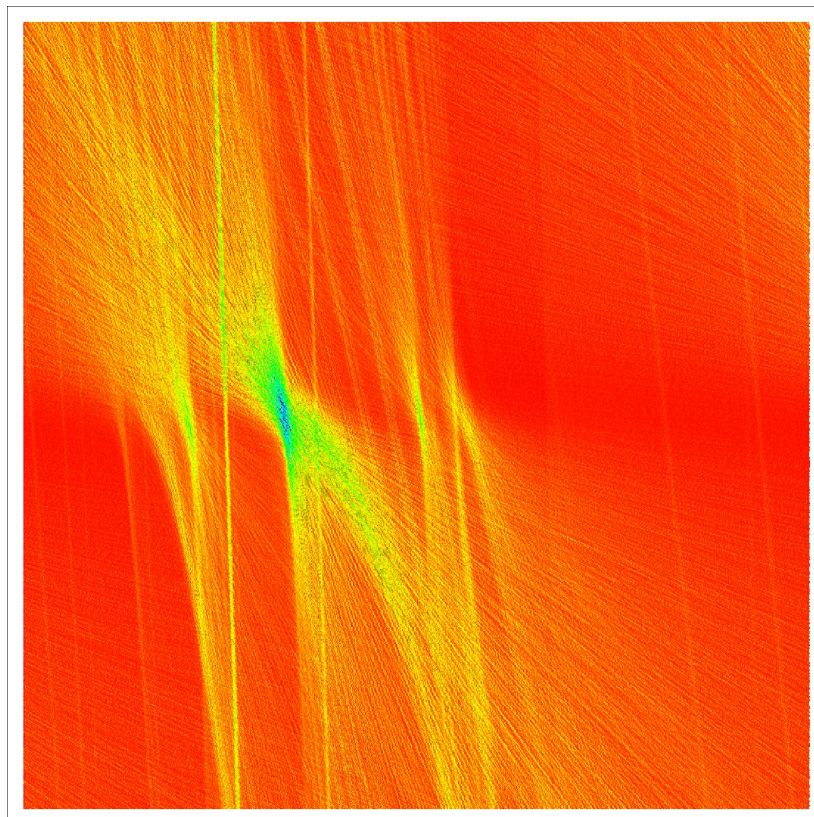


**An all-solid state laser system for the laser ion source RILIS
and
in-source laser spectroscopy of astatine
at ISOLDE/CERN**



Dissertation
by
Sebastian Rothe
Born in Erfurt, Germany

Institut für Physik
Johannes Gutenberg-Universität Mainz
20 September 2012

First referee:

Second referee:

Day of the examination: 24.09.2012

D77

Abstract

This doctoral thesis describes the extension of the resonance ionization laser ion source RILIS at CERN/ISOLDE by the addition of an all-solid state tunable titanium:sapphire (Ti:Sa) laser system to complement the well-established system of dye lasers. Synchronous operation of the so called Dual RILIS system of Ti:Sa and dye lasers was investigated and the potential for increased ion beam intensity, reliability, and reduced setup time has been demonstrated. In-source resonance ionization spectroscopy was performed at ISOLDE/CERN and at ISAC/TRIUMF radioactive ion beam facilities to develop an efficient and selective three-colour ionization scheme for the purely radioactive element astatine. A LabVIEW based monitoring, control and measurement system was conceived which enabled, in conjunction with Dual RILIS operation, the spectroscopy of high lying Rydberg states, from which the ionization potential of the astatine atom was determined for the first time experimentally.

Contents

Abstract	iii
List of Figures	xi
List of Tables	xv
Abbreviations and acronyms	xxi
1 Introduction	1
1.1 ISOLDE	1
1.2 The Resonance Ionization Laser Ion Source RILIS	2
1.3 Objective of the thesis	3
I Theory and Methods	5
2 Atom light interaction	7
2.1 Electronic structure of the atom	7
2.1.1 Energy levels of the hydrogen atom	7
2.1.2 Hydrogen-like atoms	8
2.1.3 Determination of ionization potentials	9
2.2 Interaction of light with matter	9
2.2.1 Blackbody radiation	9
2.2.2 Boltzmann statistics	10
2.2.3 Einstein coefficients	10
2.3 Lifetimes and line functions	12
3 Tunable lasers	13
3.1 Laser principle	13
3.2 Ti:Sa laser	15
3.2.1 Ti:Sa - a vibronic laser medium	15

3.3	The four level vibronic laser	16
3.4	Dye laser	18
3.5	Wavelength selection in tunable lasers	20
3.5.1	Resonator modes	20
3.5.2	Resonator mirrors	20
3.5.3	Lyot-Filter	22
3.5.4	Thin etalon	23
3.5.5	Thick etalon	23
3.5.6	Grating	23
3.6	Generation of higher harmonics	24
3.7	Mathematical description of laser radiation	26
3.7.1	Gaussian beams	26
3.7.2	Matrix optics	28
4	Resonance ionization and applications	33
4.1	Laser ionized radioactive ion beams	34
4.2	In-source resonance ionization spectroscopy	36
4.2.1	Determination of nuclear properties	37
4.2.2	Ionization scheme development	37
4.3	Particle registration	37
4.3.1	Faraday cup	37
4.3.2	Alpha decay spectroscopy detector	38
4.3.3	ISOLTRAP MR-ToF	38
II	Apparatus	39
5	Design of Ti:Sa lasers and frequency conversion units for ISOLDE RILIS	41
5.1	State of the art Ti:Sa laser systems for laser ion sources and RIMS	41
5.2	Motivation and considerations for the new design	42
5.3	Ti:Sa cavity optimization	45
5.4	Construction of the Ti:Sa lasers	45
5.5	Frequency conversion unit	47
6	Characterization of the Ti:Sa laser system	49
6.1	Operational characteristics	49
6.1.1	Tuning range of the Ti:Sa lasers	49
6.1.2	Synchronization of the Ti:Sa lasers	51
6.1.2.1	Q-switching	51
6.1.2.2	Gain tuning	52

6.1.2.3	Independent pump lasers	54
6.1.3	Pulse-jitter of the Ti:Sa	54
6.1.4	Wavelength stability of the Ti:Sa lasers	55
6.2	Additional functionality of the Ti:Sa lasers	57
6.2.1	Narrow-band Ti:Sa	57
6.2.1.1	Determination of the line width of the NB-Ti:Sa	60
6.2.1.2	Reducing the line-width by reduction of the gain	63
6.2.1.3	In-source spectroscopy of the hyperfine structure of gold	63
6.2.1.4	Automatic tuning of the NB-Ti:Sa	64
6.2.2	Amplification of Ti:Sa pulses	65
6.2.3	Intra-cavity SHG	68
7	Implementation of the Ti:Sa lasers to RILIS	71
7.1	Two laser systems at RILIS	71
7.1.1	New RILIS layout	71
7.1.2	Beam transport to HRS	71
7.2	The Dual RILIS	79
7.2.1	Synchronization	80
7.2.2	Ti:Sa-only mode	81
7.2.3	Backup mode	81
7.2.3.1	A Dual RILIS ionization scheme for nickel	81
7.2.3.2	A Dual RILIS ionization scheme for cadmium	84
7.2.4	Mixed mode	85
7.2.4.1	Dual RILIS operation for silver	86
7.2.4.2	A new ionization scheme for calcium	86
8	RILIS data acquisition and processing	89
8.1	RILIS Server-client architecture	89
8.2	Implementation of the infrastructure	91
8.3	RILIS control programs	93
8.4	RILIS monitoring	94
8.5	Signals from ion detectors	94
8.6	Data recorder for in-source laser spectroscopy	96
8.6.1	Step-wise scan and average	96
8.6.2	Continuous scanning	96
8.7	Systematic errors caused by the data acquisition	96
9	The RILIS ionization scheme database	101

III In-source laser spectroscopy of astatine	105
10 In-source spectroscopy of astatine	107
10.1 Astatine: History and Properties	107
10.2 Ionization scheme development for astatine	109
10.2.1 Motivation and objectives	109
10.2.2 Ground state transitions	111
10.2.3 Ionization threshold	114
10.2.4 Search for second excited states	117
10.2.5 Comparison of ionization schemes for astatine	118
10.2.6 Spectroscopy of the excited states	121
10.2.7 Scan for second excited states and auto-ionizing resonances	121
10.2.8 Determination of the laser ionization efficiency	122
10.2.9 Isotope shifts	123
10.3 Precision measurement of the ionization potential of astatine	126
10.3.1 Measurement procedure for Rydberg scans	126
10.3.2 Determination of the first and second step level energy	132
10.3.3 Graphical analysis of the Rydberg spectra	134
10.3.3.1 Extraction of the ionization limit	135
10.3.3.2 Visualization of the position of the ionization limit in a $\delta - E$ plot	139
10.3.3.3 Series visualization and identification by the modulo method	141
10.3.4 Detailed Rydberg-Ritz analysis of the Rydberg spectra	145
10.3.4.1 Results for <i>dataset 1</i>	145
10.3.4.2 Results for <i>dataset 2</i>	145
10.3.4.3 Assignment of the series	149
10.3.5 Final result for the ionization potential of astatine and error analysis .	150
10.3.6 Discussion	152
IV Conclusion and outlook	155
11 Conclusion	157
11.1 The Dual RILIS	157
11.2 First laser spectroscopy of astatine	158
12 Outlook	159
V Appendix	161

A	Overview of the variables in the LabVIEW shared variable environment	163
B	Scaling the datasets for the ionization threshold measurement of astatine	165
C	Additional results from the threshold fit process	169
C.1	Fit results for the different scaling factors	169
C.2	Fit results for other elements	171
D	Laser scans of second excited states of astatine	175
E	Targets and parameters used for astatine spectroscopy runs	179
F	The PSB supercycle structure observed with the Faraday cup.	181
G	Graphical analysis for other elements	183
H	Tables of observed Rydberg resonances in astatine	189
I	Hyperfine structure of ^{205}At	197
	References	199
	Acknowledgements	215

List of Figures

3.1	Absorption and fluorescence spectrum of Ti:sapphire	15
3.2	Configuration-coordinate diagram for the Ti^{3+} ion coupled to the crystal field and the phonons of the sapphire host.	17
3.3	Jablonski diagram of a laser dye molecule	19
3.4	Wavelength selection in the Ti:Sa resonator	21
3.5	Reduction of laser bandwidth using a thick etalon	24
3.6	Paraxial ray and optical system	29
4.1	Illustration of the selective two step photo-ionization scheme for atoms	33
4.2	Schematic representation of the mass-separator and laser ion-source	34
5.1	Sketch of the CERN-Ti:Sa laser cavity.	43
5.2	Beam waist of the pump beam and the resonator mode calculated with the ABCD formalism	46
5.3	Photograph of a CERN-Ti:Sa cavity	47
5.4	Photograph of the frequency conversion unit.	48
6.1	Tuning ranges of the Ti:Sa laser	50
6.2	Efficiency of the Ti:Sa laser	51
6.3	Comparison of different makes of Pockels cells	53
6.4	Measurement of the pulse jitter of the Ti:Sa laser	54
6.5	Performance of the Ti:Sa wavelength stabilization	56
6.6	Optical layout of the narrow-band Ti:Sa cavity	57
6.7	Fringe pattern of the NB-Ti:Sa measured with the WS7 wavemeter	58
6.8	Mode structure of the NB-Ti:Sa observed with the Atos LM007 wavemeter	59
6.9	Setup for the FPI measurements of the NB-Ti:Sa	60
6.10	Mode structure of the NB-Ti:Sa observed with the scanning FPI	61
6.11	FPI signals for different Ti:Sa operation modes	62
6.12	Determination of the line-width of the NB-Ti:Sa	62
6.13	Mode structure of the NB-Ti:Sa measured at different output powers	63
6.14	Hyperfine structure of gold measured with the NB-Ti:Sa	64

6.15	Setup for the Ti:Sa single-pass amplification	66
6.16	Single-pass Ti:Sa amplification	66
6.17	Amplifier output at different amplifier pump pulse delays	67
6.18	Schematic view of the intracavity setup used in Jyväskylä	68
6.19	Performance of the intracavity SHG	69
6.20	Photograph of the opto-mechanical setup for intra-cavity frequency doubling	70
7.1	Photograph of the RILIS laser table	72
7.2	Photograph of the Ti:Sa system on the RILIS laser table	73
7.3	Photograph of the previous HRS launch path	75
7.4	Drawing of the HRS launch system.	76
7.5	Photograph of the new HRS launch path	77
7.6	Photograph of the lower platform of the HRS launch system	78
7.7	Schematic layout of the Dual RILIS	79
7.8	Oscilloscope trace of the laser pulses of the synchronized laser systems	80
7.9	Ionization scheme for nickel	82
7.10	Synchronization of the Ti:Sa laser and the dye laser system	83
7.11	Saturation measurement for the transition to the auto-ionizing transition in the nickel ionization scheme	84
7.12	Isotope shift of the auto-ionizing transition used in the nickel ionization scheme	85
7.13	Compared ionizationschemes for silver	86
8.1	Schematic layout of the RILIS server-client architecture	90
8.2	Schematic layout of the RILIS monitoring and control system	92
8.3	Website showing the status of the RILIS	94
8.4	ISOLDE Vistars screen with implemented RILIS status	95
8.5	Spectrum of auto-ionizing states in manganese for the RILIS DAQ benchmark	97
8.6	Systematic wavelength offset at different scan speeds	98
8.7	Offset distribution before and after the scan speed correction	99
9.1	Front page of the RILIS-DB website	102
9.2	Example of the available data for an ionization scheme of astatine	103
9.3	Editing of an existing scheme.	103
10.1	Absorption spectrum of astatine	108
10.2	Stages of the ionization scheme development for astatine	110
10.3	Laser parameters for the verification of the first step transitions in astatine	111
10.4	Photograph of the windmill α -decay spectroscopy setup	112
10.5	Typical α -decay spectra for astatine	113
10.6	Laser scans across the first-step transitions in astatine	114
10.7	Laser scans across and above the ionization potential of astatine	115

10.8	Illustration of the fit routine for the ionization threshold	116
10.9	Screenshot of the TRIUMF <i>Strip-Tool</i> showing the first astatine signal	118
10.10	Second excited states in astatine	119
10.11	α -spectrum for astatine	120
10.12	Comparison of eight different ionization schemes for astatine	120
10.13	Saturation measurements for astatine schemes	122
10.14	Isotope shifts of the 216 nm transition	125
10.15	Conditions of target #455	127
10.16	High resolution laser-scan across the ionization potential of astatine	129
10.17	Target information for the second Rydberg scan	130
10.18	Second laser-scan across the ionization potential of astatine	131
10.19	Determination of the first and second step level energies	132
10.20	Illustration of the steps for the graphical analysis of the Rydberg spectrum .	136
10.21	Quantum defect histogram for different set limits	137
10.22	Variation of maximum histogram counts at different set limits	138
10.23	$\delta - E_{\text{set}}$ -plot for astatine	140
10.24	$\delta - n^*$ -plot for astatine	142
10.25	Method for identification of series members by gating on the quantum defect	143
10.26	Identified series members using the gating method	144
10.27	Quantum defects and assignment of the series members in <i>dataset 1</i>	146
10.28	Residuals of the first order Rydberg fit to the three series observed in <i>dataset 1</i>	146
10.29	Assignment of the series members in <i>dataset 2</i>	147
10.30	Residuals of the second-order Rydberg-fit to the seven series observed in <i>dataset 2</i>	148
10.31	Distribution of the quantum defects of the members of Rydberg series in other halogens	149
10.32	Comparison of different wavemeters	150
B.1	Comparison of scaling methods	166
B.2	Visualization of the minimum error method	167
C.1	Fit results for different scaling factors	170
C.2	Fit results of the threshold method for different elements	172
C.3	Dependency of the H.val from the IP	173
D.1	Compilation 1 of astatine laser scans	176
D.2	Compilation 2 of astatine laser scans	177
F.1	Visualization of the structure of the PSB supercycle	182
F.2	Visualization of the PSB supercycle optimized for spectroscopy	182
G.1	Max histogram plots for gold data	184

G.2	Graphical visualization for gold	185
G.3	Graphical visualization for astatine <i>dataset 2</i>	186
G.4	Graphical visualization for gallium	187
G.5	Graphical visualization for technetium	188
I.1	Hyperfine structure of ^{205}At	198

List of Tables

5.1	Parameters applied to calculate the mode matching in the resonator	45
6.1	Specification of the purchased mirror sets.	49
7.1	Fit results for the isotope shift measurements of the different nickel isotopes .	84
7.2	Comparison of ionization schemes for cadmium	85
7.3	Laser properties for the ionization of silver	87
10.1	Spectroscopic information on astatine, obtained from absorption spectroscopy.	108
10.2	Calculated values for the first ionization potential of astatine.	109
10.3	Fit results for the ionization threshold, obtained with different combinations of scaling factors for the datasets.	117
10.4	Results from the in-source spectroscopy of first and second excited states in astatine	123
10.5	Scanned regions for second excited states	124
10.6	Scanned regions for third excited states	124
10.7	In-target production rates for astatine isotopes.	124
10.8	Isotope shifts of astatine isotopes for the two transitions at 216 nm and 795 nm	125
10.9	Choice of ionization scheme for the laser-scan across the ionization potential of astatine	126
10.10	Laser settings for the spectroscopy of Rydberg states	127
10.11	Laser settings for the second Rydberg scan of astatine	130
10.12	Results from the Rydberg fit of the series in <i>dataset 1</i>	145
10.13	Results from the Rydberg-Ritz fit of the series in <i>dataset 2</i>	148
10.14	Intermediate results with statistical and systematic errors.	152
10.15	Comparison of experimental and theoretical values for the first ionization potential of astatine	153
A.1	Devices listed at the RILIS server and status of implementation	164
C.1	Fit results for the ionization threshold for different elements.	171

E.1	Targets used for astatine spectroscopy runs	180
G.1	Results of the MaxH fit and the conventional Rydberg analysis for gold . . .	183
H.1	Resonances observed in the Rydberg spectrum of astatine.	189

Abbreviations and acronyms

8P8C	8 Position 8 Contact modular connector configuration
ABRABLA	ABRasion-ABLAtion model
AI	Auto-Ionizing
AR	Anti-Reflex
ASCII	American Standard Code for Information Interchange text-file character encoding
B3LYP DK6	Becke, 3-parameter, Lee-Yang-Parr, Douglas-Kroll Hamiltonian of the 6th order
BBO	β Barium Borate, Ba(BO ₂) ₂
Behlke	Behlke Power Electronics GmbH, Am Auernberg 4, 61476 Kronberg im Taunus, Hessen, Germany
BiBO	Bismut triborate
BMBF	Bundesministerium für Bildung und Forschung (Fed- eral Ministry of Education and Research)
BNC	Bayonet Neill–Concelman radio frequency coaxial cable connector
BRF, BiFi	BiRefringent Filter
BS	Beam Sampler, Beam Splitter
CAD	Computer-Aided Design
CASTECH	CASTECH Inc., Fuzhou, Fujian 350003, China
CAT5	Category 5 twisted pair cable
CERN	Conseil Européen pour la Recherche Nucléaire
CISD	Configuration Interaction Singles & Doubles
COLLAPS	COLlinear LAsEr SPectroscopy
COMPLIS	Collaboration for spectroscopic Measurements using a Pulsed-Laser Ion Source
CRIS	Collinear Resonance Ionization Spectroscopy
CVL	Copper Vapour Laser
CW	Continuous Wave
DAQ	Data AcQuisition
DB	Data Base

DC	Direct Current
DC CCSD(T)	Dirac-Coulomb Coupled-Cluster approach with Single, Double and perturbative Triple excitations
DCM	4-dicyanomethylene-2-methyl-6-(p(dimethylamino)styryl)-4H-pyran
DE9	D-shaped, E size sub-miniature plug with 9 connectors
DLL	Dynamic Link Library
EA	Electron Affinity
EdgeWave	EdgeWave GmbH - Innovative Laser Solutions, Schumanstr. 18 B, 52146 Würselen, Germany
EN-STI-ECE	CERN ENgineering department, Sources, Targets & Interactions group, Equipment Controls and Electronics section
EPICS	Experimental Physics and Industrial Control System
FC	Faraday Cup
FC	Fiber Coupler
FC490	ISOLDE Faraday Cup, 490 centimetres down the beam line
FC558	ISOLDE Faraday Cup, 558 centimetres down the beam line
FCU	Frequency Conversion Unit
FEBIAD	Forced Electron Beam Induced Arc Discharge
FESA	Front-End Software Architecture
FHG	Fourth Harmonic Generation
FPI	Fabry-Perot Interferometer
FS	Fused Silica
FSR	Free Spectral Range
FURIOS	Fast Universal Resonant laser IOn Source
GANIL	Grand Accélérateur National d'Ions Lourds
GISELE	GANIL Ion Source using Electron Laser Excitation
GPN	General Purpose Network
GPS	General Purpose Separator
GSI	Gesellschaft für Schwerionenforschung (GSI Helmholtzzentrum für Schwerionenforschung GmbH), Darmstadt, Germany
He-Ne	Helium-Neon Laser
HHG	Higher Harmonics Generation
HighFinesse	HighFinesse GmbH - Laser and Electronic Systems, Auf der Morgenstelle 14D, 72076 Tübingen, Germany

HR	High-Reflecting mirror
HRIBF	Holifield Radioactive Ion Beam Facility
HRS	High Resolution Separator
HV	High Voltage
IC	Intra-Cavity
IC-SHG	Intra-Cavity Second Harmonics Generation
IGISOL	Jyväskylä Ion Guide Isotope Separator On-Line
INTC	ISOLDE and Neutron Time-of-Flight Experiments Committee
Inventor	Autodesk Inventor 2010
IP	Ionization Potential
IR	Infrared
IRIS	Investigation of Radioactive Isotopes at Synchrotron
ISAC	Isotope Separation and ACceleration facility
ISCOOL	ISolde ion beam COOLer and buncher
ISOL	Isotope-Separator On-Line
ISOLDE	Isotope Separator On Line DETector
ISOLTRAP	ISOLDE tandem Penning trap mass spectrometer
JAPC	Java API for Parameter Control
JYFL	Department of Physics, University of Jyväskylä
LabVIEW	Laboratory Virtual Instrumentation Engineering Workbench
LARIS	LAser Resonance Ionization Spectroscopy
LARISSA	LAser Resonanz Ionisation für Spektroskopie in Selektiven Anwendungen
LASER	Light Amplification by Stimulated Emission of Radiation
LAYERTEC	LAYERTEC GmbH, Ernst-Abbe-Weg 1, 99441 Mellingen, Germany
LINOS	LINOS GmbH, Göttingen, Germany
LIS	Laser Ion Source
LM007	ATOS Lambdameter LM-007 Wavelength meter
Mathematica	Mathematica 8.0
MaxH	Maximum Histogram
MCA	Multi Channel Analyser
MCDF	MultiConfiguration relativistic Dirac-Fock
MCP	Micro-Channel Plate detector
MEM	Maximum Error Method
MPM	Multi-PowerMeter Optometer P-9801

MR-ToF	Multi-Reflection Time-of-Flight
NB	Narrow-Band
NB-Ti:Sa	Titanium:Sapphire laser in Narrow-Band configuration
Nd:YAG	Neodymium-doped Yttrium Aluminium Garnet
Nd:YLF	Neodymium-doped Yttrium Lithium Fluoride
Newport	Micro-Controle Spectra-Physics S.A., 9, rue du Bois Sauvage, 91055 Évry Cedex
OC	Output Coupler mirror
Origin	Origin 8.6, OriginLab Corporation
ORNL	Oak Ridge National Laboratory
PAM	Pico Ampere Meter
PC	Pockels Cell
Perle	Perle Systems GmbH, Schlachte 12/13, 28195 Bremen, Germany
Photonics	Photonics Industries international, Inc., 390 Central Avenue, Bohemia, NY 11716, USA
PHP	PHP: Hypertext Pre-processor
PLC	Programmable Logic Controller
PNPI	Petersburg Nuclear Physics Institute
PPP	Protons Per Pulse
PSB	Proton Synchrotron Booster
Q-switching	Quality factor switching
RADE	Rapid Application Development Environment (for LabVIEW by the CERN Industrial Controls and Electronics group)
RI	Resonance Ionization
RIB	Radioactive Ion Beam
RILIS	Resonance Ionization Laser Ion Source
RILIS-DB	RILIS collaborative element ionization scheme Data Base
RIMS	Resonance Ionization Mass Spectrometry
RIS	Resonance Ionization Spectroscopy
RISIKO	Resonanz Ionisations Spektroskopie In Kollinearer Geometrie
RJ45	Registered Jack 45, Modular connector, 8 position 8 contact configuration
ROI	Region Of Interest
RS-232	Recommended Standard 232 serial communications computer port (also EIA-232 by Electronic Industries

	Association)
SHG	Second-Harmonic Generation
SHV	Safe High Voltage radio frequency coaxial cable connector
Sirah	Sirah Laser- und Plasmatechnik GmbH, Ludwig-Erhard-Strasse 10, 41564 Kaarst, Germany
SNLO	Select Non-Linear Optics, Dr. A. Smith, AS-Photonics, LLC
SP-EHHA	SPiegelsatz (mirror set), Endspiegel (high reflector), Hohlspiegel (curved mirror), Auskoppelspiegel (output coupler)
SPI	Serial Peripheral Interface
SVE	Shared Variable Engine
TEM	TEM Messtechnik GmbH, Großer Hillen 38, 30559 Hannover, Germany
Thorlabs	Thorlabs, Inc., 56 Sparta Avenue, Newton, NJ 07860, USA
Ti:Sa	Titanium:Sapphire
TN	Technical Network
TRILIS	TRIUMF Resonant Ionization Laser Ion Source
TRIUMF	TRI-University Meson Facility
UC	United Crystals Company, 65 Linwood Road North, Port Washington, NY 11050-1439, USA
UC	Uranium Carbide
USB	Universal Serial Bus
UTP	Unshielded Twisted Pair
UV	Ultraviolet
VI	Virtual Instrument
VISTARS	Fixed Display Framework (FDF) CERN machine status display service
WS6	HighFinesse WS/6 High Precision Wavelength meter
WS7	HighFinesse WS/7 Super Precision Wavelength meter

Chapter 1

Introduction

1.1 ISOLDE

The ISOLDE (Isotope Separator On-Line DEvice) is a radioactive ion beam facility, located at CERN in Geneva, Switzerland. Ion beams of rare isotopes that cannot be found in nature are produced and delivered to different experiments that allow fundamental research in the fields of nuclear physics, particle and astrophysics, solid state physics, atomic physics as well as biology and nuclear medicine.

The ISOLDE project was proposed in 1964 and was approved by CERN's Director General. It started operation as an experiment at CERN in 1967 [RK70, JR00]. After several upgrades and a move of the experiment to use the CERN Proton Synchrotron Booster (PSB) in 1992 [KFJ⁺92], CERN management decided to integrate ISOLDE into the accelerator complex of CERN as a full-scale facility [FWB00]. Today ISOLDE is a user facility that can produce more than 1000 isotopes of 70 chemical elements [Sto12]. Johnson and Richter described the ISOLDE target as ‘(...) a small chemical factory’ [JR00]. The availability of a great variety of accessible isotopes and chemical elements from the light (Li) to the heaviest (Rn) is due to continual research and development of the target and ion source unit [Lin03]. The diversity of beams is as important feature of a radioactive ion beam (RIB) facility as the efficiencies of the target and the ion source [Kö2].

The choice of target material and composition is only one of the aspects that define the ion beam output. The choice of ion source, which is coupled to the target, is also an important factor. The ion source type and the target material has to be chosen and optimized for the element of interest to optimize the efficiency and the selectivity [BHH⁺86]. At ISOLDE, a high energy proton beam at 1.4 GeV, supplied by the PSB, impinges onto a thick target. The protons intensity can reach 2 μ A and this beam induces nuclear reactions in the target material (fission, multi-fragmentation and spallation). The reaction products are then evaporated from the heated target and diffuse as atoms towards the coupled ion source in which they are then ionized to a singly charged state (mostly 1⁺). After extraction and acceleration to energies up to 60 keV the isotope of interest is selected by dipole magnet separators.

Of the different types of ion sources that can be installed inside the ISOLDE target unit, the most simple is the surface ion source. Elements with a sufficiently low ionization potential can be efficiently ionized in this tubular metal cavity [BHH⁺86]. Elements with high ionization potentials can be ionized using the more complex plasma ion source [SR92] which is based on the FEBIAD (forced electron beam induced arc discharge) principle [KR76]. The selectivity of these ion sources for a desired chemical element is very limited. To date the only ion source at ISOLDE that can selectively ionize a chosen chemical element is the Resonance Ionization Laser Ion Source (RILIS). Because of its high degree of selectivity and efficiency as well as the great number of different beams available, it has become the most frequently used ion source at ISOLDE.

1.2 The Resonance Ionization Laser Ion Source RILIS

The laser ionization of the reaction products in the ISOLDE target relies on the resonant absorption of photons from the interacting laser radiation field by the outermost electron of the atom. This valence electron which is step-wise excited until, in the ionization step, its energy is greater than its binding energy (the ionization potential of that given element). In 1972 Ambartsumian and Letokhov reported selective two-step photo-ionization of rubidium atoms using ruby-laser pumped dye lasers [AL72]. From this starting point the technique of resonance ionization spectroscopy evolved and led to the development of numerous applications [HL94] and ionization schemes (e.g. [Sal90]). The resonance ionization technique is today routinely applied as a selective and efficient source for radioactive ions, proposed by Letokhov and Lee [L⁺84, Lee85] and formulated by Kluge *et al.* [HJKW85]. This high efficiency selective laser ion source was first demonstrated at the IRIS facility at PNPI Gatchina (Russia) in 1991 by Alkhazov (et al.) [ABB⁺91]. The test of a laser ion source was carried out successfully under on-line conditions at ISOLDE, during which selective laser ionization of tin, thulium, ytterbium and lithium with an efficiency in the order of 10-20% was demonstrated [MFK⁺93]. In the same year the permanent installation of a laser ion source for ISOLDE was requested and a copper vapour laser (CVL) pumped dye laser system, provided by the Institute of Spectroscopy of the Russian Academy of Sciences (Troitsk, Russia) was brought to ISOLDE. The first physics experiment with the RILIS as ion source (ISOLDE experiment IS333) was performed only one year later in 1994 [FJJ⁺95]. The copper vapour pump laser was in operation from 1991 to 2008 and was successfully used to produce ion beams of 26 different elements [FBL⁺08]. Since 2008, the RILIS laser system was upgraded in several stages. The ageing CVL was becoming difficult to maintain as the annual demand for RILIS ionized beams increased. It was replaced by a custom made solid-state Nd:YAG pump laser developed by *Edgewave GmbH* and state-of-the-art dye lasers purchased from *Sirah Laser und Plasmatechnik GmbH* [MBF⁺10, FBF⁺12].

The latest step in this upgrade process is subject to this thesis: The installation of a comple-

mentary all solid-state laser system based on Nd:YAG laser pumped tunable titanium:sapphire (Ti:Sa) lasers.

Already in 2003, Köster *et al.* [KFM03] pointed out that tunable Ti:Sa lasers ‘(...) might be used to complement the dye lasers in the IR range (...)’.

The tunable Ti:Sa lasers that they referred to were initially developed and adapted for the application in resonance ionization mass spectrometry for routine operation for ultra trace analysis of plutonium [WBG⁺03, GHK⁺04].

Since then, the Ti:Sa lasers were successfully tested at different radioactive ion beam facilities for their application as a laser ion source. Tests were performed at TRIUMF-ISAC (Vancouver, Canada), IGISOL (Jyväskylä, Finland), ORNL-HRIBF (Oak-Ridge, USA) [RGH⁺04, MNB⁺05, LBB⁺06, LBD⁺09, LACC⁺10]. A great effort was put into the development of new ionization schemes. To date there are ionization schemes of more than 37 elements tested with Ti:Sa lasers.

For the spectroscopy of Rydberg resonances and the development of new ionization schemes, a grating assisted Ti:Sa laser was constructed and the ionization potential of technetium and actinium were deduced from the analysis of observed Rydberg resonances [MGR⁺10, RRH⁺12]. The development of ionization schemes is usually performed off-line with stable or very long lived isotopes. For radioactive elements and their isotopes that cannot be studied off-line, the required spectroscopy work has to be performed on-line and is then called in-source spectroscopy. This was demonstrated for the development of a polonium ionization scheme at ISOLDE [CMF⁺08]. This scheme was applied later for the determination of nuclear charge radii [CDS⁺11].

1.3 Objective of the thesis

The ISOLDE-RILIS laser system shall be upgraded to incorporate an additional branch of all solid-state tunable lasers and in this way expand the well-established system of dye lasers. On top of a number of advantages in respect to spectral coverage and overall performance, this step will significantly reduce the time needed to switch between different excitation schemes or different elements in RILIS routine operation, as one system can be set-up and tuned while the other is in use. The new laser system will consist of broadly tunable nanosecond titanium:sapphire (Ti:Sa) lasers that will be designed on basis of the solid-state Ti:Sa laser constructions in operation at University of Mainz and elsewhere. They will be built and put into operation during the thesis. The combination of dye and Ti:Sa holds the potential to improve ionization schemes. In the letter of intent to the INTC [AAB⁺10] the ISOLDE users pointed out the relevance of the availability of radioactive ion beams of astatine for extending the studies of β -delayed fission in the lead region [AEH⁺10], measurements of hyperfine structure and isotope shifts to determine the nuclear charge radii of astatine. It was also suggested in this letter of intent, to collaborate with TRIUMF for the laser spectroscopy

activities of astatine[Las12]. For radioactive elements in general and astatine in particular, resonance ionization in-source spectroscopy with broad-band lasers will be deployed to develop ionization schemes, subsequently precision spectroscopy of high lying Rydberg levels can be used to deduce the first ionization potential of these elements with high accuracy. First on-line measurements with astatine are planned in collaboration with the TRILIS group at TRIUMF, Vancouver. As future improvement, high resolution in-source spectroscopy using a narrow bandwidth Ti:Sa laser can be performed to investigate hyperfine splitting and isotope shifts.

Part I

Theory and Methods

Chapter 2

Atom light interaction

The part of the work at hand describes the processes of the generation of photons and discusses their use for the study of atomic properties. The underlying principle is the atom-light interaction for which the main ingredients will be explained in this chapter.

2.1 Electronic structure of the atom

2.1.1 Energy levels of the hydrogen atom

The Hamilton operator for the hydrogen atom which consists of a proton with mass m_p and charge $+e$ and an electron with mass m_e and charge $-e$ [Dem10] is

$$\mathcal{H} = -\frac{\hbar^2}{2m_p}\Delta_1 - \frac{\hbar^2}{2m_e}\Delta_2 - \frac{e^2}{4\pi\epsilon_0 r}. \quad (2.1)$$

The Laplace operators $\Delta_{1,2}$ relate to the radii \mathbf{r}_1 and \mathbf{r}_2 of the electron and the proton. The motion of the system can be separated into the centre of mass motion (cm) and a particle with reduced mass $\mu = m_e + m_p / (m_e + m_p)$ at a position r relative to the cm at $r = 0$. The wave functions that describe the relative system are the solution of the Schrödinger equation

$$-\frac{\hbar^2}{2\mu}\Delta\psi - \frac{e^2}{4\pi\epsilon_0 r}\psi = E\psi \quad (2.2)$$

The solution is obtained using a separation ansatz in spherical coordinates

$$\psi(r, \theta, \phi) = R(r)Y_l^m(\theta, \phi) \quad (2.3)$$

using the radial function $R(r)$ and the $Y_l^m(\theta, \phi)$. In order to obtain the eigenvalues determined by the Coulomb potential one solves the radial equation, which depends on r . This is executed in [Dem10]. The energy levels E_n are given

$$E_n = -\mu \frac{e^4}{8\epsilon_0^2 h^2} \frac{1}{n^2} \quad (2.4)$$

$$= -\frac{R^*}{n^2}. \quad (2.5)$$

2.1.2 Hydrogen-like atoms

For alkaline or hydrogen-like atoms, the inner electrons have a charge of $-(Z-1)e$ and shield the charge of $+Ze$ of the nucleus. The average radius of the fully occupied orbital is given by r_c . For a large distance r of the electron from the nucleus the potential $V(r)$ of the Hamiltonian describing this system can be written as

$$V(r) = -\frac{e}{4\pi\epsilon_0 r} \quad (2.6)$$

This is the same Coulomb potential as in the hydrogen case. For positions of $r < r_c$ the potential depends on the charge distribution given by the electrons and the nucleus. One defines an effective potential $V_{\text{eff}}(r)$

$$-\frac{Ze}{4\pi\epsilon_0 r} < V_{\text{eff}}(r) < -\frac{e}{4\pi\epsilon_0 r} \quad (2.7)$$

The energy spectrum can be expressed using the Rydberg formula and an effective principal quantum number $n^* = n - \delta_{n,l}$ that is modified by the quantum defect δ

$$E_{n,l} = -\frac{R^*}{n^{*2}} \quad (2.8)$$

$$= -\frac{R^*}{(n - \delta_{n,l})^2} \quad (2.9)$$

The quantum defect depends on the principal quantum number n and the angular momentum l . The quantum defects are larger for s-electrons $l = 0$ and decrease for increasing angular momentum. This can be explained with the different probability of presence in the core and therefore resulting in a smaller deviation from the hydrogen Coulomb potential.

The dependence of δ from n can be expressed using a Taylor series expansion for the quantum defect. This is known as the Ritz expansion. [Rit11, DS91]

$$\delta(n) = A + \frac{B}{(n - A)^2} \quad (2.10)$$

And we obtain the Rydberg-Ritz formula

$$E_{n,l} = -\frac{R^*}{\left(n - A + \frac{B}{(n-A)^2}\right)^2} \quad (2.11)$$

2.1.3 Determination of ionization potentials

Ritz pointed out that the term energies of the Rydberg-series of a hydrogen-like atom can be expressed as [DS91, Sea83]

$$E_n = -\frac{2R_M}{2n^{*2}} \quad (2.12)$$

For further reading reference is given to the review about Rydberg atoms [Gal88] and [SD11]. Interaction with electric field and the blackbody radiation is described in [CG78] and [GC79].

2.2 Interaction of light with matter

The interaction of light with matter is subject to both main parts of this work. The basic formulas are used to obtain cross sections and life times. The explanations follow the book [Koe76]

2.2.1 Blackbody radiation

The radiation density $\rho\nu$ in a bandwidth $d\nu$ of the electromagnetic radiation emitted from an ensemble of atoms in thermal equilibrium at a temperature T is described by Planck's law:

$$\rho(\nu)d\nu = \frac{8\pi\nu^2}{c^3} d\nu \frac{1}{e^{h\nu/kT} - 1} h\nu \quad (2.13)$$

$$= n(\nu)d\nu f_{BE}(\nu, T) E(\nu) \quad (2.14)$$

With h Planck's constant, k Boltzmann's constant and the c speed of light. One can separate the formula into three parts: The mode density $n(\nu)$ [modes/cm³/s⁻¹]. The Bose-Einstein statistics $f_{BE}(\nu, T)$ which describes the fundamental occupation probability of each mode with photons of the energy $E(\nu)$.

2.2.2 Boltzmann statistics

If one considers an ensemble of atoms that can be in a ground state $|1\rangle$ or an excited state $|2\rangle$. The energy difference of these states $E_2 - E_1 = h\nu_{21}$ corresponds to the frequency ν_{21} of a photon.

At a given temperature T of the atoms the number of atoms in state $|1\rangle$ and $|2\rangle$ is given by N_1 and N_2 , respectively. Their relative population is expressed by the Boltzmann ratio

$$\frac{N_2}{N_1} = \frac{g_2}{g_1} e^{-\frac{h\nu_{21}}{kT}} \quad (2.15)$$

The factors g_1 and g_2 are the grade of degeneracy of the two levels. For the further discussion an idealized non degenerate system is regarded ($g_1 = g_2 = 1$).

For a Nd:YAG laser emission line at $\lambda = 1064 \text{ nm}$ at room temperature ($T = 300 \text{ K}$), relative population is $2.6 \cdot 10^{-20}$.

2.2.3 Einstein coefficients

The states $|1\rangle$ and $|2\rangle$ of the atoms in an ensemble are connected by a radiative transition driven by a photon of the energy $h\nu_{21} = E_2 - E_1$. Under idealized conditions of a non degenerate two-level system one can assume:

$$N_1 + N_2 = N_{\text{tot}} = \text{const.} \quad (2.16)$$

Three types of interaction can then be described:

Absorption Absorption occurs when a photon with a frequency ν_{21} is removed from the light field and excites one of the atoms from the level to the upper level. This means that the number of atoms in $|1\rangle$ decreases proportional to the amount of photons of the frequency ν in the light field. This is expressed as follows

$$\frac{\partial N_1}{\partial t} \equiv \dot{N}_1 = -B_{12}\rho(\nu)N_1 \quad (2.17)$$

With B_{12} is the proportional constant and $\rho(\nu)$ is the radiation density, called the Einstein-B coefficient. The product $B_{12}\rho(\nu)$ is understood as the probability per unit frequency that the transition takes place.

Spontaneous emission If an atom is in the upper level it may radiate a photon into the light field to reach the energetic lower level. Considering the ensemble of photons, this is proportional to the population in the upper level and a probability constant:

$$\dot{N}_2 = -A_{21}N_2 \quad (2.18)$$

The constant A_{21} is characteristic for a pair of energy levels. It is called the spontaneous transition probability or the Einstein-A coefficient. This statistical emission of photons is called fluorescence.

Stimulated emission In the presence of a radiation field $\rho(\nu_{21})$ containing photons of the energy $h\nu_{21}$ an induced emission takes place which depopulates the upper level:

$$\dot{N}_2 = -B_{21}\rho(\nu_{21})N_2 \quad (2.19)$$

Einstein's relations From the assumption (eqn. 2.16) that no other loss channels are present in the two-level system, one obtains:

$$\dot{N}_1 = -\dot{N}_2 = B_{21}\rho(\nu)N_2 - B_{12}\rho(\nu)N_1 + A_{21}N_2 \quad (2.20)$$

For the thermal equilibrium the population is constant ($\dot{N}_1 = \dot{N}_2 = 0$) and one yields

$$B_{21}\rho(\nu)N_2 + A_{21}N_2 = B_{12}\rho(\nu)N_1 \quad (2.21)$$

$$\frac{N_2}{N_1} = \frac{B_{12}\rho(\nu)}{B_{21}\rho(\nu) + A_{21}} \quad (2.22)$$

Using the Boltzmann equation (eqn 2.15) for the expression N_2/N_1 one obtains

$$\rho(\nu_{21}) = \frac{A_{21}/A_{12}}{g_1/g_2 B_{21}/B_{12} \exp[h\nu_{21}/kT] - 1} \quad (2.23)$$

By comparison of the coefficients with the Planck formula (Eqn. 2.14) one obtains Einstein's relations:

$$\frac{A_{21}}{B_{21}} = \frac{8\pi\nu^2 h\nu}{c^3} \quad (2.24)$$

$$B_{21} = \frac{g_1}{g_2} B_{12} \quad (2.25)$$

If the levels are not degenerated $g_1 = g_2$ the Einstein-B coefficients for stimulated emission and absorption are equal $B_{21} = B_{12}$.

2.3 Lifetimes and line functions

The solution of the rate equation for the spontaneous emission (eqn. 2.18) is

$$N_2(t) = N_2(0) \exp \left[\frac{-t}{\tau_{21}} \right] \quad (2.26)$$

With the lifetime τ_{21} for spontaneous radiation of the state $|2\rangle$ given as the inverse

$$\tau_{21} = \frac{1}{A_{21}} \quad (2.27)$$

Doppler broadening If an atom is in motion in the direction z with the velocity v its transition frequencies at rest ω_0 become Doppler shifted.

$$\omega = \omega_0(1 + v_z/c) \quad (2.28)$$

If one regards an ensemble of atoms in thermal equilibrium, the velocities are Maxwell-Boltzmann distributed. the number density $n(v_z)dv_z$ is given by

$$n(v_z)dv_z = \frac{N}{\sqrt{\pi}v_w} e^{-(v_z/v_w)^2} \quad (2.29)$$

With v_w the most probable velocity given by

$$v_w = \sqrt{\frac{2k_B T}{m}} \quad (2.30)$$

in which k_B is the Boltzmann constant and T is the equilibrium temperature, m is the mass of the atom and N is the atom density. A substitution $v_z = (\omega - \omega_0)c/\omega_0$ gives an expression for $n(\omega)d\omega$ which is the definition of the Doppler-broadened intensity profile

$$P(\omega) = P(\omega_0) \exp \left[-\left(c \frac{\omega - \omega_0}{\omega_0 v_w} \right)^2 \right] \quad (2.31)$$

This is a Gaussian function centred at ω_0 with a width $\delta\nu_D$ given by the Doppler width

$$\delta\nu_D = \frac{2\nu_0}{c} \sqrt{\frac{2RT}{M} \ln 2} \quad (2.32)$$

Chapter 3

Tunable lasers

The RILIS technique requires a number of tunable lasers. Two different types of tunable lasers are most suitable: Organic-dye lasers and solid-state titanium:sapphire (Ti:Sa) lasers.

3.1 Laser principle

A laser is an optical oscillator that produces coherent radiation, by stimulated emission of light. It consists of an active gain medium, a pump source and a resonator. The active media of the lasers described in this chapter, are organic dye molecules dissolved in a liquid solvent or Ti^{3+} ions embedded in an Al_2O_3 host-crystal (sapphire, corundum). The pump sources are commercial frequency doubled Nd:YAG lasers.

Two different processes play a role when light interacts with the laser medium: Amplification by stimulated emission of photons into the resonator mode and losses caused by absorption and spontaneous emission.

Losses originating from scattering and absorption in the active medium are described by a damping constant α_s . Other losses are caused by the reflectivity $\mathcal{R} < 1$ of the resonator mirrors with the reflectivity \mathcal{R}_1 and \mathcal{R}_2 . The loss coefficient for the mirrors is normalized to the round trip length $2d$ and is given by [ST07]

$$\alpha_m = \alpha_{m1} + \alpha_{m2} = \frac{1}{2d} \ln \frac{1}{\mathcal{R}_1 \mathcal{R}_2} \quad (3.1)$$

The loss per round trip is then given by adding the two coefficients:

$$\alpha_r = \alpha_s + \alpha_m \quad (3.2)$$

The amplifier gain can be defined as [ST07]

$$\gamma_0(\nu) = N_0\sigma(\nu) \quad (3.3)$$

and is determined by the equilibrium population density difference $N_0 = N_2 - N_1$ and the transition cross section

$$\sigma(\nu) = \frac{\lambda^2}{8\pi\tau_{\text{sp}}}g(\nu) \quad (3.4)$$

where τ_{sp} is the effective spontaneous lifetime of the excited level ($\propto 1/A_{21}$), $g(\nu)$ is the transition line shape and $\lambda = \lambda_0 n$ is the wavelength in the medium with refractive index n . The optical feedback required for laser operation is obtained by placing the amplifier medium into an optical resonator. For a Fabry-Perot type resonator the phase shift coefficient k is given by

$$k = \frac{2\pi\nu}{c} \quad (3.5)$$

Two lasing conditions have to be fulfilled [ST07]:

$$\text{Gain condition} \quad \gamma_0(\nu) > \alpha_r \quad (3.6)$$

$$\text{Phase condition} \quad 2kd = 2\pi n, \quad (n = 1, 2, \dots) \quad (3.7)$$

The phase condition defines longitudinal and transverse resonator modes. The longitudinal modes are described in section 3.5.1. Transverse resonator modes are considered in [ST07]. To satisfy the gain condition one obtains that $\gamma_0 > 0$ must be positive. This is true for $N_2 > N_1$ in the so called population inversion. Adding wavelength dependent losses $\alpha(\nu)$ to the resonator is the basic concept for wavelength selection in tunable lasers as described in section 3.5.

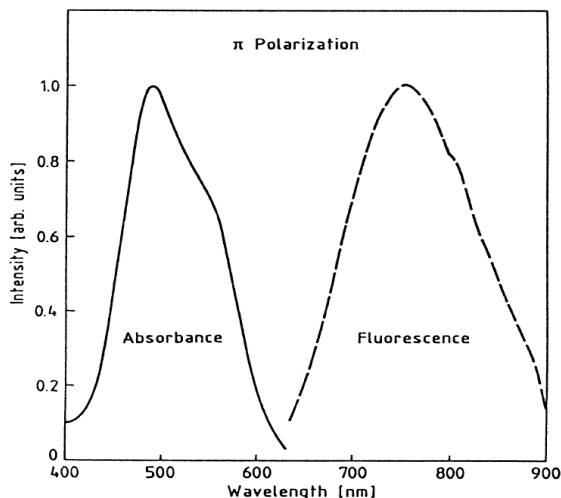


Figure 3.1: Absorption and fluorescence spectrum of Ti:sapphire (Figure taken from [RAA⁺06]).

3.2 Ti:Sa laser

Lasing of titanium-doped sapphire ($\text{Ti}^{3+}:\text{Al}_2\text{O}_3$) was demonstrated by Moulton *et al.* in 1982 [M⁺82]. The first pulsed operation was observed as the Ti:Sa crystal was pumped when the 503 nm output of a flashlamp pumped Coumarin-504 dye laser [Mou86]. Eggleston *et al.* describe the characteristics and kinetics of gain switched Ti:Sa lasers pumped by a frequency doubled Nd:YAG laser [EDK88].

Absorption and fluorescence spectroscopy of the Ti:Sa medium was performed by Moulton [Mou86] and the results are shown in Figure 3.1. The absorption band in the blue-green range of the visible spectrum allows pumping with the 532 nm output of a frequency doubled solid-state Nd:YAG laser. The broad gain bandwidth of about 400 nm allows the construction of a widely tunable laser.

3.2.1 Ti:Sa - a vibronic laser medium

An introduction to the theory of solid-state tunable lasers is given in [Sen02, RAA⁺06], a detailed description with respect to Ti:sapphire can be found in [Mou86, ASH86]. The active ion in the Ti:Sa laser medium is the Ti^{3+} ion. It has a closed [Ar] shell and a single $3d$ electron. The ion is embedded in a sapphire host in which it substitutes the Al^{3+} ion in $\approx 0.25\%$ of the lattice sites of the Al_2O_3 crystal.

The Hamiltonian \mathcal{H}_T of the Ti^{3+} ion in a vibrating lattice system consists of the contribution from the Hamiltonian for the ion \mathcal{H}_I , the crystal field generated by a static lattice \mathcal{H}_{CF} and the Hamiltonian describing the vibration of the lattice \mathcal{H}_V :

$$\mathcal{H}_T = \mathcal{H}_I + \mathcal{H}_{CF} + \mathcal{H}_V \quad (3.8)$$

The static crystal lattice which is described by \mathcal{H}_{CF} leads to a splitting of the 5-fold¹ degenerate electronic level of the ion. The cubic field contribution results in a three-fold degenerate ground state 2T_2 and a two-fold degenerated excited state 2E . The energy difference ${}^2E - {}^2T_2$ was obtained from absorption spectroscopy at liquid nitrogen temperature (77 K). A diffuse double-humped band was observed (c.f. Fig. 3.1) with maxima at 18450 cm^{-1} and 20300 cm^{-1} corresponding to 540 nm and 490 nm, respectively. This additional splitting originates from contributions from the trigonal field components [HH68].

The crystal field effects depend on both the ionic coordinates and the electronic coordinates. If one assumes that the lattice ions re-orientate adiabatically with respect to the electronic coordinates (Born-Oppenheimer approximation), one can decouple $(\mathcal{H}_I + \mathcal{H}_{CF})$ and \mathcal{H}_V . Small oscillations of the lattice can be approximated by a parabolic potential V_L . The resulting eigenstates $|n\rangle$ are the eigenstates of the harmonic oscillator with eigenenergies E_n

$$E_n = h\nu_{\text{phon}}(n + 1/2) \quad (3.9)$$

where h is Planck's constant, n is the vibronic quantum number and ν_{phon} is the phonon frequency.

As the vibronic and the electronic-crystal-field are decoupled one can write the eigenvalues E_T as

$$E_T = E_{CF} + h\nu_{\text{phon}}(n + 1/2) \quad (3.10)$$

This describes the electron-phonon coupling of the system. The total energy given by the crystal field splitting has a superimposed manifold of equally spaced vibrational levels. This is illustrated in a configuration-coordinate diagram displayed in Fig. 3.2. The equilibrium-distance Q between the Ti^{3+} ion and the neighbouring lattice ion depends on the electronic state of the Ti^{3+} ion. The arrows indicate the radiative (green and red arrows) and non-radiative (dashed arrows) transitions, that form the four level laser scheme of the Ti:Sa laser.

3.3 The four level vibronic laser

The four level system of the Ti:Sa laser is shown in Fig. 3.2. Starting in the vibronic ground state ($n = 0$) of the electronic level 2T_2 , denoted as $|g\rangle$, the ion can absorb a photon from the

¹Neglecting spin.

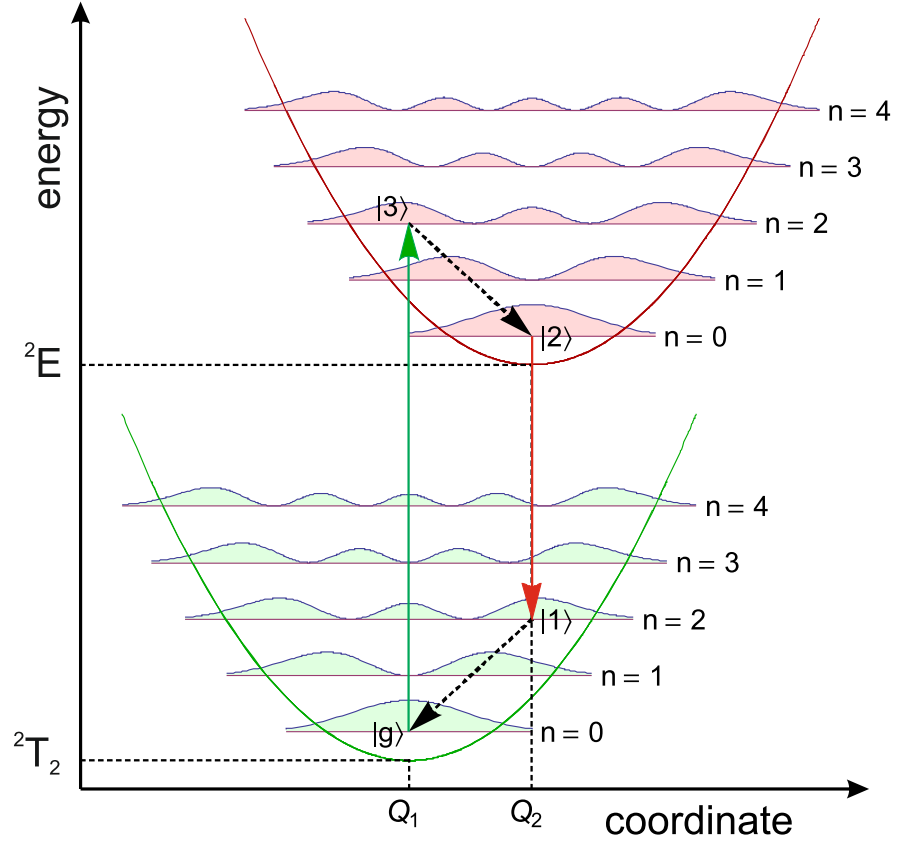


Figure 3.2: Configuration-coordinate diagram for the Ti^{3+} ion coupled to the crystal field and the phonons of the sapphire host. The coordinate Q is the distance from the Ti^{3+} ion to the next neighbour. The degenerate energy levels of the Ti ion are split to 2T_2 and 2E in the crystal field. Phonon coupling leads to vibronic states on top of the electronic levels. The waves plotted at the vibronic levels are probability density. The equilibrium coordinate is different for the two electronic states as a result of changing ion-lattice coupling. The arrows indicate the path for lasing in a four level scheme. Dashed arrows indicate fast radiation-less decay into the vibronic ground state. The vertical green arrow indicates absorption of a photon, the vertical red arrow indicates one possible transition to one of the vibrational states in the lower electronic state. The fact that the radiative transitions follow a vertical line is explained by the Franck-Condon principle

pump laser field and become excited to the 2E electronic state. As the change of the electronic configuration is much faster than the re-orientation of the ion in the lattice (Born-Oppenheimer approximation), the coordinates can be considered as static. The overlap of the wavefunction is greatest for a vibronic level $n > 0$ of the excited level ($n = 2$ in the picture). This vertical transition is described by the Franck-Condon principle [FD26, Con26]. The excited state $|3\rangle$ decays fast to the $n = 0$ vibrational ground-state of the 2E electronic level noted as $|2\rangle$, before it fluoresces. This is known as the Kasha rule. [AW12]. The fluorescence occurs again vertically to the state $|1\rangle$. The spectral width of the transition is given by the possible final vibrational states. A fast radiation-less decay from $|1\rangle$ brings the ion back to the vibrational ground state $|g\rangle$. In such schemes the emission spectrum is independent of the pump wavelength. This is reflected in the Kasha-Vavilov rule [AW12]. Regarding an ensemble of Ti ions, inversion is reached when the population N_2 in the upper laser level $|2\rangle$ is greater than the population N_1 of the lower laser level $|1\rangle$. This is easily achieved as the fluorescence lifetime $\tau_{21} = 3.2 \mu\text{s}$ is much longer than the lifetime of the lower laser level which is in the order of picoseconds.

3.4 Dye laser

The dye laser is also a vibronic laser, therefore the principles mentioned before also apply for this type of tunable lasers. The active medium of dye lasers is an ensemble of conjugated aromatic organic molecules. These molecules exhibit a widely spread system of de-localized π electrons, resulting in a high photon absorption cross-section. Fig. 3.3 shows the Jablonski diagram [Jab35] (level scheme) of a dissolved dye. The scheme consists of electronic singlet states S and electronic triplet states T . The levels are broadened by vibrational states of the molecule. By absorption of a photon from the pump field the dye is excited from the S_0 to the S_1 state. A fluorescence photon is emitted when the molecule is de-excited from the lowest vibrational state to a vibrational state $n > 0$ of the S_1 state (Kasha's rule). The transition $S_1 \rightarrow T_1$ is dipole forbidden as it includes a spin-flip.

If the vibronic states of S_1 and T_1 overlap, a non-radiative transition to the triplet state is probable. This is called intersystem crossing. Triplet states are disadvantageous for the lasing process for two reasons. Firstly, the $T_1 \rightarrow S_1$ transition creates a loss for the lasing process as the forbidden transition $T_1 \rightarrow S_0$ is long-lived. The process is called phosphorescence. Secondly, the T_1 state can be further excited by absorption of pump photons or photons emitted from other dye molecules. This reduces the quantum efficiency of the laser.

To remove the triplet states from active area, the dye solution is circulated at high speeds through the laser resonator. This also allows cooling of the dye solution.

Further information about dye lasers can be found in [Dem10, Ren12, Sch73, Wal74].

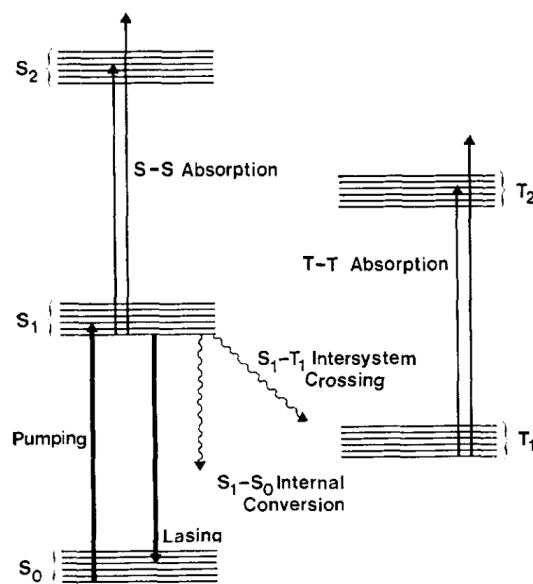


Figure 3.3: Jablonski diagram of a laser dye molecule [Wal74]. The molecule exists in electronic singlet or triplet states S, T . The levels are broadened by vibrational bands of the molecule. Lasing occurs from the vibrational ground state of the excited singlet state S_1 to a vibrational state of the S_0 electronic state. Non-radiative transitions lead to triplet states that reduce the quantum efficiency of the laser.

3.5 Wavelength selection in tunable lasers

The general approach for the selection of the desired wavelength is to introduce losses for unwanted frequencies. Figure 3.4 shows schematically the stages of wavelength selection applied for the Ti:Sa laser. The amplifier gain $g(\nu)$ is given by the laser medium. The length of the resonator is fixed and sets the free spectral range (spacing in frequency) of the resonator modes. Depending on the chosen mirror set the supported wavelengths are limited to a range between 50 and 50 nm. For wavelength selection within the mirror set range, two tunable elements are used: A three-plate Lyot filter and a thin Fabry-Perot etalon.

3.5.1 Resonator modes

The high reflecting mirror (HR) and the output coupler mirror (OC) build the boundary for the laser cavity. This resonator is a Fabry-Perot resonator. The frequencies that are constructively superimposed are called resonator modes. They are defined by the distance d of the two mirrors. The frequency difference $\Delta\nu_{\text{FSR}}$, the free spectral range (FSR), is given by

$$\Delta\nu_{\text{FSR}} = \frac{c}{2d}. \quad (3.11)$$

with c the speed of light. The spectral width $\delta\nu$ of each of the resonator modes is determined by the reflectivity ($\mathcal{R}_1, \mathcal{R}_2$) of the cavity mirrors

$$\delta\nu = \frac{\Delta\nu_{\text{FSR}}}{\mathcal{F}}. \quad (3.12)$$

For the Ti:Sa resonator with a typical length $d = 0.5$ m the FSR is $\Delta\nu_{\text{FSR}} = 0.3$ GHz. With the finesse \mathcal{F} of the resonator given by the amplitude reflectances $r_i = \sqrt{\mathcal{R}_i}$ [ST07]:

$$\mathcal{F} = \frac{\pi\sqrt{|r_1 r_2|}}{1 - |r_1 r_2|}. \quad (3.13)$$

The transmittance function $\mathcal{T}(\nu)$ of a Fabry-Perot resonator can then be expressed as [ST07]

$$\mathcal{T}_{\text{resonator}}(\nu) = \frac{\mathcal{T}_{\text{max}}}{1 + (2\mathcal{F}/\pi)^2 \sin^2[\pi\nu/\Delta\nu_{\text{FSR}}]}. \quad (3.14)$$

3.5.2 Resonator mirrors

The laser resonator is built from dielectric mirrors. They are made from a glass substrate which is coated with multiple layers of dielectric material (e.g. $\text{SiO}_2/\text{TiO}_2$) [Lay11]. The

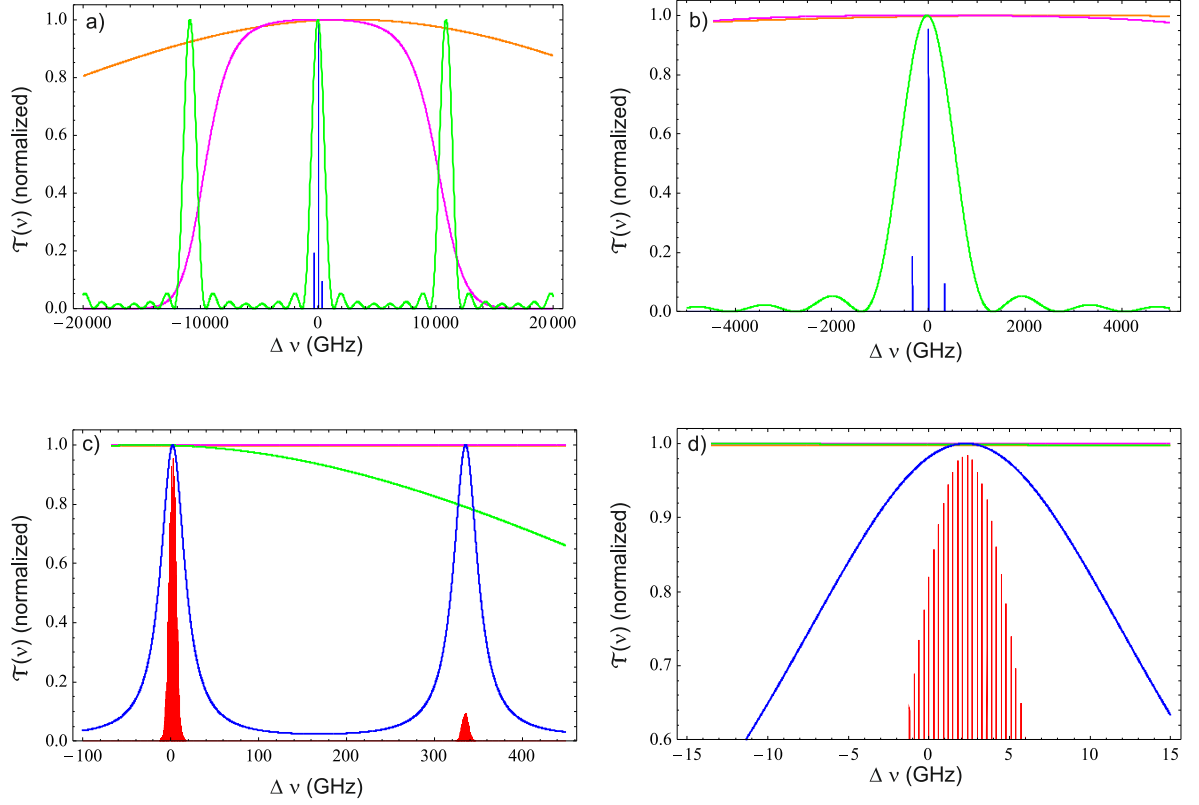


Figure 3.4: Wavelength selection in the Ti:Sa resonator. The graphs show schematically the transmission functions $\mathcal{T}(\nu)$ of the different frequency selective elements and their combination. The vertical lines plotted under the envelopes illustrate the signal gain after ten round trips in the resonator. The offset of each graph is $\nu_0 = 374.6$ THz, corresponding to a wavelength of 800 nm. a) The normalized gain curve $g(\nu)$ of the Ti:Sa medium is plotted in orange. The combined transmission curve of the cavity mirrors (magenta) selects one transmission maximum of the Lyot filter (green curve). b) Zoom to the selected Lyot mode. The signal obtained from the thin etalon is shown as blue spikes. The losses in the resonator (not indicated) prevent the two side modes from lasing c) The etalon fringes are plotted as the blue curve. The resonator modes are drawn as red spikes. The side mode at 350 GHz is not amplified due to losses in the resonator d) Zoom into one etalon maximum. The resonator modes with a FSR of 0.3 GHz become resolved. The signal from the resonator has a width of ≈ 4 GHz when 40% loss is assumed.

behaviour of these layers can be calculated using the matrix formalism, (c.f. section 3.7.2). Further explanations of matrix theory of multilayer optics are found in [ST07]. The cavity mirrors are coated such that they have a high reflectivity ($\mathcal{R} > 99.9$) in a certain wavelength range (e.g. 910-1070 nm) and high transmission for wavelength towards the gain maximum.

3.5.3 Lyot-Filter

The Lyot filter used in the Ti:Sa cavity is constructed from three birefringent crystals with different thicknesses. It is therefore also called birefringent filter (BRF, BiFi) or a birefringent tuner.

A p-polarized laser beam travelling through a birefringent medium is split into an ordinary (o) and an extra-ordinary (e) beam. Both are polarized perpendicular to each other. The difference of the two refractive indices n_o and n_e for the two axes of the crystal, causes a phase shift of $\delta = (2\pi/\lambda)(n_e - n_o)L$ for the transmitted light of the wavelength λ and the thickness of the plate L . This wavelength dependent retardation results in elliptical polarization. This causes reflection and therefore losses for the s-polarized fraction at Brewster surfaces inside the resonator. For a phase of $\delta = 2m\pi$ the polarization is unchanged and no losses occur. The transmission through one plate is given by [Dem07]:

$$\mathcal{T}(\lambda) = \mathcal{T}_0 \cos^2 \left(\pi \frac{\Delta n L}{\lambda} \right). \quad (3.15)$$

Combining N birefringent plates with thickness such that the next plate has twice the thickness of the previous, one obtains a total transmission function [KS92]

$$\mathcal{T}(\lambda) = \frac{\sin^2 \left(\frac{2^N \pi (n_e - n_o) l}{\lambda} \right)}{2^{2N} \sin^2 \left(\frac{\pi (n_e - n_o) l}{\lambda} \right)^2}, \quad (3.16)$$

The free spectral range $\Delta\nu_{\text{FSR}}$ is given by the thinnest plate ($L = l$), the spectral width $\delta\nu$ is defined by the thickest plate ($L = D$):

$$\Delta\nu_{\text{FSR}} = \frac{c}{\Delta n l} \quad (3.17)$$

$$\delta\nu = \frac{c}{2^{N-1}} \Delta n D. \quad (3.18)$$

The Lyot filter can be tuned by changing Δn . If the angle between the optical axis of the crystal and the propagation direction of the laser beam is changed by rotating the filter, the index n_e is changed.

3.5.4 Thin etalon

A tunable spectral filter like a Fabry-Perot etalon is an effective means of suppressing unwanted frequencies in the laser resonator. For the application in the Ti:Sa laser a thin (typically $d = 0.3$ mm) glass substrate, with a broad-band reflective coating of $\mathcal{R} = 40\%$ on both sides is used. The formalism to obtain the transmission is exactly the same as for the laser resonator. The only difference is that d is to be replaced with the optical path length nd , where n is the refractory index of the etalon material. The tuning of the etalon is performed by changing the angle θ with respect to the beam propagation direction which changes the optical path length inside the etalon. An expression for the transmission is given in [ST07]:

$$\mathcal{T}_{\text{etalon}}(\nu) = \frac{\mathcal{T}_{\text{max}}}{1 + (2\mathcal{F}/\pi)^2 \sin^2[\pi\nu/\Delta\nu_{\text{FSR}} \cos \theta]} \quad (3.19)$$

For an etalon with $d = 0.3$ mm and a reflectivity of $\mathcal{R} = 40\%$ one obtains $\Delta\nu_{\text{FSR}} = 300$ GHz and $\delta\nu = 90$ GHz. The graphs shown in Fig. 3.4 c) and d) were calculated with parameters close to those from the Ti:Sa laser system. The resonator signal was estimated by calculating $(\mathcal{T}_{\text{tot}})^{10}$ for 10 round trips in the cavity. If one assumes further that modes below the lasing threshold of a gain of 0.6 are suppressed due to losses, one obtains a laser line width of ≈ 4 GHz. At this point the bandwidth of the Ti:Sa laser radiation is comparable to the dye lasers used at RILIS for the production of radioactive ion beams.

3.5.5 Thick etalon

Another application of RILIS is the in-source laser spectroscopy using a narrow-band dye laser. In order to complement the in-source spectroscopy capabilities of RILIS, the narrow-band operation of the Ti:Sa (NB-Ti:Sa) is desired.

The line-width reduction in the NB-dye laser is achieved by inserting a thick etalon. This concept was introduced by [Hän72]. The resulting transmission and expected signal from the NB-Ti:Sa, equipped with a thick etalon is shown in Fig. 3.5. The calculations were performed assuming a thick uncoated etalon with a thickness $d=6.35$ mm, made from a YAG substrate². The laser line width can be reduced to < 1 GHz.

3.5.6 Grating

Gratings are widely used as the wavelength selective elements in dye lasers [Hän72, Lit78] and were recently introduced to the Mainz-Type Ti:Sa laser systems and are available at Mainz-RISIKO, TRIUMF-ISAC and IGISOL [Mat10, TBC⁺10, RMK⁺12]. The commercial

²Specifications were proposed by Volker Sonnenschein, University of Jyväskylä. The etalon was purchased from *Layertec*.

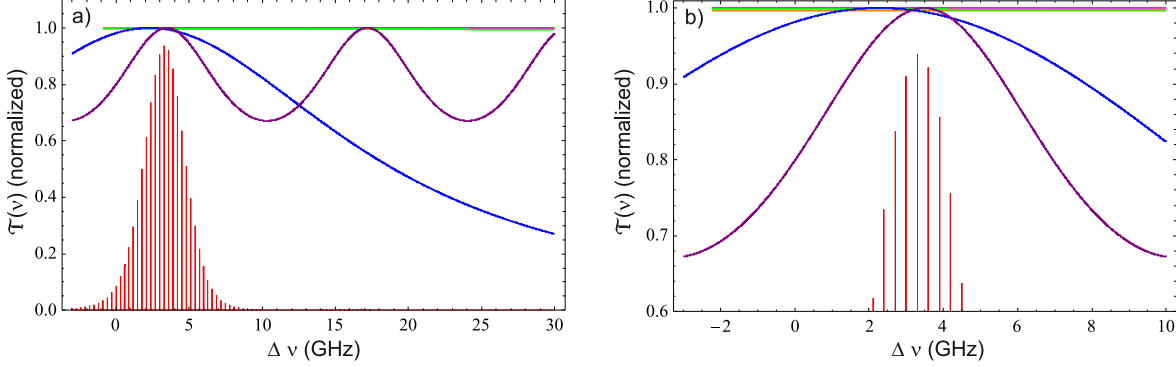


Figure 3.5: Reduction of laser bandwidth using a thick etalon. a) The transmission curve of the low finesse thick etalon is illustrated as the purple curve. b) Zoom to the transmission maximum of the thick etalon. The line width of the NB-Ti:Sa laser is ≈ 1 GHz, assuming a laser threshold gain requirement of 0.6.

Ti:Sa laser system used at ORNL-HRIBF is based on gratings for the wavelength selection [GGs⁺08]. The use of gratings allows scanning the tunable laser continuously over a wide range of wavelengths. The grating based Ti:Sa lasers were used for scheme development [RSG⁺11] and determination of ionization potentials from spectroscopy of Rydberg series [MGR⁺10]. The frequency selection in tunable lasers is discussed in [Dem07, Koe76, ST07]. The application to Ti:Sa lasers is explained detailed in [Hor03].

3.6 Generation of higher harmonics

The accessible wavelength range of the RILS lasers can be extended by the generation of higher harmonics of the fundamental laser radiation. The process is based on non-linear optical effects when laser light passes through optical dense media. The process of the generation of the second harmonic and frequency summing is described in [ST07, Boy68]. Here the basic formulae are introduced.

In a dielectric medium, the relation between the polarization density \mathcal{P} and the electric field of a plane wave $\mathcal{E} = E_0 \cos(\omega t - kz)$ is linear for small E_0 .

$$\mathcal{P} = \epsilon_0 \chi \mathcal{E} \quad (3.20)$$

Where χ is the linear susceptibility which relates the material constants refractive index n and the dielectric constant ϵ to $n^2 = \epsilon/\epsilon_0 = 1 + \chi$.

When the field strengths of the applied wave reaches values comparable to interatomic electric fields, a non-linear response of the medium is obtained. This can be described mathematically

in a non-linear polarization function. A Taylor series of equation 3.20 about $\mathcal{E} = 0$ can be used to express the response function

$$\mathcal{P} = \epsilon_0 \chi \mathcal{E} + 2d\mathcal{E}^2 + 4\chi^{(3)}\mathcal{E}^3 + \dots = \epsilon_0 \chi \mathcal{E} + \mathcal{P}_{\text{NL}} \quad (3.21)$$

With d the second order non-linear coefficient. The process of frequency doubling also referred to as second harmonic generation (SHG) is based on a second order non-linear effect so that higher orders than (2) can be neglected.

$$\mathcal{P}_{\text{NL}} = 2d\mathcal{E}^2 \quad (3.22)$$

The optical non-linear medium can be described as a source \mathcal{S} of radiation in a scattering process

$$\mathcal{S}(t) = -\mu_0 \frac{\partial^2}{\partial t^2} \mathcal{P}_{\text{NL}} \quad (3.23)$$

$$= -\mu_0 \frac{\partial^2}{\partial t^2} 2d\mathcal{E}^2 \quad (3.24)$$

$$= -\mu_0 2d \frac{\partial^2}{\partial t^2} E_0^2 \cos^2(\omega t - kz) \quad (3.25)$$

$$= -\mu_0 2d E_0^2 \frac{\partial^2}{\partial t^2} \frac{1}{2} (\cos(2\omega t - 2kz) + 1) \quad (3.26)$$

$$= 4\mu_0 \omega^2 d E_0^2 \cos(2\omega t - 2kz) \quad (3.27)$$

The electromagnetic wave generated by the source \mathcal{S} depends on the square of the input amplitude E_0^2 and oscillates at a doubled input frequency 2ω .

To allow the source wave at a frequency $\omega_3 = 2\omega$ with a wave vector \mathbf{k}_3 to be emitted, two conditions, referred to as the frequency matching condition and the phase-matching condition have to be met

$$\omega_1 + \omega_2 = \omega_3 \quad (3.28)$$

$$\mathbf{k}_1 + \mathbf{k}_2 = \mathbf{k}_3 \quad (3.29)$$

For the SHG the degenerated case of $\omega_1 = \omega_2$ is regarded. When the waves travel collinear and using the dispersion relation $|\mathbf{k}| = n(\omega)\omega/c$, the conditions simplify to

$$2\omega_1 = \omega_3 \quad (3.30)$$

$$2n_1\omega_1 = n_3\omega_3 \quad (3.31)$$

with $n(\omega)$ the frequency dependent refractive index.

While the frequency condition is automatically satisfied, the phase condition is impossible to match in optical isotropic media. In anisotropic media, such as birefringent crystals, the refractive index n_e of the extraordinary wave depends on the angle θ in which it is travelling with respect to the crystallographic axis. For the so called Type-I phase matching (e-e-o), in which the fundamental wave is extraordinary (e) and the second harmonic wave is ordinary (o), the refractive indices are defined as $n_1 = n(\theta, \omega)$ and $n_3 = n_o(2\omega)$ respectively. The Type-I phase-matching condition is then defined as

$$n(\theta, \omega) = n_o(2\omega). \quad (3.32)$$

Phase matching and efficient frequency doubling can be achieved by the choice of an appropriate non-linear medium and the phase matching angle θ . The software tool *SNLO*³ is useful to list the properties and calculate phase matching angles for various non-linear media and applications. Its functions are described in [Smi00].

3.7 Mathematical description of laser radiation

The radiation emitted by a laser resonator can be described mathematically through the use of a Gaussian beam approximation. A matrix formalism is introduced to calculate the transport through complex optical systems and for the development of laser resonators,.

3.7.1 Gaussian beams

Laser beams can be described mathematically as Gaussian beams. Here a brief development of the description of the Gaussian beam shall be given. This and further details can also be found in [ST07].

A monochromatic wave is characterized by its amplitude $a(\mathbf{r})$, its phase $\phi(\mathbf{r})$ and its frequency $\omega = 2\pi\nu$ and can be expressed as:

$$u(\mathbf{r}, t) = a(\mathbf{r})\cos[\omega t + \phi(\mathbf{r})]. \quad (3.33)$$

To be able to later separate spatial and temporal parts, one writes the cosine part in a complex form

$$u(\mathbf{r}, t) = \text{Re} \{U(\mathbf{r}, t)\} = \frac{1}{2} [U(\mathbf{r}, t) + U^*(\mathbf{r}, t)], \quad (3.34)$$

³Developed from A. Smith, AS-Photonics, LLC

and considers only the first summand

$$U(\mathbf{r}, t) = a(\mathbf{r})e^{i\phi(\mathbf{r})}e^{i\omega t} \quad (3.35)$$

as it solves the wave equation

$$\nabla^2 U - \frac{1}{c^2} \frac{\partial^2 U}{\partial t^2} = 0 \quad (3.36)$$

Now we can separate the temporal amplitude and the spatial (time independent) amplitude $U(\mathbf{r}) = a(\mathbf{r})\exp[i\phi(\mathbf{r})]$ and obtain:

$$U(\mathbf{r}, t) = U(\mathbf{r})e^{i\omega t}. \quad (3.37)$$

Inserting equation 3.37 into the wave equation (3.36) and with the wavenumber $k = \omega/c$ one obtains a differential equation for the complex amplitude $U(\mathbf{r})$

$$\nabla^2 U + k^2 U = 0. \quad (3.38)$$

This is the time-independent wave equation, also known as the Helmholtz equation. Its solutions are plane waves and spherical waves:

$$U(\mathbf{r})_{\text{plain}} = Ae^{-i \mathbf{k} \mathbf{r}} \quad U(r)_{\text{spherical}} = \frac{A}{r} e^{-i k r}. \quad (3.39)$$

With A a complex constant, k is the absolute value of the wave vector and $r = \sqrt{x^2 + y^2 + z^2}$ is the absolute value of the position vector.

Fresnel approximation For laser beams travelling in z direction, one can consider $x^2 + y^2/z^2 \ll 1$. Application of this leads to the Fresnel approximation of the spherical wave

$$U(z)_{\text{Fresnel}} \approx \frac{A}{z} e^{-i k \frac{x^2+y^2}{2z}} e^{-i k z}. \quad (3.40)$$

This is a plane wave $e^{-i k z}$ travelling in z direction, with a complex paraboloidal envelope

$$A(\mathbf{r})_{\text{p}} = \frac{A_1}{z} e^{-ik \frac{x^2+y^2}{2z}}. \quad (3.41)$$

The paraboloidal wave, centred at $z = 0$, is now shifted replacing $z \rightarrow z + iz_0 = q(z)$ one obtains the complex envelope of the Gaussian beam:

$$U(\mathbf{r}) = \frac{A}{iz_0} \frac{w_0}{w(z)} \exp \left[-\frac{x^2 + y^2}{w^2(z)} \right] \exp \left[-ikz - ik \frac{x^2 + y^2}{2R(z)} + i\zeta(z) \right]. \quad (3.42)$$

with the parameters of the Gaussian beam:

$$\text{Beam width} \quad w(z) = w_0 \sqrt{1 + \left(\frac{z}{z_0} \right)^2}, \quad (3.43)$$

$$\text{Wavefront radius of curvature} \quad R(z) = z \left[1 + \left(\frac{z_0}{z} \right)^2 \right], \quad (3.44)$$

$$\text{Gouy-Phase} \quad \zeta(z) = \arctan \left[\frac{z}{z_0} \right], \quad (3.45)$$

$$\text{Beam waist} \quad w_0 = \sqrt{\frac{\lambda z_0}{\pi}} \quad (3.46)$$

$$\text{Inverse of the q-parameter} \quad \frac{1}{q(z)} = \frac{1}{R(z)} - i \frac{\lambda}{\pi w^2(z)} \quad (3.47)$$

The beam width $w(z)$ is the transversal distance from the z -axes where the amplitude has decreased to $1/e$ of the maximum.

The intensity of the Gaussian beam is given by $I(\mathbf{r}) = |U(\mathbf{r})|^2$:

$$I(\mathbf{r}) = I_0 \left(\frac{w_0}{w(z)} \right)^2 e^{-2 \frac{(x^2 + y^2)}{w^2(z)}}. \quad (3.48)$$

This yields a Gaussian distribution in transversal direction, hence the name Gaussian beam.

3.7.2 Matrix optics

The ABCD matrix formalism can be used to calculate the optical paths in simple telescopes as well as more complicated systems as laser-resonators in paraxial approximation. This section introduces the basics. Further details can be found in [ST07, Men07]

The ray-transfer matrix A paraxial ray is defined by its distance y and its angle θ to the optical axis (c.f. Fig. 3.6). The ray $\{y_1, \theta_1\}$ passing an optical system of dimensions given by the two transverse planes z_1 and z_2 is defined by $\{y_2, \theta_2\}$.

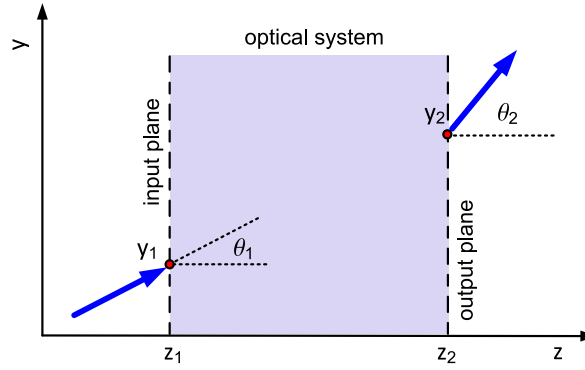


Figure 3.6: Paraxial ray and optical system. The optical system is placed between z_1 and z_2 . Rays are defined by their angle θ and the distance y to the optical axis z .

In the paraxial approximation, angles are sufficiently small so that $\sin[\theta] \approx \theta$ and the relation between $\{y_1, \theta_1\}$ and $\{y_2, \theta_2\}$ becomes linear. One obtains:

$$\begin{pmatrix} y_2 \\ \theta_2 \end{pmatrix} = \begin{pmatrix} A & B \\ C & D \end{pmatrix} \begin{pmatrix} y_1 \\ \theta_1 \end{pmatrix}. \quad (3.49)$$

As an example the matrix M_P for the propagation in the optical path d and the matrix M_L for transmission through a thin lens with focal length f are given:

$$M_P = \begin{pmatrix} 1 & d \\ 0 & 1 \end{pmatrix} \quad M_L = \begin{pmatrix} 1 & 0 \\ -\frac{1}{f} & 1 \end{pmatrix}. \quad (3.50)$$

Matrix formalism for Gaussian beams The ABCD matrix formalism can be applied to Gaussian beams. The complex q -parameter (eqn. 3.47) is the vector containing the information about radius of curvature of the wave fronts and the beam waist. The q -parameter q_2 of the outgoing beam can be calculated using the same matrix elements of the ray transfer matrix, but with following formalism:

$$q_2 = \frac{A q_1 + B}{C q_1 + D}. \quad (3.51)$$

The beam waist w_0 and the wave front radius can be calculated from the q -value:

$$\frac{1}{w_0^2} = -\frac{\pi n}{\lambda} \text{Im} \left[\frac{1}{q} \right] \quad (3.52)$$

$$\frac{1}{R} = \text{Re} \left[\frac{1}{q} \right]. \quad (3.53)$$

For the calculation of a complex system, the ray transfer matrices for each individual optical component are multiplied. One obtains a single matrix that describes the complete optical system. This method was used to calculate the mode matching inside the Ti:Sa resonator and for the test of stability. The results of this calculation are shown in Chapter 5.3. The implemented algorithm used a 4x4 matrix to perform calculations in the sagittal plane and the tangential plane simultaneously.

The resonator cavity can be expressed by a matrix \mathcal{M}_R . The cavity is stable under the following condition:

$$\frac{1}{2} |\text{tr}[\mathcal{M}_R]| < 1 \quad (3.54)$$

with $\text{tr}[\mathcal{M}]$ the trace of the matrix.

The Gaussian beam that describes the resonator mode is determined by the complex q -value that fulfils the phase condition (see eqn. 3.7) for a round trip in the resonator

$$q = q\mathcal{M}_R \quad (3.55)$$

To calculate the beam waist of the resonator mode depending on the position z inside the resonator one has to describe the resonator matrix as a function of z . This was implemented in *Mathematica* using a piecewise defined function [Rot09].

Chapter 4

Resonance ionization and applications

In 1972 Ambartzumian and Letokhov [AL72] demonstrated selective two-step photo-ionization of rubidium atoms. This ionization mechanism was illustrated in the original paper as shown in Fig. 4.1.

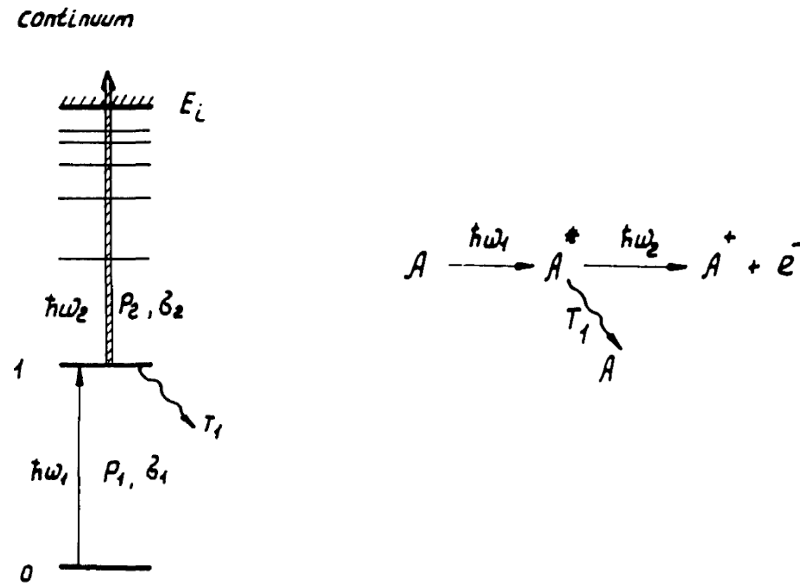


Figure 4.1: Illustration of the selective two step photo-ionization scheme for atoms [AL72]. On the left: The atomic energy levels are indicated by horizontal lines of which the ground state (0), the excited state (1) and the ionization potential E_i are indicated. The energies $\hbar\omega_1$ and $\hbar\omega_2$ of the two applied photons are indicated by arrows. The laser power and the cross section P and σ are indicated for each transition step. T_1 is the lifetime of the excited state (1). The reaction diagram on the right describes the interaction of the atom (A) with a first photon ($\hbar\omega_1$) that leads to an excited atom (A^*). A^* can decay to A or react with a second photon $\hbar\omega_2$ to become a singly charged positive ion A^+ and release one electron e^- .

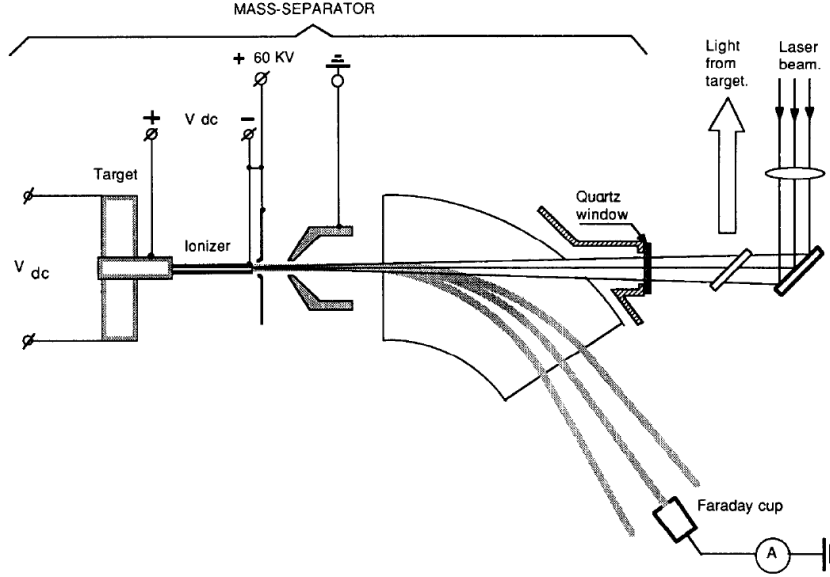


Figure 4.2: Schematic representation of the mass-separator and laser ion-source [MFK⁺93]. The target and ionizer can be heated resistively. The target unit is set to a positive potential of up to 60 kV. The extraction electrode is grounded. The RILIS laser beams are transmitted through a quartz window and through the dipole mass separator magnet into the ionizer tube. A fraction of the laser beam is reflected for monitoring. The separated ion beam can be detected with a Faraday cup.

The theory and applications of resonance ionization are explained in numerous review articles, e.g. the one by Hurst *et al.* [HPKY79] and the text books of Letokhov and Hurst [Let87, HP88]. A basic introduction can also be found in the books by Demtröder [Dem08, Dem10]. The resonance ionization of atoms and its use for nuclear physics was reviewed by Fedosseev *et al.* [FKM12]

4.1 Laser ionized radioactive ion beams

The application of resonance ionization as an efficient and selective laser ion source was proposed by Letokhov and Lee [L⁺84, Lee85] and formulated in [HJKW85]. The operation of the ISOLDE Resonance Ionization Laser In Source (RILIS) was first described in [MFK⁺93]. A conceptual illustration, taken from this reference, is given in figure 4.2.

The concept of the isotope separator on-line (ISOL) is described in [RBC⁺94, K02]. A beam from the PSB (not in the figure) impinges on a thick target installed at one of the two ISOLDE mass separator front-ends. Within the target, proton induced nuclear fission, fragmentation

or spallation reactions produce radioactive isotopes. The sealed target container is heated to temperatures of 2300 K which allows the products to diffuse through the target material and effuse through a transfer line into the coupled ionizer whose temperature can be controlled independently. The ionizer tube is made of a refractory metal (typically tungsten or tantalum) and has a length of 30 mm and an inner diameter of 3 mm. The RILIS lasers excite and ionize the atoms inside the hot cavity. The photo-ions are then extracted and accelerated in an electrostatic potential of 60 kV. The ion beam is then mass separated using the GPS or HRS dipole magnets and transported to the experiments located in the ISOLDE hall.

ISOL efficiency The radiogenic total ion beam intensity i from an ISOL target can be calculated [KÖ1]

$$i = \Phi \cdot \sigma \cdot N \cdot \eta_{\text{target}} \cdot \eta_{\text{ion}} \cdot \eta_{\text{sep}} \cdot \eta_{\text{transp}} \quad (4.1)$$

The in-target production is given by $(\Phi \cdot \sigma \cdot N)$ with the flux of the primary particle, the production cross section of the desired isotope and the number of target atoms. This is multiplied by the release efficiency from the target, the ionization efficiency, the efficiency of the separator magnets and the beam transport efficiency. Decay losses are included in the different efficiencies.

To obtain pure beams of rare isotopes (one mass A of one element Z) a combination of target material with the appropriate ion source has to be found. The release of the desired element and the contaminants from the target is dependent on the in-target chemistry and volatility of the products. Conventional ion sources, like the surface ion source, may be selective with respect to ionization potentials or chemistry. A list of chemical and physical selection techniques is given in [KÖ1] and references therein. Often the isobaric contamination may be an isotope of a neighbouring element with similar chemical behaviour, or with much higher production rates, in which case the degree of Z -selectivity is not sufficient. The RILIS provides this additional Z -dependence as it increases the ion fraction of the desired element in the source.

RILIS selectivity The atomic selectivity¹ of the laser ion source is one the mayor advantages of the RILIS with respect to other ion sources that are used at ISOLDE. For the laser ion source one can define the selectivity s as the ratio of the ion current i measured with the lasers on resonance and with the lasers off resonance².

$$s = \frac{i(\text{laser on})}{i(\text{laser off})} = \frac{\eta_{\text{surf}} + \eta_{\text{RILIS}}}{\eta_{\text{surf}}} = 1 + \frac{\eta_{\text{RILIS}}}{\eta_{\text{surf}}} \quad (4.2)$$

¹Sometimes this is, confusingly, referred to as chemical selectivity.

²In practice the same result is obtained when the first step laser is blocked instead of detuned.

The selectivity is an enhancement factor with respect to the surface ionization efficiency of hot cavity ionizer tube. Its efficiency η_{surf} depends on the ionization potential IP of the atom and the work function Φ_i of the ionizer material [Dre68, Kir81]

$$\alpha = \frac{n_+}{n_0} = \frac{g_+}{g_0} \exp \left[\frac{\text{IP} - \Phi_i}{kT} \right] \quad (4.3)$$

$$\eta_{\text{surf}} = \frac{n_+}{n_+ + n_0} = \frac{\alpha}{\alpha + 1} \quad (4.4)$$

where α is the ratio of the densities of ions to neutrals, g_0 and g_+ are the grade of degeneracy of the atom and the ion state, respectively.

Laser ionization efficiency The selectivity of the laser ion source is proportional to the photo-ionization efficiency of the resonance ionization. The ionization efficiency in a multi photon process is derived from rate equations for the populations. This is worked out in [Let87, HPKY79]. The RI process is said to be saturated, when all atoms that are addressed by the applied laser scheme are converted to a positive ion plus an electron. The flux and fluence conditions have to be met [Van97]: To meet the flux, the ionization rate $\Gamma_i = F\sigma_i$ has to be larger than the rate β in which the excited state decays into a state that is inaccessible for the lasers (dark state).

$$F\sigma_i \gg \beta \quad (4.5)$$

σ_i is the ionization cross section and F is the photon flux (in $\text{cm}^{-2}\text{s}^{-1}$).

The fluence condition ensures that enough photons are available for the ionization step

$$\phi\sigma_i \frac{g_2}{g_1 + g_2} \gg 1, \quad (4.6)$$

where ϕ is the fluence of photons (in cm^{-2}) and g_1, g_2 are the statistical weights of the ground state and the excited state.

4.2 In-source resonance ionization spectroscopy

Resonance ionization mass spectrometry (RIMS) combines the atomic (Z) selectivity of the laser with the mass selectivity (A) of a mass separator. The samples investigated can be handled in an off-line laboratory as they are mostly stable elements or weakly radioactive long-lived isotopes. This method is applied for example for ionization scheme development or ultra trace analysis [RSG⁺11, GHK⁺04]. As the lasers are scanned, a non-selective detector

provides the ion signal. For the investigation of short-lived and scarcely produced isotopes, the sample to be investigated has to be replenished continuously. This can be achieved at on-line isotope separator facilities, as it was reported by Alkhazov *et al.* [ABD⁺92] in 1992. They applied resonance ionization spectroscopy inside the ion source. After mass separation, the ion beam was sent to an isotope selective α -decay spectroscopy setup, which allowed the detection of photo-ions of the isotopes of interest within an isobaric background of surface ions.

4.2.1 Determination of nuclear properties

In-source laser spectroscopy was first used to study isotope shifts of atomic transitions in ytterbium isotopes [ABD⁺92]. From the isotope shifts one can determine the difference of the mean-square charge radius $\delta_{A,A'}\langle r^2 \rangle$ between the two isotopes A and A' . Analysis of the hyperfine structure yields spectroscopic magnetic dipole and electric quadrupole moments μ_I Q_s . These and further applications are explained in the review from Cheal and Flanagan [CF10] and references therein. For these measurements, the scanning RILIS laser is operated in narrow-band mode.

4.2.2 Ionization scheme development

An efficient RILIS ionization scheme is the basis for performing in-source laser spectroscopy as well as for the production of intense ion beams of a certain element. For radioactive elements that cannot be handled in the laboratory the ionization scheme development has to be performed on-line. This was the case for polonium where different ionization paths were investigated and the existence of a second excited state was confirmed [CMF⁺08]. In this work in-source laser spectroscopy is used to develop an RILIS ionization scheme for the purely radioactive element astatine.

4.3 Particle registration

The maximum ion rate that can be obtained for a certain isotope is determined by equation 4.1. The composition of the ion beam depends on the production cross section and ionization efficiency of possible contaminants. These factors set limits to the sensitivity and type of detection that can be used to detect the photo-ions.

4.3.1 Faraday cup

The simplest way to detect the photo-ions is to use a Faraday cup. Several Faraday cups are implemented in the ISOLDE beam instrumentation system. The acquired ion current can be accessed from the ISOLDE FESA framework and recorded using e.g. LabVIEW. The

practical sensitivity is 0.2 pA [Foc11], corresponding to an ion rate of $1.2 \times 10^6 \text{ s}^{-1}$. The Faraday cup requires a certain integration time, which is set by the pico-ampere-meter (PAM). The integration time of the PAM used at ISOLDE is usually set to 500 ms. This gives rise to a systematic error when using this detector for continuous laser scans. This virtual frequency shift is investigated in section 8.7.

4.3.2 Alpha decay spectroscopy detector

Photo-ions of α -decaying isotopes can be detected sensitively and selectively using an α -decay spectroscopy detector. This detection method was applied by Alkahazov *et al.* [ABD⁺92] to detect photo-ions of neutron deficient ytterbium isotopes within a significantly higher background of surface ionized isobars. The α -particle emitted from a certain isotope, has a characteristic energy. This enables filtering (gating) of the recorded α -energy spectrum for the desired isotope. In some cases an almost background-free ion signal is obtained. In this work, photo-ion rates as low as 1 s^{-1} were detected. A disadvantage of this detector is the delayed signal and the rather long collection time of up to $\approx 120 \text{ s}$ (two PSB supercycles) per frequency step. For in-source spectroscopy at ISOLDE, the so called ‘*windmill*’ detector setup is used. A description can be found in [AEH⁺10]. In this setup, the ion beam is implanted into one of ten thin carbon foil catchers ($30 \mu\text{g}/\text{cm}^2$), mounted on a rotating wheel. Two silicon detectors are used to register α -particles with an efficiency of 66%.

4.3.3 ISOLTRAP MR-ToF

A different approach to detect-photo ions of an isotope of interest within an isobaric background of surface ions, is to use the multi-reflection time-of-flight mass spectrometer (MR-ToF) of the ISOLTRAP experiment. It features a suppression ratio of 10^4 and a mass resolving power of 10^5 . A bunch of ions is injected into the device and is then reflected n times by two electrostatic mirrors. This increases the travel distance to several hundreds or thousands of meters and therefore the mass resolution, which is based on time-of-flight separation, is increased. Ion bunches, corresponding to discrete mass components of the ISOLDE ion beam, are detected using a micro-channel plate (MCP) ion detector. Further details of the ISOLTRAP MR-ToF can be found in [WBB⁺12].

Part II

Apparatus

Chapter 5

Design of Ti:Sa lasers and frequency conversion units for ISOLDE RILIS

5.1 State of the art Ti:Sa laser systems for laser ion sources and RIMS

High repetition rate tunable nanosecond Ti:Sa lasers were developed at the University of Mainz with the goal to replace a copper vapour laser based dye laser system in use for the ultra trace analysis of plutonium. [WBG⁺03, GHK⁺04]. The first in-group constructed Ti:Sa lasers were described and characterized in the Ph.D. thesis of Roland Horn [Hor03]. Horn described a Z-shaped resonator with a total length of 460 mm. The folding angle of the cavity was 17.5°. To achieve the best overlap of the pump beam and the resonator mode, the 20 mm long Ti:Sa crystal was placed slightly asymmetrically in the central focussed beam path between the two curved folding mirrors. Different frequency ranges were obtained using different mirror sets, a three-plate Lyot filter and an etalon. Pulse synchronization of individual lasers was achieved using Pockels cells as a Q-switch. The laser line-width was determined to be 4-8 GHz, depending on the output power.

This Ti:Sa laser design was successively improved in terms of the output power of the fundamental as well as the second and third harmonic frequencies. The results obtained with intra-cavity frequency doubling and single-pass Ti:Sa amplification were reported in the Diploma thesis of Thomas Kessler [Kes04]. He also constructed a double-side pumped Ti:Sa laser. A new pump geometry was introduced by Christoph Mattolat [Mat10] in which the Ti:Sa crystal is placed such that the pump beam is focussed after passing through the crystal. This prevents damage to the surface while increasing the maximum single-side pump power. Continuous wavelength tuning of the Ti:Sa laser over a wide range of ≈ 250 nm was achieved by replacing the high reflective cavity mirror with a grating [Mat10, TBC⁺10, RMK⁺12]. The output power and beam quality of this grating-based laser is sufficient for laser spectroscopy applications [RFG⁺10, MGR⁺10]. As a possible alternative, a commercial Ti:Sa system from *Photonics Industries, Inc.* is used at HRIBF at ORNL [GGs⁺08]. However, the output powers

specified (<1 W fundamental) [Pho11] were too low to be considered for on-line application at RILIS. Yuan Liu from ORNL reported [Liu12] that after an upgrade of the Ti:Sa lasers and implementation of individual pump lasers, a peak output power of 2.5 W was reached and that the synchronization without Pockels cells is possible. This improved performance was deemed suitable for on-line operation.

An injection seeded Ti:Sa laser with a line-width of 20 MHz was developed in the Diploma work of Christoph Mattolat [Mat06] and was further refined within his Ph.D. work [Mat10]. This unit was used for high resolution resonance ionization spectroscopy (RIS) of aluminium [KTM⁺08] and a demonstration of two-photon spectroscopy [Klu85] of silicon, which was performed inside the hot cavity. [Mat10].

A frequency conversion unit (FCU), capable of production up to the fourth harmonics of the fundamental output of the Ti:Sa lasers, was developed by Simone Sirotzki [Sir04]. A new optical layout of this FCU was introduced in my Diploma thesis [Rot09].

5.2 Motivation and considerations for the new design

In the framework of this thesis, the mechanical design of the Ti:Sa laser cavities was revised with consideration of their use under on-line conditions at RILIS. Experiences gained during my diploma work in the working group LARISSA at the University of Mainz, Germany and the laser ion source FURIOS LIS of IGISOL at JFL, (Jyväskylä, Finland), as well as research visits to TRILIS at TRIUMF-ISAC (Vancouver, Canada) and RILIS at ISOLDE led to the conclusion that the different Ti:Sa designs could be merged into the CERN-Ti:Sa layout.

The Ti:Sa cavities were re-drawn using a state of the art CAD program (*Autodesk Inventor 2010*). This gave the freedom to question previous design solutions and implement new features. Individual design considerations and solutions are described in the following paragraphs.

Pre-aligned alignment laser and beam sampling A general constraint at RILIS is the necessity of efficient use of ISOLDE beam time. Thus, the time required to tune the lasers from one element to another has to be as short as possible. To align the Ti:Sa lasers after a change of one or more cavity mirrors, a He-Ne laser is used. Previously the He-Ne laser was mounted in front of the cavity to be aligned and was then directed into the resonator using two mirrors. This pre-alignment procedure has to be performed carefully as it defines the path of the resonator mode inside the cavity. The new design incorporates the two mirrors needed for the He-Ne pre-alignment into the Ti:Sa unit. The position and direction of the incident He-Ne beam is fixed using a fiber-coupler which is mounted permanently into the front plate. A single-mode fiber is used to transport the output of the He-Ne¹ to the adjustable fiber

¹He-Ne laser with a rated output power of 10 mW was fiber-coupled using a fiber port from Thorlabs (Type PAF-X-7-B)

couplers².

The second He-Ne alignment mirror is mounted onto a magnetic base. When the Ti:Sa is in operation this base is exchanged with a second base on which a beam sampler plate is mounted. This pick-off sends a fraction of the emitted Ti:Sa laser beam via a second fiber-coupler to the wavemeter and the pulse timing monitor.

This setup is highlighted yellow in the sketch shown in Fig. 5.1.

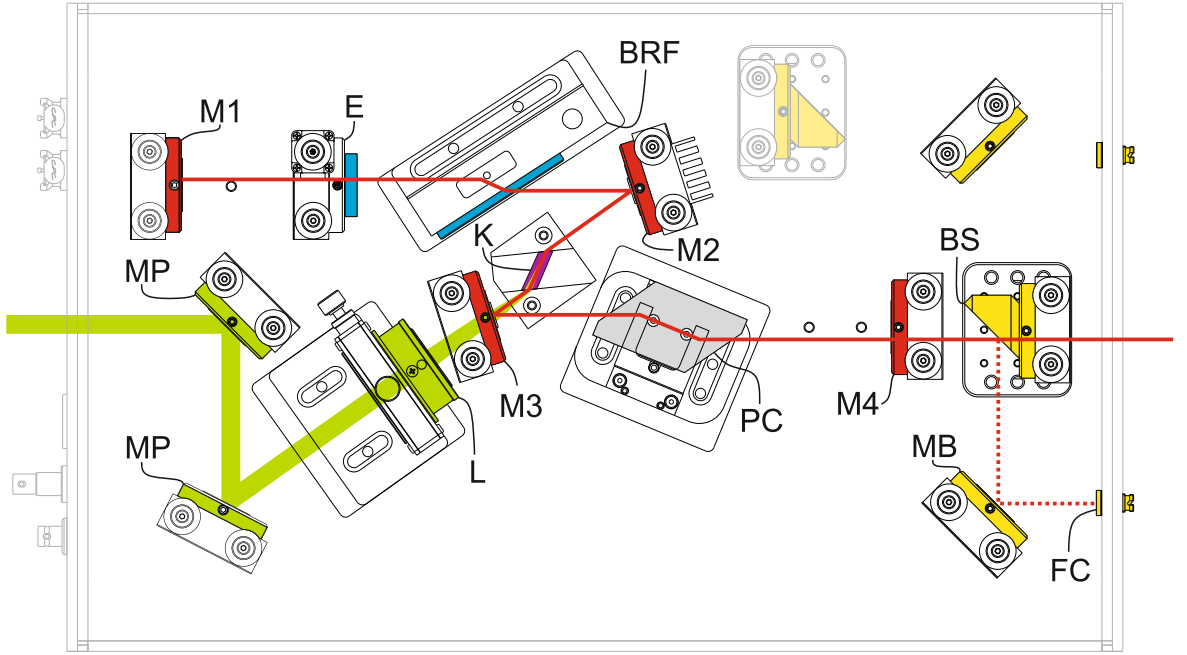


Figure 5.1: Sketch of the CERN-Ti:Sa laser cavity. The resonator is created by the mirrors M1 to M4 (red). The pump beam (green) is aligned with two mirrors (MP) and focussed with a lens (L) into the Ti:Sa crystal (K). The frequency selective tuning elements (blue) are an etalon (E) and a birefringent filter (BRF). A Pockels cell (PC) can be used as a Q-switch for the synchronization with other lasers. A fraction of the emitted laser light is reflected by the beam sampler (BS) and the broad band mirror (MB) into the fiber coupler (FC).

Minimised degrees of freedom The alignment and optimization of the Ti:Sa laser should be as easy as possible for the (up to seven) RILIS operators. Therefore it is advantageous to minimize the free parameters available for (de-) tuning of the laser cavities.

The beam height in the resonator was chosen to be 25.4 mm (1 inch). Mounting slots for the three axis focussing lens mount (L), the Pockels cell adjuster (PC) and the rotation mount of

²Thorlabs CFC-2X-B

the Lyot filter (BRF) were designed with a depth compatible with this beam height. The base plate therefore has a thickness of 30 mm. One edge of the mounting slots defines the angle in which the element has to be placed in order to meet the Brewster angle in the resonator and as a guide for the coarse z-adjustment of the lens mount.

The distance between the curved mirrors as well as the position of the Ti:Sa crystal is fixed.

Remote control For the remote control of the wavelength, one of the manual micrometre thumb screws of the etalon mount was replaced by a miniature stepper-motor driven linear actuator³. The electrical connection is fed through the base plate using a standard 8-pin RJ⁴ connector. In view of a future automated cavity alignment, each mirror mount was equipped with a dedicated electrical feed-through of the same type.

Installation of the Pockels cell driver The fast high voltage switch⁵, that is used for driving the Pockels cell, was mounted under the base plate of the cavity. This saves space inside the unit and prevents air fluctuations originating from the active cooling of this device. A high voltage feed-through is mounted into the base plate and is used to connect the Pockels cell with the driver. This minimizes the length of the HV-cable and therefore the impedance load for the switch. Additional SHV and BNC feed-throughs are mounted into the front panel of the laser housing to connect the DC high voltage input and the trigger signal to the switch.

Considerations for future applications Additional space in the resonator was reserved for the installation of one additional etalon to obtain narrow-band mode operation of the Ti:Sa and for intra-cavity frequency conversion.

Usability and safety The optomechanics used in the design are mainly commercially available and therefore makes use of a proven design. The rotation mount for the Lyot filter is an improved version of a development from the TRILIS group. All openings in the front and back plate of the laser housing are threaded with a standard⁶ thread (1 inch). This permits the attachment of beam tubes for the safe transport of the pump beam and the Ti:Sa laser beam. The side panels of the housing were designed to slide into a groove in the front and back panels for easy removal.

³Provided from TEM Messtechnik GmbH

⁴As used for CAT5 patch cables commonly used for Ethernet connections.

⁵Type GHTS-8 from Behlke Power Electronics GmbH, Germany

⁶Fits Thorlabs-SM1

5.3 Ti:Sa cavity optimization

The ABCD formalism, as introduced in section 3.7.2, was used to calculate optimal parameters for the Ti:Sa cavity and mode-matching of the pump beam. A *Mathematica* program which was developed during my Diploma work [Rot09] was used to calculate the mode size in the resonator. The folding angle was adjusted to obtain a circular beam profile by matching the sagittal and the tangential beam waist of the Ti:Sa mode. The parameters used for the determination of the mode matching are listed in Table 5.1, the result is shown in Fig. 5.2. To guarantee efficient use of the pump beam, the expansion factor of the pump telescope and the pump lens position were adapted such that the pump beam waist inside the crystal is always greater than the Ti:Sa resonator mode waist.

Table 5.1: Parameters applied to calculate the mode matching in the resonator

Name	Value	Dimension
crystal length	20	mm
path length high reflector	215	mm
path length crystal to curved mirror 1	50	mm
path length crystal to curved mirror 2	20	mm
path length output coupler	190	mm
radius curved mirror	75	mm
wavelength resonator mode	850	nm
focal length pump lens	80	mm
focal length telescope lens 1	-50	mm
focal length telescope lens 2	150	mm
folding angle	17.69°	

5.4 Construction of the Ti:Sa lasers

The machining work of the Ti:Sa baseplate and housing was carried out by the mechanical workshop of the University of Mainz. A photograph of the assembled Ti:Sa cavity is shown in Fig. 5.3. Three Ti:Sa cavities were produced for use at CERN. Four additional cavities were produced for the use at the LARISSA group in Mainz and the working group of Prof Dr J. Maultzsch (Technical University Berlin, Germany).

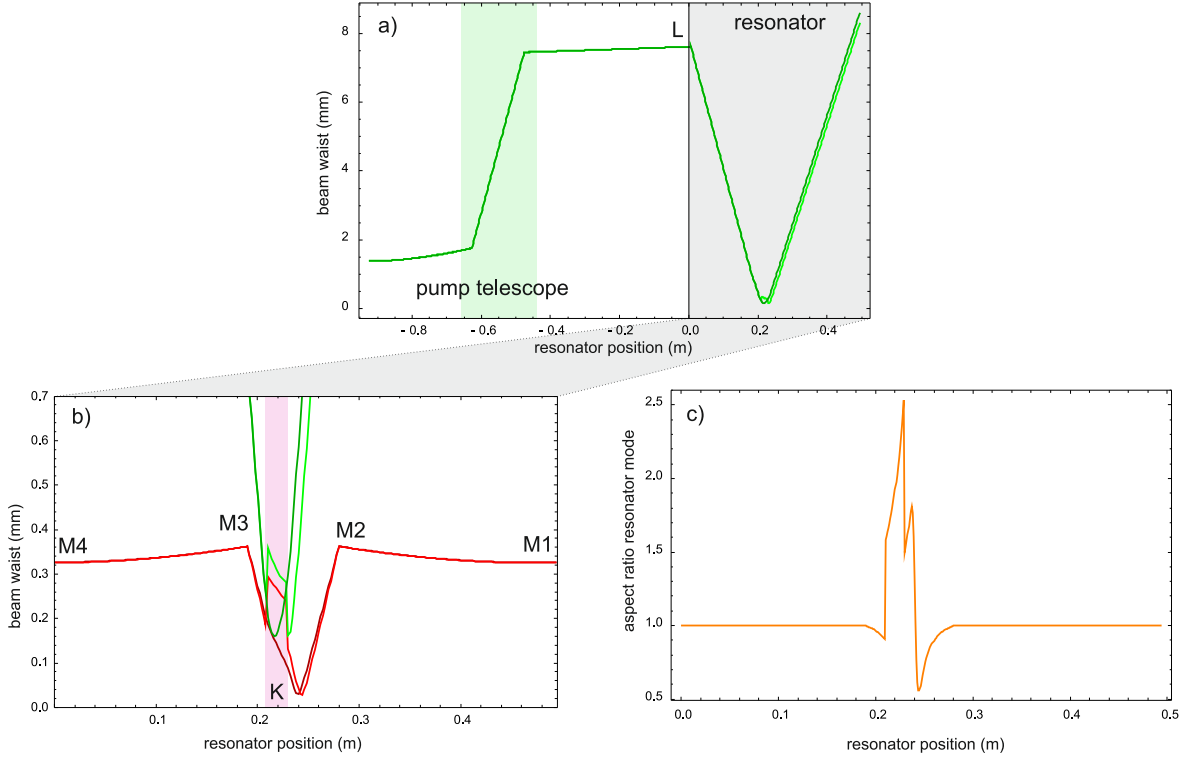


Figure 5.2: Beam waist of the pump beam and the resonator mode calculated with the ABCD formalism. a) Beam waist of the pump beam relative to the position of the cavity. The first lens of the pump telescope is placed at -0.6 m. The two transversal directions with respect to the Brewster-surfaces in the resonator are indicated by different shades of green colours. b) Beam waist of the pump beam (green) and the resonator mode (red) plotted for the different transversal directions. The overlap of the pump beam inside the crystal K (placed at ≈ 0.2 m). c) The angle of the folding curved mirrors (M2, M3) is chosen such that the aspect ratio at the high reflector and the output coupler (M1, M4) equals unity.



Figure 5.3: Photograph of a CERN-Ti:Sa cavity. The mirror mounts are color-coded to reduce the likelihood of accidental mis-tuning. Green mounts control the pump beam. The red mounts hold the high reflecting and the output coupling cavity mirror. The blue mount holds an etalon for manual control. In this cavity, no Pockels cell is installed, but its square mounting slot can be seen on the baseplate.

5.5 Frequency conversion unit

The generation of higher harmonics (HHG) of the laser output is achieved by the use of non-linear processes, described in section 3.6. The setup for HHG was refined [Rot09] and a new design with reduced degrees of freedom was developed. A detailed description can be found in [RMM⁺11]. The FCUs were also machined at the mechanical workshop of the University of Mainz. Two units were delivered to GANIL for the GISELE project [LACC⁺10]. A photo of the prototype that was assembled prior to surface treatment, is shown in Fig. 5.4

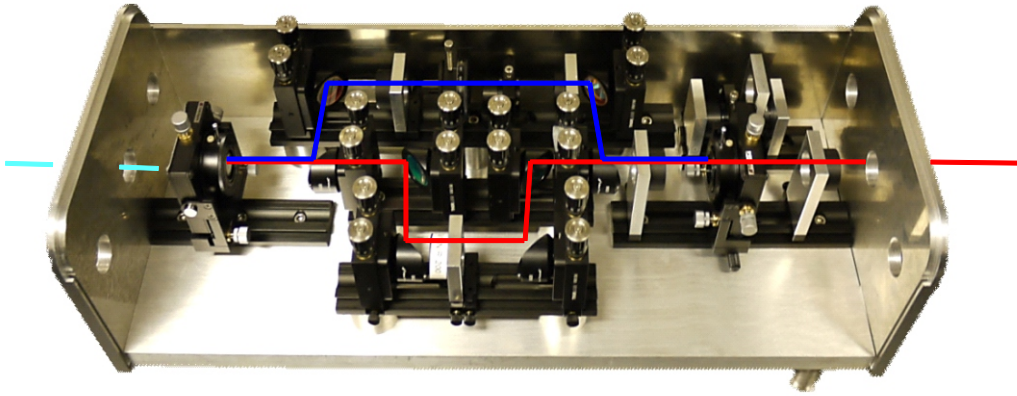


Figure 5.4: Photograph of the frequency conversion unit before anodization. The side panels can be removed for easier alignment. The holes in the front and back panel are threaded with Thorlabs-compatible SM1 threads. The unit allows generation of higher harmonics up to the fourth harmonic of one fundamental wavelength. The additional holes in the front and back panel allow for frequency mixing of different lasers. The FCU in the photograph is set up for frequency tripling, the fundamental, second harmonic and third harmonic beam path are indicated (red, blue, cyan).

Chapter 6

Characterization of the Ti:Sa laser system

6.1 Operational characteristics

6.1.1 Tuning range of the Ti:Sa lasers

Mirror sets To tune the Ti:Sa laser to different wavelengths, a selection of differently coated mirror sets is required. The specifications listed in table 6.1 were based on experiences from the LARISSA group in Mainz. The mirror sets were purchased from LAYERTEC¹. Mirror set 0 is a broad band mirror set, which was successfully used in the grating based Ti:Sa laser [Mat10]. Experiences had shown that for the curved mirrors a substrate with a diameter of 12.7 mm (1/2 inch) is sufficient to transmit the pump beam. This allows more of the substrates to be placed in one sputtering charge and therefore reduces the manufacturing costs. The curved cavity mirrors have to be mounted in adapters to fit in the standard 1 inch mirror mounts. The back side is anti-reflex-coated (AR) for the pump wavelength $\lambda_{\text{pump}} = 532 \text{ nm}$. All other mirrors are broad-band AR-coated (650-1000 nm) on the back side. This reduces losses and prevents etalon effects. The mirror substrates are made of fused-silica. The output couplers have a wedge angle of 30°.

Table 6.1: Specification of the purchased mirror sets.

set	curved mirrors (H) & high reflectors (E)	output couplers (A)
0	650-1000 nm	650-1000 nm, R=80%
1	650-760 nm	650-720 nm, R=80%
2	750-850 nm	750-850 nm, R=70%
3	840-940 nm	840-940 nm, R=80%
4	900-1050 nm	910-1000 nm, R=80%

¹LAYERTEC GmbH, Germany

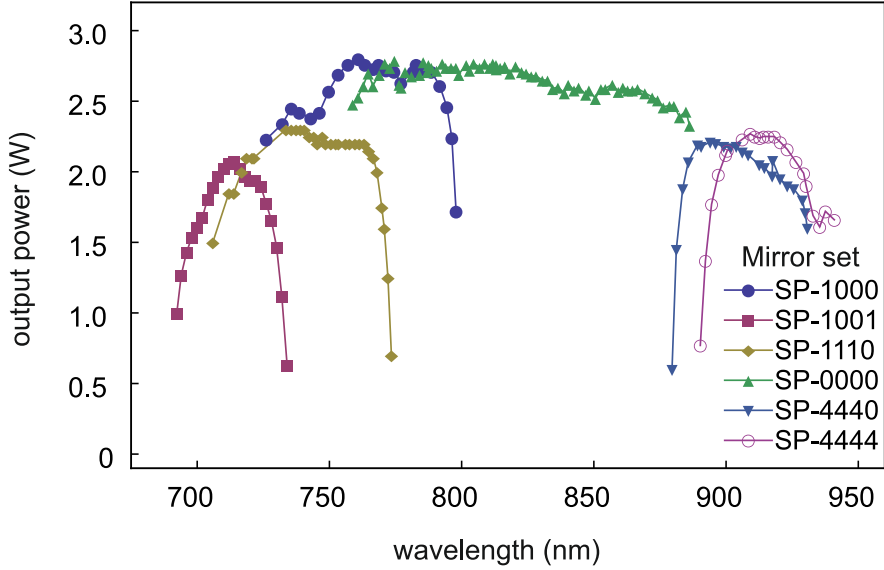


Figure 6.1: Tuning ranges of the Ti:Sa laser using different mirror sets. The applied pump power was 10 W. The curve labelled with green triangles was obtained with the full broad band mirror set. In this set, the end points are delimited by the tuning range of the birefringent filter.

Tuning range The fundamental tuning range of the Ti:Sa lasers was measured for different mirror-sets (and combinations). The result is shown in figure 6.1. A mirror set designation is denoted in the form²: SP-*EHHA*. While *E* is the number of the high reflecting end mirror, *H* are the numbers of the curved mirrors (usually the same) and *A* is the number of the output coupler.

It turns out that in principle only mirror sets 0, 1 and 4 are required to obtain any wavelength that may be produced by the Ti:Sa laser. This was possible by application of the broadband mirror set SP-0000. This mirror set incorporates a broadband dielectric mirror type BB1-E03, purchased from *Thorlabs*. This mirror type, however does not sustain the high power stored in the resonator when the Ti:Sa is pumped with 25 W. In these cases, the specific high reflecting mirror from mirror sets 2 or 3 should be installed. It is worth to procure broad-band high reflecting resonator mirrors.

Efficiency The efficiency of the Ti:Sa laser was measured with mirror set SP-1110 installed. An etalon and the birefringent filter were used to tune the laser to $\lambda = 735$ nm. The lasing threshold was observed at a pump power of $P \approx 5$ W. A linear fit of the points obtained above 10 W pump power gave a slope efficiency of $\eta_{\text{slope}} = 25.5\%$. This value is comparable to

²The naming originates from German: SP - Spiegelsatz (mirror set), *E* - Endspiegel, *H* - Hohlspiegel (curved mirror), *A* - Auskoppelspiegel (output coupler)

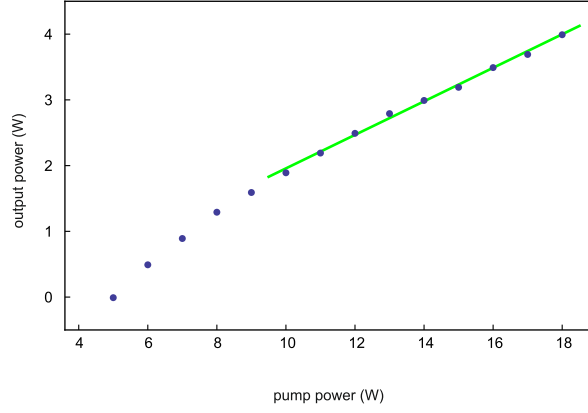


Figure 6.2: Efficiency of the Ti:Sa laser. The slope efficiency is defined as the slope of the line fitted to the points above 10 W pump power. The efficiency is $\eta_{\text{slope}} = 25.5\%$.

other Ti:Sa cavities constructed at TRIUMF and Mainz. The data are shown in Fig. 6.2.

6.1.2 Synchronization of the Ti:Sa lasers

For the application of the Ti:Sa lasers in a multi-step ionization scheme, it is required that the laser pulses of different lasers are emitted at the same time. In general, the pulse built up time depends on the gain of the resonator. As the gain curve $g(\nu)$ of the laser medium is wavelength dependent, the pulses emitted from different cavities are a priori not synchronized. The time between the pump pulse and the Ti:Sa pulse varies also with the alignment of the cavity. An optimal aligned cavity shows a smaller delay. In the following three methods are described to synchronize the laser pulses emitted from the Ti:Sa lasers.

6.1.2.1 Q-switching

A conventional method to synchronize laser pulses is the so-called Q-switching. The quality factor Q is defined as the ratio of the energy stored in the resonator and the loss per round trip. The Q-switch device is placed inside the laser resonator and reduces the quality factor. This prevents lasing. At a certain moment the Q-switch changes its state so that the resonator returns to its nominal Q-value and the built up of the laser pulse can start. [Koe76]

So called Pockels cells are used to Q-switch the Ti:Sa lasers. These cells are based on crystals that become birefringent when placed inside a high electrostatic field. The voltage applied to the cells can be tuned to achieve a phase retardation of $\lambda/4$. When laser beam passes a second time through the Pockels cell, a total phase shift of $\lambda/2$ is obtained and the polarization is rotated. The losses induced by the Brewster surfaces inside the resonator (Lyot filter, Ti:Sa crystal, Pockels cell) are higher than the resonator gain and the lasing condition is not

satisfied.

Performance test of different Pockels cells Prior to the final design of the Ti:Sa resonator, the performance of Pockels cells made by different companies were tested in Ti:Sa resonators at the University of Mainz. The pulse repetition rate of the pump laser³ was set to 7 kHz and the wavelength of the Ti:Sa was tuned with an etalon and the birefringent filter to $\lambda = 814$ nm. Brewster-cut Pockels cells made from KD*P were purchased from *United Crystals Co.*⁴, and *LINOS*⁵. A custom made straight Pockels cell⁶ was delivered from *LINOS*. The windows of the straight cell were anti-reflex coated for a wavelength range from 680 nm to 950 nm and the cell was filled with a index matching liquid. The signal pulse that opens the Pockels cell was delayed with within a range of $2 \mu\text{s}$ while the output power of the laser was recorded.

Figure 6.3 shows the time tuning curves of the different cells. The conventionally used Brewster-cut cells show a similar behaviour. The cells from UC show a slightly lower performance, which could be explained by a mis-alignment of the cell and/or the Ti:Sa cavity. The Linos-AR cell shows unacceptable insertion losses, although the slope of the performance curve is smaller and is intersecting the curves obtained with the Brewster cells at ≈ 1300 ns. At this point the temporal profile of the Ti:Sa pulse showed a double structure. Finally, the cells from UC were purchased for economic reasons and their favourable dimensions.⁷ The long⁸ life-time of the Ti:Sa medium allows to delay the pulse by up to $2 \mu\text{s}$. A power loss of 10% was observed when the pulse was delayed ≈ 250 ns.

6.1.2.2 Gain tuning

A different approach to synchronize the Ti:Sa laser pulses is to change the gain. A reduction in gain leads to a delayed lasing. This can be realized by tuning either the pump power or the overlap of the pump beam and the resonator mode. The RILIS pump beam distribution to the Ti:Sa cavities incorporates polarizing beam splitter cubes and half-wave phase retardation plates to allow the variation of the splitting ratio. Fine tuning of the gain and thus the synchronization can be achieved by detuning the focus of the pump lens. This approach is suitable when two Ti:Sa wavelengths are required.

³Clark ORC 1000

⁴DKDP, Brewster cut, Custom made by *United Crystals Co.*, USA

⁵BPC 8 755 nm

⁶LM 8 IM OEM (680- 950nm)

⁷They were less expensive than the LINOS make by a factor of 5 and were available in a diameter of 35 mm which fits to commercially available Pockels cell positioners such as type EOP from *Siskiyou Co.*, USA.

⁸Compared to the ≈ 10 ns of the laser dye

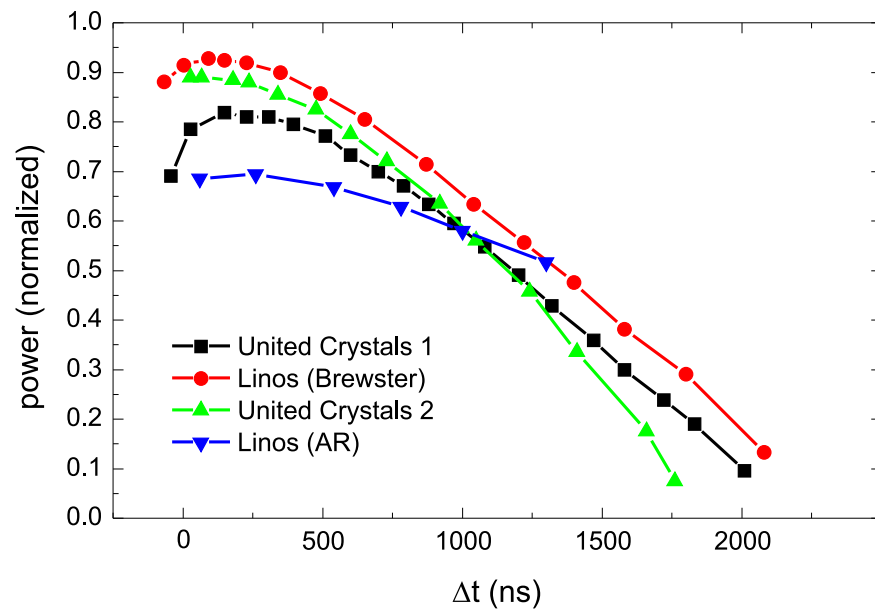


Figure 6.3: Comparison of different makes of Pockels cells. The curves were normalized to the power obtained before inserting the cell into the resonator. The performances of the Brewster-cut cells are comparable. Although the slope of the performance curve of the straight cell (Linios-AR) is smaller, the insertion losses are too high.

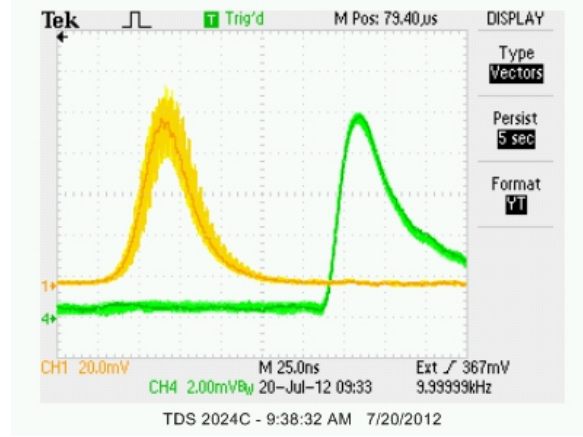


Figure 6.4: Measurement of the pulse jitter of the Ti:Sa (yellow curve) and the Edgewave YAG laser (green curve). The photo-diode used to monitor the YAG laser was not suitable to resolve the short pulse-length. The pulse jitter of the free-running Ti:Sa laser is 7.2(1.0) ns.

6.1.2.3 Independent pump lasers

The most convenient way to synchronize the Ti:Sa lasers is to use independent pump lasers for each cavity and to delay their triggering pulse. This approach is realized in the (upgraded) commercial Ti:Sa system used at ORNL [Liu12]. The RILIS Ti:Sa system comprises two pump lasers. A combination of Pockels cells and independently pumped lasers would give the best performance in terms of jitter and output power.

6.1.3 Pulse-jitter of the Ti:Sa

A pulse jitter of the Ti:Sa pulses leads to fluctuations in laser ion current. To quantify the effect, a measurement of the pulse jitter of a free-running Ti:Sa (without Pockels cell) was performed in the following way: The leaking output⁹ through the high reflecting mirror of the Ti:Sa cavity was directed onto a photo diode¹⁰. The pulse structure could then be observed with an oscilloscope. The pump pulse trigger signal was obtained from the T_0 signal of the digital delay generator. For the jitter measurement, the oscilloscopes display setting was selected as persistent (5 s). The position of the peak was adjusted for the inflection point of the rising edge to cross the 0 V line of the oscilloscope. The cursor function was then used to determine the horizontal range covered by the pulse. A screen shot of the oscilloscope showing the pulse of Ti:Sa 1 (2.6 W output power at 802.9 nm) and the pulse of the *Edgewave* ND:YAG laser is displayed in Fig. 6.4. The jitter of the Ti:Sa laser was evaluated to 7.2(1.0) ns.

⁹The power leaking through the HR is in the order of 30 mW

¹⁰DET10A/M from Thorlabs

6.1.4 Wavelength stability of the Ti:Sa lasers

The stability of the laser wavelength is one of the key aspects for a stable production of radioactive ion beams using RILIS. Drifts may occur due to temperature dependence of wavelength determining elements in the laser resonator. During the RILIS operational period in 2011 a wavelength stabilization system was developed, installed into the Ti:Sa laser cavities and implemented into the RILIS Monitoring and Control System (described in chapter 8). To stabilization system actively the tilting angle of the etalon in a feedback loop. The wavelength of the Ti:Sa laser mainly depends on the temperature in the RILIS. This is shown in the top panel of Fig. 6.5 in which the wavenumber difference from a set value is plotted against the temperature of the inlet of the chilled air to the RILIS room. The temperature difference inside the Ti:Sa is much smaller. A long term measurement of the etalon temperature and the wavelength obtained from the Ti:Sa was evaluated and gave a temperature dependence of $\approx 1 \text{ cm}^{-1}\text{K}^{-1}$. The lower panel of Fig. 6.5 shows a second long-term measurement with the wavelength stabilization system enabled. The temperature dependence is negligible and the frequency is stabilized to better than 0.04 cm^{-1} . These results and the wavelength stabilization project is described in more detail in the B.Sc. thesis of Ralf Rossel [Ros11].

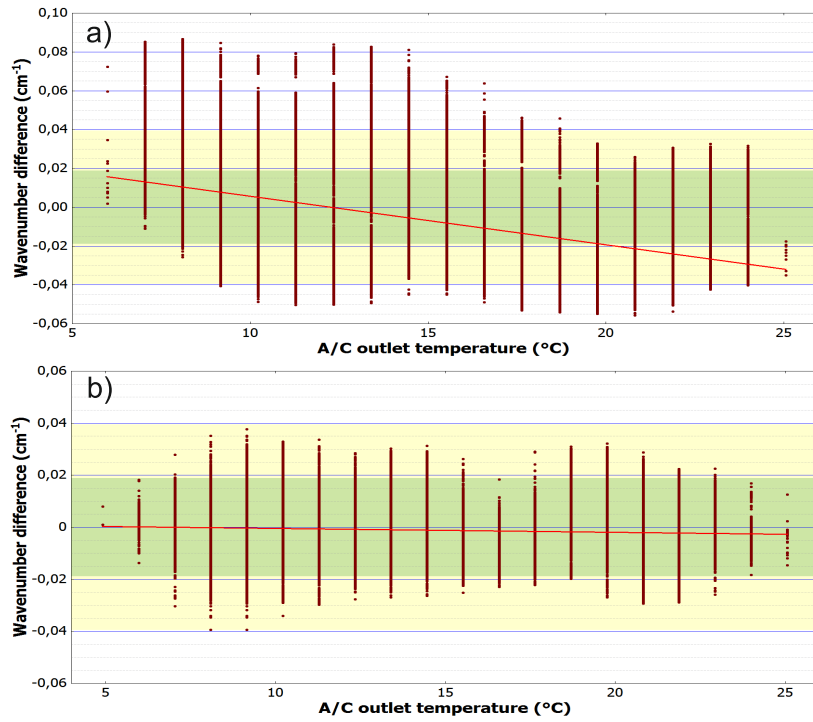


Figure 6.5: Performance of the Ti:Sa wavelength stabilization [Ros11]. a) Shows the non-stabilized Ti:Sa laser. A temperature dependent drift in a range of 0.14 cm^{-1} was observed. b) When the stabilization system is enabled, the temperature dependence is negligible and the laser output was stable within a range of 0.04 cm^{-1}

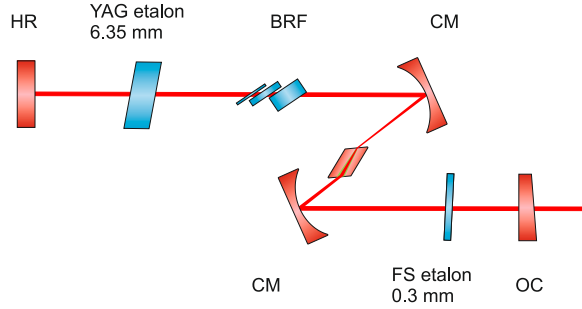


Figure 6.6: Optical layout of the narrow-band Ti:Sa cavity. The frequency tuning elements are indicated in blue colour: The birefringent filter and the two etalons: 0.3 mm fused silica (FS) with a 40% reflective coating on both sides and an uncoated 6.35 mm thick, polished YAG substrate.

6.2 Additional functionality of the Ti:Sa lasers

For specialized applications, the Ti:Sa lasers can be operated in a non-standard configuration. The narrow band mode in which the laser line width is reduced to below 1 GHz as well as results for intra-cavity frequency doubling and single-pass amplification of Ti:Sa pulses are described in the following sections.

6.2.1 Narrow-band Ti:Sa

To apply the RILIS lasers for in-source spectroscopy, a narrow line width of well below 1 GHz is desirable. The use of injection-seeded Ti:Sa lasers was reported [KTM⁺08, RMK⁺12], but not considered (yet) for on-line application for two reasons: Firstly, the laser line width of 20 MHz is too narrow for addressing the Doppler-broadened ensemble (in the order of GHz) in the hot cavity of the ISOLDE ion source, and secondly, the locking of the cavity is highly complex and too sensitive to acoustical noise.

Optical Layout The approach to reduce the laser line-width followed in this work was analogue to the way the RILIS narrow-band dye laser is operated. Inserting a second, etalon¹¹ with a thickness of $d = 6.35$ mm into the Ti:Sa cavity yields an additional reduction of line-width. A schematic sketch of the dual etalon Ti:Sa is shown in Fig. 6.6.

The relative alignment of both etalons has to be performed carefully to avoid multi-mode operation of the laser. Otherwise a laser scan of e.g. a hyperfine structure would result in recording of additional peaks (“ghosts”) in the spectrum. To allow for manual mode cleaning, the mode structure of this NB-Ti:Sa was visualized in different wavemeters (WS7 and ATOS LM007) and a scanning 4 GHz-FPI. The results are analysed in the following paragraphs.

¹¹Purchased from LAYERTEC

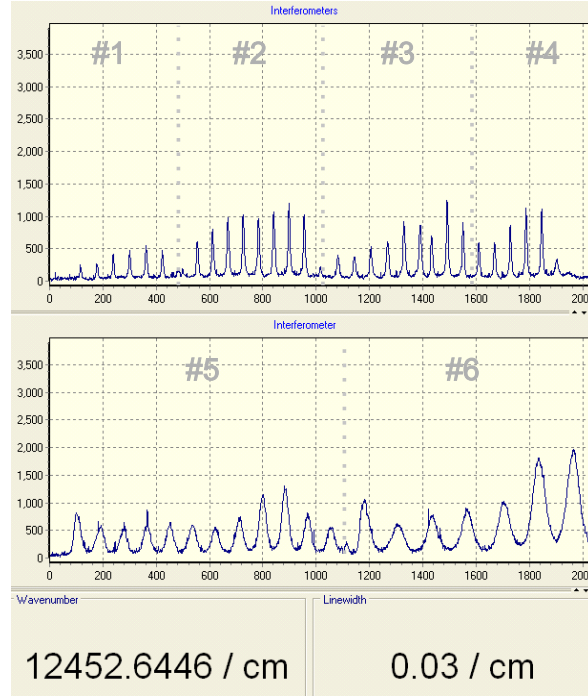


Figure 6.7: Fringe pattern of the NB-Ti:Sa measured with the WS7 wavemeter. All six interferometers show a clean fringe pattern. The line-width measurement of the WS7 software gives 0.03 cm^{-1} , corresponding to 900 MHz

NB-Ti:Sa spectrum measured with the wavemeters The wavelength of the NB-Ti:Sa was measured with the Atos and the WS7 wavemeter to be $12452.6381 \text{ cm}^{-1}$ and $12452.6446 \text{ cm}^{-1}$, respectively. The line-width measurement of the WS7 gave a value of $\Delta\nu = 0.03 \text{ cm}^{-1}$, corresponding to 900 MHz. Fig. 6.7 shows a screen shot of the WS7 software displaying the interferometer pattern of the single-mode NB-Ti:Sa. All interferometers show a clean fringe pattern. Fig. 6.8 shows the mode structure of the NB-Ti:Sa observed with the *Atos LM007* wavemeter in comparison. The mode structure changes when the thin etalon is tilted and when the birefringent filter is detuned.

NB-Ti:Sa spectrum measured with a scanning FPI To further analyse the mode structure of the NB-Ti:Sa, a fraction of the output beam was coupled to a scanning FPI¹² with a free spectral range of 4 GHz. A combination of fiber splitters¹³ was used to split the sampled light from the NB-Ti:Sa to observe it simultaneously in a wavemeter and the FPI.

¹²FPI-100-0750-4 from *TOPTICA*

¹³FCMM625-90A-FC from *THORLABS*

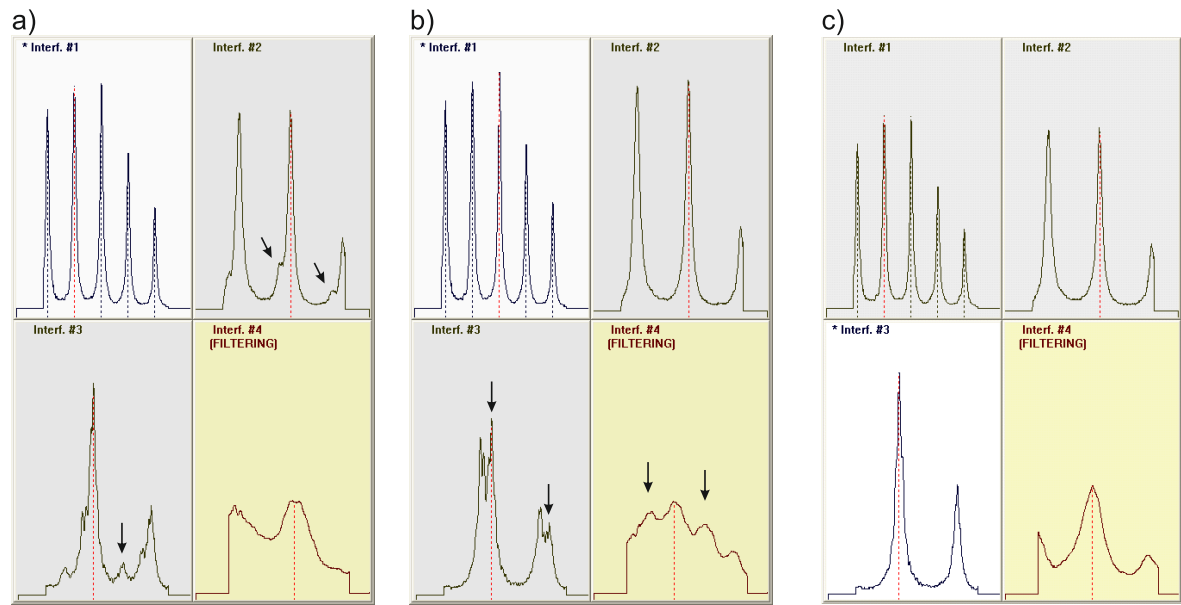


Figure 6.8: Different mode structures of the NB-Ti:Sa were observed with the Atos LM007 wavemeter. a) Birefringent filter is detuned. Interferometer #3 and #4 show multi-mode structures indicated by arrows. In this case, a second mode can be observed in the grating spectrometer of the WS6 wavemeter (not shown). b) The birefringent is corrected, but the thin etalon is detuned. Interferometers #2 and #3 show multi-mode structure. Side peaks are indicated by arrows. c) The thin etalon is corrected. All interferometers show a clean fringe pattern.

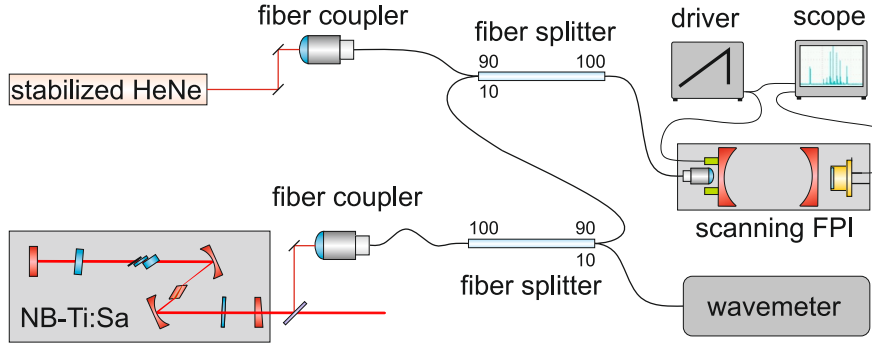


Figure 6.9: Sketch of the setup used for the measurement of the mode structure with the scanning FPI. A first fiber splitter (ratios are indicated) was used to divert Ti:Sa light to the FPI and to the wavemeter simultaneously. A second fiber splitter allowed to couple the Ti:Sa light and the reference light from the He-Ne together into the FPI. The FPI driver was set to ramp the FPI cavity with a rate of 20 Hz. The amplified photo-diode signal was observed in an oscilloscope.

The fiber splitters also allowed to couple the light from a frequency stabilized He-Ne laser into the scanning FPI together with the NB-Ti:Sa. This setup is illustrated in Fig.6.9.

The oscilloscope was set to peak detection mode and was triggered by the rising edge of the He-Ne laser signal in the FPI. A screen shot of the oscilloscope is shown in Fig.6.10 indicating that the Ti:Sa was operating in single mode. Arrows indicate the positions of the He-Ne laser in the spectrum. One can see 6 separated resonator modes with a single Gaussian envelope. This single-mode operation is strictly speaking a single-etalon-mode operation. This prevents "ghosts" in the spectrum and a misinterpretation of the spectrum by the wavemeter that could lead to shifted wavelength readings.

Several oscilloscope traces were recorded while the laser was operated in broadband-mode (thick etalon removed) and with a detuned thin etalon which resulted in multi-mode operation. These traces are shown together with the single mode operation in Fig. 6.11. The spectrum is zoomed so that the He-Ne fringes (broad peaks) are on the left and on the right end of the graph. The thin spikes are single laser pulses that are resolved because the scanning speed of the FPI mirror was set to ≈ 20 Hz. At a repetition rate of 10 kHz a number of 500 laser shots is required to build one spectrum.

6.2.1.1 Determination of the line width of the NB-Ti:Sa

The Ti:Sa resonator modes are resolved by the FPI. The oscilloscope was set to single-shot recording. No averaging took place, therefore single laser pulses were recorded as the mirror of the FPI was sweeping through the spectrum. The line-width of the NB-Ti:Sa laser is determined by the envelope of the resonator modes between the He-Ne peaks. To calculate

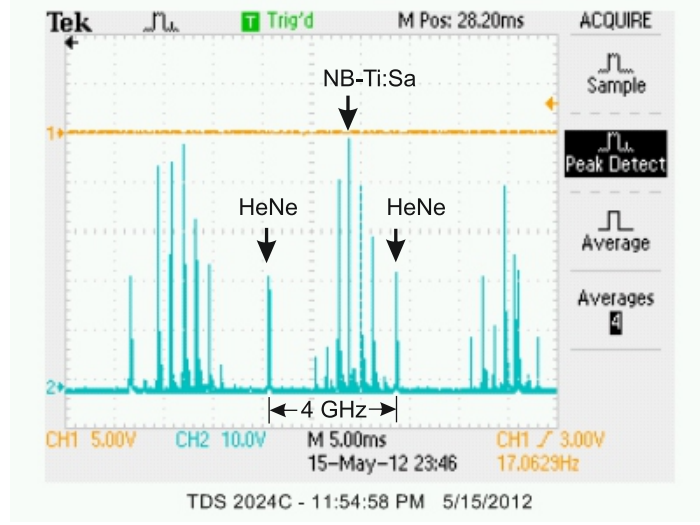


Figure 6.10: Mode structure of the NB-Ti:Sa observed with the scanning FPI. The two peaks of the He-Ne laser are indicated. They are used for the calibration of the 4 GHz FSR. In between the He-Ne peaks (arrows), six resonator modes (arrow) of the NB-Ti:Sa are present and resolved.

the envelope, a multiple Gauss fit was applied to a single trace of the oscilloscope. This is shown in Fig. 6.12 a). The He-Ne peaks were used to determine the scaling factor from FPI time domain to the frequency domain. The scaled peak positions and peak heights of the resonator modes were then plotted (Fig. 6.12 b)) and fitted with a Gaussian shape. For the Ti:Sa operating with the 0.3 mm thin etalon and the 6 mm thick YAG etalon, a line-width of $\Delta\nu_{\text{FWHM}} = 0.99(9)$ GHz corresponding to $\Delta\nu_{1/e} = 0.84(8)$ GHz was determined. The average distance of the resonator modes is $\Delta\nu_{\text{Res}} = 367$ MHz.

$$\Delta\nu_{\text{fsr}} = \frac{c}{2d} \quad (6.1)$$

with a optical resonator length of $d = 486$ mm the calculated FSR of 307 MHz shows a discrepancy of 20%.

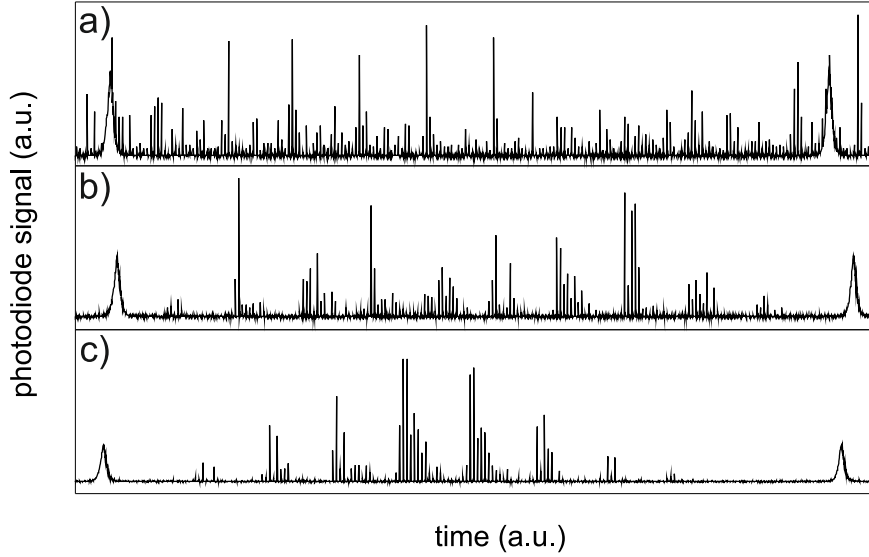


Figure 6.11: FPI signals for different Ti:Sa operation modes. The three panels show oscilloscope traces recorded from the FPI photo-diode signal, the broad peaks at the left and at the right of the spectrum originate from the He-Ne and indicate the FSR of 4 GHz. The thin separated spikes are single laser shots of the Ti:Sa. a) Normal broadband operation, without a thick etalon. b) The Ti:Sa is equipped with the thick etalon, but the thin etalon is detuned, resulting in a multi-mode spectrum. c) The thin etalon was adjusted for the Ti:Sa to operate in single-mode.

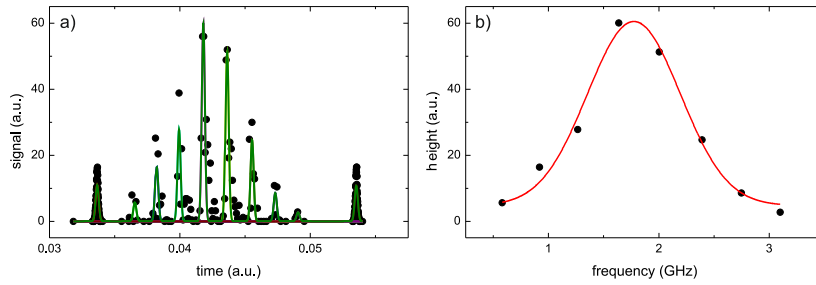


Figure 6.12: Determination of the linewidth of the NB-Ti:Sa. a) Oscilloscope trace of the 4 GHz FPI. Gaussian profiles were fit to the resonator modes and to the He-Ne peaks. The distance of the He-Ne peaks is 4 GHz. The distance between the resonator modes is 367 MHz b) The envelope of the Ti:Sa spectrum was fit with a Gaussian shape. The full width at half maximum is 0.99(9) GHz

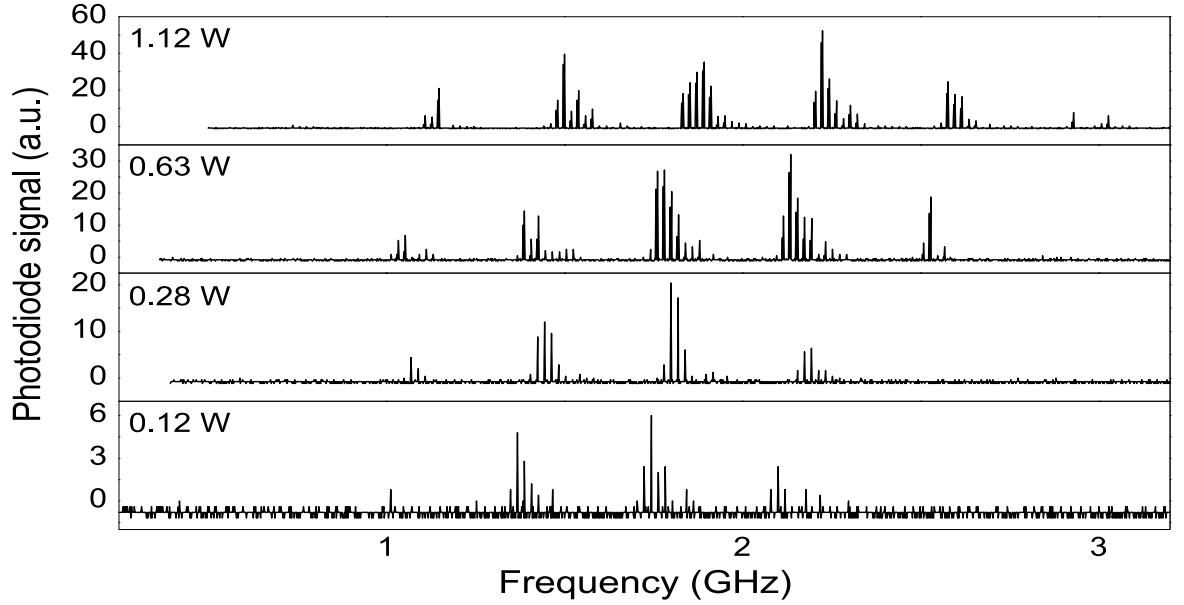


Figure 6.13: Mode structure of the NB-Ti:Sa measured at different output powers. The single laser pulses are resolved as the spikes in the signal. Single-shot scans of the mode structure at four different output powers were recorded. A reduction of the output power reduces the laser line-width from 900 MHz to 600 MHz.

6.2.1.2 Reducing the line-width by reduction of the gain

Decreasing the pump power of the NB-Ti:Sa and thereby reducing the resonator gain, leads to a further reduction of the line-width of the laser. The mode structure was recorded at different output powers of the NB-Ti:Sa. The plots are shown in Fig. 6.13. At an output power of 1.12 W, six resonator modes were observed. At a reduced output power of 0.12 W, only four resonator modes were observed. This corresponds to a reduction of the laser line width from 900 MHz to 600 MHz. By using a bow-tie ring cavity configuration which prevents spatial hole burning effects caused by the standing-wave in the Z-shaped Ti:Sa cavity a further reduction would be possible. The reduced output power could then be amplified in the Ti:Sa amplifier described in section 6.2.2. This upgrade is foreseen for the near future.

6.2.1.3 In-source spectroscopy of the hyperfine structure of gold

To demonstrate the capabilities of the data acquisition and the NB-Ti:Sa laser, in-source spectroscopy of the hyperfine structure of stable ^{197}Au was performed. The fundamental output of the NB-Ti:Sa was frequency tripled and used in the first step of the three step ionization scheme $\{267.7^{\text{NB-Ti:Sa}}|306.3^{\text{Dye}}|532\}$. A step-wise laser scan was performed. For

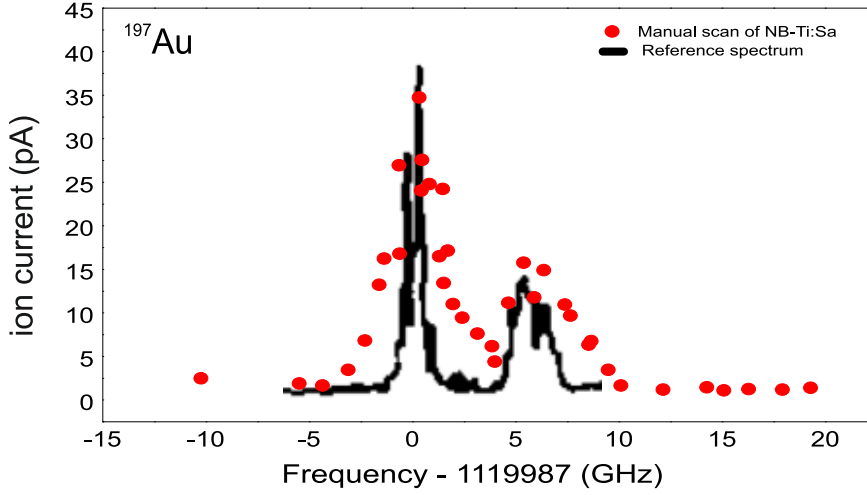


Figure 6.14: Hyperfine structure of gold measured with the NB-Ti:Sa. A reference scan of the hyperfine structure, taken from [LPA⁺92], was calibrated and scaled accordingly and was superimposed for reference. The two separated structures with a distance of ≈ 5 GHz could be resolved.

each new tilt angle of the thick etalon, which defines a new laser frequency output, the thin etalon had to be re-tuned manually to ensure single mode operation. The wavenumber and ion beam current were both averaged over the time of 10 proton pulses (≈ 30 s). The scan results are shown in Fig. 6.14. For reference, it is superimposed with a measurement obtained with the COMPLIS spectroscopy setup [LPA⁺92]. The two separated peaks have a width of 2.8(2) GHz and are separated by $\Delta\nu(6s^2S_{1/2} \rightarrow 6p^2P_{1/2}^o) = 6.0(2)$ GHz. This value agrees within the error with a more precisely measured value of $\Delta\nu(^2S_{1/2}) = 6.099309(10)$ GHz given in [FPR60]. The peak width corresponds to the expected Doppler width of $\delta\nu_D = 2.7$ GHz ($T = 2200$ K).

This measurement is considered as a proof of concept for the application of the NB-Ti:Sa for in-source laser spectroscopy and was therefore not further analysed.

6.2.1.4 Automatic tuning of the NB-Ti:Sa

For the application of the NB-Ti:Sa for in-source laser spectroscopy, an automatic scanning of this laser is required. A scanning method was implemented and is currently under investigation. The algorithm was implemented in LabVIEW as follows: The thick etalon is moved towards a new desired central wavelength. To ensure single-mode operation the thin etalon is sweeps in two directions until the line-width, detected by a wavemeter (*WS7*) increases and reaches a threshold. The etalon is then moved to a central position as calculated from the total step

count for the sweep. A new wavelength can be set and the thin etalon can be centred in less than 20 s. The step size for the thick etalon is currently limited, but the implementation of a lookup table and upgrading to piezo-actuated etalon mounts will increase the scan speed. To ensure reliable single-mode operation, the interferometer patterns of the wavemeters and the scanning FPI could be analysed automatically.

6.2.2 Amplification of Ti:Sa pulses

The amplification of Ti:Sa pulses was described in [Kes04]. Investigations presented in this work were carried out with two independent pump lasers¹⁴ for the oscillator and the amplifier.

Oscillator-amplifier setup For the test of the Ti:Sa pulse amplification, an oscillator-amplifier configuration was set up using two Ti:Sa laser cavities. The first cavity was a fully equipped as a standard Ti:Sa laser. Its output was sent into the second cavity, in which only the Ti:Sa crystal and the curved mirrors were installed. A telescope ($f_1 = f_2 = 50$ mm) was used for matching the oscillator mode and amplifier pump inside the amplifier crystal. A schematic view of the setup is shown in Fig. 6.15. The oscillator and the amplifier were pumped by independent pump lasers, which allowed specific control of the timing of the pump and the amplifier pulse.

Results from the pulse amplification A linear dependency of the amplification efficiency from the oscillator power as well as from the amplifier pump power was observed (see Fig. 6.16). The maximum observed amplification factor was $A_F = 2.2$.

To determine the optimal timing of the oscillator pulse and the amplifier pulse, the amplifier pump pulse was delayed with respect to the oscillator pump pulse. The power of the amplifier was recorded for each time delay. The result is shown in Fig. 6.17. If the amplifier pulse arrives at the Ti:Sa crystal later than the oscillator pulse, amplification cannot take place. The smooth peak structure at the beginning is a convolution of the oscillator pulse and the amplifier pulse. The exponential decrease from 73 ns to 5000 ns represents the excitation life time of the amplifier medium. The decay constant was determined from a fit to $\tau = 1845(56)$ ns, which is smaller than the fluorescence life time of Ti:sapphire $\tau_f = 3200$ ns [EDK88]. This oscillator-amplifier concept can certainly be improved in term of photon efficiency and may be used to increase the output power of the widely tunable grating based Ti:Sa lasers as well as the injection seeded Ti:Sa laser that lack output power. For the NB-Ti:Sa the trade-off between line-width and output power can be resolved by using the oscillator-amplifier concept. The amplifier setup requires a small foot-print and can be attached to any oscillator lacking power.

¹⁴The availability of two pump lasers at the same time was scarce. The lasers were repaired and upgraded frequently by the manufacturer.

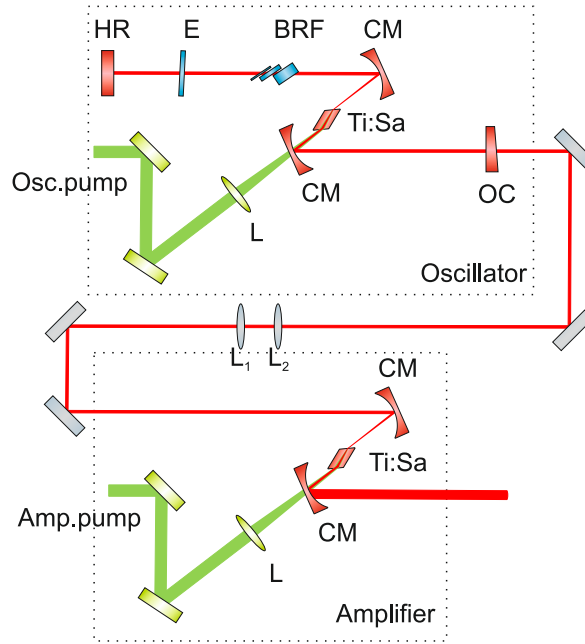


Figure 6.15: Setup for the Ti:Sa single-pass amplification. Two Ti:Sa cavities were used to simplify the setup. The planar cavity mirrors were removed from the second cavity to build the amplifier. A telescope (L_1, L_2) is used to match the mode size of the oscillator and the amplifier.

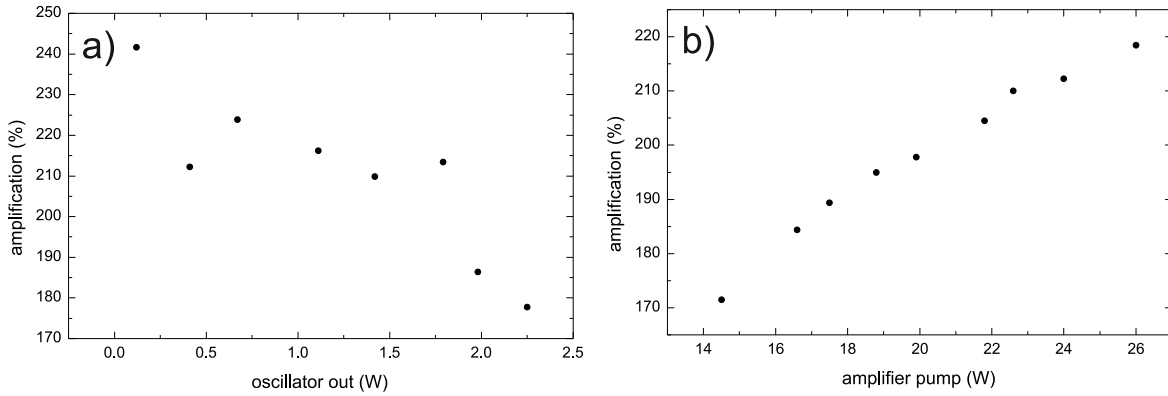


Figure 6.16: Single-pass Ti:Sa amplification. a) The amplification was calculated for different oscillator powers. In general a linear trend is observed. The points at 0.4 W and 1.8 W do not follow the trend. This may be caused by misalignment. b) The amplifier pump power was increased while the oscillator power was fixed. A maximum amplification factor of $A_F = 2.2$ was achieved.

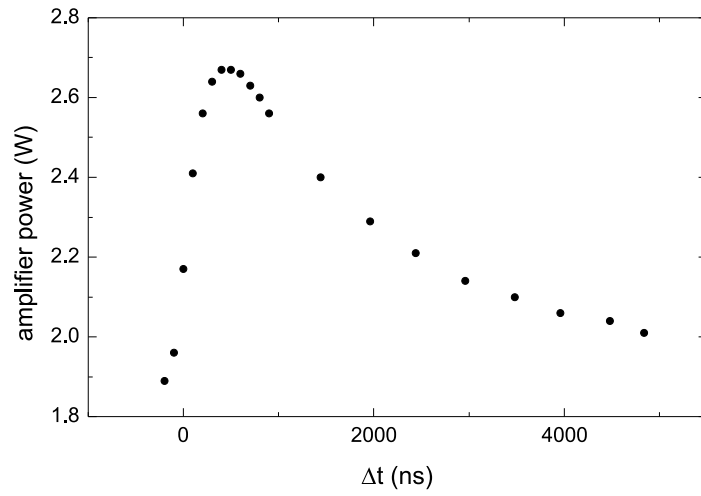


Figure 6.17: Amplifier output at different amplifier pump pulse delays. The amplifier pump pulse was delayed with respect to the oscillator pump pulse. If the amplifier pulse arrives later than the oscillator pulse, no amplification can be observed ($\Delta t < 0$). When the pulses arrive simultaneously at the amplifier crystal, the amplification is maximised. The tailing on the right of the peak is attributed to the life time of the amplifier medium.

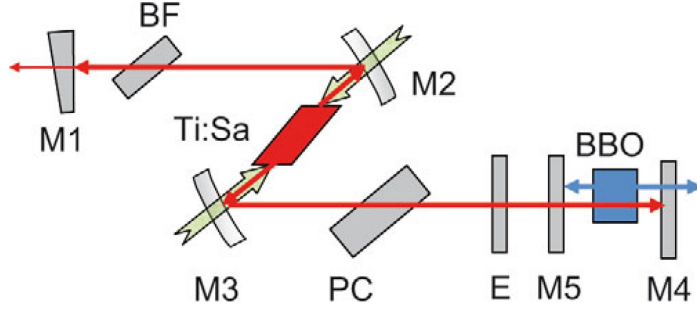


Figure 6.18: Schematic view of the setup for intra-cavity frequency doubling used in Jyväskylä [RMK⁺12]. The cavity mirrors are denoted as M1 to M4. The birefringent tuner (BF) and the etalon (E) are used to select the fundamental wavelength. A Pockels cell (PC) can be used for Q-switching the cavity and allows for synchronization of the SHG pulses with other lasers. The nonlinear crystal (BBO) is placed inside the resonator. The second harmonic beam travelling in the direction of the M4 can exit the resonator as this mirror is transparent for this wavelength range. The Z-shaped cavity layout allows two counter-propagating resonator modes to build up in the resonator. The second harmonic light travelling towards M3 is reflected towards the output mirror M4.

6.2.3 Intra-cavity SHG

Intra-cavity frequency doubling inside the Ti:Sa resonator was investigated in the Diploma work by Thomas Kessler [Kes04]. An efficiency of $\approx 12\%$ was reported with an additional lens introduced into the resonator. This concept was considered as too complicated and unstable. As the output powers of the Ti:Sa lasers have improved, a re-evaluation of the feasibility of the intra-cavity frequency doubling was launched. This second initiative to investigate intra-cavity (IC) frequency doubling for the Ti:Sa lasers was conducted in collaboration with and at the FURIOS group at the University of Jyväskylä during a research visit of mine. Details and more recent results were published in [RMK⁺12].

Intra-cavity frequency doubling at Jyväskylä A broad-band AR-coated BBO crystal was placed inside the Ti:Sa cavity at a distance of ≈ 60 mm from the curved mirror in the branch of the HR mirror (see Fig. 6.18). The output power of the fundamental and the second harmonic passing through the HR mirror were measured simultaneously in different power-meters after separation using dichroic mirrors. The different output powers were obtained by de-optimizing the laser cavity. A fitted parabola shows the quadratic dependence between SHG power and fundamental power as expected. The IC-SHG performance obtained during the tests in Jyväskylä is shown in 6.19.

The introduction of a dichroic beam splitter mirror (high transmittance for infra-red and highly reflective for SHG) allowed to overlap the two counter-propagating SHG laser beams

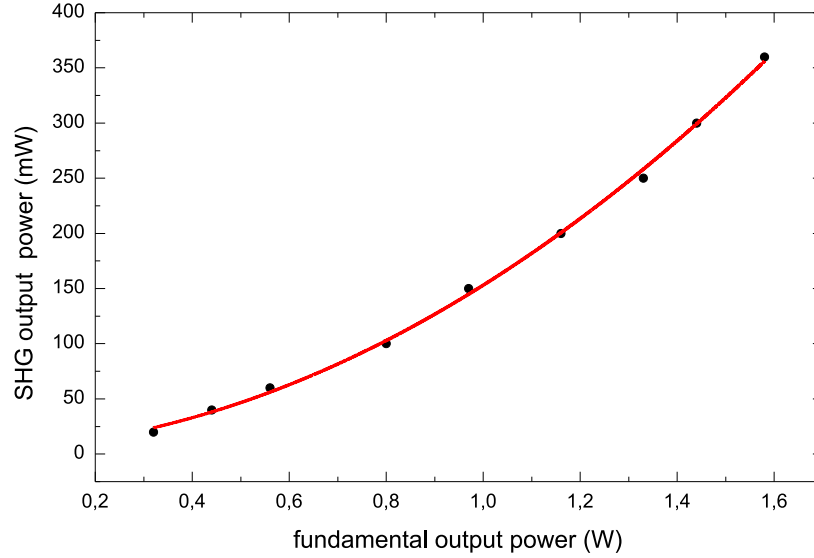


Figure 6.19: Performance of the intracavity SHG

and produce 800 mW of blue light at 843.08 nm. The setup was further refined and a SHG output of 2.45 W with a slope efficiency (Pump to UV) of $\eta_{\text{slope}} = 10\%$ was obtained. These results are published in [RMK⁺12].

The CERN Ti:Sa design was prepared to accommodate a setup for intra-cavity second harmonics generation (IC-SHG) shown in a photograph in Fig. 6.20 shows the simple opto-mechanical arrangement used for this. A broad-band AR coated BiBO crystal with a length of 7 mm¹⁵ was used as non-linear medium and a dichroic separator mirror¹⁶ was used to overlap the two SHG laser beams. The maximum extracted power was 2 W of blue light. The power, however was not stable and degraded with time. A correction of the crystal angle was required to re-gain the power. A possible explanation is that the crystal temperature increased due to absorption which resulted in a detuning of the phase match. These effects need to be investigated further. The advantage in intra-cavity doubling lies in the fact that no focussing is required to obtain high energy densities inside the non-linear medium. This improves the beam shape of the second harmonic beam which improves beam transport to the target and increases the efficiency of the subsequent third or fourth harmonic generation.

¹⁵Purchased from *CASTECH*

¹⁶Layertec, HR SHG Ti:Sa, HT fundamental Ti:Sa

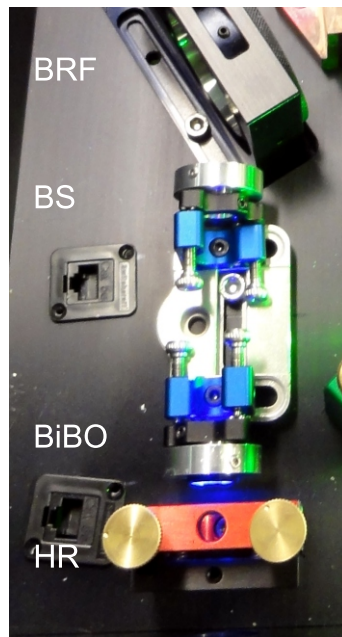


Figure 6.20: Photograph of the setup for intra-cavity frequency doubling. The non-linear crystal (BiBO) is placed inside of the resonator on a kinematic mirror mount between the birefringent filter (BRF) and the end mirror (HR) of the Ti:Sa cavity. The beam splitter (BS) overlaps the two counter-propagating second harmonic beams.

Chapter 7

Implementation of the Ti:Sa lasers to RILIS

In this chapter the prerequisites for the operation of the Ti:Sa laser system in the environment of the RILIS laser cabin and the implementation process are described, followed by a summary of the on-line operation of the new lasers.

7.1 Two laser systems at RILIS

7.1.1 New RILIS layout

Prior to the installation of the Ti:Sa lasers, it was necessary to re-think the overall laser layout to achieve the optimal arrangement for the operation of two complementary laser systems. Two laser tables were added to hold the two *Credo* dye laser as well as the *Edgewave* pump laser. A second laminar flow unit was installed to reduce dust in the air at the new Ti:Sa area. Additional laser safety screens were installed. Care was taken to ensure to maintain easy access to each of the tunable lasers for ease of setup and alignment. A photograph of the RILIS laser setup is shown in Fig. 7.1 and a closer view of the Ti:Sa laser system is shown in Fig. 7.2. The Ti:Sa system is installed at one side of the laser table and uses about the space of the old CVL pump laser.

7.1.2 Beam transport to HRS

The previous HRS launch system consisted of two uncoated right angle prisms and one high reflective mirror at the laser table level. A 40x40 mm uncoated prism and a second HR mirror were installed beneath the laser table to send the beams to the HRS separator room. Fig. 7.3 shows the old HRS launch path. The use of prisms has the advantage of being wavelength independent. The main disadvantage, however, is the reflection losses of $\approx 4\%$ per surface. After two prisms only 85% of the light is transmitted. The fact that the laser beams exit the room at an angle of 65° lead to a mixing of the controls for horizontal and vertical movement of the laser beams which is inconvenient when using the remote controlled mirror mounts.

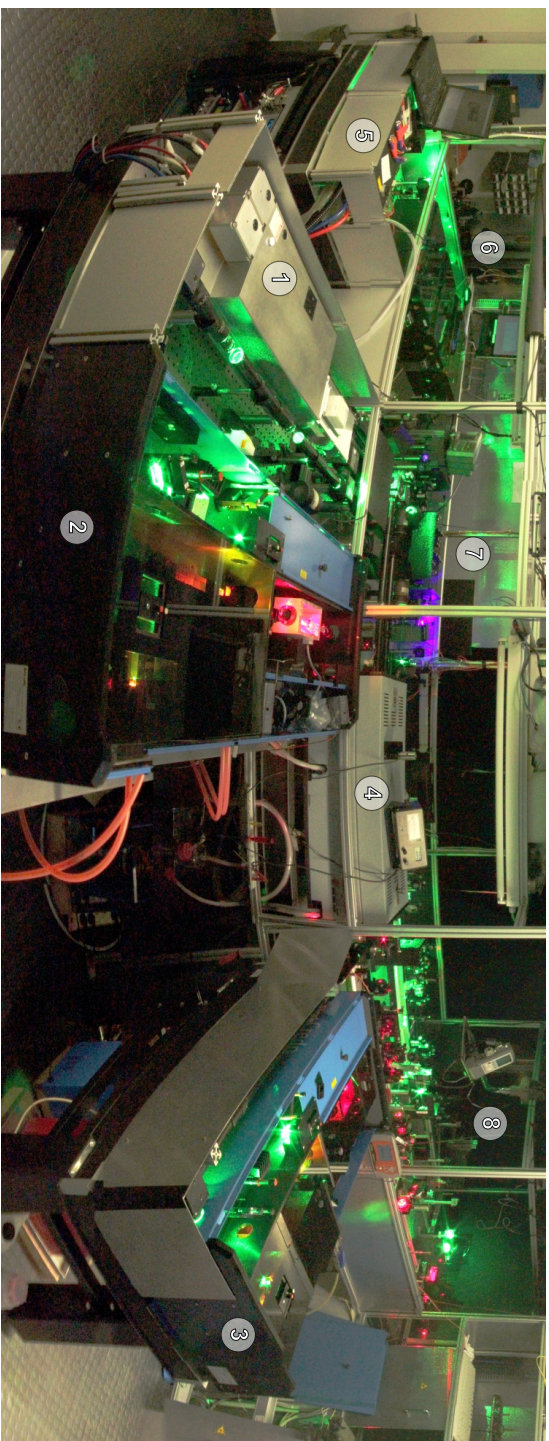


Figure 7.1: Photograph of the RILIS laser table. (1) The *Edgewave* Nd:Yag pump laser for the dye system and for non-resonant ionization. (2) and (3) The two *Credo* dye lasers from *Sirah*. (4) The Narrow-band dye laser from *MSS*. Circled 5 One of the two *Photonics* Nd:YAG pump lasers for the Ti:Sa system. (6) The three RILIS Ti:Sa laser cavities. (7) Frequency conversion unit. (8) Laser beam transport and focussing.

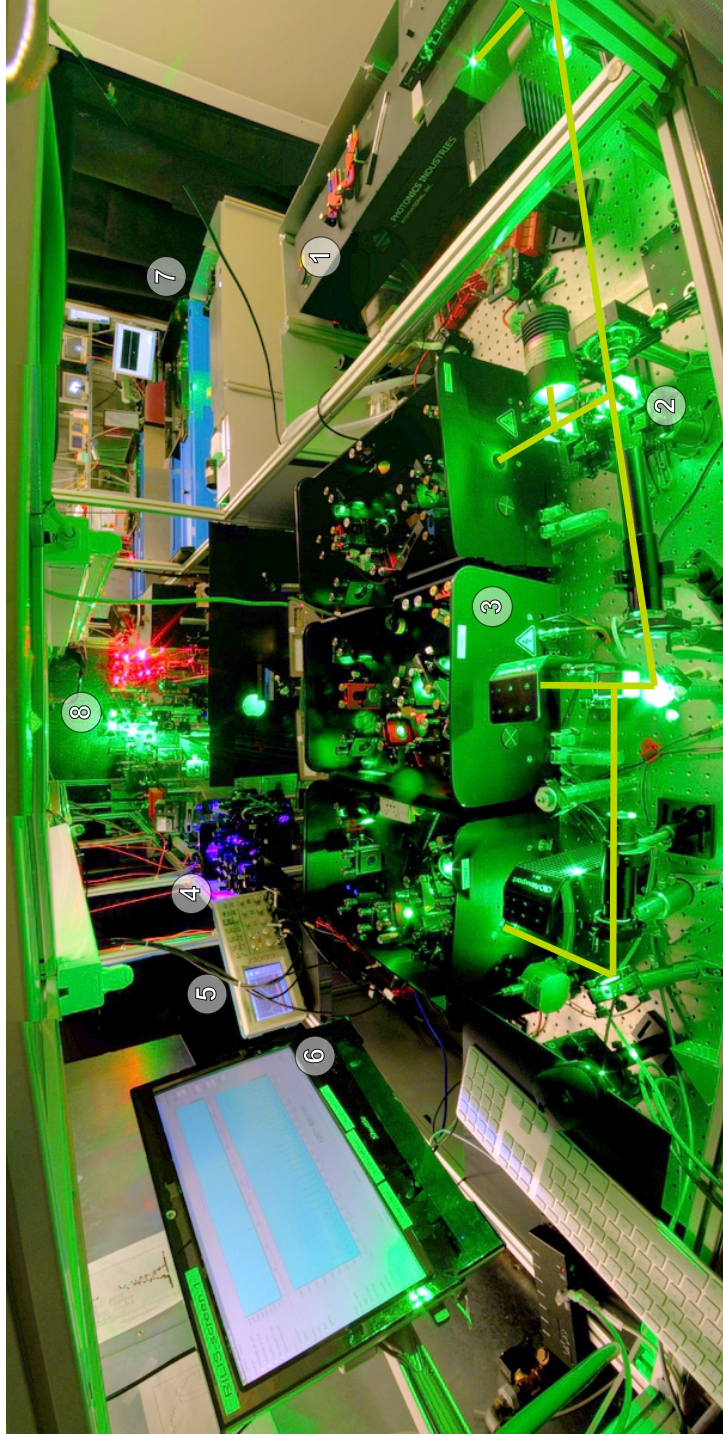


Figure 7.2: Photograph of the Ti:Sa system on the RILIS laser table. ① Photonics Nd:YAG pump laser. Next to it is space for the second pump laser which was upgraded at the time the picture was taken. ② Pump beam distribution system. A combination of half-wave plates and polarizing beam splitter cubes allows individual adjustment of the pump power delivered to each of the Ti:Sa cavities. ③ Three Ti:Sa laser cavities. ④ Frequency conversion unit. ⑤ Oscilloscope for monitoring the temporal overlap of the laser pulses from the Ti:Sa lasers and the *Edgewave* Nd:YAG. ⑥ Display of the Ti:Sa laser wavelengths. ⑦ Edgewave Nd:YAG pump laser for the dye system (hidden behind laser safety screen), also used for non-resonant ionization. Credo dye laser from Sirah (blue housing). ⑧ Focussing system and beam launch towards the GPS and the HRS targets.

To improve the system and reduce transport losses, which is particularly important for the Ti:Sa lasers which generally have a lower power output, a new launch system was designed and built.

The laser beam transport and launch-point for the HRS target was re-designed to match the following requirements:

- reduction of losses
- independent control of horizontal and vertical beam positions
- allowance for transport and control of four independent laser beams

The new HRS launch platform was first designed in *Autodesk Inventor* to check the feasibility of different launching configurations. First the space was determined within which the turning mirrors have to be positioned such that each laser beam can reach the end of the ionizer tube. Then the mirror mounts and opto-mechanics were added. Finally the frame was built. Figure 7.4 shows the design phase of the launch system.

The launch system was built from commercial aluminium profiles and a $1 \times 1 \text{ m}^2$ breadboard purchased from *Newport*. The breadboard was water-cut by the machine shop into the three required parts. The base-plate is bolted to the concrete floor. The remote actuated mirror mounts from the old system were re-used. Fig. 7.5 shows a photograph of the new HRS launch path and Fig. 7.6 shows a detail of the lower platform of the launch.

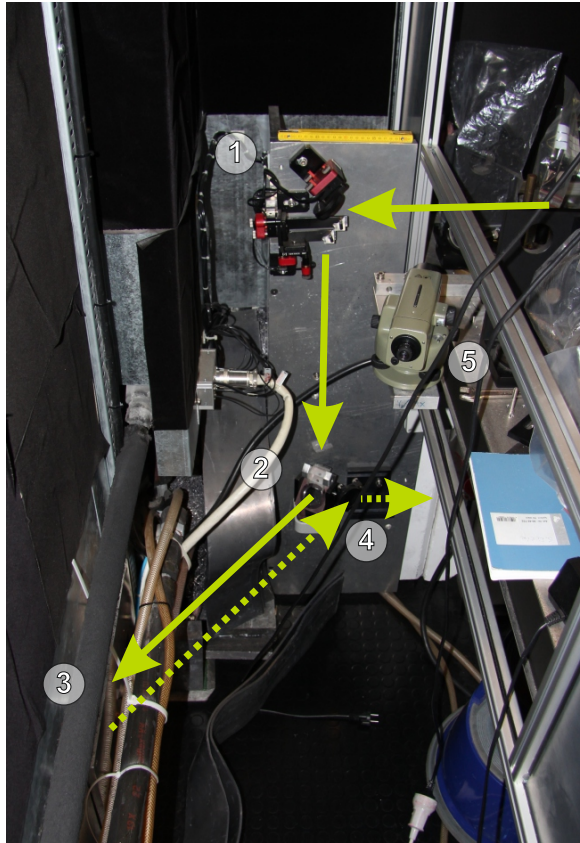


Figure 7.3: Photograph of the previous HRS launch path. The solid arrows indicate the direction of the laser beams. The dashed arrows indicate the path for the reference beam that is reflected back to the observation point. ① Motorized mirror mounts holding two prisms and a 2 inch mirror. ② Manual mirror mounts holding one prism and one 2 inch mirror. ③ Transport tube to the HRS separator room. ④ One mirror mount holding a broad-band aluminium mirror, reflecting the reference beams to the observation area. ⑤ Theodolite for the observation of the ion source.

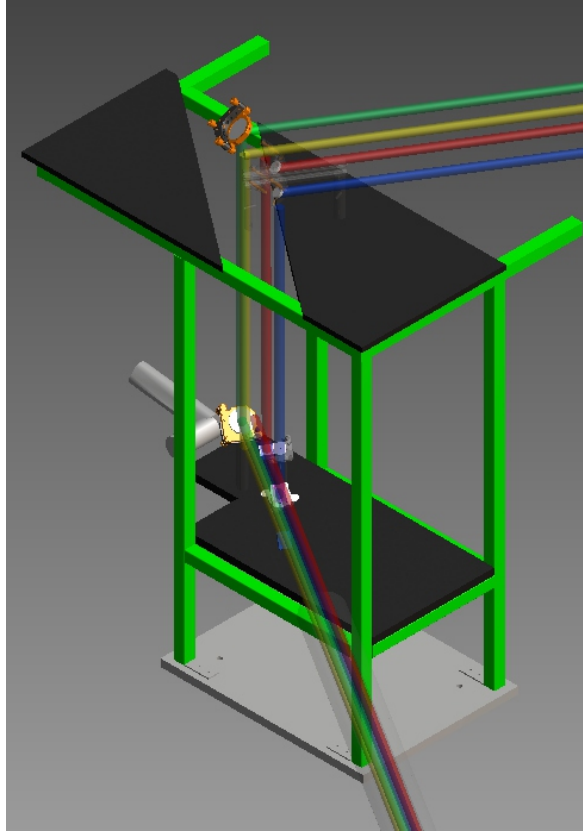


Figure 7.4: The laser beams originate from the top right corner. The upper platform is cut in an angle such that the upper mirrors can be positioned in line with the exiting laser beams to the HRS on the lower level. This configuration ensures 90° angles and allows four laser beams to be sent to the ion source.

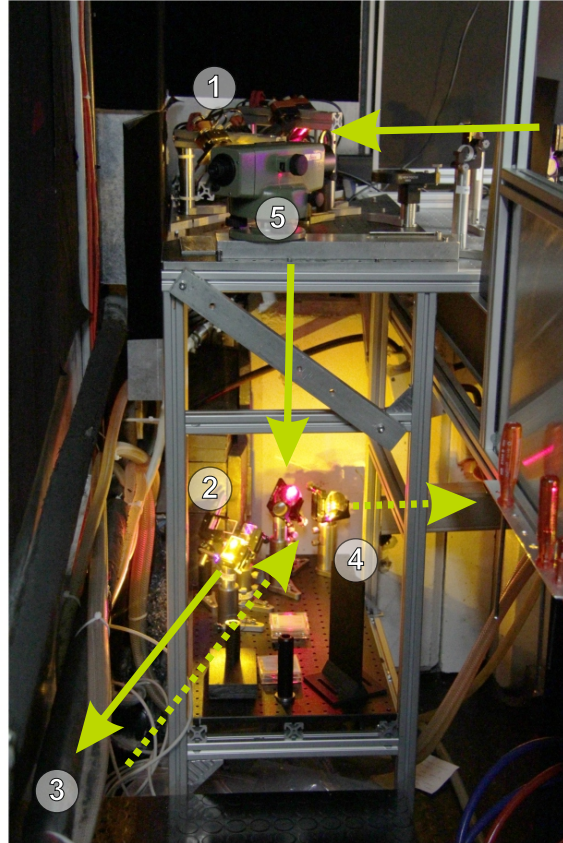


Figure 7.5: Photograph of the new HRS launch path. (1) Motorized mirror mounts. (2) Four mirror mounts launching the laser beams towards the HRS separator zone. (3) Transport tube to the HRS separator zone. (4) One mirror mount holding a broad-band aluminium mirror, reflecting the reference beams to the observation area. (5) Theodolite for observation of the ion source.

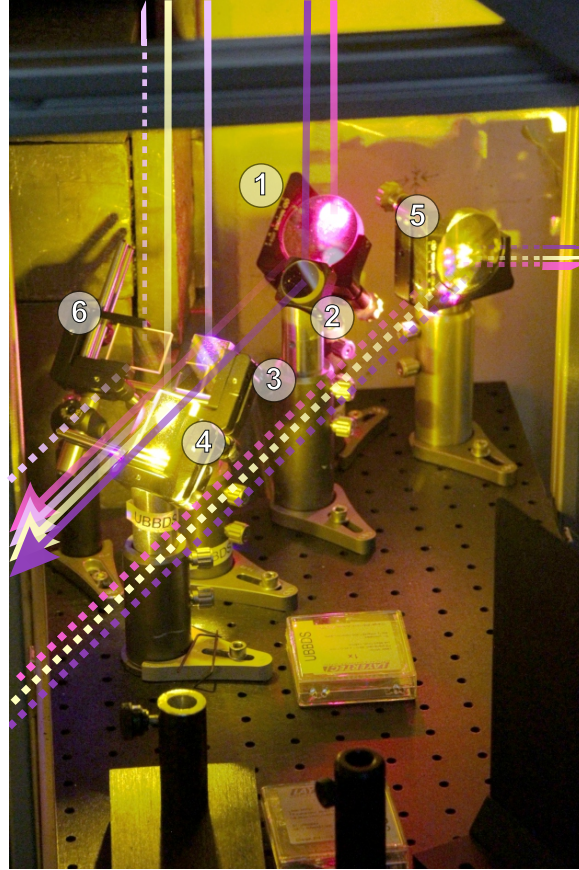


Figure 7.6: Photograph of the lower platform of the HRS launch system. The solid lines indicate the beam paths to the separator zone, the dashed lines indicate the beam paths of the reflected light from the reference plates. (1) - (4) Launch mirrors into the HRS separator zone. (3) Mirror directed to ISCOOL. (5) Mirror sending returning sampled beams to the observation point. (6) Mirror reflects sampled ISCOOL beam to a dedicated observation point.

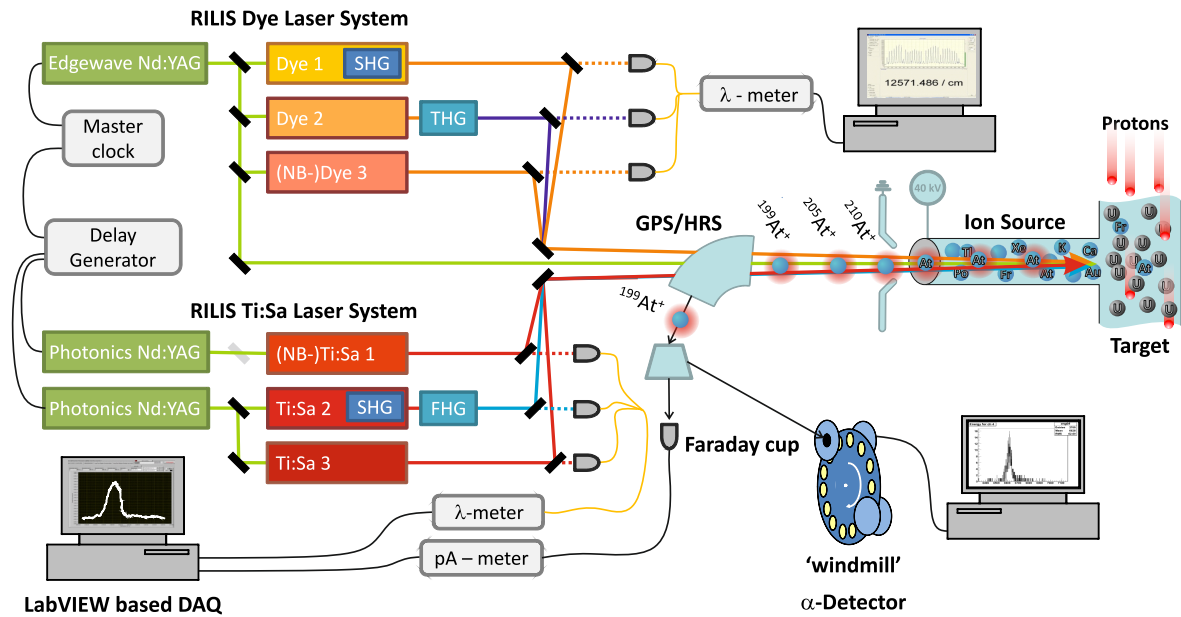


Figure 7.7: Schematic layout of the Dual RILIS (windmill detector from [AEH⁺10]). The pump lasers of the two laser systems are synchronized using a digital delay generator for the trigger pulses. Three dye lasers and three Ti:Sa lasers are available. Frequency conversion units allow generating up to the 4th harmonic of the fundamental frequency of the lasers. The RILIS laser beams are focussed into the ionizer coupled to the ISOLDE target. Wavemeters (λ - meter) monitor the wavelength of each laser. For the application in in-source laser spectroscopy the ions are detected with a Faraday cup or with a dedicated α -spectroscopy setup.

7.2 The Dual RILIS

The installation of the new laser system was aiming to allow an independent side by side operation complementing the existing dye laser system to allow a reduction in setup time. The independent operation mode is called *Dye-only* and *Ti:Sa-only*. During the on-line operation of one or the other laser system, different new modes of operation were investigated. These are the *backup-mode* in which two different laser types generate the same wavelength needed within a certain ionization scheme. When operating in the so called *mixed-mode*, a different ionization scheme is realized by the application of the other laser type. A schematic view of the Dual RILIS layout and the application for the in-source spectroscopy of astatine is shown in Fig. 7.7.

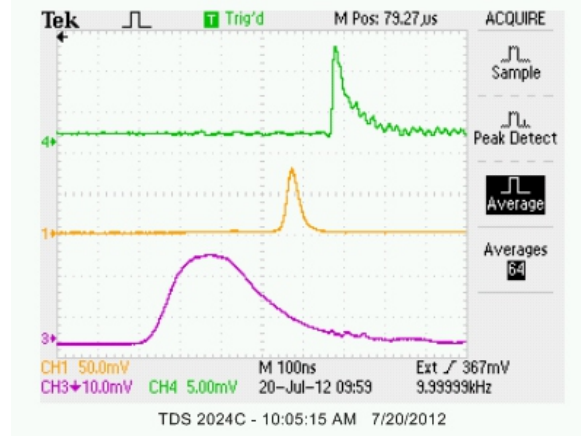


Figure 7.8: Oscilloscope trace of the laser pulses of the synchronized laser systems. From top to bottom: *Edgewave* Nd:YAG, Ti:Sa, *Photonics* Nd:YAG. The temporal resolution of the photo-diode used to record the top trace was not high enough to resolve the 8 ns pulse width of the *Edgewave* laser.

7.2.1 Synchronization

One of the mayor prerequisites for the geared operation of the two laser systems is the possibility to synchronise laser pulses generated by the two different laser types. The Ti:Sa laser pulse synchronization is well controlled and is realized (as described in 6.1.2) usually by adjusting the pump power. The dye laser pulse synchronization is achieved by the use of optical delay lines. The synchronization of the pump lasers of the two systems remained to be tested. The pump laser for the dye lasers obtains its trigger from a digital delay generator¹ operating at a repetition rate of 10 kHz. One of the output channels of this master clock is synchronized to the internal T_0 signal. This channel is connected to the external trigger input of a second digital delay generator located at the Ti:Sa site. This master/slave configuration allows an independent operation of the Ti:Sa and dye system as well as their synchronisation. To monitor the synchronization of the two laser systems, the photo-diode signal of the *Edgewave* pump laser is displayed on the oscilloscope used for the monitoring of the Ti:Sa laser pulses. An oscilloscope trace showing the photo-diode signals of the two Nd:YAG pump lasers (*Edgewave* and *Photonics*) and one of the Ti:Sa lasers is shown in Figure 7.8. The measured jitter of the laser pulses with respect to the T_0 -master-trigger signal is 1.4(4) ns for the *Edgewave*, 9.6(1.2) ns for the *Photonics* and 7.2(1.0) ns for Ti:Sa 1.

The results of the investigations of the different modes shall be given for cases studied during on-line conditions at RILIS. Time limitations did not allow performing the required set of measurements that would be needed to fully characterize the applied ionization schemes.

¹Quantum Composers

7.2.2 Ti:Sa-only mode

The implementation of the Ti:Sa only operation was the primary goal of the second laser system. To achieve this, the Ti:Sa laser pulses need to be synchronized. In the case where three Ti:Sa lasers are required for operation, e.g. a three-colour ionization scheme with a last step transition to an auto-ionizing state, the use of Pockels cells is required for optimal conditions.

For the ionization schemes which require a non-resonant ionization step laser, it was shown that instead of the fundamental output of a Ti:Sa laser, the radiation from the *Edgewave* Nd:YAG laser can be used. The pulse-jitter of the Nd:YAG laser is five times smaller than for the Ti:Sa lasers and the pulse duration is 8 ns. This configuration requires only two Ti:Sa lasers and their synchronization can be realized by adjusting the pump power or by independently pumping the lasers².

The Ti:Sa only mode was first applied for the ionization of astatine isotopes. Several ionization schemes for astatine were investigated. The full details of these measurements are given in Chapter 10. During RILIS operation ytterbium and praseodymium were successfully ionized with the Ti:Sa only mode. The scheme for Pr was $\{461.9^{\text{Ti}}|900.0^{\text{Ti}}|532\}$. The scheme used with ^{174}Yb was $\{267.3^{\text{Ti}}|532\}$.

7.2.3 Backup mode

In the backup mode one of the required wavelengths for an ionization scheme can be produced efficiently by a dye laser or a Ti:Sa laser. Depending on the requirement, either the two beams simultaneously can be transported, or the just most powerful beam can be used. In the case for the ionization of zinc, the first step wavelength at 213 nm, was produced with both laser systems. This enabled operation of the harmonics crystals well below damage threshold, improving the stability of the operating conditions. An additional benefit was that, when a dye change of the dye laser was required the users were still able to use the ion beam. Two other elements ionized in the backup mode are nickel and cadmium. Details are given in the next sections.

7.2.3.1 A Dual RILIS ionization scheme for nickel

The dye lasers were set to ionize nickel in the $\{305^{\text{Dye}}|617^{\text{Dye}}|748^{\text{Dye,Al}}\}$ scheme also shown in Fig. 7.9. The maximum recorded laser powers measured on the table were 260 mW, 3.9 W and 2.4 W for the first, second and third step, respectively. The ion current for ^{58}Ni , measured with FC.490, was 3 nA. The third step leads to an auto-ionizing resonance. The wavelength of 748 nm can be produced efficiently by one of the Ti:Sa lasers. From previous experience, it

²This was not applied as always one of the two pump lasers for the Ti:Sa system was with the manufacturer for refurbishing and repair.

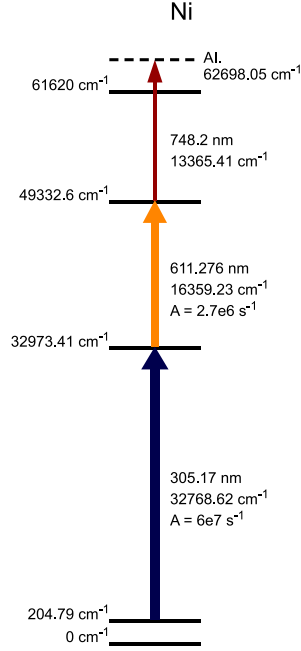


Figure 7.9: Ionization scheme for nickel

was seen that this last step may not be saturated. The higher output power of the Ti:Sa laser in this wavelength range can therefore potentially increase the ionization efficiency of nickel. For the test of the Dual RILIS backup operation, Ti:Sa laser 1 was tuned to a frequency of 13361.5 cm^{-1} . The laser was equipped with the mirror-set SP-1000, the $d = 0.3 \text{ mm}$ etalon and was pumped with a power of 16.4 W . The maximum output power was 4.5 W . Using the Ti:Sa laser, a maximum ion current of 6 nA was measured. With respect to the dye laser, the efficiency was increased by a factor of 2.

Synchronization test of Dye and Ti:Sa lasers During the investigations of the Ni ionization scheme, it was possible to perform a measurement of the dependence of the pulse synchronization on the ion current. The Photonics Nd:YAG laser obtains its trigger from the slave digital delay generator. The ion signal can be used for the final optimization of the synchronization of the dye laser pulses and the Ti:Sa pulse. To investigate the dependence, the delay of the Photonics trigger was changed manually in steps of 10 ns and the ion current of ^{58}Ni was recorded. The result is shown in Fig. 7.10. The observed peak is a convolution of the pulse-length of all involved laser pulses, the lifetime of the excited states and the jitter between the laser pulses. A deconvolution was not attempted. The full width at half maximum of the fitted Voigt curve is $46(2) \text{ ns}$. The width is dominated by the Ti:Sa pulse-length. In

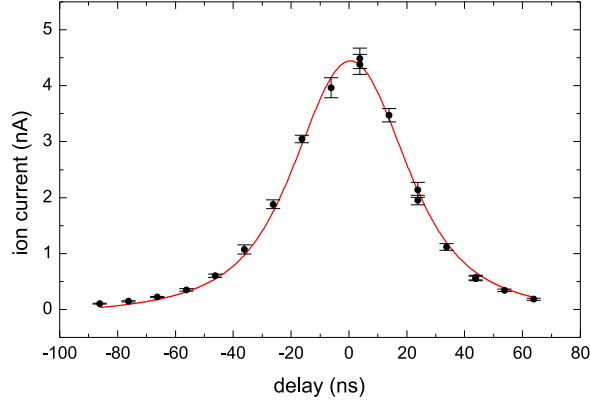


Figure 7.10: Synchronization of the Ti:Sa laser and the dye laser system. The trigger signal sent to the Ti:Sa pump laser was delayed within a range of ≈ 160 ns and the ion current of ^{58}Ni was recorded. A Voigt curve was fitted to the data. The full width at half maximum is 46(2) ns.

this example, the possible jitter between the two laser systems does not limit the ionization efficiency.

Saturation measurement of the AI step A saturation measurement was performed for the third step at 748 nm, produced with the Ti:Sa laser. A polarizing Glan-Taylor prism in combination with a tunable $\lambda/2$ plate³ was inserted before the focussing telescope. Rotating the waveplate enables the adjustment of the laser power of the beam transmitted to the ion source between 3.34 W to almost 0 W (not measurable with the same powermeter head). The power (P) was measured for each step and the average ion current (y) of ^{58}Ni , measured with FC.490 was noted. Two measurements were performed. The result is shown in Fig. 7.11. Saturation curves with a linear term (7.1) were fitted to the two datasets.

$$y = y_0 + A \frac{P/P_{\text{sat}}}{P/P_{\text{sat}} + 1} + BP \quad (7.1)$$

The fit results for the saturation level P_{sat} are 0.37(19) W and 1.13(64) W for measurement 1 and 2 respectively. These results show the large uncertainties in these saturation measurements caused by minor misalignments during power variation. However, it was shown that the increase of efficiency was caused by the increased laser power of using the Ti:Sa lasers.

Isotope shifts of the auto-ionizing state The isotope shift of the auto-ionizing state was investigated for the five stable nickel isotopes $^{58,60,61,62,64}\text{Ni}$. The Ti:Sa laser was scanned

³Purchased from *Alphas*

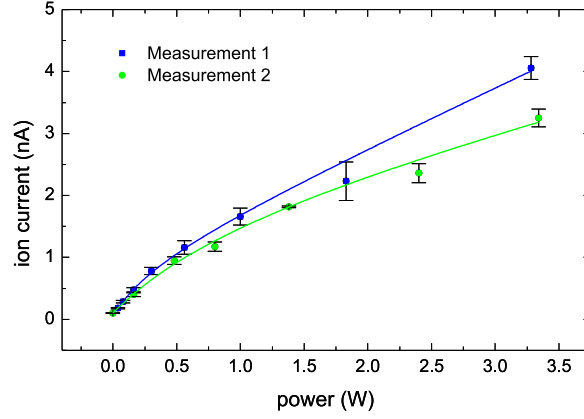


Figure 7.11: Saturation measurement for the transition to the auto-ionizing transition in the nickel ionization scheme.

manually across the resonance while the wavelength (WS6) and the ion current (FC.490) were recorded continuously. The plots are shown in Fig. 7.12. Gaussian peak shapes were fit to the resonances, the results are summarized in Tab. 7.1. A line fit of the type $\nu[A] = aA + b$ for the nickel isotopes with mass number A gives the linear parameters $a = -0.0320(12) \text{ cm}^{-1}$ and $b = 13363.336(76) \text{ cm}^{-1}$.

Table 7.1: Fit results for the isotope shift measurements of the different nickel isotopes. The errors from the fit are indicated.

Isotope	Centroid (cm-1)	Width (cm-1)	Height (%)	abundance (%)
⁶⁴ Ni	13361.289(2)	0.33	0.74	0.93
⁶² Ni	13361.354(2)	0.34	3.43	3.63
⁶¹ Ni	13361.396(2)	0.39	1.16	1.14
⁶⁰ Ni	13361.417(2)	0.36	25.24	26.22
⁵⁸ Ni	13361.481(2)	0.38	69.43	68.07

7.2.3.2 A Dual RILIS ionization scheme for cadmium

For the RILIS operation to ionize cadmium, the standard RILIS dye laser setup was prepared, but the Ti:Sa laser 1 as also setup to provide the first excitation step. It was tuned to $10923.118 \text{ cm}^{-1}$. After frequency quadrupling, a power of 48 mW at 228 nm was obtained from 2.3 W fundamental power. Table 7.2 summarizes the comparison of the different combinations of used lasers for the first step. The highest efficiency was observed for the case where both the

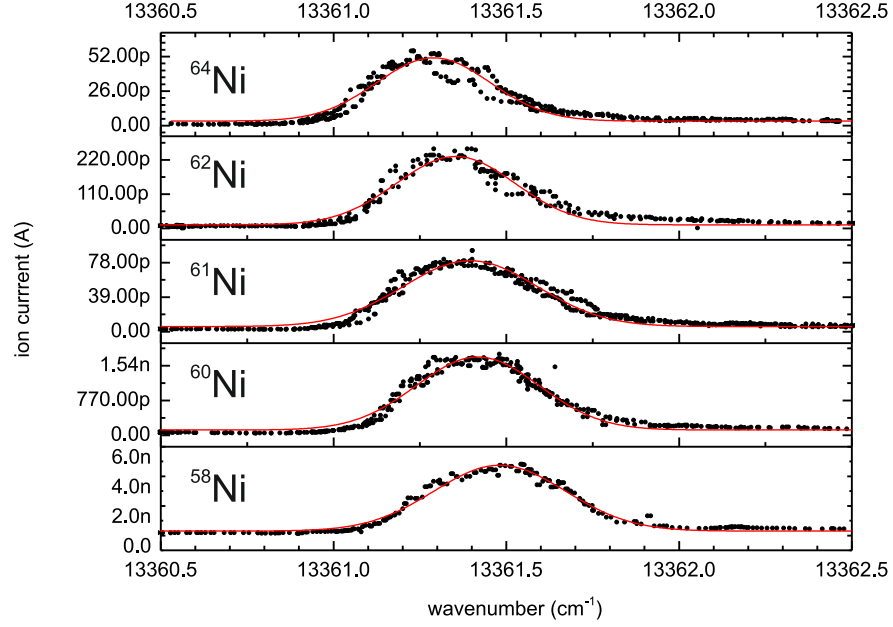


Figure 7.12: Isotope shift of the auto-ionizing transition used in the nickel ionization scheme.

Ti:Sa and the dye generated 228 nm laser beams were sent to the target. It was demonstrated that the scheme using the Ti:Sa can be applied in future without significant change in the ionization efficiency.

Table 7.2: Comparison of ionization schemes for cadmium

Scheme	ion current (pA)
$\{228^{\text{Ti}} 644^{\text{Dye}} 532\}$	100
$\{228^{\text{Ti}} 228^{\text{Dye}} 644^{\text{Dye}} 532\}$	120
$\{228^{\text{Dye}} 644^{\text{Dye}} 532\}$	110
lasers blocked	1.3

7.2.4 Mixed mode

In the mixed mode the two laser systems produce different wavelength for the same step which results in a different ionization scheme.

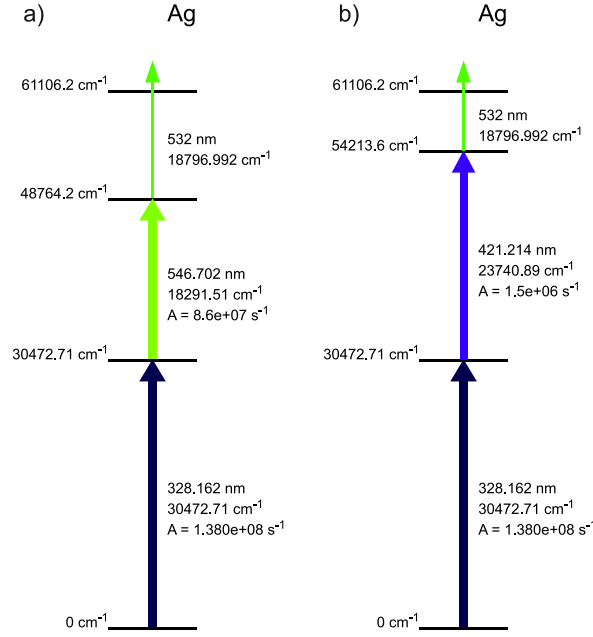


Figure 7.13: Compared ionizationschemes for silver

7.2.4.1 Dual RILIS operation for silver

Two different ionization schemes for silver were compared during RILIS operation. In this case the second step in the dye laser scheme (Fig. 7.13 a)) at 546.7 nm was replaced by the 421.2 nm wavelength produced by a frequency doubled Ti:Sa laser. Table 7.3 is a summary of the lasers that were used and shows the turn-off-matrix for the combinations of different second steps. The ion current of radiogenic ^{111}Ag was recorded on FC.490. The measurement was made during a period of proton unavailability but the long half-life (≈ 7.5 d) and slow release of ^{111}Ag meant that this was feasible. The Ti:Sa generated second step yields 38% of the maximum ion current when the dye second step was applied. The transition probability of the transition used for the Ti:Sa scheme was calculated from listed relative intensities [SM05] to be $A = 1.5 \cdot 10^6 \text{ s}^{-1}$. The transition probability for the second step in scheme a) is listed with $A = 8.6 \cdot 10^7 \text{ s}^{-1}$. This could explain the lower performance of the mixed scheme. Limited time did not allow for further investigations.

7.2.4.2 A new ionization scheme for calcium

The users of experiment IS-529 (Spins, Moments and Charge Radii Beyond ^{48}Ca) asked to enhance the production of their Ca ion beam using the RILIS lasers. The Ti:Sa only ionization scheme $\{422.8^{\text{Ti}}|732.8^{\text{Ti}}|532\}$ that was initially applied, used a frequency doubled Ti:Sa laser

Table 7.3: Laser properties for the ionization of silver

Step	1	2	2	3
Laser	Dye	Dye	Ti:Sa	Edgewave
Wavelength (nm)	328.1	546.7	421.2	532
Power (W)	0.55	4	0.4	33.5
Ion current (pA)	Turn-off-matrix			
-1.53(1)	0	1	0	1
37(3)	1	1	0	1
13(1)	1	0	1	1

as first step and a fundamental Ti:Sa laser and the *Edgewave* Nd:YAG as second and third step. During time for setup and laser optimization, laser scans for other possible second and third steps were performed. This scheme development is subject to the Ph.D. Thesis of Daniel Fink [Fin]. Some details can also be found in [FFF⁺12]. The new scheme showed a high selectivity (laser on/off) of $s = 100$. The high value hints that the cavity material was modified during the operation so that the surface ionization efficiency was reduced. However, this example shows the advantage in the availability of tunable lasers held in stand-by and the possibility of continuous data recording. This procedure of on-the-fly ionization scheme development will be followed whenever possible.

Chapter 8

RILIS data acquisition and processing

The large amount of parameters of the RILIS installation has to be monitored by the operator to ensure the optimal performance of the laser ion source. Presently the RILIS is operated in an on-shift mode 24/7 with 8 h shifts per operator. The lack of a machine protection system as well as remotely accessible status information of the RILIS requires the permanent presence of an operator in the RILIS laser cabin. While the development of a machine protection system was taken care of by the EN-STI-ECE group, the monitoring and control system was developed by RILIS. The choice of the integrated development environment LabVIEW and a Server-Client architecture enabled the parallel development of monitoring tools without interfering with regular operation. Soon after implementation, the sole monitoring and status display tools evolved to data recorders that are now part of the measurement programs. The implementation of a measurement system for RILIS improved the spectroscopic application of the laser ion source both for in-source spectroscopy and on-the-fly ionization scheme development. Remote control of the laser wavelength is key to in-source laser spectroscopy and to automated wavelength stabilization. It eventually enables automatic isotope shift correction. Some of the key aspects are described in the BSc thesis of R.E. Rossel [Ros11] that was supervised. The full scope of applications that were developed will be published elsewhere [RR⁺].

8.1 RILIS Server-client architecture

The data acquisition and -processing for RILIS operation is structured in four layers *Hardware*, *Drivers*, *Server* and *Processing*. Figure Fig. 8.1 shows a schematic overview illustrating the conceptual design.

Hardware The lowest layer consists of electronic equipment such as a laser power meter or the water flow meter inside a water-chiller. Some devices such as Faraday cups or the PSB (Proton Synchrotron Booster) can be accessed as *virtual hardware* through the ISOLDE

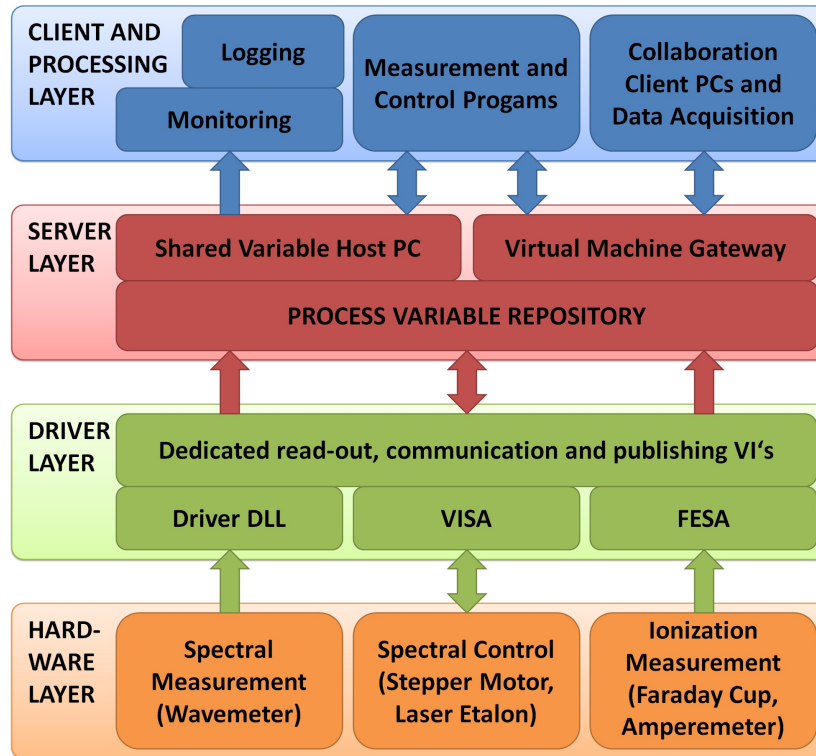


Figure 8.1: The four layers of the RILIS server-client architecture. The hardware layer represents all mechanical parts (e.g. stepping motor, wavemeter) or virtual devices (e.g. Faraday cup). The driver layer represents the LabVIEW VI's that establish the communication to the device and store the acquired values in a variable hosted at the server. The server layer is the Shared Variable Engine of LabVIEW. Each RILIS parameter or acquired value is represented as a variable. The high level monitoring, control and measurement VI's build the processing layer. These programs can all run independently on different computers within the network.

middle ware¹.

Driver The *driver layer* contains the driver-software which establishes and manages the communication with the hardware. The driver is linked to a set of network accessible variables that are specifically generated for each device and hosted on a dedicated server.

Server The server contains a virtual representation of every device and its parameters. It is accessible throughout the network this allows that the lower driver layer and the higher processing layer can be independently distributed throughout any computer that has access to the server.

Processing The *processing layer* represents all the applications written to display status information, control equipment or record measurements. This server-based architecture allows for the synchronous recording of asynchronously acquired data. The recording client can save a selected set of relevant process variables for a measurement (e.g. wavelength and ion current) without waiting for the each driver process to refresh all the available parameters.

Distributed systems The network connection to the server allows both the driver layer and the processing layer to be distributed to different computers. As only the link to the virtual devices (variables) on the server are fixed, the driver and hardware can easily be developed or exchanged without affecting the software layer.

8.2 Implementation of the infrastructure

The distributed system structure is realized by the *Shared Variable Engine* (SVE) as a part of the *LabVIEW* development environment. Programs of the processing layer and the driver software were written as *LabVIEW VIs* allowing the use of the shared variables hosted on the server. The processing VIs are stored in a network folder² and can be started locally on any computer that is connected to the network. The drivers may have to run on a dedicated computer that is physically connected to the device to be controlled. An overview is given in Fig. 8.2. The devices that are or are planned to be accessible on the RILIS server are summarized in Tab. A.1 in Appendix A. The important parameters for laser spectroscopy, wavelength and ion signal, are already implemented. The full implementation is described in [RR⁺].

¹FESA, JAPC, RADE

²The RILIS workspace is accessible from the CERN DFS

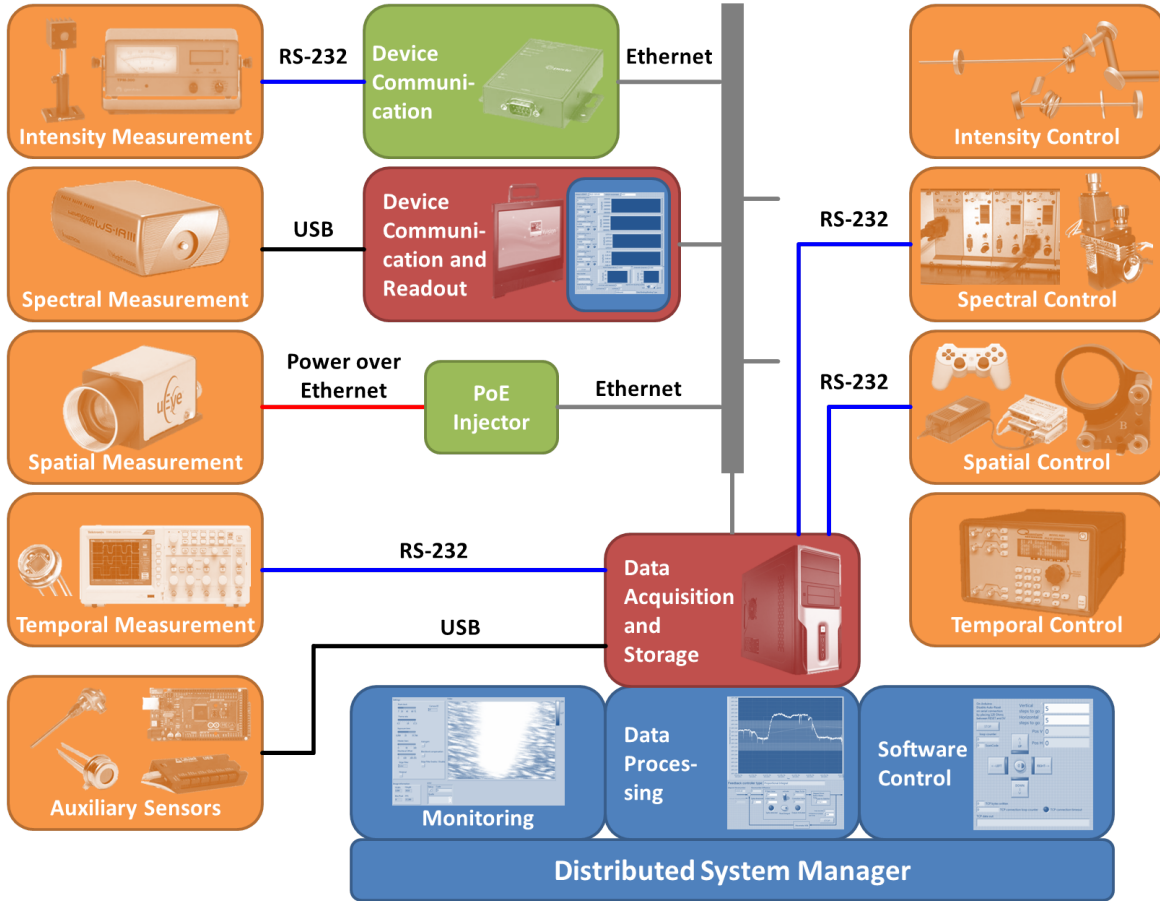


Figure 8.2: Schematic layout of the RILIS monitoring and control system [RRM⁺12]. The most critical parameters (intensity, spectral, spatial and temporal) of the RILIS lasers can be controlled and monitored. The scheme shows the hardware used to measure or control each parameter and how the data flow is organized. Orange boxes: indicate monitor or control hardware. Green: hardware interfaces for different communication standards. Red: Front-end computers and server. Blue: LabVIEW programs and architecture.

Approach to the RS-232 communication Many of the devices use the RS-232 communication standard to transmit and receive commands. The RS-232 as a standard has certainly advantages, but also disadvantages: The form factor of the connector complicates the installation of the cables to the cable trays. Some approaches were made to compensate the disadvantages.

The RS-232 cables were self-made from one Ethernet patch cable (UTP CAT-5) and two adapters (DE9 to 8P8C). Patch cables are easily available in any length and better shielded, allowing higher cable lengths for a given baud rate. The adapters are available in male and female. The need of a physical connection between the computer running the driver and the device can be avoided using so-called *device servers*³ which make RS-232 devices accessible from within the Ethernet.

Laser wavelength The laser wavelength is mainly measured by the two wavemeters WS6 or WS7. These require proprietary software from the manufacturer running on a Windows machine. The LabVIEW driver has to run on the same machine as it links to a *dll* from the wavemeter software. The driver also provides information which channel of the wavemeter is in use and what the exposure time is. The driver allows error treatment for obviously non-physical measurements (data crunching) such as negative wavenumbers.

Laser power The laser power can be acquired from different powermeters which communicate via the RS-232 protocol either directly to a connected to a computer or via a device server to the Ethernet. The *Multi Powermeter*⁴ can read up to 8 channels and is used for constant monitoring.

PSB parameters Several VIs read out additional parameters from the PSB which are relevant for the in-source laser spectroscopy. It is necessary to acquire information of the pulse sequence of the CERN PSB super-cycle, the integrated proton current and protons per pulse (PPP). These are accessible via the CERN RADE LabVIEW library⁵.

8.3 RILIS control programs

Remote wavelength control and active stabilization of the Ti:Sa wavelength The wavelength of the Ti:Sa lasers can be controlled remotely by changing the angle of the resonator-internal etalon. This is realized by a stepping motor actuated mirror mount. An

³E.g. IOLAN DS from Perle Inc.

⁴Optometer P-9801 from *Gigahertz-Optik GmbH*, Germany

⁵This library represents a middle-ware interface to the CERN accelerator front-end computers and beam diagnostic hardware.

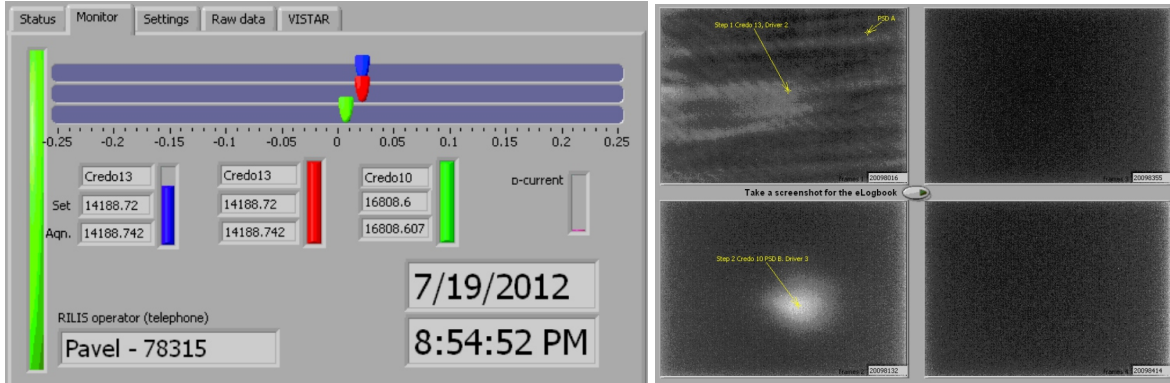


Figure 8.3: Website showing the status of the RILIS. [RR12]

active wavelength stabilization for the Ti:Sa lasers was implemented during the Bachelors thesis [Ros11].

Control programs for the dye laser system The *Edgewave* pump laser and the two tunable dye lasers from *Sirah* are also remotely controllable using their specific software. The communication is established via the RS-232 protocol. The control software was implemented in LabVIEW by the manufacturers, who kindly agreed to provide the source code for adaptation to RILIS requirements.

8.4 RILIS monitoring

The most critical parameters of the RILIS lasers are displayed together on the screen of the RILIS server. A screen-shot of this display is published to a laser status website and is accessible from outside CERN networks via any desktop computer or smart-phone (Fig. 8.3). To increase the presence of RILIS to the ISOLDE users, the status of RILIS is also displayed in the VISTARS screens (Fig. 8.4).

8.5 Signals from ion detectors

The main values which need to be recorded for in-source laser spectroscopy are the laser wavelength of the scanned laser and a photo-ion signal. Different detectors are available to detect these ions either directly or indirectly via characteristic α -decay (as described in 4.3).

Faraday cup The Faraday cups (FC) are a part of the ISOLDE beam diagnostic system and can be read via the FESA framework within RADE and are thus directly accessible from

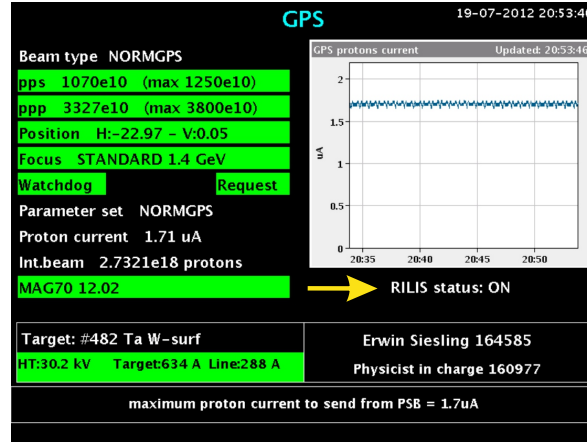


Figure 8.4: ISOLDE Vistars screen with implemented RILIS status [Pis12]

LabVIEW.

MCP An MCP is available in the central beam line. The data acquisition is performed using a *LeCroy* oscilloscope that could publish information directly via LabVIEW.

Alpha station The detection of laser ions via their characteristic α -decay energy spectrum gives in many cases almost background-free signals. When performing in-source laser spectroscopy on short-lived isotopes with low production cross-sections, the whole α -spectrum is recorded for later off-line analysis. This procedure, however, hinders on-line laser optimization on each isotope of interest so that one relies on the settings that were made for a reference isotope. A live α -signal would greatly enhance the optimization of RILIS and also would enable reference laser scans on known isotopes at a higher speed. Such a mode of operation is currently under development and will most likely be tested during upcoming in-source spectroscopy runs.

ISOLTRAP MR-ToF The (MR-ToF) is a high resolution mass separator that is used to pre-filter the sample to be injected into the penning traps of ISOLTRAP. Details to this device can be found in [WBB⁺12]. Its high resolution is sufficient to separate isobars and isomers. After passing the MR-ToF, the ions are detected with an MCP and the time of flight spectrum is recorded. Laser on/off measurements help to identify the region of interest (ROI) for a given isotope.

The integrated number of ions detected within a ROI is published by an ISOLTRAP LabVIEW program to a shared variable⁶.

⁶The RILIS server and the ISOLTRAP computers are connected to isolated CERN networks TN and GPN.

8.6 Data recorder for in-source laser spectroscopy

Two programs were developed to record spectroscopic data.

8.6.1 Step-wise scan and average

This program averages wavenumber and ion signal over time until a set condition is reached. These conditions may be a time elapsed, number of proton pulses impinged on the target or completed PSB super-cycles. The conditions can be set according to the signal quality. This program was used for the in-source spectroscopy of the hyperfine structure of ^{205}At and ^{197}Au (see sections I and 6.2.1.3).

8.6.2 Continuous scanning

This program reads the wavelength and ion signal periodically from the server and writes the data into an ASCII file while the laser wavelength is steadily scanned. The read-out interval was usually fixed at 250 ms. This recording method is required for wide scans across several 100 cm^{-1} . A mayor disadvantage, however, is an intrinsic time-lag of the detector which causes a discrepancy of the ion-signal and the wavelength. A possibility to correct this effect is presented in the next section.

8.7 Systematic errors caused by the data acquisition

Each Faraday cup in ISOLDE is equipped with a dedicated pico-ampere meter ⁷ that digitizes the measured current and transmits it via *profibus* to the ISOLDE Frontend PLCs. The readout of the ISOLDE Faraday cups is delayed by a constant time that is linked to the integration time of 500 ms (see also section 4.3.1). Knowledge of this constant is important to reduce systematic errors occurring for spectroscopy in constant laser scan mode. A benchmark measurement of this time constant is presented this section.

Recording reference data To study the temporal behaviour of the RILIS DAQ, a set of reference measurements was performed. The element chosen for this was manganese. The main reason for this choice was that the RILIS lasers were already set to ionize Mn. Another advantage was that recently, a new ionization scheme needed to be developed for the change in pump lasers from CVL to Nd:YAG and therefore several independent spectra measured in an other apparatus were available, serving as a reference[MBF⁺10].

The variables are therefore published to a *Virtual Machine*.

⁷It is also possible to temporarily disconnect the ISOLDE pico-ampere meter and connect a different pico-ampere meter (Keithley) which might have more features and can be read directly via RS-232.

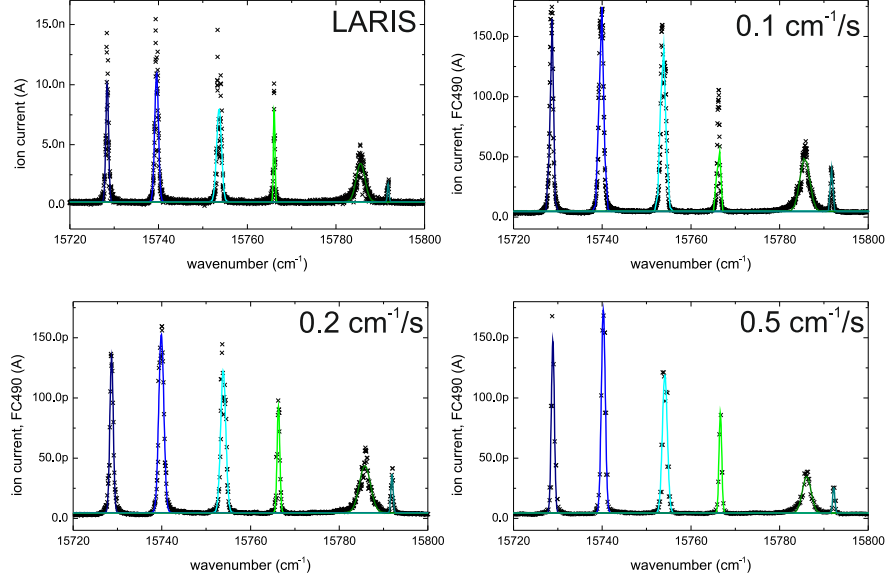


Figure 8.5: Spectrum of autoionizing states in manganese for the RILIS DAQ benchmark. Example spectra for the reference measurement from the LARIS laboratory and spectra obtained with different scan speeds at RILIS.

One of the dye lasers was used to scan across six auto-ionizing resonances. Fig. 8.5 shows an example of these scans, obtained with a scan speed of 0.1, 0.2 and 0.5 cm^{-1}/s and a scan obtained at the LARIS laboratory. The straight lines indicate fitted Gaussian profiles. The crosses indicate the data points. The amount of data points is reduced at higher scan speeds.

Determination of the DAQ time constant In total 12 spectra were taken at RILIS with different set scan speeds at $\pm 0.5 \text{ cm}^{-1}/\text{s}$, $\pm 0.2 \text{ cm}^{-1}/\text{s}$ and $\pm 0.1 \text{ cm}^{-1}/\text{s}$. From the LARIS measurement a set of 6 spectra was used for reference. Each peak was fit with a single Gaussian profile. The centroid position was tabulated. For each of the six resonances in the spectrum, the average position was calculated, both from the RILIS data and the LARIS data independently. This is now called the internal reference and the external reference, respectively. The scan speed of each spectrum was extracted from a linear fit to the wavelength and time-stamp data (not shown). The difference of each peak position from both the internal and the external reference was calculated. The difference was then plotted against the measured scan speed as shown in Fig. 8.6

The result for the correction function from the linear fit is:

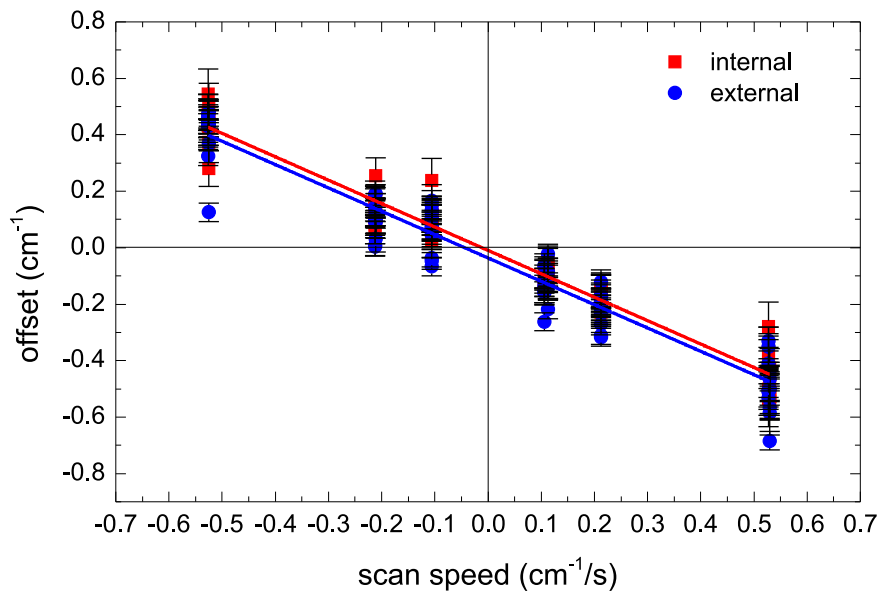


Figure 8.6: Systematic wavelength offset at different laser scan speeds. The fitted lines have the same slope showing that the correction factor is independent from the chosen reference. The blue curve however is shifted by 0.03 cm^{-1} . This is a systematic error, originating from the uncertainty of the different wavemeters used at RILIS and at LARIS.

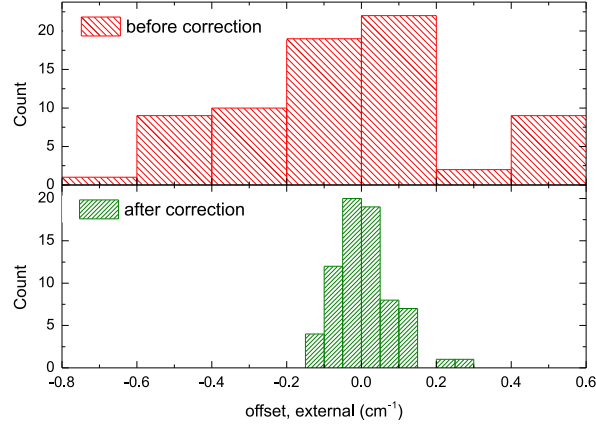


Figure 8.7: Offset distribution before and after the scan speed correction. The distribution width is significantly reduced after the correction.

$$\nu_{\text{int}} = -s \, 0.829(20) \, \text{s} - 0.010(6) \, \text{cm}^{-1} \quad (8.1)$$

$$\nu_{\text{ext}} = -s \, 0.827(25) \, \text{s} - 0.036(7) \, \text{cm}^{-1} \quad (8.2)$$

where ν is the corrected wavenumber and s is the applied scan speed in units of cm^{-1}/s . The slope of the two lines is identical within the error,

Performance of the correction procedure To check the performance of this correction method, the distribution of the calculated offsets before and after correction is plotted in Fig. 8.7. The width is reduced from $0.68 \, \text{cm}^{-1}$ to $0.15 \, \text{cm}^{-1}$.

Chapter 9

The RILIS ionization scheme database

Ionization scheme data are a crucial resource for operators of laser ion sources at radioactive ion beam facilities. This information exists as many unconnected repositories in each facility, stored in a non-standardized way (e.g. *PowerPoint* slides, webpages, logbooks). New and more efficient schemes are developed quite often, but are sometimes not considered important enough to be published in a journal - so the exchange of information between the laser ion sources is limited to private communication. In an attempt to overcome this, an open RILIS database of ionization schemes (RILIS-DB) has been initiated. It is a web based platform that displays ionization schemes available for each element of the periodic table and also allows registered users to enter ionization schemes which they are using or have developed.

The project started as a *Mathematica* program that converted information stored in an Excel table into html code that was then uploaded to a server. This method was time-consuming and only one person entered the old and new data to the database. A recent approach, which was conceived as part of this thesis, is a web based database (DB) which is accessible to members of the community. This RILIS-DB is written by Martin Klein in PHP and uses a text based format for data storage. The front page of the website, hosted at www.cern.ch/riliselements, is shown in Fig.9.1. Since the first launch, the database was developed and improved, based on the bug reports and feature requests posted by the community.

Each scheme is stored in an individual dataset, containing information about the energy levels, ionization potential, transition strengths and configuration. Additional information displays the laser types used, ionization efficiencies and the facility where the scheme is in use. An example of available data for astatine is given in Fig.9.2. Entering or updating data is possible from any internet browser by editing a form as shown in Fig.9.3. Lines in configuration are interpreted as \LaTeX code which facilitates the typesetting of superscripts and subscripts. Any value entered can be linked to one reference stored in an attached reference database. The references are stored in the \BIBTeX format. The *exposed to* setting enables the editor of a scheme to select who is able to access it. This enables the sharing of unpublished results within the community or the use of the database as a tool to visualize untested schemes which are compiled based on a literature research. Details are subject to a publication [KR⁺].

Welcome to RILIS Elements (beta)

[Element](#) [Hydrogen H 1](#) • [Periodic table](#) • [Listview](#) • [References](#)

[Add Scheme](#) • [Settings](#) • [Atomic Data](#) • [Logout](#)

H																	He
Li	Be											B	C	N	O	F	Ne
Na	Mg											Al	Si	P	S	Cl	Ar
K	Ca	Sc	Ti	V	Cr	Mn	Fe	Co	Ni	Cu	Zn	Ga	Ge	As	Se	Br	Kr
Rb	Sr	Y	Zr	Nb	Mo	Tc	Ru	Rh	Pd	Ag	Cd	In	Sn	Sb	Te	I	Xe
Cs	Ba		Hf	Ta	W	Re	Os	Ir	Pt	Au	Hg	Tl	Pb	Bi	Po	At	Rn
Fr	Ra		Rf	Db	Sg	Bh	Hs	Mt	Ds	Rg	Cn	Uut	Uuq	Uup	Uuh	Uus	Uuo
La	Ce	Pr	Nd	Pm	Sm	Eu	Gd	Tb	Dy	Ho	Er	Tm	Yb	Lu			
Ac	Th	Pa	U	Np	Pu	Am	Cm	Bk	Cf	Es	Fm	Md	No	Lr			
Feasible			Dye schemes tested				Ti:Sa schemes tested				Dye and Ti:Sa schemes tested						

25.06.2011 v0.05 • PSE • This is a BETA version (for preview purposes only)

Figure 9.1: Front page of the RILIS-DB website

Ionization Scheme (4) At_216.3_915.5_532N Community .pdf export test

Level	Energy (cm ⁻¹)	Configuration	Wavelength, vac. (nm)	Energy (cm ⁻¹)	Transition strength (s ⁻¹)	Notes
E ₀	0	6p ⁵ 2p ⁰ _{3/2}				
E ₁	46233.64	6p ⁴ (3P) 7s 4p _{3/2}	216.293	46233.64		11558.41 cm ⁻¹ , 865.171 nm
			915.457	10923.5		
E ₂	57157.14					
			532	18796.992		
IP	75128					

Efficiency:

Used at: CERN, TRIUMF

Lasers used: Dye, Ti:sapphire, Nd:Yag, Edgewave, Photonics, LEE

Used: online

Notes:

Updated: 04.09.2011 by Sebastian Rothe

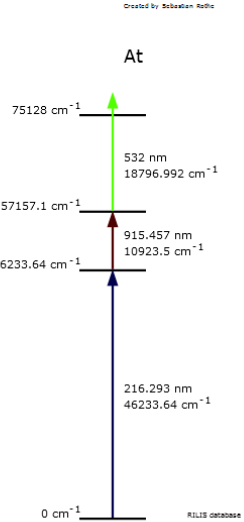


Figure 9.2: Example of the available data for an ionization scheme of astatine

Scheme 4 • 085[Astatine] • move • copy • delete

Level	Energy (cm ⁻¹)	Configuration	Wavelength, vac. (nm)	Energy (cm ⁻¹)	Transition strength (s ⁻¹)	Notes
E ₀	0	6p ⁵ 2P ⁰ _{3/2}				
						11558.41 cm ⁻¹ , 865.171 nm
E ₁	46233.64	6p ⁴ (3P) 7s 4P _{3/2}				
E ₂	57157.14					
			532			
Ryd.						
IP						
AI						

Efficiency:

Used at: ☐ Mainz • ☒ CERN • ☐ IGISOL • ☐ GANIL • ☐ LLN • ☒ TRIUMF • ☐ PNPI • ☐ ORNL • other:

Lasers used: ☒ Dye • ☐ CVL • ☒ Ti:sapphire • ☒ Nd:Yag • ☒ Edgewave • ☒ Photonics • ☐ Cr:Forsterite • ☐ ORC • ☒ LEE • other:

Tested: ☒ online • ☐ offline

Reference:

Figure 9.3: Editing of an existing scheme.

Part III

In-source laser spectroscopy of astatine

Chapter 10

In-source spectroscopy of astatine

In this chapter the results of the in-source laser spectroscopy focused on astatine isotopes are presented. The first section summarizes the properties of astatine and the motivation for the development of astatine ion beams at ISOLDE. The stages that were required to identify an efficient multi-step RIS scheme for astatine are described in the second section. The third section deals with the precise determination of its first ionization potential from the spectroscopy of high-lying Rydberg states.

10.1 Astatine: History and Properties

The existence of Element 85 was predicted since Mendeleev presented his Periodic Law in 1869 [Men69]. The element was discovered in 1940 by Corson *et al.* who produced it artificially by bombardment of a bismuth target with α -particles [CMS40] and later named it astatine after the Greek word ἄστατος for unstable [CMS47]. The isotope ^{218}At ($t_{1/2} = 1.5$ s) is the astatine nuclide with the highest natural abundance yet its quantity within the outermost mile of the earth's crust was calculated by I. Asimov to be only 68.6 mg [Asi53]. An overview on the other astatine isotopes is given in [FT12].

Following the discovery and based on the possibility of artificial production of astatine, different studies on this radioactive element were performed. The chemical properties deduced are summarized in a number of review articles [JLS49, And59, NNTK68, Bro87]. A general compilation of bibliography related to astatine was compiled by Berei *et al.* [BV92]. The application of astatine for cancer treatment using targeted α -therapy was reported in 1981 by Bloomer *et al.* [BMN⁺81] with further results described in [Bro86, ZRA⁺08]. In parallel theoretical methods were developed to predict astatine chemistry in aqueous solution [CSSG⁺11]. Nevertheless, one of the prominent unknown properties of astatine of fundamental relevance is its ionization energy or ionization potential (IP).

In 1964 R. McLaughlin reported the first (and only) optical spectroscopy experiment on this element, performed on a 70 ng sample of $^{209-211}\text{At}$ [McL64]. The astatine sample was produced by bombarding a bismuth target with α -particles at an energy of 50 MeV in the

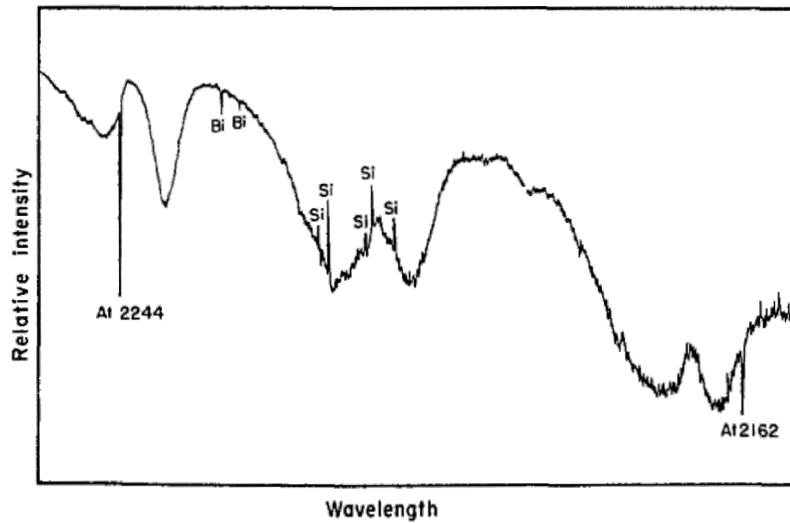


Figure 10.1: Absorption spectrum of an astatine sample, measured 35.42 h after production [McL64]. Two absorption lines observed at 2244 Å and 2161 Å were assigned to astatine.

reaction $^{209}\text{Bi}(\alpha, xn)^{209+x}\text{At}$ ($x = \{1, 2, 3\}$) and then transferred into a dedicated glass cell for absorption spectroscopy. Fig. 10.1 shows the absorption spectrum recorded 35.42 h after the production of the sample. Two newly observed absorption lines at wavelengths of 224.401 nm and 216.225 nm were assigned to astatine; table 10.1 summarizes the corresponding information.

Table 10.1: Spectroscopic information on astatine, obtained from absorption spectroscopy and the assignments given in [McL64].

wavelength (nm)	Term lower level	Term excited level	Transition energy (cm^{-1})
224.401	$6p^5 \ ^2P_{3/2}^0$	$6p^4 7s \ ^4P_{5/2}$	44549.3
216.225	$6p^5 \ ^2P_{3/2}^0$	$6p^4 7s \ ^4P_{3/2}$	46233.6

The IP of an element is the binding energy of the valence electron which is responsible for its chemical behaviour. Many groups predicted this energy for astatine. Some of the results are summarized in Table 10.2. Early extrapolations from the IP data for neighbouring elements gave values of IP(At) from 9.2 to 10.4 eV [FS50, Var53, FH55, Kis60]. However, recent, more precise theoretical treatments [MvW06, CLD10] cluster around 9.3 eV.

Table 10.2: Calculated values for the first ionization potential of astatine.

Author	Year	Method	IP (eV)
Finkelburg <i>et al.</i> [FS50]	1950	extrapolation	9.5(2)
Varshni <i>et al.</i> [Var53]	1953	extrapolation	10.4
Finkelburg <i>et al.</i> [FH55]	1955	extrapolation	9.2(4)
Kiser <i>et al.</i> [Kis60]	1960	extrapolation	9.5
Küchle <i>et al.</i> [KDSP91]	1991	CISD (+CPOL+SCC)	9.42
Mitin <i>et al.</i> [MvW06]	2006	B3LYP DK6	9.24
Chang <i>et al.</i> [CLD10]	2010	MCDF, up-shift	9.35(1)
Fritzsche <i>et al.</i> in [RAA ⁺]		MCDF	9.24(15)
Pershina <i>et al.</i> in [RAA ⁺]		DC CCSD(T)	9.307(25)

10.2 Ionization scheme development for astatine

10.2.1 Motivation and objectives

The development of an efficient ionization scheme for astatine at CERN was triggered by the letter of intent INTC-I-086 [AAB⁺10]. The envisaged spectroscopy program described therein was split into three stages:

1. Verification of the only two known optical transitions ascribed to At
2. Development and refinement of RILIS schemes
 - a) Search for second step transitions or
 - b) Search for first step transitions if stage 1 is not successful
3. Search for third step transitions and determination of the ionization potential of astatine

The ISOLDE and Neutron Time-of-Flight Experiments Committee (INTC) gave a following comment: “The Committee decided to strongly endorse the physics case and asked the standing group for the upgrade of ISOLDE to give the first stage of the proposed astatine RILIS development high priority” [Her10]. The five stages of the corresponding ionization scheme development are sketched in Fig. 10.2 and described in the following sections. Details will be subject to further publications [RAA⁺, L⁺].

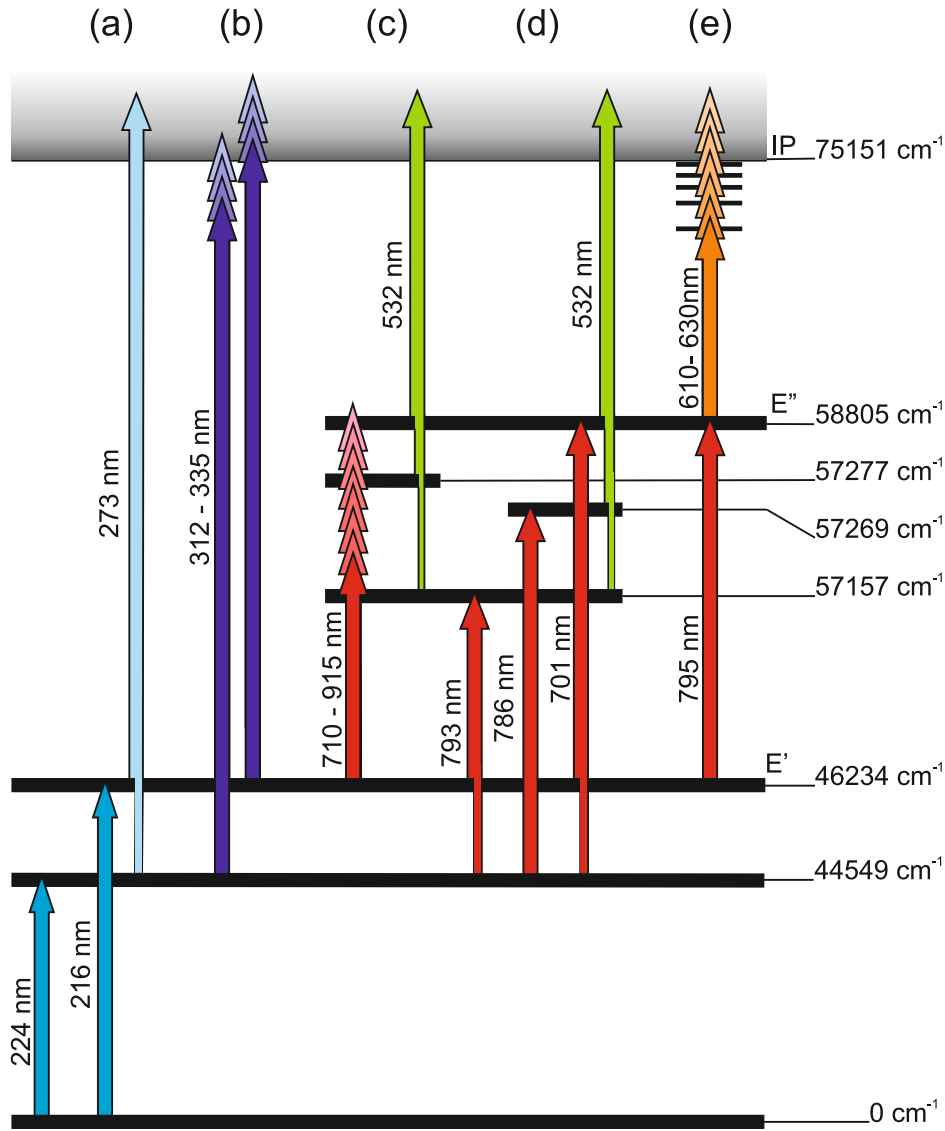


Figure 10.2: Stages of the ionization scheme development for astatine. (a) Verification of the two transitions from the ground state at $\lambda_1 = 216 \text{ nm}$ and 224 nm . (b) Ionization threshold: Scan of the ionizing laser wavelength λ_2 . (c) Development of a three-color scheme: Scan of λ_2 in the infra-red region for second excited states starting with $\lambda_1 = 216 \text{ nm}$ first step. (d) Verification of the levels found by exciting via the $\lambda_1 = 224 \text{ nm}$ first step. (e) Rydberg series: A wavelength scan of the ionizing laser (λ_3) in the visible range using the $\{216|795|\lambda_3\}$ excitation path. [RAA⁺]

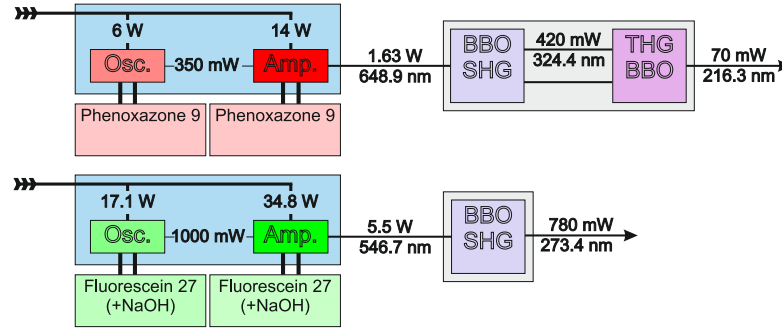


Figure 10.3: Laser parameters for the verification of the first step transitions in astatine.

10.2.2 Ground state transitions

For the verification of the transitions at 216 nm and 224 nm, predicted by [McL64], the RILIS dye laser system was initially set to produce the 216 nm wavelength and later on tuned to 224 nm. A wavelength of 273 nm was chosen as the non-resonant ionization step to ionize astatine in the two-colour scheme: {216|273} or {224|273}, respectively. The parameters of the lasers used for this first spectroscopy are given in Fig. 10.3. Two *Credo* dye lasers were pumped with the SHG output of the *Edgewave* Nd:YAG pump laser.

For photo-ion detection the ISOLDE GPS magnet was tuned to mass ^{199}At and the ion beam was directed to hit the α -detectors of the ‘windmill’ [AEH⁺10] positioned at the LA1 beam line. A photograph of the windmill setup is shown in Fig. 10.4. The beam was implanted into thin $30\text{ }\mu\text{g}/\text{cm}^2$ carbon foils which were then rotated to face a Si-detector, where the α -decay spectrum of the implanted sample was measured. Typical spectra with and without laser ionization are shown in Fig. 10.5.

Spectrum a) was taken with ionization lasers on and the mass separator set to $A = 199$. The short lived isotope ^{199}At is most pronounced. In addition, decay signals of the long-lived isotopes ^{202}At and ^{200}At are visible. Spectrum b) was obtained with the lasers blocked. The decay peaks attributed to the long lived isotopes ^{200}Po and ^{202}Po were accumulated during beam line optimization on various masses. For the in-source spectroscopy, the photo-ion signal was obtained by integration of the strong α -peak at 6600 keV of ^{199}At over a given time, which was set to typically one or two PSB-supercycles of $\approx 60\text{ s}$.

Fig. 10.6 shows laser-scans across the two transitions (cf. Fig. 10.2 a)). The maximum count rate using the 216 nm transition and non-resonant ionization at 273 nm was as little as 1 s^{-1} . This emphasizes the power of the sensitive and almost background-free detection method. These two laser-scans confirm McLaughlin’s assignments of these lines as ground state transitions of astatine with values of $46233.61(2)\text{ cm}^{-1}$ and $44549.29(6)\text{ cm}^{-1}$ in agreement with the transition energies listed in [SM05]. The laser-scan across the 224 nm transition shows an asymmetry that may originate from unknown fluctuations of overlap of the laser

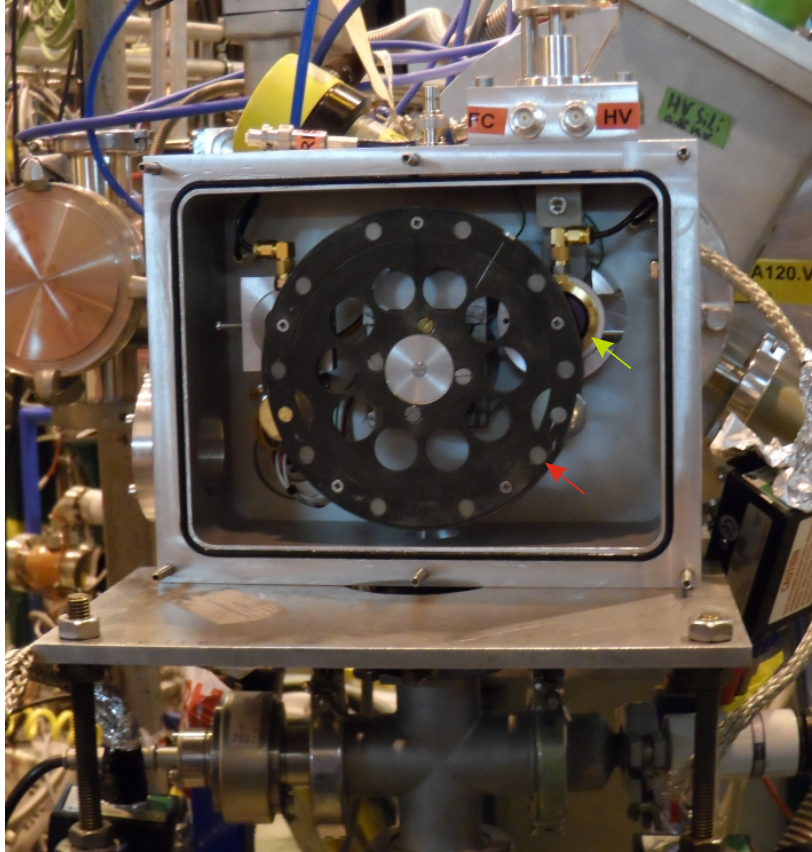


Figure 10.4: Photograph of the windmill α -decay spectroscopy setup mounted to the ISOLDE LA1 beam line. The green arrow indicates the position of one of the Si-detectors. The red arrow points at one of the ten carbon foil catchers into which the ion beam was implanted.

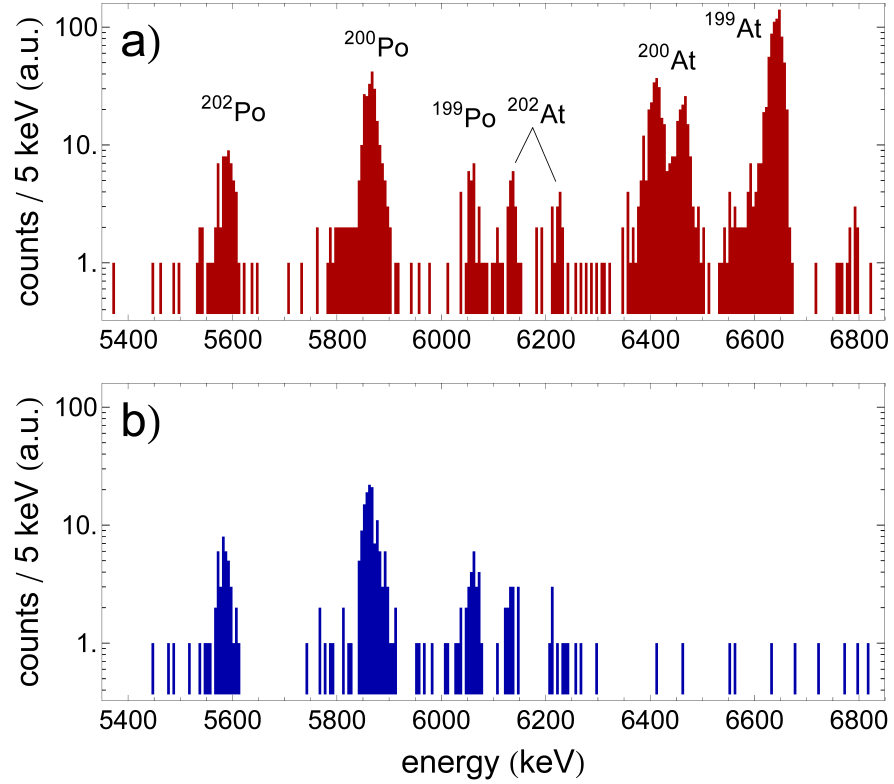


Figure 10.5: Typical α -decay spectra for astatine. The mass separator was set to mass ^{199}At . a) Laser on: The identified α -energy peaks are indicated. The most prominent is the ^{199}At decay peak of an energy of 6643 keV. b) Laser off: The energy region above 6300 keV shows only single events. The Peaks at lower energies stem from long-lived decay products and from contamination of the detectors with ^{202}At .

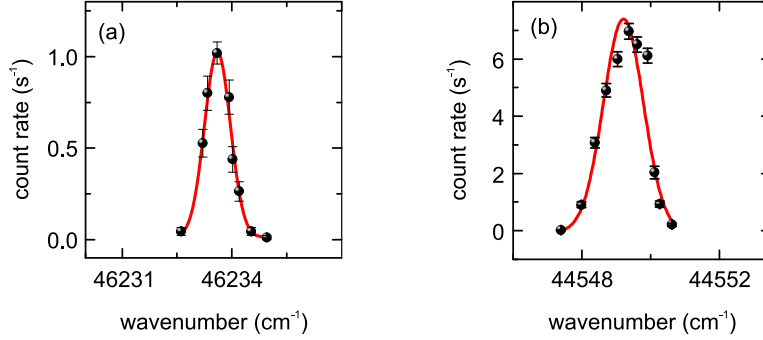


Figure 10.6: Laser scans across the first-step transitions in astatine detecting the ^{199}At α -decay. a) 216 nm. b) 224 nm

beams or astatine production in the target.

10.2.3 Ionization threshold

A first determination of the ionization potential of astatine from the ionization threshold was carried out. For this purpose, scans of the second step laser wavelength in the two-colour ionization schemes $\{216|\lambda_2\}$ and $\{224|\lambda_2\}$ were performed (Fig. 10.7). These measurements revealed an onset of ionization.

Initially this threshold measurement was the only available information on the ionization potential of astatine. Fig. 10.7 shows the raw data obtained in three measurements under slightly different conditions. All scans were obtained with a fixed first step wavelength whilst tuning the ionizing laser wavelength between 625 nm and 670 nm. The first panel shows the data obtained with the first step laser fixed to the 216 nm transition. No significant change in count rate was observed, while varying the second laser wavelength. Then the first step wavelength was changed to 224 nm and the second step wavelength was varied in the same range as before (panel 2). Afterwards, the beam pointing was changed to optimize the laser ion signal; a three-fold higher ion signal was obtained (panel 3). In order to see the onset of ionization, the count rate is plotted versus the total photon energy $\nu_{tot} = \nu_1 + \nu_2$.

To jointly analyse the data, it was necessary to scale the individual datasets properly, compensating for the different conditions during the data taking. This procedure is discussed in appendix B.

To find a fit function and a proper value for the ionization threshold, a literature research was not fruitful. For the saddle-point method, as described e.g. in [Got10], the three-sigma level above background was defined as the threshold. In contrast to the in-source collinear geometry, the data for the saddle point method in [Got10] was taken in a transversal configuration. Therefore, comparing with other spectroscopic reference data for laser spectroscopy in the

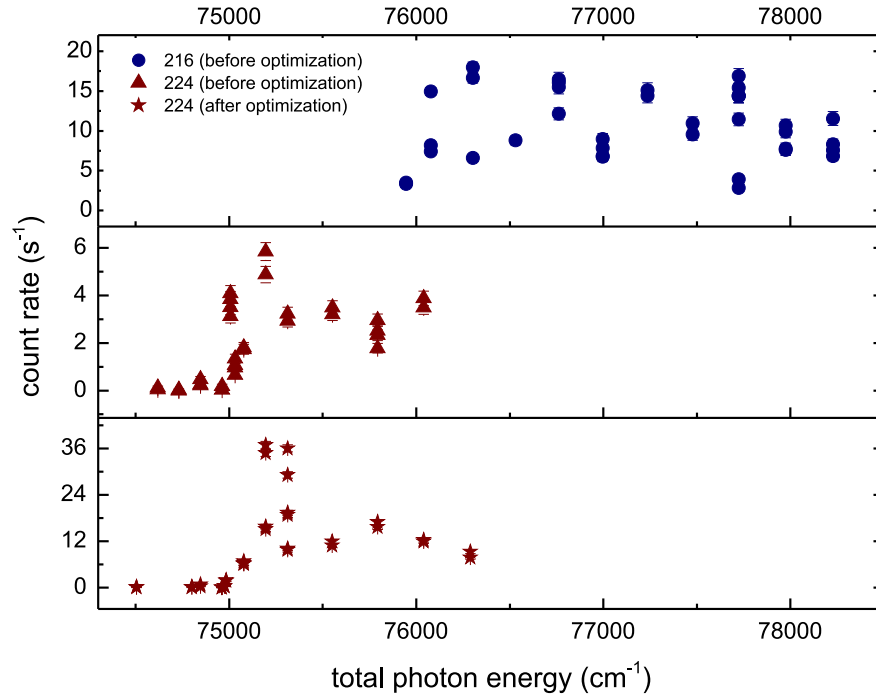


Figure 10.7: Laser scans across and above the ionization potential of astatine with different first steps and under different measurement conditions. The top panel shows the scan of the second step laser wavelength λ_2 while the first step wavelength was fixed at $\lambda_1 = 216$ nm. The two lower panels show the scans of λ_2 in the same wavelength range but with the first step wavelength set to $\lambda_1 = 224$ nm, which results in a different scan range for the total photon energy. The difference in maximum photo-ion count rate was due to optimization of the laser beam positions in the source. Further explanations are given in the text.

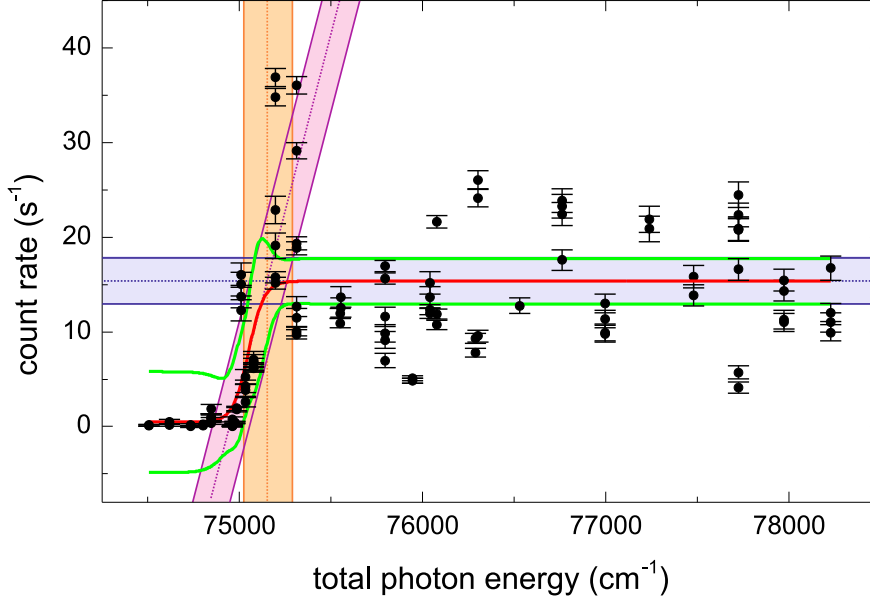


Figure 10.8: Illustration of the fit routine for the ionization threshold. The data points with the scaling set $f = \{1.45; 3.91; 1\}$ was fitted with a sigmoid curve Eqn. 10.1 (red) and the 3σ confidence interval is indicated (green curves). The orange vertical bar indicates the position and the uncertainty of the ionization threshold.

region of the ionization potential that was performed earlier under similar conditions as for the astatine data, the ionization potential was always found at higher energies than the value at three sigma above background (see appendix C.2). For a conclusive data analysis an analytical fit curve was applied. The chosen sigmoid curve (S-curve) is given by:

$$y = \frac{A_1 - A_2}{1 + e^{\frac{x_0 - x}{\beta}}} + A_2 \quad (10.1)$$

The ionization threshold was defined as the intersection between the tangent in the inflection point of the curve and the line $y = A_2$. The fitting routine was implemented in *Mathematica* and the result is illustrated in Fig. 10.8. The blue and purple shaded bars indicate the 3σ confidence interval and the orange vertical bar indicates the position of the ionization threshold.

To gain confidence for the result, the fit routine was applied to different combinations of scaling factors for the dataset; Results obtained for each method are given in Table 10.3. Except for the first two combinations, all the results are in a range between 75128 cm^{-1} and 75138 cm^{-1} . The IP obtained from run 7 (Raw data) and 8 (MEM & Average) are identical, the error however is reduced by $\approx 20\%$. The final result for the first ionization potential for

astatine, deduced from the ionization threshold is:

$$\text{IP}_{\text{Thr}}(\text{At}) = 75129(75) \text{ cm}^{-1}$$

Table 10.3: Fit results for the ionization threshold, obtained with different combinations of scaling factors for the datasets.

Run	f_1	f_2	f_3	IP (cm ⁻¹)	Error (cm ⁻¹)	Method
1	-	1	-	75114	129	Raw
2	-	-	1	75104	2309	Raw
3	-	1	1	75128	122	Raw
4	-	3.9	1	75137	77.7	MEM
5	-	4	1	75137	77.6	Slope
6	-	5.7	1	75138	81	Average
7	1	1	1	75129	95.6	Raw
8	1.5	3.9	1	75129	75	MEM & Average
9	1.7	5.7	1	75134	76.4	Average

For further verification of this value, this method and definition was tested with spectroscopic data from different elements, obtained under similar conditions (hot cavity, pulsed laser system). The results are discussed in appendix C.2.

10.2.4 Search for second excited states

Starting from the results obtained with RILIS at CERN-ISOLDE, the next investigations on the optical properties of astatine were performed at the ISAC-TRIUMF radioactive beam facility with the TRILIS laser ion source. A description of the Ti:Sa laser based system can be found in [PLA⁺07]. Performing the wide range searches for new transitions in astatine at TRIUMF is particularly advantageous since the TRILIS setup includes a wide range tunable grating-based Ti:Sa laser [TBC⁺10] and the cyclotron delivers a CW proton beam, allowing the amount of astatine in the ion source reaching a steady-state condition and the ion signal to be recorded continuously. To obtain a clean and unambiguous astatine ion signal, the alpha spectroscopy setup at the 8 π detector [GBB⁺] was used and provided a continuous scaler signal. The signal was visualized with the *Strip Tool* of the EPICS based control system at ISAC [KBDH99]. A screen shot showing the first astatine signal is presented in Fig. 10.9. The applied laser scheme is shown schematically in Fig. 10.2 c). The output of an intra-cavity doubled Ti:Sa laser was frequency doubled externally to obtain the 216 nm first step. The second step laser was scanned while a frequency doubled Nd:YLF laser was used for non-resonant ionization. Three second excited states were found during this campaign. The

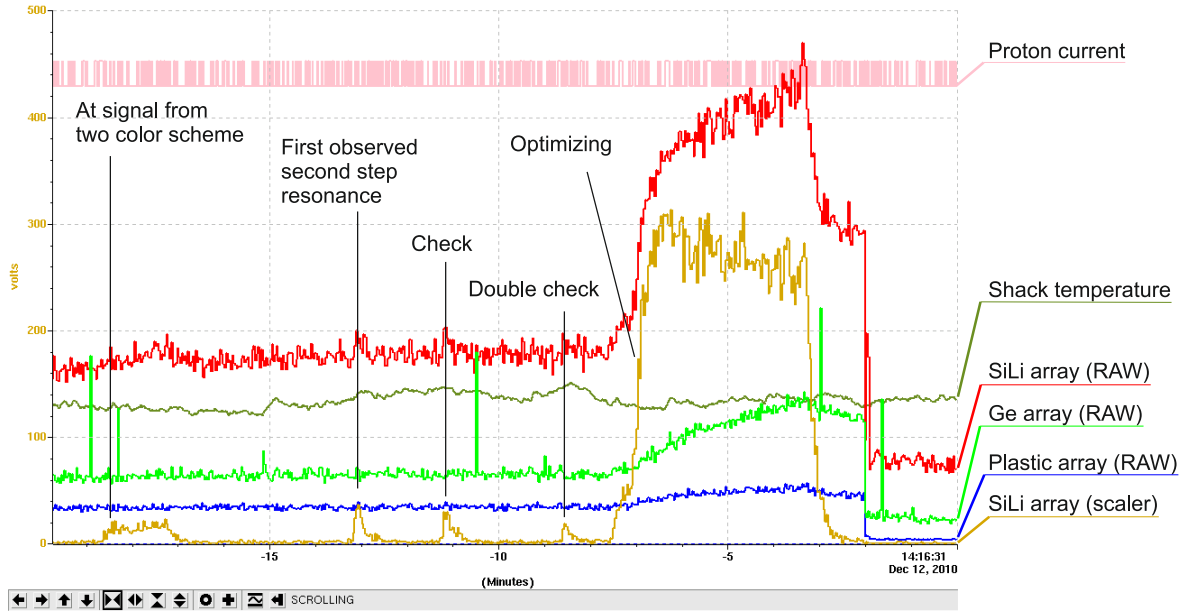


Figure 10.9: Screenshot of the TRIUMF *Strip-Tool* showing the first astatine signal.

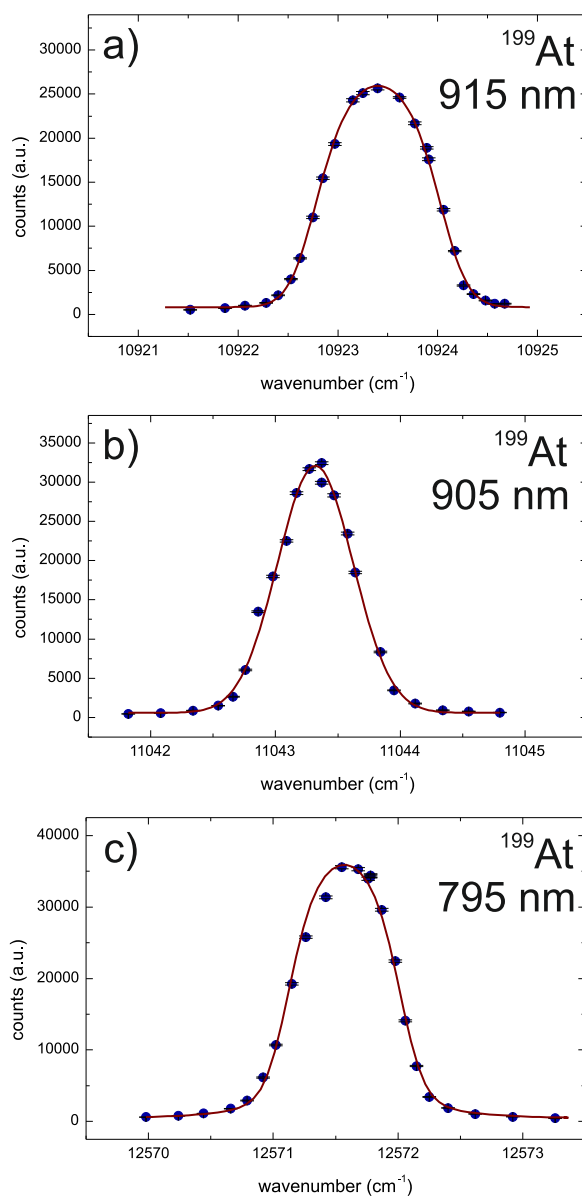
resonance curves are shown in Fig. 10.10. The full description of this campaign and other results regarding the optical spectrum of astatine isotopes obtained at TRIUMF-ISAC is subject to a publication [L⁺].

A typical α -spectrum measured with the ISAC tape station is shown in Fig. 10.11.

10.2.5 Comparison of ionization schemes for astatine

The newly found second steps were confirmed during a second measurement campaign at CERN. Here the RILIS Ti:Sa lasers and dye lasers were used in mixed schemes. In all cases, the *Edgewave* laser output at 532 nm was applied as the non-resonant ionization step. Eight ionization schemes using dye and Ti:Sa lasers, were tested, as indicated in Fig. 10.2 d). The maximum ion current measured with a Faraday cup and with a magnet setting of $A = 205$ using the different ionization schemes is summarized in Fig. 10.12. Five out of the eight tested resonant ionization schemes show reasonable and rather comparable performances with efficiencies differing by only about a factor of 2. As most efficient ionization scheme for astatine the Ti:Sa scheme $\{^{216}\text{Ti}|^{915}\text{Ti}|532\}$ was identified.

Saturation measurements were performed for the first and the second step transition in the scheme $\{^{216}\text{Ti}|^{795}\text{Ti}|532\}$. In the scheme $\{^{216}\text{Ti}|^{915}\text{Ti}|532\}$ the saturation of the second step was measured. Saturation curves (Eqn. 10.2) were fitted to the data obtained for the 795 nm and the 216 nm steps. A saturation curve with an additional linear term (Eqn. 10.3) which

Figure 10.10: Second excited states in astatine. [L^+]

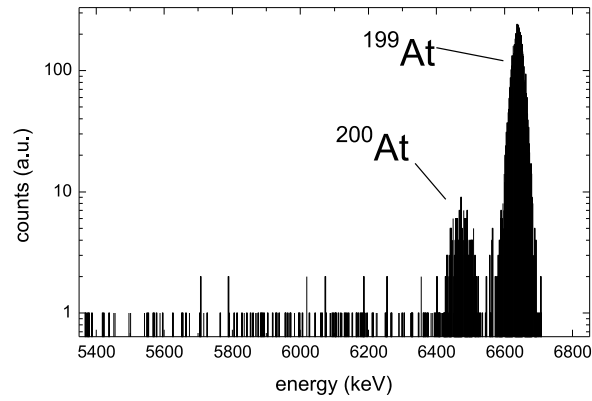


Figure 10.11: Typical α -energy spectrum for ^{199}At obtained during the in-source spectroscopy of astatine isotopes at TRIUMF. The counts under the peak attributed to ^{199}At were integrated and gave the photo ion signal in the precise laser-scans.

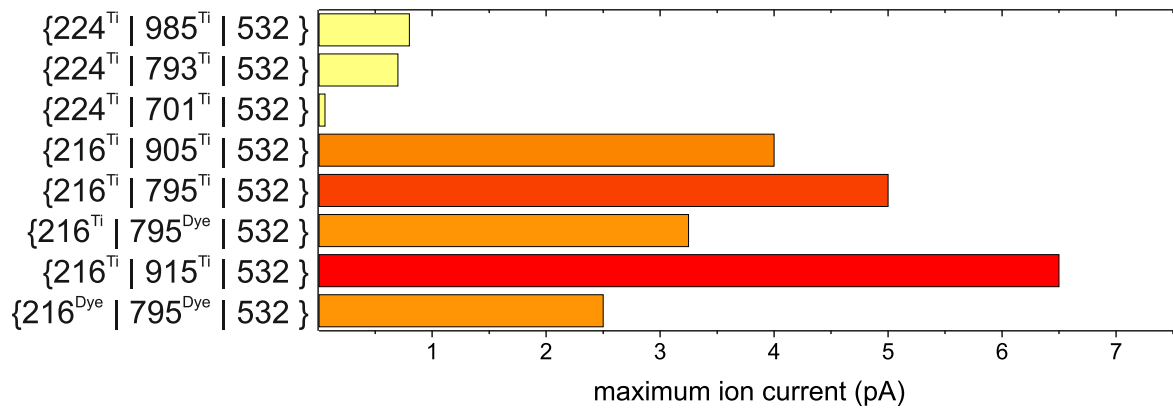


Figure 10.12: Comparison of different ionization schemes for astatine. The Ti:Sa schemes using the 216 nm first steps are more efficient than the schemes based on the 224 nm first step.

takes the non-resonant ionization by these photons into account, was fitted to the data for the 915 nm step. In the formulas y is the ion signal, A is the amplitude, P is the set laser power, P_{sat} is the saturation parameter and C is the slope in the linear term.

$$y = y_0 + A \frac{\frac{P}{P_{\text{sat}}}}{\frac{P}{P_{\text{sat}}} + 1} \quad (10.2)$$

$$y = y_0 + A \frac{\frac{P}{P_{\text{sat}}}}{\frac{P}{P_{\text{sat}}} + 1} + CP \quad (10.3)$$

The resulting plots with fitted saturation curves are shown in Fig. 10.13. Saturation levels for the first and second step wavelengths $P_{\text{sat}}[\lambda]$, obtained from the fit, are $P_{\text{sat}}[216 \text{ nm}] = 22(8) \text{ mW}$, $P_{\text{sat}}[795 \text{ nm}] = 700(500) \text{ mW}$ and $P_{\text{sat}}[915 \text{ nm}] = 32(10) \text{ mW}$. The power of the non-resonant step was provided by a fraction of the output of the *Edgewave* dye pump laser and was fixed at $P[532 \text{ nm}] = 30 \text{ W}$. Time constraints did not allow for a saturation measurement of this step.

10.2.6 Spectroscopy of the excited states

Spectroscopic results for the letter of intent INTC-I86 [AAB⁺10] were obtained in different campaigns and under different conditions of the target and the lasers. Also different detectors were used. A collection of scans is plotted in Fig. D.1 and D.2 in appendix D; results from the fits to these data are summarized in Table 10.4. Only one of the 18 scans reveals a double structure. As the transition is heavily power broadened, this effect may result from a changing mode distribution of the Ti:Sa while scanning. The observed resonance while scanning the Ti:Sa laser at 12729 cm^{-1} (see D.1 5)) is an artefact as a result from the Ti:Sa being multi-mode. The used ISOLDE targets and conditions for these measurements are summarized in table E.1 in appendix D.

10.2.7 Scan for second excited states and auto-ionizing resonances

An extension of the search for second and third excited states was performed by scanning the dye lasers. The tables 10.5 and 10.6 summarize the scanned regions and gives information about the lasers used. No resonances were observed during these scans. The laser alignment was carefully checked before, during and after each scan. Nevertheless, it is not advisable to fully exclude these regions for any further experiments, just based on the absence of any signal which could have been caused by some unknown complication.

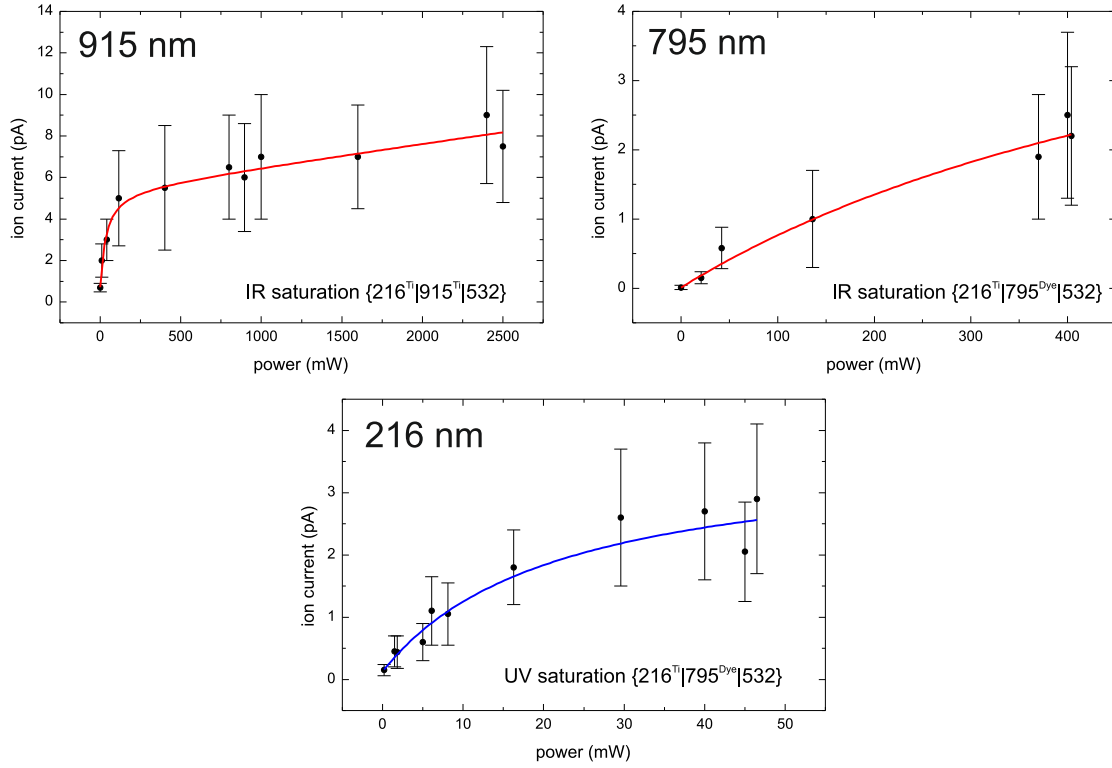


Figure 10.13: Saturation measurements for the first and second step of two different astatine ionization schemes.

10.2.8 Determination of the laser ionization efficiency

As no calibrated sample for astatine is available, the ionization efficiency can only be estimated from the predicted in-target production. Cross sections for the reaction $^1\text{H}(^{238}\text{U}, X)$, $E = 1$ GeV for the production of heavy nuclides was studied in an inverse kinematics reaction at GSI [TSTG⁺03]. The results can be scaled from 1 GeV to 1.4 GeV as shown in [GJS⁺02]. Based on this assumption and in comparison with the measured yields for thallium isotopes, the yield for $^{204-206}\text{At}$ was estimated [Bar11]. The yield for the same isotopes was also calculated [Got12], based on ABRABLA calculations [LGK⁺06]. Both results are compared in Table 10.7. The two results differ by a factor of about 0.35, which may originate from a slightly incorrect scaling from 1 GeV to 1.4 GeV and from the extrapolation of the thallium yield in the first method. For the estimation of the efficiency, a conservative value from [Got12] was adopted and correspondingly a lower limit for the ionization efficiency of astatine was calculated. The maximum ion current of ^{205}At was measured with the FC.490 Faraday cup with a proton current of $1\ \mu\text{A}$. This calculates to an ion rate of $r = 1.2 \times 10^9\ \mu\text{C}^{-1}\text{s}^{-1}$. In

Table 10.4: Results from the in-source spectroscopy of first and second excited states in astatine. Further details are given in the text. The measurement marked with * is an artefact from the side band of a multi-mode operation of the Ti:Sa and this may also have affected the laser-scan of the first step**. Statistical errors are indicated for the centroid position ν of the transition. The width is denoted as w . The unit of the amplitude as A indicates the detector type. Values in pA were obtained with a FC and values given in s^{-1} are results from the α -decay spectroscopy.

Scan step	ν (cm^{-1})	w (cm^{-1})	A	Scheme	Mass	Fig.
905	11043.156(20)	0.74	3.5 pA	$\{216^{\text{Ti}} 905^{\text{Ti}} 532\}$	205	1
915	10923.57(62)	0.40	6.5 pA	$\{216^{\text{Ti}} 915^{\text{Ti}} 532\}$	205	2
795	12571.539(42)	1.4	6.4 pA	$\{216^{\text{Ti}} 795^{\text{Ti}} 532\}$	205	3
216	46233.928(43)	0.52	3.3 pA	$\{216^{\text{Ti}} 795^{\text{Ti}} 532\}$	205	4
(785)	12728.982(8)*	0.2	0.075 pA	$\{224^{\text{Ti}} 785^{\text{Ti}} 532\}$	205	5)
224	44550.256(6)**	0.49	0.57 pA	$\{224^{\text{Ti}} 785^{\text{Ti}} 532\}$	205	6
701	14255.201(11)	0.37	0.042 pA	$\{224^{\text{Ti}} 701^{\text{Ti}} 532\}$	205	7
793	12607.560(12)	0.49	0.4 pA	$\{224^{\text{Ti}} 793^{\text{Ti}} 532\}$	205	8
224	44549.949(12)	0.54	0.28 pA	$\{224^{\text{Ti}} 793^{\text{Ti}} 532\}$	205	9
795	12570.870(16)	0.85	200 pA	$\{216^{\text{Dye}} 795^{\text{Dye}} 532\}$	217	10
216	46234.868(11)	0.78	86 pA	$\{216^{\text{Dye}} 795^{\text{Dye}} 532\}$	217	11
915	10923.444(7)	0.6	43 s^{-1}	$\{216^{\text{Dye}} 915^{\text{Ti}} 532\}$	196	12
216	46233.678(3)	0.67	54 s^{-1}	$\{216^{\text{Dye}} 915^{\text{Ti}} 532\}$	196	13
216	46233.611(16)	0.69	0.92 s^{-1}	$\{216^{\text{Dye}} 273^{\text{Dye}}\}$	199	14
224	44549.304(56)	1.3	12 s^{-1}	$\{224^{\text{Dye}} 273^{\text{Dye}}\}$	199	15
915	10923.466(12)	0.6	150 pA	$\{216^{\text{Dye}} 915^{\text{Ti}} 532\}$	211	16
915	10923.452(15)	0.52	130 pA	$\{216^{\text{Dye}} 915^{\text{Ti}} 532\}$	205	17
216	46233.909(10)	0.72	96 pA	$\{216^{\text{Dye}} 915^{\text{Ti}} 532\}$	205	18

a second conservative assumption, FC.490 measures not only ^{205}At , but also the full intensity of the two neighbouring masses $A = 204$ and $A = 206$. From this and assuming the largest in-target production, the minimum laser ionization efficiency calculates to $\eta_{\text{laser}} > 4\%$

10.2.9 Isotope shifts

Laser scans for the five astatine isotopes $^{196,199,205,212,217}\text{At}$ were performed for the 216 nm transition during several measurement campaigns. A compilation of the obtained scans is shown in Fig. 10.14 and the centroid positions from the Gaussian fit is given together with the results from scans across the 795 nm transition in table 10.8. These preliminary results can be used as a guideline to extrapolate the transition frequencies for other isotopes asked by the ISOLDE users and were the basis for a research proposal (P-319) to the INTC: "Beta-delayed

Table 10.5: Scanned regions for second excited states

scheme	dye range (nm)	total energy (cm^{-1})
{216 DCM 532}	595.2 ... 679.8	60944 ... 63034
{216 DCM 532}	610.1 ... 689.6	60734 ... 62624
{216 R6G 532}	579.7 ... 609.7	62634 ... 63484

Table 10.6: Scanned regions for third excited states

scheme	dye range (nm)	total energy (cm^{-1})
{216 795 F127}	540.5 ... 583.1	75955 ... 77305
{216 795 R6G}	579.7 ... 602.4	76055 ... 75405

fission, laser spectroscopy and shape-coexistence studies with radioactive At beams“ [AAB⁺12] which was accepted by the INTC and is scheduled for 2012.

During the on-line RILIS operation for the ISOLDE experiment IS534 (“Beta-delayed fission, laser spectroscopy and shape-coexistence studies with radioactive At beams”) the second step transition at 795 nm was scanned with the narrow band Ti:Sa laser, revealing the hyperfine structure of ²⁰⁵At. This measurement is considered as a prove of concept for the upcoming in-source spectroscopy measurements as well as for the application of the narrow-band Ti:Sa laser. Details are discussed in Appendix I.

Table 10.7: In-target production rates for astatine isotopes.

Production rate ($10^9 \mu\text{C}^{-1} \text{s}^{-1}$)		
At isotope	[Bar11]	[Got12]
204	3.54	10.5
205	3.39	9.6
206	2.95	8

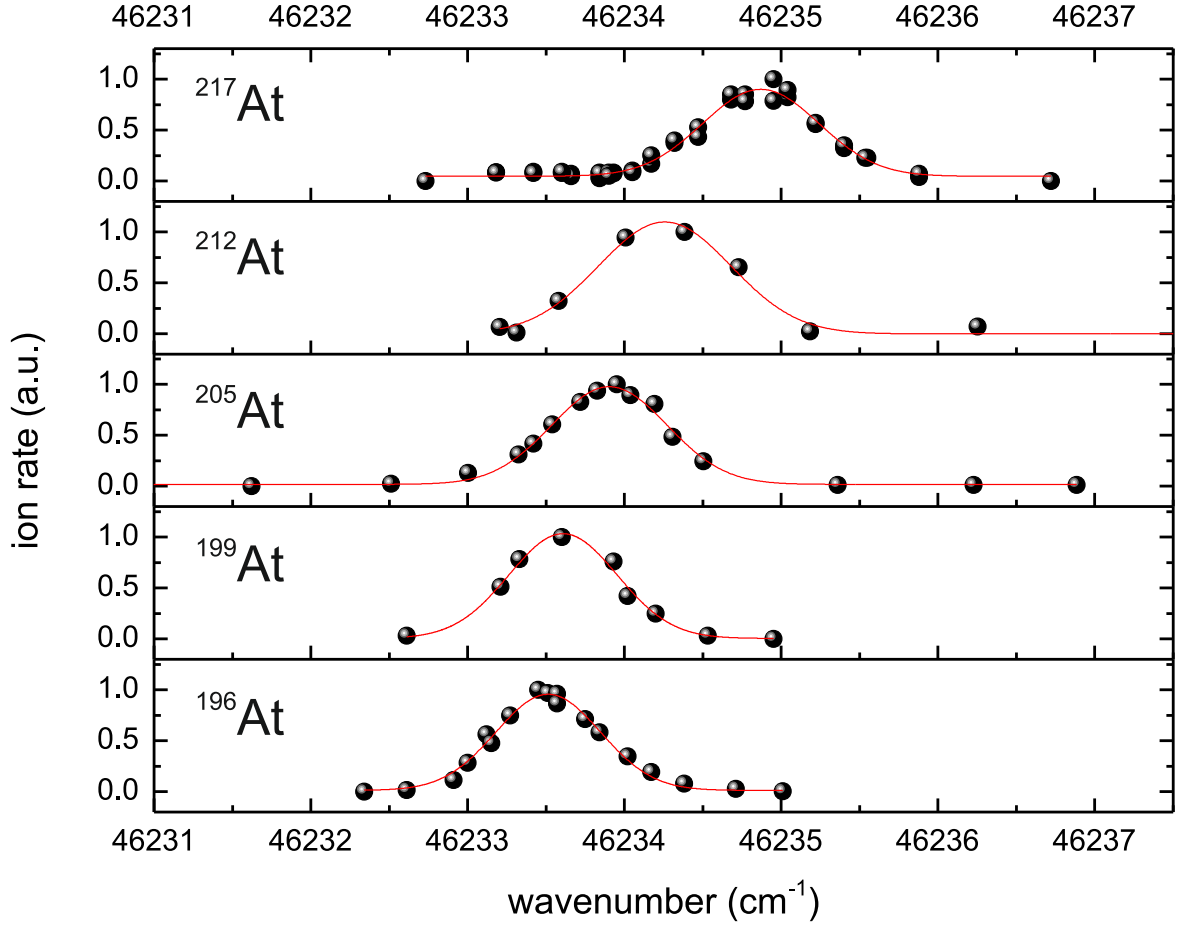
Figure 10.14: Isotope shifts of the 216 nm transition ($6p^5, J = 3/2 \rightarrow 6p^4 7s, J = 3/2$) in astatine.

Table 10.8: Isotope shifts of astatine isotopes for the two transitions at 216 nm and 795 nm

Isotope	216 nm		795 nm	
	Centroid (cm^{-1})	Shift (GHz)	Centroid (cm^{-1})	Shift (GHz)
^{196}At	46233.51(1)	-11.7(5)		
^{199}At	46233.61(2)	-8.9(6)	12571.59(1)	6.4(4)
^{205}At	46233.90(1)	0	12571.38(2)	0
^{212}At	46234.26(3)	10.6(9)		
^{217}At	46234.87(1)	29.0(5)	12570.87(2)	-15.1(6)

10.3 Precision measurement of the ionization potential of astatine

To obtain a more precise value for the ionization potential of astatine than the result from the ionization threshold method presented in Section 10.2.3, a high resolution, continuous scan across the ionization potential was envisaged. This work was performed in conjunction with the search for a more efficient ionization scheme. For a scan of the laser frequency with a total photon energy just below the ionization potential, high lying Rydberg levels are expected to appear in the spectrum of astatine, as observed e.g. for its lighter homologues iodine and bromine [BBG81, RGB84]. Therefore searching this energy region for resonances is referred to as a *Rydberg scan*. The observation and analysis of a Rydberg series would lead to a determination of the $\text{IP}(\text{At})$ with high precision. For this additional laser spectroscopic work on the astatine ionization scheme, several short term beam times were scheduled¹. Due to time restrictions, the scanning range was limited by the laser dyes that were used for the on-going RILIS run or for the next requested element in the schedule. Two of these additional time slots were used for wide range laser-scans across the ionization threshold of astatine $\text{IP}_{\text{Thr}}(\text{At}) = 75129(75) \text{ cm}^{-1}$. During the second run efforts were made to study the positions of the intermediate states more precisely.

Before discussing the two scans that are referred to as *dataset 1* and *dataset 2*, the laser requirements are analysed and a method will be introduced to visualise the different series in the Rydberg spectra. In the same section an algorithm is presented that allows determining the ionization potential without analysing any of the resonances in the spectrum. Finally the two datasets are treated with the established Rydberg-Ritz formalism to deduce the ionization potential as it was applied for other elements, e.g. technetium [MGR⁺10].

10.3.1 Measurement procedure for Rydberg scans

Table 10.9: Choice of ionization scheme for the laser-scan across the ionization potential of astatine

second excited level (cm^{-1})	required tuning range (nm)	possible dye
58805	610...615	DCM
57277	558...562	Pyrromethene 580
57269	558...562	Pyrromethene 580
57157	554...558	Fl27

From table 10.9 it becomes clear that for the scan across the ionization potential, starting from one of the possible second excited states, a dye laser is required.

¹This was possible e.g. during stable beam tuning to REX-ISOLDE occupying the central beam line, while a suitable target was mounted to the other front-end and protons were available.

Data taking of *dataset 1*

Before this measurement, the RILIS was set to ionize cadmium (c.f. 7.2.3.2) and the two *Credo* dye lasers were both operating with DCM dye. With this dye it was possible to prepare the RILIS lasers for the first scan of the ionization potential of astatine within only a few hours². This included the time required to adjust the frequency quadrupled Ti:Sa from 228 nm (for Cd), to 216 nm (for At) as well as redirecting the laser beams from the HRS to the GPS target. The other Ti:Sa lasers were already set to produce the wavelengths for the second steps at 915 nm and 795 nm. Laser powers used are summarized in Table 10.10. Before the measurement the scheme $\{216^{\text{Ti}}|915^{\text{Ti}}|532\}$ was used to check the yield of ^{205}At . An ion current of 47(7) pA was obtained on FC.490 with a proton current of $1.7 \mu\text{A}$ and a laser-off background gave a reading of -3.5(8) pA. The scheme $\{216^{\text{Ti}}|795^{\text{Ti}}|532\}$ delivered an ion current of 10 pA under the same target conditions.

Table 10.10: Laser settings for the spectroscopy of Rydberg states

Wavelength (nm)	Power (W)	Laser
532	35	Edgewave
915	1.65	Ti:Sa 1
864	1.86	Ti:Sa 2
216	0.033	FHG Ti:Sa 2
795	2.02	Ti:Sa 3
610	4.65	Credo 10, DCM

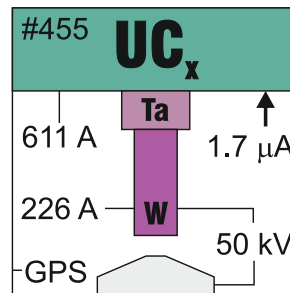


Figure 10.15: Conditions of target #455 during the laser spectroscopy measurements. The uranium carbide target was coupled to the GPS front-end. The target and tungsten line heating were set to 611 A and 226 A, respectively. The extraction voltage was set to 50 kV and the proton beam intensity was typically $1.7 \mu\text{A}$.

Target #455-UC-W was used at the GPS to produce astatine isotopes. Details about the

²The notice time for the availability of a time window for the measurement was in the same range.

target conditions are given in Fig. 10.15. The mass separator was set to transmit ^{205}At . The third step laser wavelength was tuned automatically across the tuning range of the DCM dye while the laser ions were collected in the Faraday cup FC.490. The available measurement time was limited so that only a scan in one direction was possible. The scan was performed in two sections at different scan-speeds $-0.251\text{ cm}^{-1}\text{s}^{-1}$ and $-0.132\text{ cm}^{-1}\text{s}^{-1}$. The measurement recorder was set to acquire the measured wavenumbers and the Faraday cup current at a rate of 4 s^{-1} . The recorded data sets were then merged and corrected for the systematic wavelength shift caused by the integration time of the Faraday cup. As the real scan-speeds differ from the set scan-speeds in the control program of the dye laser, the recorded wavenumbers were plotted against their time stamp and the slope of a fitted line was taken as the average scan-speed of the measurement. The result of this first laser-scan across the ionization potential of astatine is shown in Fig. 10.16. Panel a) shows the full scan range between 15523 cm^{-1} and 16599 cm^{-1} . The reading from the Faraday cup gave a background of $\approx -5\text{ pA}$. The lowest members of a Rydberg series can be observed at about 15845 cm^{-1} . The peaks get more pronounced approaching the ionization limit as shown in the zoom of the spectrum in panel b). The members of lower principal quantum numbers n exhibit a splitting into three well resolved peaks that may belong to different series or different total angular momentum j . Detailed view of one of the resolved members is shown in panel c). At this level of spectral resolution, also the pulsed nature of the ISOLDE ion beam becomes visible. The periodic break down in recorded ion beam current is a result of the pulsing extraction that is turned off regularly for $\approx 20\text{ ms}$ on arrival of the proton pulse on the target. A description is presented in Appendix F.

Data taking of *dataset 2*

A second time slot of ISOLDE beam time was allocated to repeat the Rydberg scan and to improve the measurement accuracy and precision of the intermediate level positions: Here target #UC-466 was used at the HRS front-end with operation conditions as given in Fig. 10.17. On a special request to the PSB operator, evenly spaced proton pulses were sent to the ISOLDE target. This was achieved by diverting a number of proton pulses to the beam dump or to other users, resulting in a reduced averaged proton current of $1.0\text{ }\mu\text{A}$. A description of the pulse structure in the PSB super-cycle is presented in Appendix F. The HRS separator was set to transmit ^{205}At .

For this measurement the same ionization scheme was used as for the first scan (c.f. Sec. 10.3.1). This time the first step wavelength at 216 nm was produced by frequency tripling of the *Credo 13* dye laser operating with DCM dye. The second step at 795 nm was generated using Ti:Sa laser 1. The scan was performed with the second dye laser (*Credo 10*) running with DCM dye. Table 10.11 summarizes the laser powers.

The spectra were taken in a continuous mode: the wavelength of the scanning dye laser and the ion current of ^{205}At measured with FC.490 were recorded with an opposite scanning direction to the scan of the first measurement. The scan was performed in two sections with

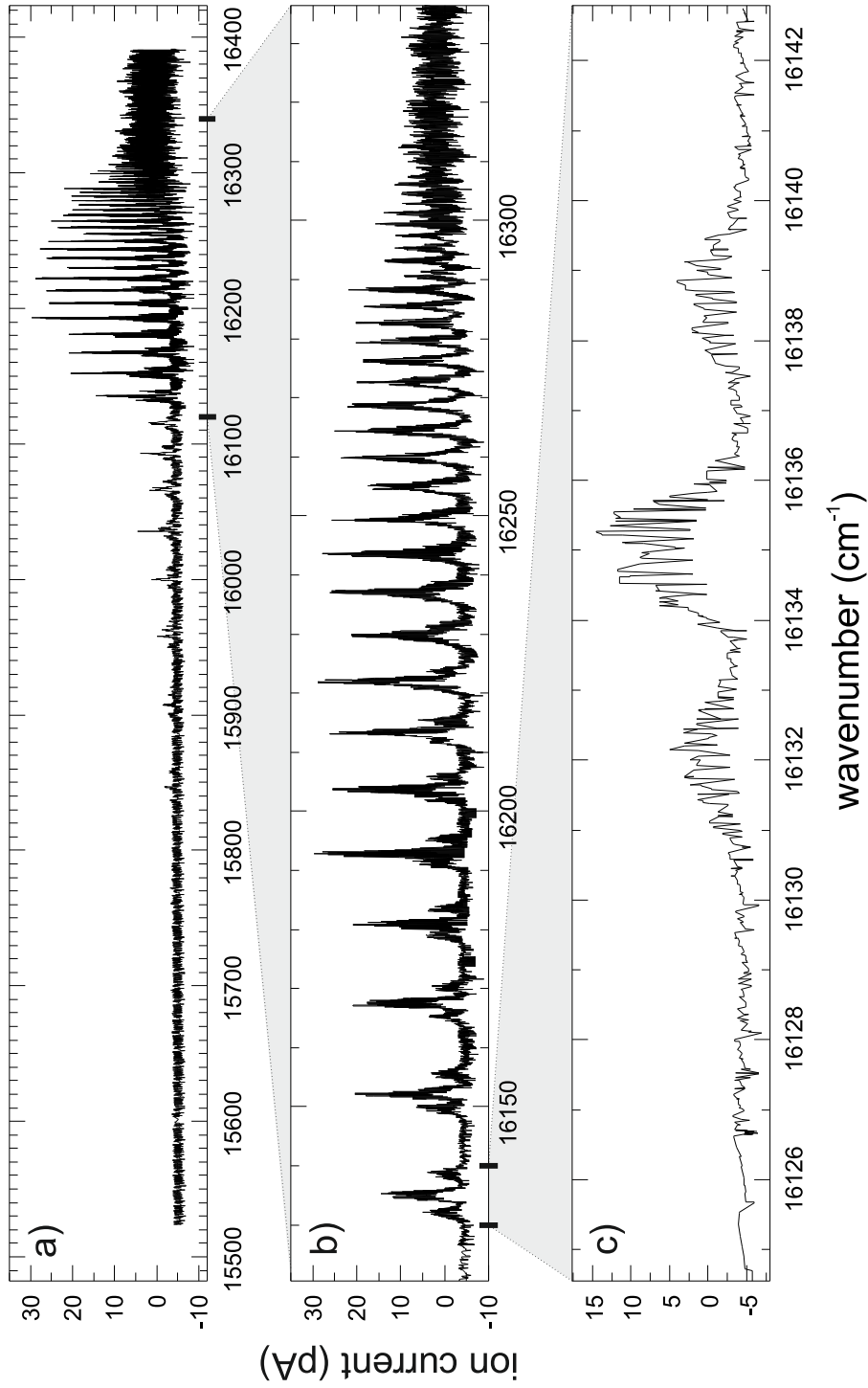


Figure 10.16: High resolution laser-scan across the ionization potential of astatine (*dataset 1*). a) Full view of the scanned region. b) Observed members of the Rydberg series showing a multiplet structure, within which up to three peaks are resolved up to wavenumbers at around 16310 cm^{-1} . c) Zoom into one of the periodic features showing three well separated resonances. The underlying regular signal drops originate from the sequence of proton pulses.

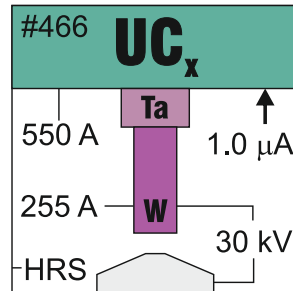


Figure 10.17: Target information for the second Rydberg scan. Target #UC-466 was used at the HRS front-end with an extraction voltage of 30.22 kV and an averaged proton current of $\approx 1 \mu\text{A}$.

Table 10.11: Laser settings for the second Rydberg scan of astatine

Wavelength (nm)	Power (W)	Laser
216	0.04	Credo 13, DCM
795	2.3	Ti:Sa 1
610	4	Credo 10, DCM

different scan-speeds of $0.199 \text{ cm}^{-1}\text{s}^{-1}$ and $0.0997 \text{ cm}^{-1}\text{s}^{-1}$. Figure 10.18 shows a laser-scan across the ionization potential of astatine (*dataset 2*).

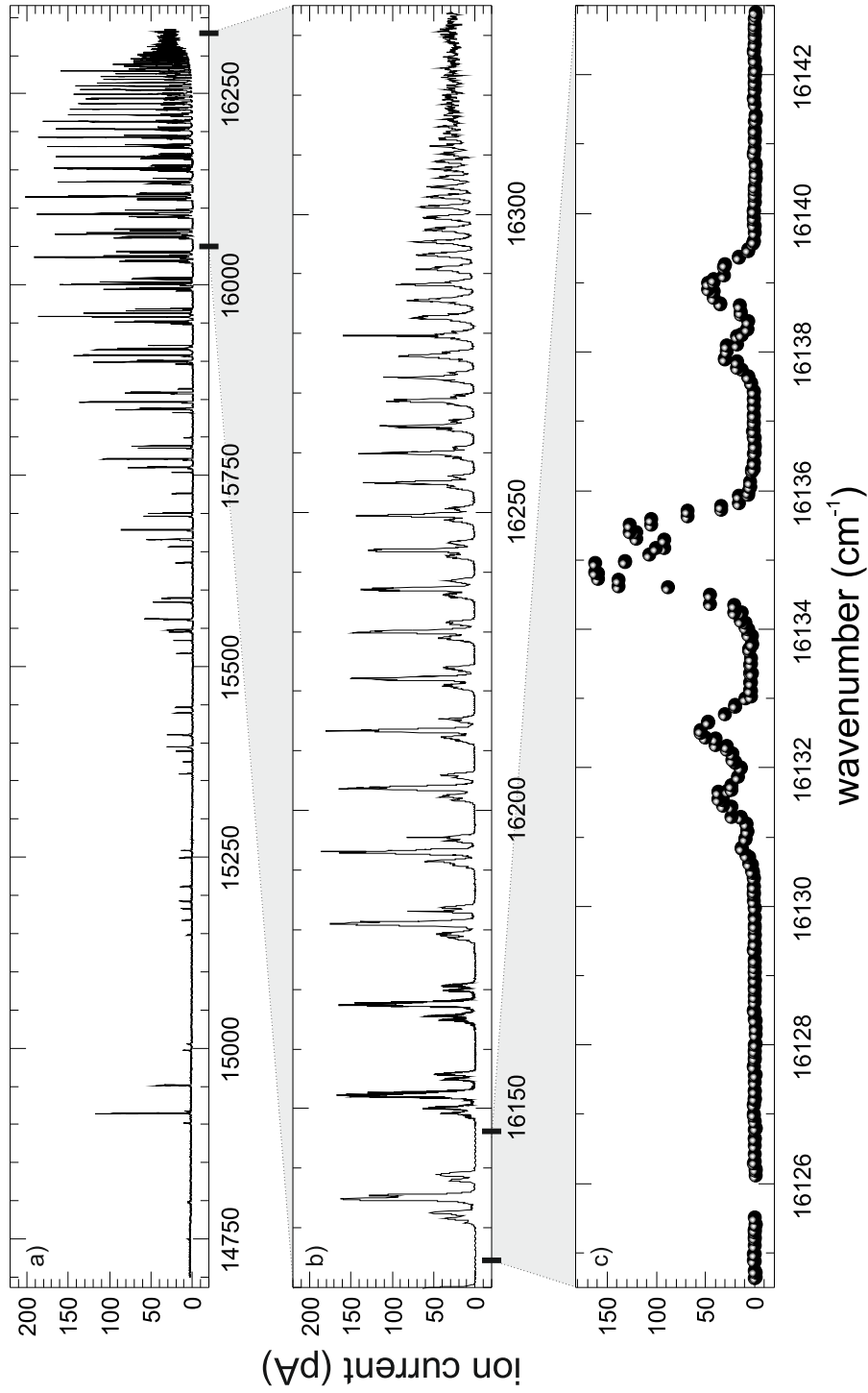


Figure 10.18: Second laser-scan across the ionization potential of astatine (*dataset 2*). a) Full view of the scanned region. b) The members of the Rydberg series exhibit up to seven resolved peaks. c) Detailed view of one of the periodic features.

10.3.2 Determination of the first and second step level energy

The energies of the intermediate steps in the three-colour scheme $\{216|795|\lambda_3\}$ used for the Rydberg scan were investigated. This increases the accuracy of the ionization potential and enables to estimate possible systematic errors.

First excited state: Several laser-scans across the first-step transition at $\lambda_1 = 216$ nm were performed with the frequency tripled dye laser. Gaussian fits were applied to the obtained spectra and corrected for the systematic offset from the data acquisition (cf. Section 8.7). The results are shown in Fig. 10.19 a). Two different groups of centroid positions are well distinguishable. Error bars indicate the statistical error only. Scans 1 – 6 were performed with the second step laser set to 12571.75 cm^{-1} while during scans 7 – 9 the second step wavelength was optimized at 12571.34 cm^{-1} . The difference of the average positions of the two groups equals 0.09 cm^{-1} and the maximum distance is 0.11 cm^{-1} . This uncertainty is to be treated as a systematic error attributed to unresolved hyperfine components. The standard deviation of 0.05 cm^{-1} for all measurements was used as the uncertainty of the result. The weighted average of all measurements gives $\nu' = 46233.97(5) \text{ cm}^{-1}$.

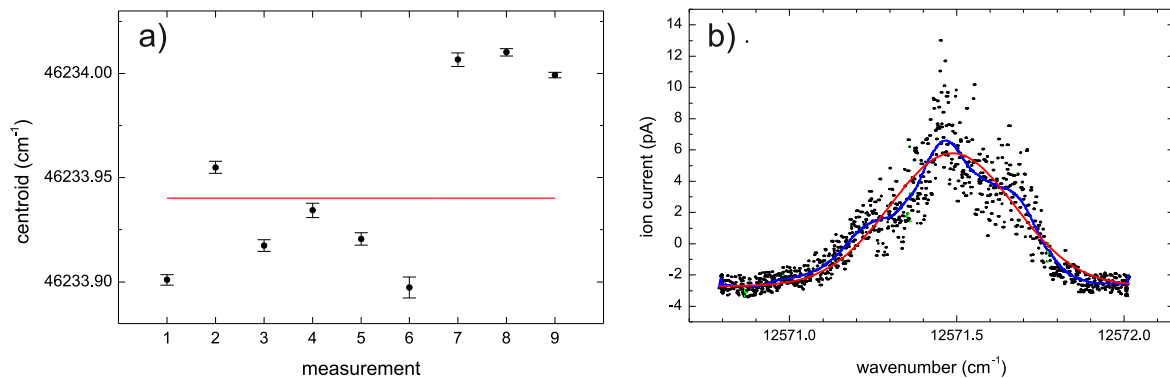


Figure 10.19: Determination of the first and second step level energies. a) Distribution of the centroid positions of the first step excitation wavenumber. The peak positions cluster in two groups. Measurements 7 – 8 were taken while the second step laser was optimized on a different wavelength. This implies a systematic error which needs to be taken into account. b) Laser scan of the second excited state. The red curve is a fitted Gaussian. The blue curve is a moving average of the data.

Second excited state: The second step laser at $\lambda_2 = 795$ nm was scanned using the motorized etalon of the Ti:Sa laser. The laser power in the ion source was reduced by defocussing the beam. Two scan directions were recorded in one file. An example of a laser-scan is shown in Fig. 10.19 b). The Gaussian fit to the structure is indicated as red line. The

blue curve is a moving average³ along the data points. An unresolved substructure is visible. The centroid positions of five laser-scans were averaged and give $\nu'' = 12571.47(3) \text{ cm}^{-1}$, with a statistical error which originates from the uncertainty of each measurement of 0.15 cm^{-1} .

³Smoothing function in *Origin*

10.3.3 Graphical analysis of the Rydberg spectra

The wavenumber $\nu[n, \delta]$ of a Rydberg state with principal quantum number n belonging to the series with a quantum defect δ is given by the Rydberg-formula:

$$\nu[n, \delta] = E''_{\text{lim}} - \frac{R_{\text{M}}}{(n - \delta)^2}, \quad (10.4)$$

with R_{M} the reduced-mass Rydberg-constant and E''_{lim} the ionization limit of the excited state denoted as E'' . In the conventional Rydberg-Ritz analysis (presented in Section 10.3.4), each resonance is attributed to a principal quantum number and the ionization limit E_{lim} and quantum defects δ are obtained from a fitted Rydberg curve.

A graphical method has been developed to visualize and analyse the content of the Rydberg spectrum as a whole. Similar techniques as applied by [LF70] were used, while here none of the resonances observed in the spectrum was fitted prior to the analysis. It will be shown that the developed methods and algorithms permit the determination of the IP(At) without a detailed Rydberg-analysis. The graphical visualization facilitates the identification of the series members. All results shown are based on *dataset 2*.

Scaling functions for the energy axis of the Rydberg spectrum were defined. For the first function, the Rydberg formula (Eqn. 10.4) was solved to obtain the effective quantum number $n^* = (n - \delta)$:

$$n^*[\nu, E_{\text{set}}] = \sqrt{\frac{R_{\text{M}}}{E_{\text{set}} - \nu}}. \quad (10.5)$$

The ionization limit E''_{lim} has now become a parameter in the scaling function, denoted as E_{set} . From n^* one can determine the remainder of the quantum defect denoted as δ' , using a modulo 1 function:

$$\delta'[\nu, E_{\text{set}}] = \text{mod}_1[\delta] \quad (10.6)$$

$$= \text{mod}_1[n - n^*] \quad (10.7)$$

$$= \text{mod}_1[-n^*] \quad (10.8)$$

$$= \text{mod}_1 \left[-\sqrt{\frac{R_{\text{M}}}{E_{\text{set}} - \nu}} \right]. \quad (10.9)$$

In the case of the Rydberg series in astatine, the remainder δ' spans from 0.9 to 0.4. The visualization would not be very intuitive. For convenience the modulo function δ' was rotated

by 0.5, which defines the shifted remainder δ^* as:

$$\delta^*[\nu, E_{\text{set}}] = \text{mod}_1[0.5 + \delta'] - 0.5. \quad (10.10)$$

$$(10.11)$$

These functions are dependent on the energy ν and the convergence limit defined here as E_{set} . For most applications presented in the following $E_{\text{set}} = 16345.42 \text{ cm}^{-1}$ was chosen, which is close to the final value for the ionization limit. The spectrum was recorded as data points $\{\nu, i\}$ consisting of the measured wavenumber ν and the photo-ion signal i . The application of the n^* and the δ^* function to the spectrum is demonstrated in Fig. 10.20 a-d). The original data $\{\nu, i\}$ is shown for reference in a). The calculated effective quantum numbers $\{n^*[\nu], i\}$ are plotted in b). The peaks in the spectrum become equidistant. The periodicity of the Rydberg resonances modulo 1 becomes visible in the detailed view c). The periodicity modulo 1 is now used to fold and overlap the whole spectrum into a region spanning only the range of $\{0; 1\}$. The additional shift of 0.5 mentioned above yields a range of $\{-0.5; 0.5\}$. The plot for $\{\delta^*[\nu], i\}$ is shown in d).

10.3.3.1 Extraction of the ionization limit

By binning the δ^* spectrum (cf. Fig. 10.20 d)) a histogram can be built which then depends only on E_{set} . The task of building such a histogram, denoted as a δ -histogram, was implemented in *Mathematica*. The quantum defect δ was calculated as $\delta = \delta^* + 3$ as the quantum defect of the main series (denoted as ϕ) was determined as $\delta = 3.17$ (see section 10.3.4). Corresponding δ -histograms are shown in Fig. 10.21; they were calculated for $E_{\text{set}} = 16345.42 \text{ cm}^{-1}$ and slightly varied around E_{set} . The central panel shows the histogram as obtained for E_{set} chosen close to the fit result. Each series that converges to this limit is visible as a broad peak in the histogram. The most pronounced peak is observed at $\delta \approx 3.16 \text{ cm}^{-1}$. This peak belongs to the main series ϕ . When E_{set} is chosen differently by $\pm 0.3 \text{ cm}^{-1}$ the main peak becomes asymmetrical. By increasing E_{set} to $\pm 1 \text{ cm}^{-1}$ the structure fades and vanishes for higher offsets.

The observation of the main-peak behaviour for changing of E_{set} off the expected ionization limit value, has led to the following simple analysis algorithm, that was implemented in *Mathematica*: A $\delta[E_{\text{set}}]$ -histogram was calculated for different E_{set} ranging from 16100 cm^{-1} to 16600 cm^{-1} . For each obtained histogram, the maximum count of all bins was plotted against the chosen energy. The result of this plot is shown in Fig. 10.22 a).

A sharp peak with a height of ≈ 75000 counts at $E_{\text{set}} \approx 16350 \text{ cm}^{-1}$ is observed on top of a background between 20000 to 40000 counts that increases smoothly towards higher energies. When limiting the search range and increasing the resolution via the number of frequency steps, a symmetrical resonance is obtained accordingly to Fig. 10.22 b). A Gaussian fit gives a value for the ionization limit for the main series (ϕ) as reached from the second excited state E'' :

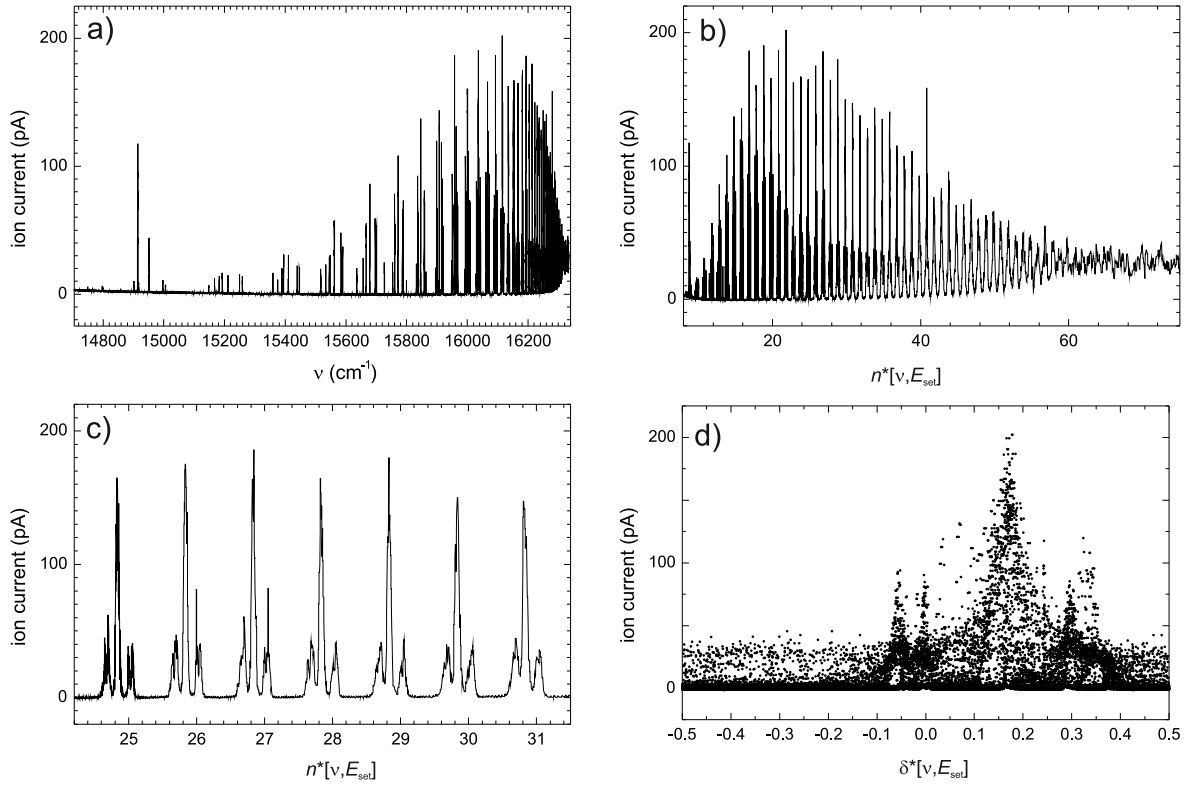


Figure 10.20: Illustration of the steps for the graphical analysis of the Rydberg spectrum. a) Raw data. b) Calculated effective quantum defects n^* for each frequency using a fixed $E_{\text{set}} = 16345.42 \text{ cm}^{-1}$. c) Zoom of the stretched spectrum. The resonances are now equidistant. d) The spectrum is folded and overlapped using the mod_1 function δ^* .

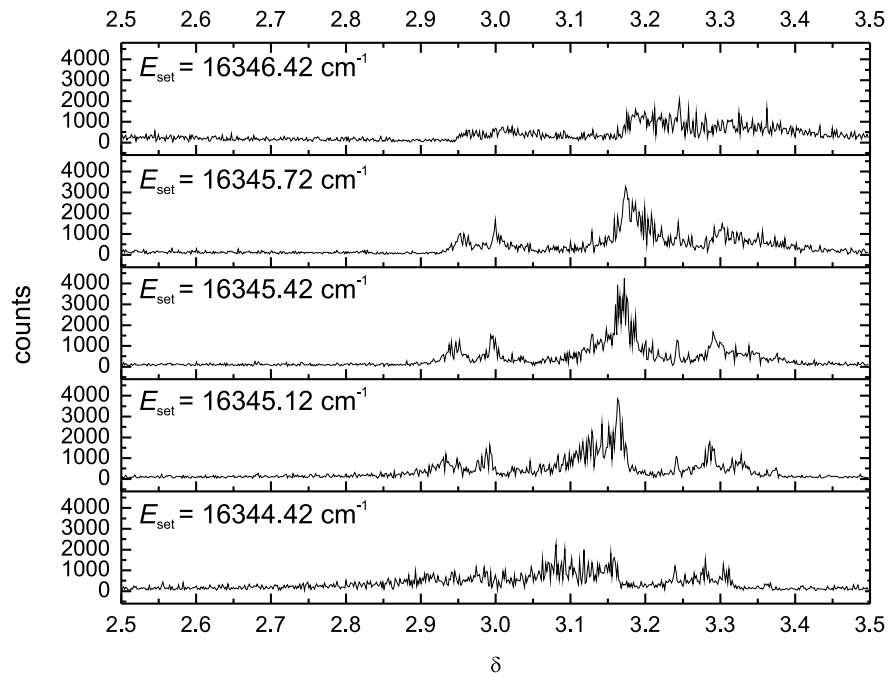


Figure 10.21: Quantum defect histogram for different set limits E_{set} off-set by $\pm 0.3 \text{ cm}^{-1}$ and $\pm 1 \text{ cm}^{-1}$.

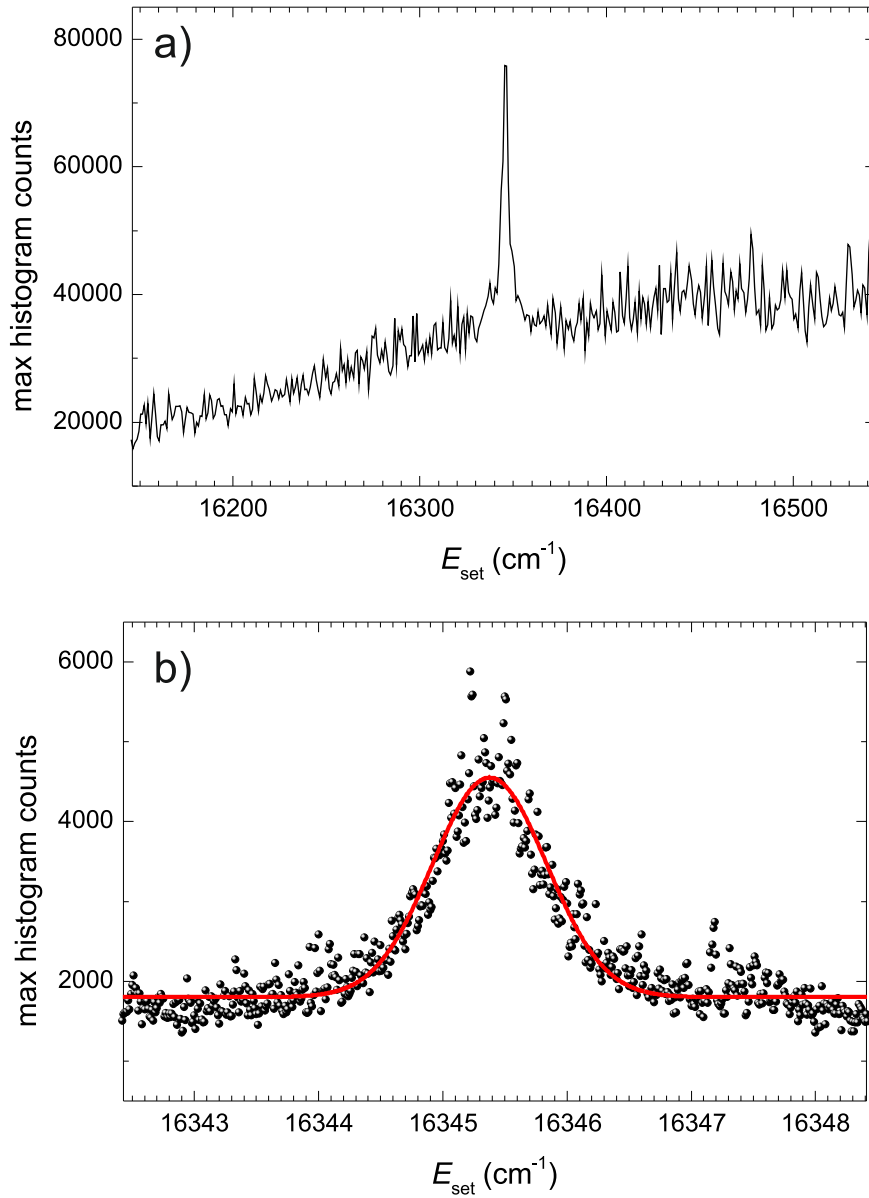


Figure 10.22: Variation of maximum histogram counts at different set limits. b) shows a zoom across the central peak. A Gaussian fit was applied to the resonance like structure and is plotted as the red curve. The position of this peak equals to $E''_{\text{lim,graph}} = 16345.337(7)$ cm^{-1} . This analysis allows the extraction of the position of the ionization limit from a Rydberg scan, without detailed analysing the obtained spectrum.

$$E''_{\text{lim,graph}} = 16345.337(7) \text{ cm}^{-1} \quad (10.12)$$

The width of the resonance is $w = 0.91(2) \text{ cm}^{-1}$. The given statistical error depends on the number of generated histograms and is therefore underestimated. Remarkably, this evaluation allows for the extraction of the position of the ionization limit from a Rydberg scan, without a detailed analysis of the individual structures of the measured spectrum. For verification this method was also applied for gold. Corresponding results are given in Appendix G.

10.3.3.2 Visualization of the position of the ionization limit in a $\delta - E$ plot

The set of δ -histograms that were calculated in the previous section was converted into a two-dimensional matrix, with each column containing the counts of a single histogram. This matrix is visualised as a contour diagram⁴: the data of each cell is given as colour information using linear scaling. Such a δ^* -histogram- E_{set} plot in the range of $E_{\text{set}} = 16345.42 \text{ cm}^{-1} \pm 15 \text{ cm}^{-1}$ is shown in Fig. 10.23. The appearance of peaks in the histograms is interpreted as a sign for E_{set} approaching the true value for the ionization limit. The most pronounced signal is observed at the point $\{0; 3.16\}$, which matches the peak in Fig. 10.22. The data relate the ionization limit of the main (ϕ) series to the quantum defect. Four other series are visible as discussed below. Once again, for verifying this visualization method was applied to Rydberg spectra of the low resolution laser-scan for astatine (*dataset 1*) as well as to data of other elements. Plots and further discussions can be found in Appendix G.

⁴This was done in *Mathematica* using the `ArrayPlot` function

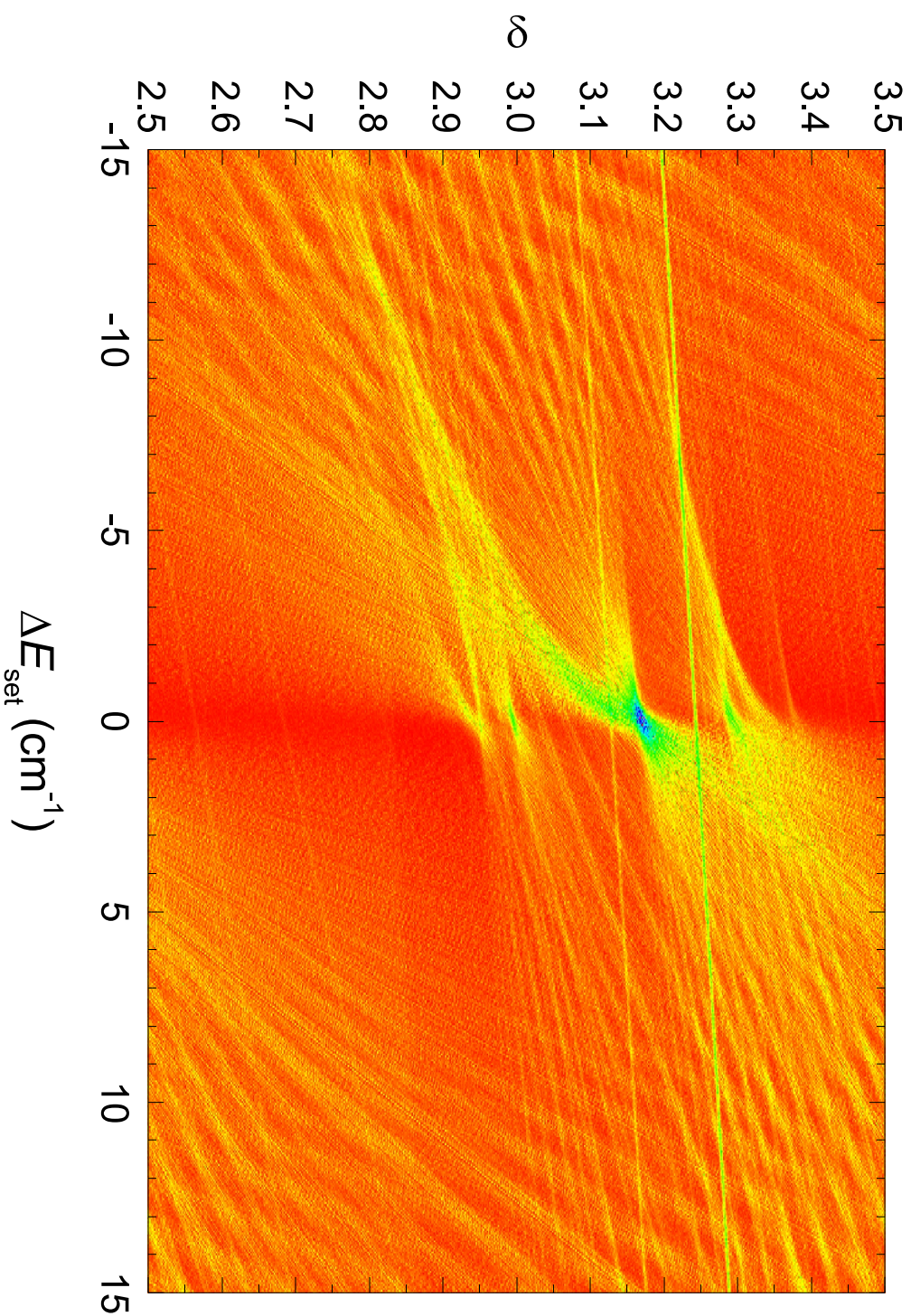


Figure 10.23: $\delta - E_{\text{set}}$ -plot for *dataset 2*. The δ -histograms for different E_{set} were registered as columns in a two dimensional matrix. The count information was converted into colour using linear scaling. The appearance of the peaks in the histogram around $\Delta E_{\text{set}} = 0 \text{ cm}^{-1}$ as well as their vanishing towards higher and lower energies respectively, is observed for series of different quantum defects also converge at the same limit. Five to seven series may be distinguished.

10.3.3.3 Series visualization and identification by the modulo method

For a visualization of the development of the different Rydberg series as a function of the principal quantum number the quantum defect δ is plotted against n^* . For this purpose each data point $\{\nu; i\}$ was converted to tuples of the form $\{n^*; \delta; i\}$. The obtained three-dimensional data is shown as a contour plot⁵ in Fig. 10.24. In total seven series are visible. The main series ϕ is visible as a horizontal “jet” emerging from $\delta^* = 3.16$ at small $n^* \approx 8$. Two other series strongly deviate from the prominent linear dependence on n^* . This behaviour can be used for the identification of the series.

Therefore the modulo analysis was used as a tool to assign series members assisting the detailed analysis of the Rydberg spectra. Fig. 10.25 a) shows the δ^* -plot in which data points were marked⁶ in a range of $\delta^* = 0.17 \pm 0.01$. In the original spectrum all structures belonging to that particular series are highlighted with a green colour in the figure, both in a zoom for a given n (b) and the full spectrum (c).

This method was applied for other quantum defects and gate with a width of ± 0.01 . The result (obtained with *Mathematica*), shown in Fig. 10.26, displays the features with a different colour used for each value of quantum defect. The series assignments indicated are defined in section 10.3.4.

⁵Contour plot functions are available in *Origin* and *Mathematica*. The intensity is colour coded in a two-dimensional plot. The presented graph was obtained using *Origin*.

⁶This was done in *Origin* using the masking tool.

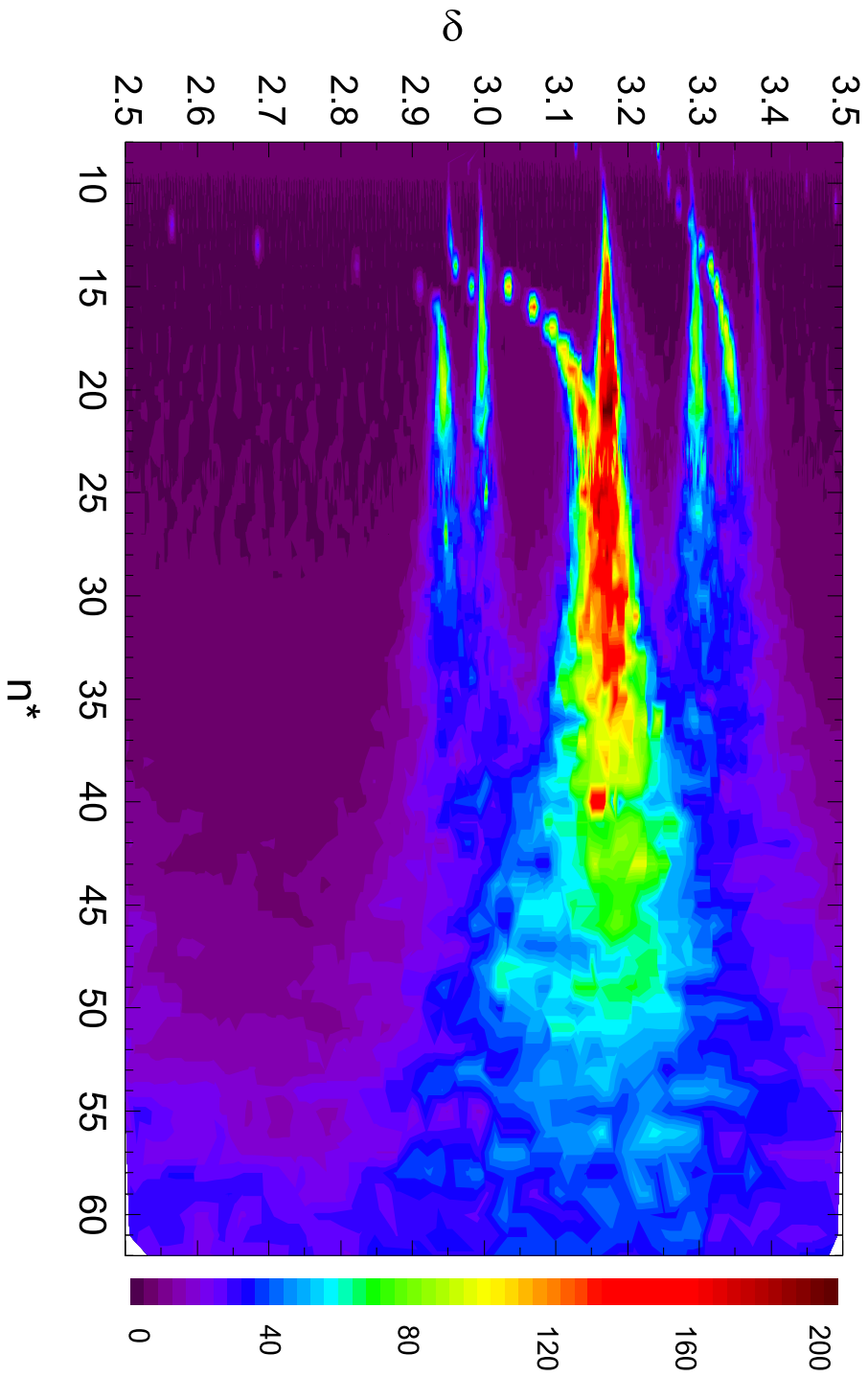


Figure 10.24: Contour plot of the $n^* - \delta$ matrix. To visualize the behaviour of each series, the two-dimensional data points $\{\nu; i\}$ from the Rydberg scan were converted into a three dimensional matrix $\{n^*; \delta; i\}$. The colour coded ion currents are given in pA. Seven series can be identified with the main series ϕ being the horizontal “jet”-like structure emerging from $\delta \approx 3.16$.

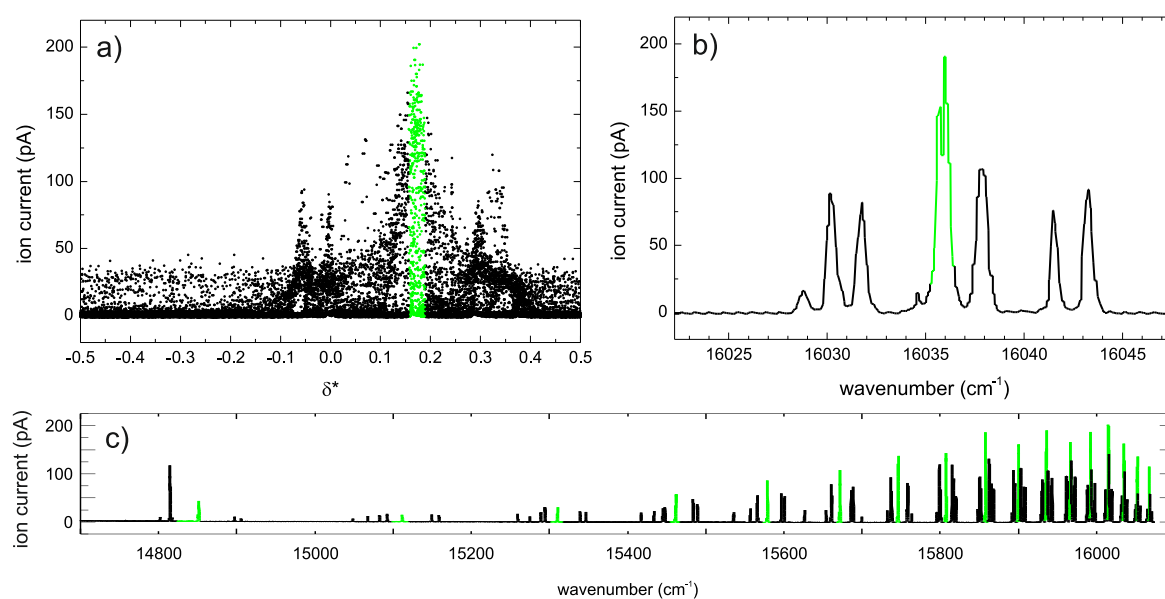


Figure 10.25: Method for identification of series members by gating on the quantum defect. a) Remainder δ^* of the quantum defect, calculated for each wavenumber using the modulo 1 function. A region of 0.17 ± 0.01 was selected (green data points). b,c) Unfolded spectrum, plotted as zoom and in total with the previously selected data points marked.

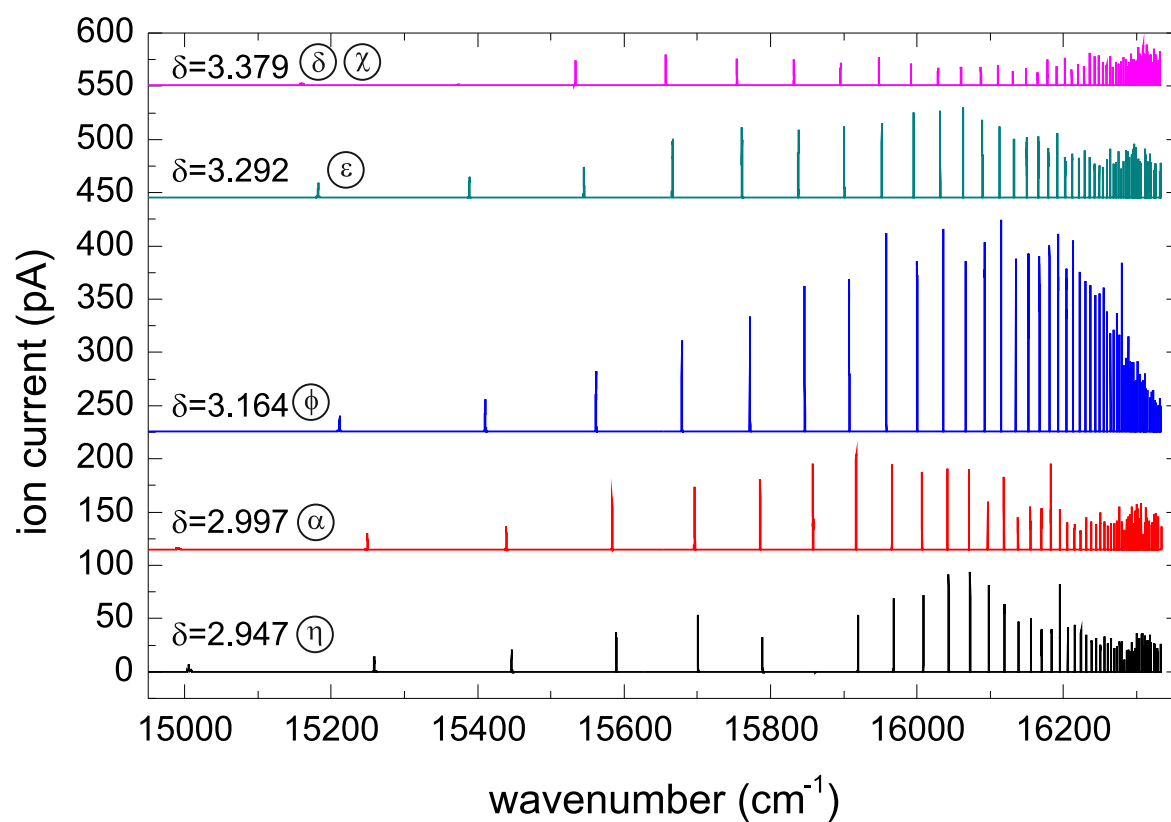


Figure 10.26: Identified series members using the gating method. The applied δ on which the data were gated is given in the plot as well as the assignment as defined in Section 10.3.4 .

10.3.4 Detailed Rydberg-Ritz analysis of the Rydberg spectra

For a detailed analysis all separated resonances observed in the spectra of the two datasets were fitted with Gaussian profiles. All sub structures were fit with multiple Gaussian peaks. Towards higher quantum numbers the peaks are no longer well resolved and structures were fitted with a single Gaussian. The centroid positions are tabulated Table H.1 (Appendix H) for all peaks observed in the second dataset.

10.3.4.1 Results for *dataset 1*

A δ versus n plot (c.f. Fig. 10.27) was created by calculating the quantum defect for each fitted peak position and the corresponding principal quantum number $n = n^* + \delta$. This approach is comparable to the series member assignment using the modulo-method as discussed before. Three series are well separated by their different quantum defects. These were assigned with arbitrary names (η , ϕ and ϵ).

Each series was fitted with the Rydberg formula in first order⁷ (Eqn. 10.13). The two free parameters were E''_{lim} and δ . $R_{\text{M}} = 109737.022009 \text{ cm}^{-1}$ is the reduced-mass Rydberg-constant for ^{205}At . The results are summarized in Table 10.12 and the residuals are plotted in Fig. 10.28.

$$\nu[n] = E''_{\text{lim}} - \frac{R_{\text{M}}}{(n - \delta)^2} \quad (10.13)$$

Table 10.12: Results from the Rydberg fit of the series in *dataset 1*

series	$E_{\text{lim}} \text{ (cm}^{-1}\text{)}$	δ	n-range
ϵ	16345.285(60)	3.3138(44)	26-37
ϕ	16345.341(28)	3.1630(31)	26-56
η	16345.296(52)	3.9559(40)	26-36

10.3.4.2 Results for *dataset 2*

The δ versus n plot, shown in Fig. 10.29 was used to identify members of the 7 series that are visible in the plot of Fig. 10.24. Arbitrary names ($\eta, \alpha, \beta, \phi, \epsilon, \delta, \chi$) were assigned. The series ϵ , ϕ and η were named according to the series already observed in *dataset 1*.

The Rydberg-Ritz formula

⁷ A second-order fit according to Eqn. 10.14 resulted in ambiguous results for the B -factor with a systematic error in the same order as the result for B .

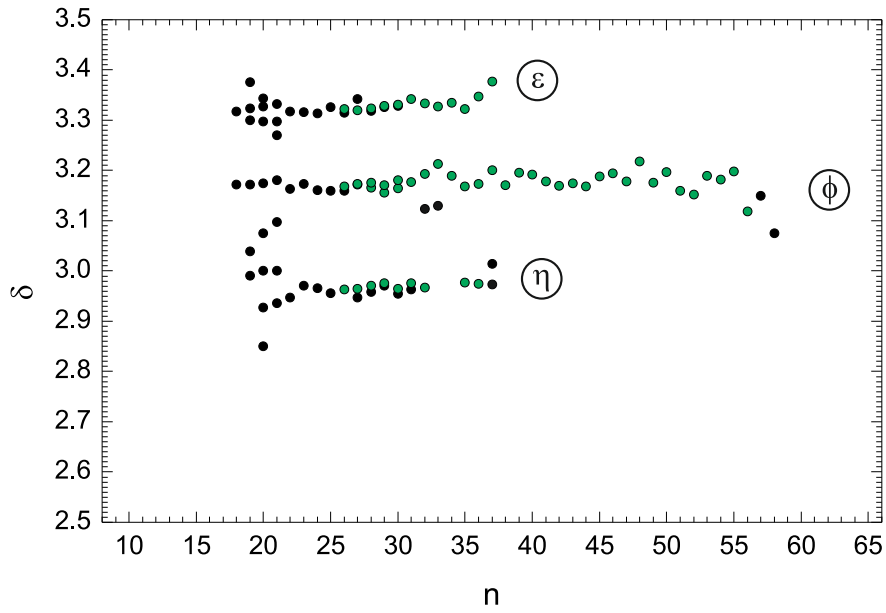


Figure 10.27: Quantum defects and assignment of the series members in *dataset 1*

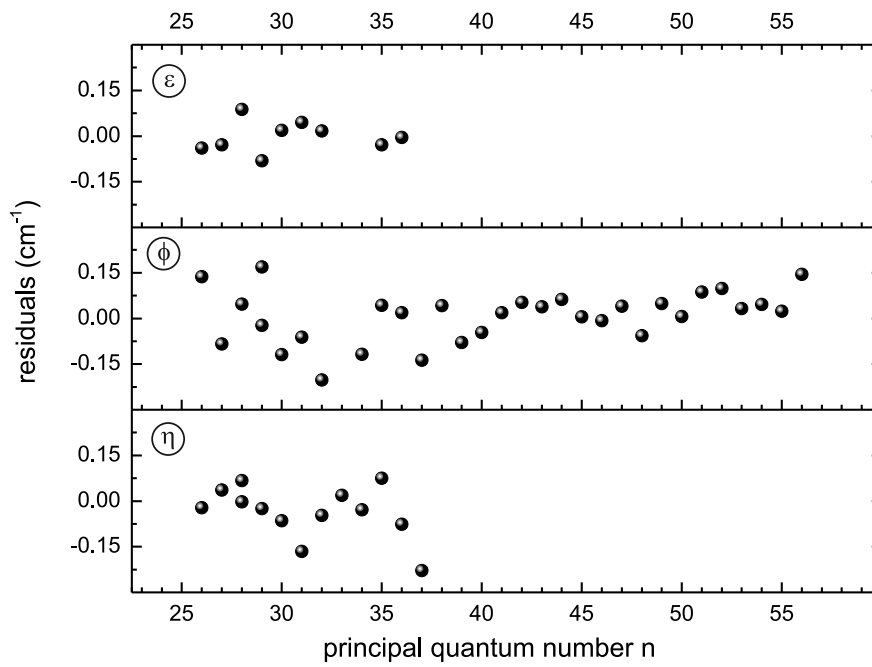
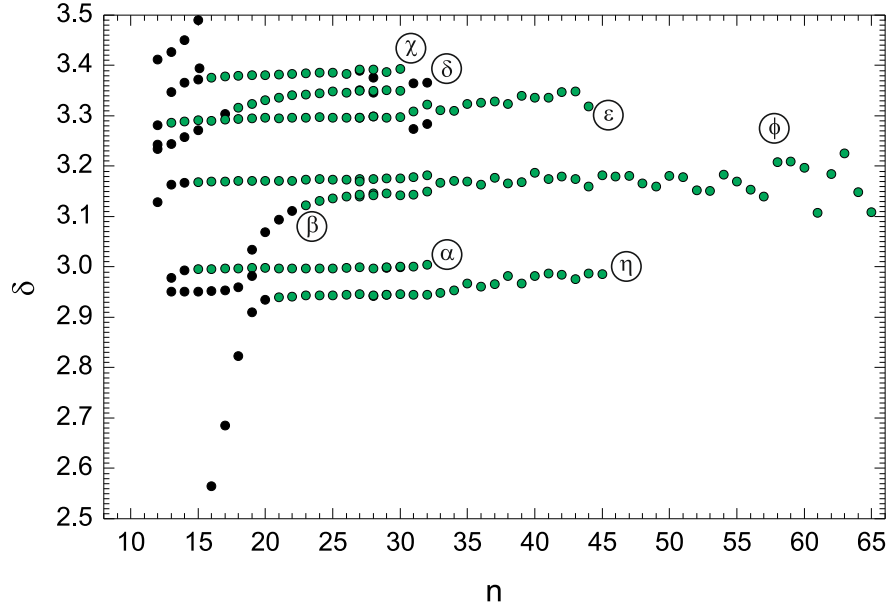


Figure 10.28: Residuals of the first order Rydberg fit to the three series observed in *dataset 1*

Figure 10.29: Assignment of the series members in *dataset 2*

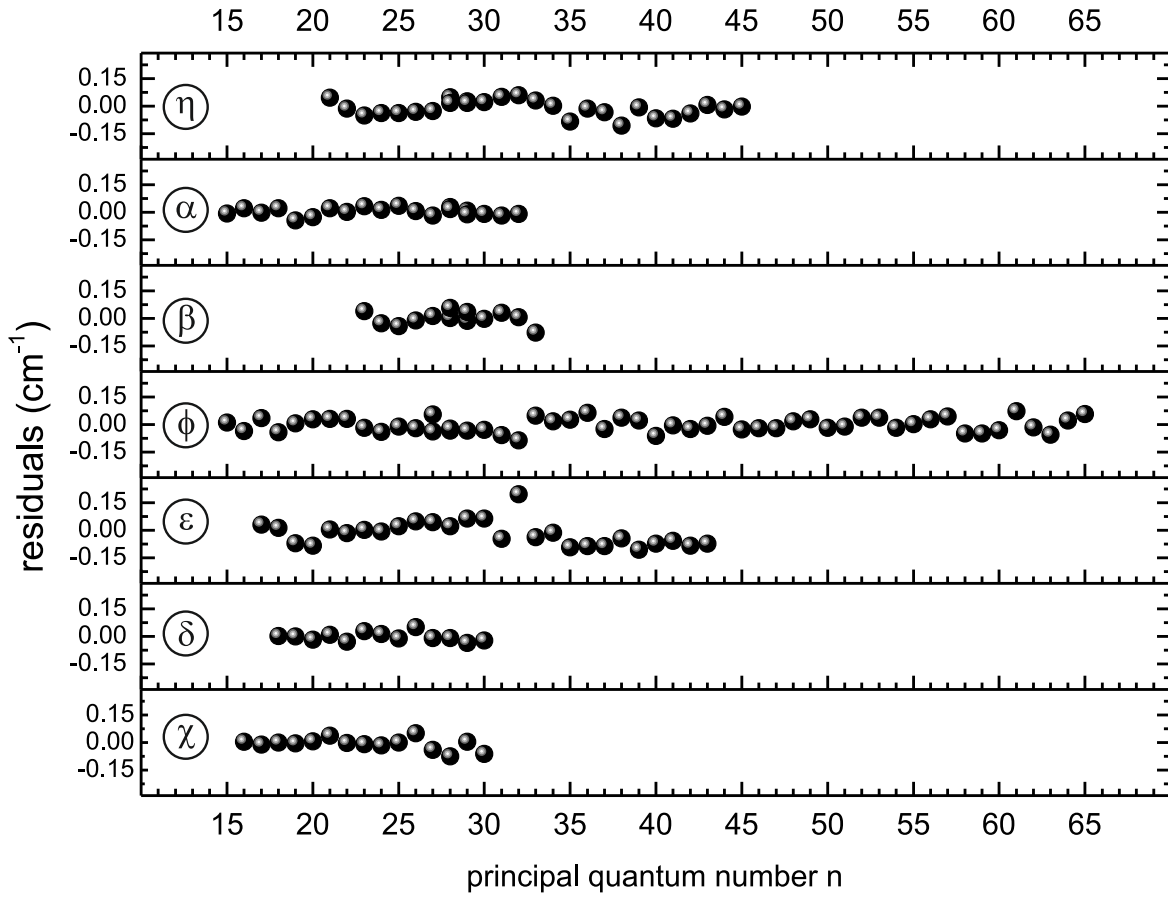
$$\nu[n] = E''_{\text{lim}} - \frac{R_M}{((n-A) - \frac{B}{(n-A)^2})^2} \quad (10.14)$$

was fit to the selected data points $\{n; \nu[n]\}$. The free parameters are the ionization limit E''_{lim} of the second excited state and the Rydberg-Ritz expansion factors A and B . While A is interpreted as the quantum defect, the factor B accounts for the dependence of δ for small quantum numbers n . $R_M = 109737.022009 \text{ cm}^{-1}$ is the reduced-mass Rydberg-constant for ^{205}At .

The fit results are summarized in Table 10.13 and the fit residuals are shown in Fig. 10.30.

Table 10.13: Results from the Rydberg-Ritz fit of the series in *dataset 2*.

series	E_{lim} (cm^{-1})	A	B	n
χ	16345.380(29)	3.3875(12)	-1.90(16)	16-30
δ	16345.706(33)	3.3947(21)	-15.96(36)	18-30
ϵ	16345.296(30)	3.2920(24)	0.00(44)	13-44
ϕ	16345.4233(90)	3.1746(7)	-0.94(10)	15-65
β	16346.01(10)	4.261(12)	-46.2(3.4)	23-33
α	16345.398(16)	3.9976(6)	-0.240(61)	15-32
η	16345.251(28)	3.9310(39)	1.8(1.1)	21-45

Figure 10.30: Residuals of the second-order Rydberg-fit to the seven series observed in *dataset 2*. The discontinuity at $n \approx 32$ arises from combining two partial scans.

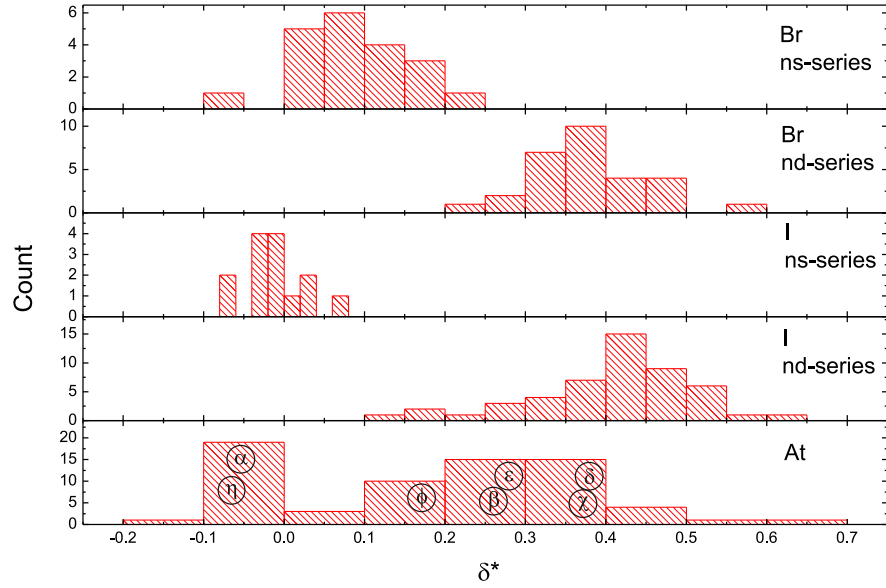


Figure 10.31: Comparison of the distribution of the quantum defects of the members of *ns* and *nd* Rydberg series in other halogens.

10.3.4.3 Assignment of the series

From the $6p^47p$ level, transitions to members of *ns* and *nd* Rydberg series are allowed. To tentatively assign the series observed in the Rydberg spectrum, the corresponding quantum defects of the series members $4s^24p^4ns$ and $4s^24p^4nd$, respectively, for bromine and $5s^25p^4ns$ and $5s^25p^4nd$, respectively, for iodine were taken from literature [SJ83] or calculated from tabulated levels [SM05]. Fig. 10.31 shows the distribution of the obtained quantum defects δ^* . For the astatine histogram (lower panel), only resonances up to $n = 21$ were taken into account, as this is the highest principal quantum number for which information of the two other halogens was reported. The positions of the quantum defects for the different observed series in astatine are indicated for comparison. Based on this a tentative assignment of the individual series was made: α and η is allocated as *ns* series and all other series as *nd* series. Assignment of total angular momentum J to the series was not attempted. Based on the assignment of *nd* for the main series ϕ and the development of the quantum defects for *nd* series for the other halogens, the integer part of the quantum defect for this series was set to 3. This defined the assignment of the principal quantum numbers for the resonances of all other series. The principal quantum numbers noted for the series α and η have to be shifted by +2 as the integer part for *ns*-series for astatine was extrapolated from the other halogens to be 5. Nevertheless, a definite assignment of n is only possible by knowledge of the series head position.

10.3.5 Final result for the ionization potential of astatine and error analysis

The ionization potential of astatine is given by the sum of the transition energies ν' and ν'' to the second excited state $E'' = \nu' + \nu''$ and the ionization limit E''_{lim} :

$$\text{IP}(\text{At}) = \nu' + \nu'' + E''_{\text{lim}} \quad (10.15)$$

$$= E'' + E''_{\text{lim}}. \quad (10.16)$$

Prior to the presentation of the final value, the errors of the contributing measurements are analysed in the following:

Wavemeters Fig. 10.32 shows a laser-scan of the first step transition recorded with ^{196}At in the $\{216^{\text{Dye}}|915^{\text{Ti}}|532\}$ scheme measured by α -detection. For each frequency step, the wavelength of the dye laser was recorded with the two wavemeters: *WS6* and *WS7*. From the Gaussian fit to the peak, a difference between the two wavelength measurements of $\Delta_{\text{WS6-WS7}} = 0.057(3) \text{ cm}^{-1}$ was found. This deviation is within the accuracy of the wavemeters, according to their specifications. The difference between the *WS7* and the *Atos LM007* wavemeter was derived during the DAQ benchmark test described in Chapter 8.7. The difference was $\Delta_{\text{WS7-LM007}} = 0.03 \text{ cm}^{-1}$. The systematic uncertainty of the wavemeter is estimated to $\Delta_{\text{wm}} = 1/2 \Delta_{\text{WS6-WS7}} = 0.03 \text{ cm}^{-1}$.

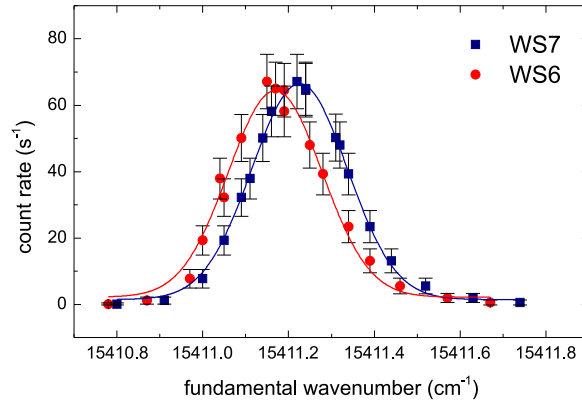


Figure 10.32: Comparison of different wavemeters. The first step resonance at 216 nm in astatine was scanned, while the wavelength was recorded with two wavemeters *WS6* and *WS7*.

Hyperfine components The unresolved sub-structures observed in the laser-scans of the first and second steps lead to additional uncertainties as indicated earlier (cf. Section

10.3.2). To estimate this systematic error, a multiple Gaussian fit with three components was applied to a laser-scan obtained for the second step transition (c.f. Fig. 10.19 b)). The maximum difference of the centroid positions of the components was determined to $\Delta_{C1-C3} = 0.42 \text{ cm}^{-1}$. Therefore the systematic error caused by unresolved structures was estimated to $\Delta_{\text{HFS}} = 0.21 \text{ cm}^{-1}$

Energy of the second excited state E'' The position of the $6p^47p$ level denoted as E'' is calculated as the sum of the photon energies ν' and ν'' required to excite this level. The values were obtained earlier from averaging a number of laser-scans with given statistical errors. Here, the systematic uncertainties shall be treated in addition. For each wavelength measurement a systematic uncertainty of Δ_{wm} has to be considered. For the first step transition ν' at $\lambda_1 = 216 \text{ nm}$, which was obtained from frequency quadrupling, a factor of 4 was to be applied for the systematic error $\Delta_{\text{wm},1} = 4 * 0.03 \text{ cm}^{-1}$. An additional uncertainty of $\Delta_{\text{HFS},1} = 0.11 \text{ cm}^{-1}$ could arise as the maximum difference between the peak positions of the first step, when the second step laser was detuned. The systematic error caused by the correction for the scan-speed is $\Delta_{\text{DAQ},1} = 0.03 \text{ cm}^{-1}$. For the second step transition ν_2 at a wavelength of 795 nm the systematic errors are $\Delta_{\text{wm},2} = 0.03 \text{ cm}^{-1}$ accounting for the wavelength measurement and the uncertainty for the unresolved structures $\Delta_{\text{HFS},2} = 0.21 \text{ cm}^{-1}$ as estimated earlier. The energy of the second excited state calculates to:

$$\begin{aligned} E'' &= \nu' + \nu'' \\ &= 46233.97(05)\{26\} \text{ cm}^{-1} + 12571.47(03)\{24\} \text{ cm}^{-1} \\ &= 58805.44(06)\{50\} \text{ cm}^{-1}. \end{aligned}$$

Result for the ionization limit E''_{lim} The results obtained from the Rydberg fit of the series observed in the two datasets were combined. All observed series but δ and β were taken into account. The result from the weighted average is

$$E''_{\text{lim}} = 16345.39(06)\{15\} \text{ cm}^{-1}$$

The statistical error is the standard deviation of the eight values that were taken into account. The systematic error of 0.15 cm^{-1} is the sum of the systematic uncertainty of the wavemeter of $\Delta_{\text{wm}} = 0.03 \text{ cm}^{-1}$ and the uncertainty from the data acquisition that was estimated to $\Delta_{\text{DAQ}} = 0.12 \text{ cm}^{-1}$.

The intermediate values and the statistical and systematic errors are summarized in table 10.14.

Final result for the first ionization potential of astatine The ionization potential of astatine is the sum of the excited level E'' and its ionization limit E''_{lim} :

Table 10.14: Intermediate results with statistical and systematic errors.

	Value (cm ⁻¹)	Δ_{stat} (cm ⁻¹)	Δ_{wm} (cm ⁻¹)	Δ_{HFS} (cm ⁻¹)	Δ_{DAQ} (cm ⁻¹)
ν_1	46233.97	0.05	0.12	0.11	0.03
ν_2	12571.47	0.03	0.03	0.21	
E''_{lim}	16345.39	0.06	0.03		0.12

$$\begin{aligned}
\text{IP}(\text{At}) &= E'' + E''_{\text{lim}} \\
&= 58805.44(06)\{50\} \text{ cm}^{-1} + 16345.39(06)\{15\} \text{ cm}^{-1} \\
&= 75150.83(09)\{65\} \text{ cm}^{-1}.
\end{aligned}$$

Using the conversion factor from CODATA [MTN08] one obtains the IP(At) in other energy units as follows:

$$\begin{aligned}
\text{IP}(\text{At}) &= 75150.83(74) \text{ cm}^{-1} \\
&= 9.317515(92) \text{ eV} \\
&= 899.0036(89) \text{ kJ/mol}
\end{aligned}$$

10.3.6 Discussion

In this work, the ionization potential was experimentally determined from a photo-ionization threshold measurement (see Section 10.2.3) and from the determination of the ionization limit of a Rydberg series that was performed alternatively, either using a graphical approach (see Section 10.3.3.1) or the conventional Rydberg-Ritz analysis (in this Section). All these values are summarized together with a selection of theoretical predictions for the IP of astatine in Table 10.15.

The results from the two experimental methods (ionization threshold and series limit) agree within their error. The deviation of the threshold value from the final result obtained with the Rydberg analysis is 21 cm⁻¹ or 0.03%. The two methods for analysing the Rydberg series agree within the error. However, it should be noted that the statistical error given for the graphical method is strongly underestimated as it depends on the chosen step-size in the binning process. This method needs to be further evaluated in that respect. Furthermore, the graphical method accounts for the ion signal strength which has its maximum at $n \approx 25$ and therefore includes a weighting mechanism. All other series members contribute to some extent to the width of the observed peak. The theoretical values were obtained from different approaches. Finkelnburg *et al.* [FH55] used an extrapolation method which was based on

Table 10.15: Comparison of experimental and theoretical values for the first ionization potential of astatine. For the experimental values (first three rows), the statistical error is given.

Method	Value (cm^{-1})	Error (cm^{-1})
Series limit, Rydberg-Ritz analysis	75150.83	0.09
Series limit, graphical	75150.78	0.06
Ionization threshold	75129	75
Extrapolation [FH55]	74200	3200
MCDF [RAA ⁺]	74500	1200
DC CCSD(T) [RAA ⁺]	75070	200

known IP's for other neighbouring elements. This value is, within the given uncertainty, in agreement with the experiment, but 1.3% too low. The most recent ab-initio calculations for the prediction of the IP of astatine were performed by Fritzsche *et al.* and Pershina *et al.*, using the Multi-Configuration Dirac-Fock (MCDF) approach and the Dirac-Coulomb Coupled-Cluster approach with single, double and perturbative triple excitations (DC CCSD(T)) [RAA⁺]. These two values agree with the experimental value within the given error. They underestimate the IP by 0.9% and 0.1%, respectively.

Part IV

Conclusion and outlook

Chapter 11

Conclusion

This chapter summarizes the sections of this work regarding the installation of the new laser system to RILIS and the spectroscopic results on astatine which were obtained with the combined laser system.

11.1 The Dual RILIS

The dye laser system of the ISOLDE laser ion source RILIS was upgraded with a second, complementary all solid-state laser system, based on tunable Ti:Sapphire lasers of the design as developed initially at Mainz University. The Ti:Sa laser cavities were re-designed for their use under on-line conditions. They now comprise a fiber-based pre-alignment system that improves the set-up speed of these lasers. The usability was improved by minimizing the available degrees of freedom. All commercial components of the new laser system were specified, procured, tested and finally the complete Ti:Sa laser system was installed to the existing RILIS laser setup. The Ti:Sa cavities fulfil the expected specifications, a slope conversion efficiency of up to $\eta = 25.5\%$ was reached. The fundamental tuning range (690 nm to 950 nm) complements the tuning range of the existing dye lasers. It was shown that the Ti:Sa lasers can be used independently to produce beams of radioactive ions in a Ti:Sa only ionization scheme. On top of that, it was demonstrated, that the solid-state system can be synchronized with the dye system. A geared operation of the two systems is possible and was named “Dual RILIS” [RFM12]. During 2011 the Dual RILIS was in operation for a record time of 2573 h - an increase of 18.5% with respect to the previous running period. The Ti:Sa lasers were applied to produce beams of nickel, zinc, astatine, gold and calcium with increased efficiency and stability for the scheduled experiments IS529 [BBB⁺11], IS518 [KBB⁺11a], IS532 [KBB⁺11b], IS534 and IS519.

The RILIS monitoring, control and data acquisition system that was developed together with and strongly supported by Ralf Rossel from the Hochschule Rhein Main Wiesbaden in the framework of his B.Sc. thesis in informatics, aside of other advantages, enabled the recording of wide range laser scans at RILIS. This was first demonstrated with the high resolution

in-source spectroscopy of astatine Rydberg states (see. next section). The RILIS monitoring system is the first stepping stone towards an on-call operation of the RILIS. At the moment it crucially assists the RILIS operator on shift and provides most valuable information to the ISOLDE users.

The availability of idle tunable lasers and the data recording software at RILIS enables on the fly ionization scheme development during the preparation phase of the RILIS lasers for a scheduled element. This new feature was e.g. successfully applied to the calcium scheme development which is subject to the Ph.D. thesis of Daniel Fink.

11.2 First laser spectroscopy of astatine

An efficient three-colour laser ionization scheme for astatine was identified with the help of the Dual RILIS. As astatine has no long lived isotopes, the required laser spectroscopy had to be performed exclusively in-source at on-line radioactive ion beam facilities in different stages: Initially two-colour ionization was applied at CERN-ISOLDE. In a second stage, at TRIUMF-ISAC, three new transitions to higher excited levels were found. This enabled the use of an efficient three-colour scheme with a powerful laser beam as the final ionization step. The Dual RILIS operation of Ti:Sa and dye lasers was demonstrated. The developed ionization scheme fulfils the letter of intent INTC-I-086 [AAB⁺10] and enables corresponding continuative studies.

These are the content of proposals INTC-P-299 [KBB⁺11a] and INTC-P-319 [AAB⁺12] which were approved by the research committee. The first RILIS astatine shifts for the corresponding experiments were scheduled in 2011 and 2012.

The availability of an efficient ionization scheme for astatine in conjunction with the new Dual RILIS features enabled the first precise measurement of the ionization potential of the astatine atom. The $\text{IP}(\text{At}) = 75150.83(71) \text{ cm}^{-1}$ was determined in different ways with the most precise result stemming from the analysis of a series of high lying Rydberg states observed. With this measurement all naturally occurring elements have an experimentally determined IP. The measurement also serves as an important benchmark of the theoretical calculation of the IP for [117]Uus [CLD10]. The recently discovered super heavy element 117 [OAB⁺10] is the heavier homologue of astatine. On the other hand, the ionization potential, as the binding energy of the valence electron, determines the chemical properties of astatine which can be predicted by means of quantum chemistry calculations [CSSG⁺11]. The latter benefits from that measured value as reference data to be used to assess the various theoretical methods used to simulate astatine chemistry [Gal12].

Chapter 12

Outlook

The electron affinity (EA) of astatine is unknown and can be measured at ISOLDE using the photo-detachment threshold method, that was applied to determine the electron affinity of iodine [HG92]. This can be measured in-source or inside the ISOLDE ISCOOL ion beam cooler/buncher. A letter of intent to the INTC is in preparation.

The narrow-band Ti:Sa laser which was set up and characterized during this work can now be used for in-source laser spectroscopy. The measurement of isotope shifts in gold and spectroscopy of exotic isotopes is scheduled for October 2012. The ISOLTRAP MR-TOF will be used as a detector for some cases. The frequency doubled output of the laser will be used to excite francium atoms inside the Collinear RIS (CRIS) beamline during a run for experiment IS471.

The narrow line-width operation of the RILIS lasers is key to in-source laser spectroscopy as well as isomer separation. To improve the capabilities and versatility additional methods for line-width reduction can be implemented. One example is the well-known pulsed dye amplification. Here, the emission of a CW, low power laser is amplified in a standard dye cell of a dye laser. The CW laser source can be a laser diode or one of the numerous CW lasers used for ISOLDE collinear laser spectroscopy experiments (COLLAPS and CRIS). The laser beams can be easily coupled to a fiber and transported to the RILIS where they are amplified. This would require further collaboration and coordination between ISOLDE experiments. For example, eventually the RILIS may operate in narrow band mode using a COLLAPS CW laser and to provide an isomer pure beam for a Coulex experiment at Miniball which was before analysed and identified using ISOLTRAP. The line-width of the narrow-band Ti:Sa laser can be reduced further if it is configured as a ring cavity and the pump power is reduced. The nominal output power could be regained through stages of single-pass amplification. To enable faster tuning of Ti:Sa lasers a different ionization scheme the grating concept will be followed up. In this case, the proposed oscillator/amplifier configuration could be used to increase the output power. The new CERN Ti:Sa lasers are designed for ease of use and reliability during standard operation, and not as a flexible platform to develop new laser concepts. Therefore a construction kit type Ti:Sa setup on a breadboard will be used for future laser

developments. Concepts to be tested are: Automatic cavity alignment, narrow bandwidth, multi-pass amplification, double crystal cavities and alternative approaches for wavelength selection. The RILIS Monitoring, Control and Measurement system will be extended with a machine protection system, which then enables on-call operation of the RILIS. The on-call operation liberates the RILIS operator from permanent presence in the noisy and radioactive¹ environment inside the RILIS and ensures that more time can be devoted to research and development.

¹25 $\mu\text{Sv/h}$ measured at the Ti:Sa laser

Part V

Appendix

Appendix A

Overview of the variables in the LabVIEW shared variable environment

Table A.1: Devices listed at the RLLIS server and status of implementation. + Fully implemented, h hardware in place or available, * foreseen

Name	unit	device	protocol	connection	refresh rate	channels	type	status
Wavenumber	cm-1	WS6	proprietary	DLL	1-500 ms	4	read	+
Wavenumber	cm-1	WS7	proprietary	DLL	1-500 ms	4	read	+
Power	W	TPM300	RS232	copper	500 ms	1	read	+
Power	W	Multi-powermeter	RS232, direct	copper	500 ms	8	read	+
Water flow	l/min	Chiller	RS232	Ethernet	1 s	1	read	h
Etalon motor	step	Owis Stepper Driver	RS232	Ethernet	1 s	3	write	+
Etalon temperature	C	LabJack	SPI ?	USB	1 s	1	read	+
RLLIS room temperature	C	Pt100 Arduino	Rs232	USB	1 s	2	read	+
Pulse delay	ns	USB oscilloscope	USB	USB	1 s	4	read	*
Set delay	ns	Digital delay generator	RS232	USB	1 s	8	write	h
Beam position	pixel	Beacam	LabVIEW	Ethernet	1 s	4	read	h
Beam stabilization	status	BEAST	RS232	Ethernet	1 s	4	read	h
Mirror steering	step	Picomotor			1 s	8	read	h
Ion current	A	HRS,FC,490	FESA	Ethernet	500 ms	1	read	+
Ion current	A	GPS,FC,490	FESA	Ethernet	500 ms	1	read	+
Ion current	A	FC,558	FESA	Ethernet	500 ms	1	read	+
Proton current	μA	PSB	FESA	Ethernet	500 ms	1	read	+
PPP	count	PSB	FESA	Ethernet	500 ms	1	read	+
ISOLTRAP MR-ToF	counts	MCA	LabVIEW	GPN/TN	variable	1	read	+
MCP	count	Lecroy	Labview	Ethernet	500 ms	1	read	h
Alpha detector	count	Windmill	n.a.	n.a.	n.a.	1	read	h

Appendix B

Scaling the datasets for the ionization threshold measurement of astatine

To analyse the data at once, it was necessary to scale the datasets, compensating for the different conditions during the data taking. This section describes how the scaling factors f_{1-3} can be found and which is the most suitable method.

Three methods were investigated: A *slope method*, an *average method* and a *minimum error method*. The visualization of the slope and average methods is shown in Fig. B.1. Fig. B.1 a) shows the raw data without any scaling. The solid lines are the result of the linear fit of the points of each data set, the dashed lines are the average of count rate registered for the total photon energy of greater than 75100 cm^{-1} . Fig. B.1 b) shows the slope method in which the scaling factor was chosen so that the gradient of the linear fitted curves are equal. This is true for $f_2 = 4$. Fig. B.1 c) shows the average method in which the factors were chosen in such a way that the averages are matching. The scaling factors are $f_1 = 1.7$ and $f_2 = 5.7$.

Since the scans for the two data sets at 224 nm as first step transition (before and after optimization) were obtained with similar set wavelengths for the second step, it was possible to find a factor f_2 using the so-called minimum error method. As shown in Fig. B.2 a), the x-axis was divided into six regions. For the data points falling into the same region, the standard deviation of the count-rate was calculated as well as the average size of the y-error bar, scaled with the applied scaling factor. To obtain a single figure of merit for each chosen scaling factor for the 224 nm (before) dataset, the standard deviation and average error bars were averaged over the six regions (cf. Fig. B.2 a)). Now f_2 was varied between 0 and 10 and the resulting errors were calculated. The result is shown in Fig. B.2 b). As expected the error bars, plotted in curve a), are linearly increasing with the applied scaling factor. The standard deviation, plotted as curve b), shows a minimum at a scaling factor of $f_2 = 3.91$. To test the dependency of the statistical error bars and the standard deviation simultaneously the figure of merit $c = (ab)^{1/2}$ was calculated and plotted as curve c). c is almost independent from the scaling factor, until $f_2 = 4$ after which c increases linearly with f . Application of a scaling factor of up to $f_2 = 4$ does not interfere with this new defined error. One also notices

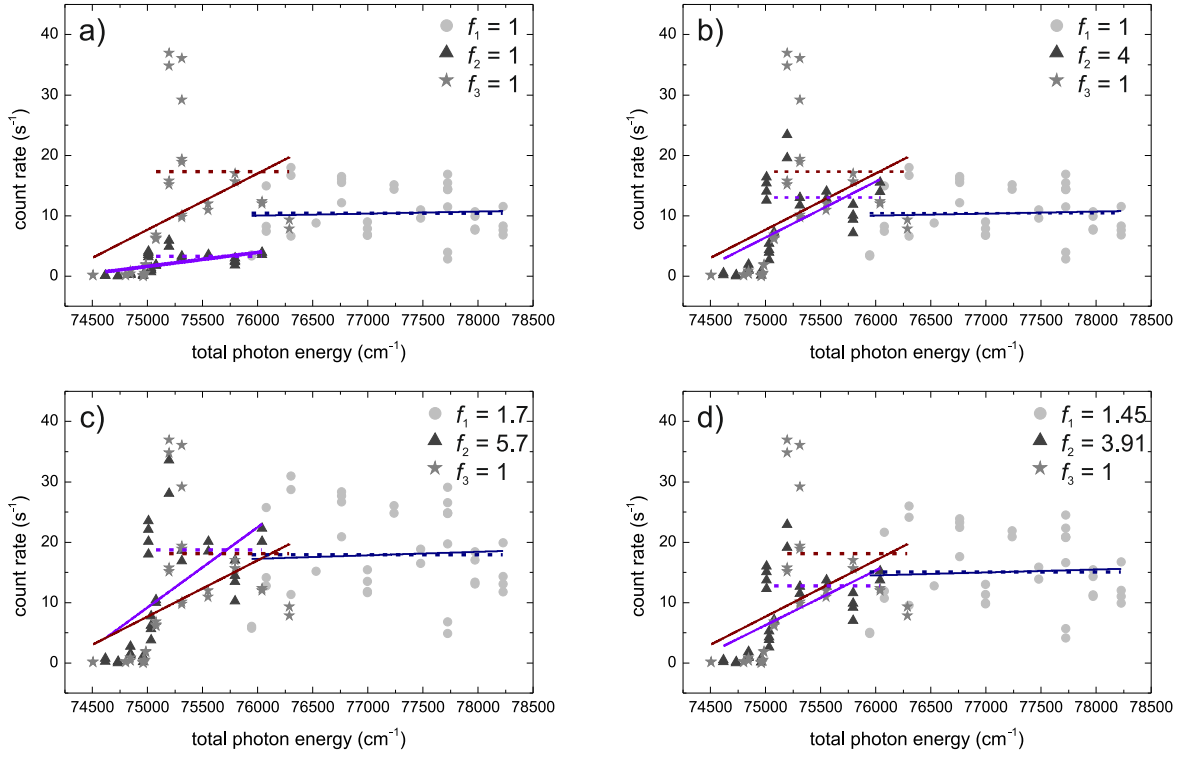


Figure B.1: Comparison of scaling methods. The solid lines are obtained from a linear fit to the whole data sub-set. The dashed lines indicate the average count-rate above 75100 cm⁻¹. a) Raw data. b) Slope method. c) Average method. d) Minimum average method. More details are given in the text.

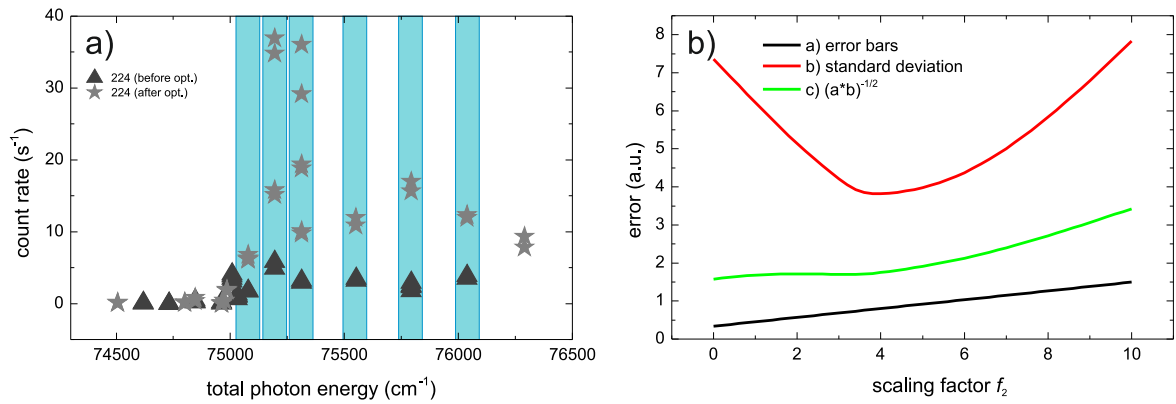


Figure B.2: Visualization of the minimum error method. a) The blue boxes indicate the six regions that were chosen for the minimum error method. b) The standard deviation and average error bars were plotted for different scaling factors f_2 .

that f_2 obtained with the minimum error method is almost identical to f_2 from the slope method. For the scaling factor f_1 for the 216 nm dataset, again two regions were found, in which similar total photon energies were applied. The factor $f_1 = 1.45$ minimizes the average distance between the three average values. The data using these scaling factors is shown in Fig. B.1 d).

Appendix C

Additional results from the threshold fit process

C.1 Fit results for the different scaling factors

Fig. C.1 shows a compilation of the fit output from the *Mathematica* fit program for different scaling factors. The algorithm worked in all cases, but for $f = \{0, 0, 1\}$ when only the data above the IP was taken into account.

Figure C.1: Fit results for different scaling factors

C.2 Fit results for other elements

The fitting algorithm was used for different datasets that were available for different elements. The data is credited to The working group LARISSA, University of Mainz. The datasets were recorded in a continuous scanning mode, therefore the amount of data points per data set is much greater than this for astatine. To have similar input for the fit algorithm, the data was chosen arbitrarily from the dataset. Table C.1 gives the fit results. The reference indicated is the work where the raw data was taken from. The fitted curves are shown in Fig. C.2. The maximum deviation of the threshold fit for the literature value was 59 cm^{-1} for uranium. The Fit error was estimated correctly from the program. This is attributed to the fact that only a small number of data points was used for the fit. In all other cases the fit represents the IP well, but the error is underestimated. As an additional investigation, for each fit the y-position at the determined IP on the fitted curve was calculated and divided by the A_2 fit parameter. This was defined as H.val. The H.val is to some extent dependent on the IP as illustrated in in Fig. C.3. This needs further investigation.

Table C.1: Fit results for the ionization threshold for different elements. Ionization potentials were taken from [SM05, MGR⁺10]

Element	IP _{lit} cm^{-1}	IP _{fit} cm^{-1}	fit error cm^{-1}	Δ IP cm^{-1}	H.val %	Points used	Reference
Ac	43398	43420	3	22	73	21500	[LARISSA]
Ga	48388	48390	4	2	86	1822	[LARISSA]
U	49957	50016	115	59	74	419	[Rae10]
Np	50536	50514	6	22	96	9848	[LARISSA]
Tc	57422	57383	4	39	99	11612	[MGR ⁺ 10]
Tc (Set 2)	57422	57378	5	44	100	2993	[MGR ⁺ 10]
Au	74409	74393	1	16	99	12834	[Mat10]
Au (Set 2)	74409	74375	2	34	100	17746	[Mat10]

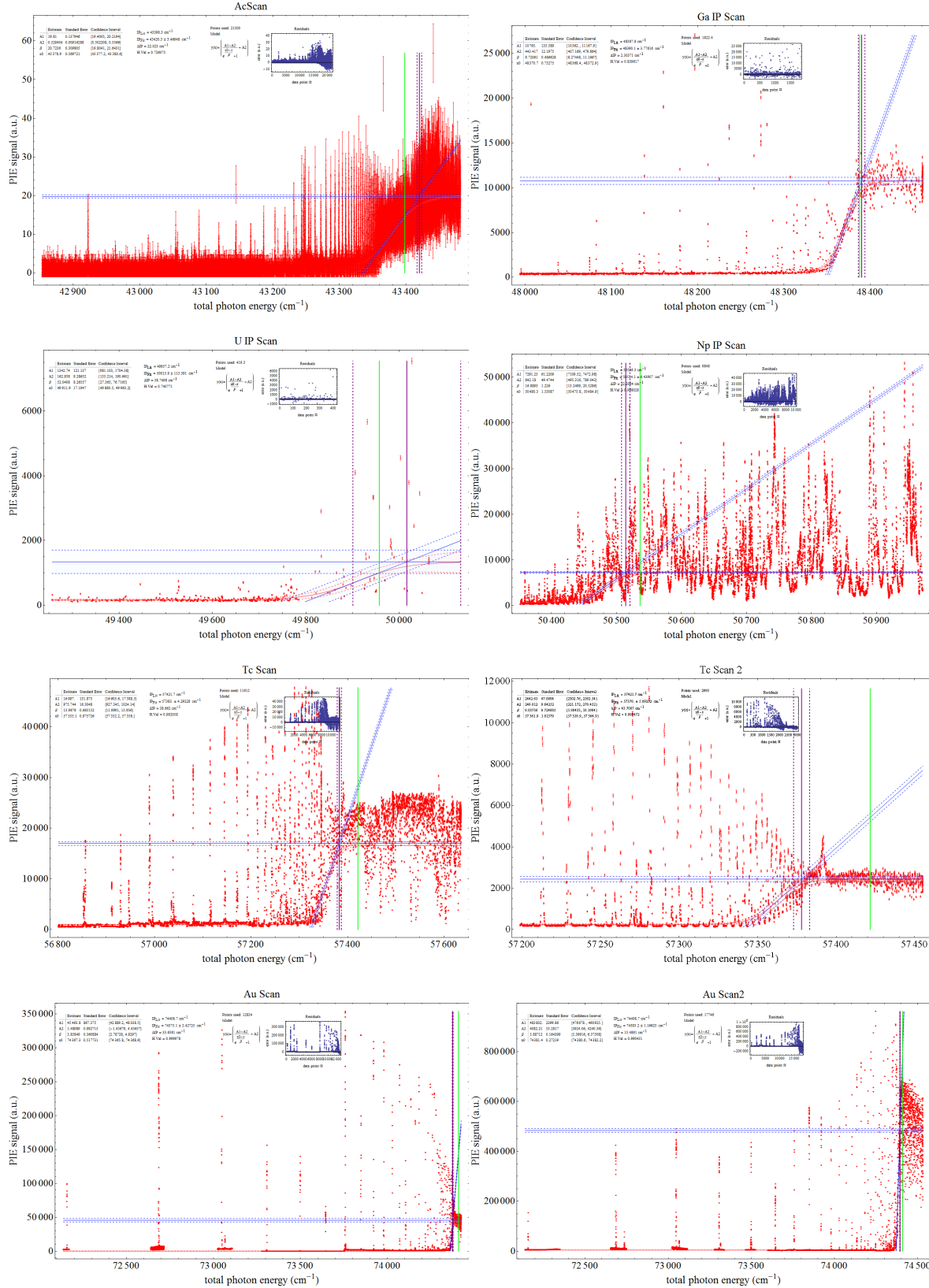


Figure C.2: Fit results of the threshold method for different elements.

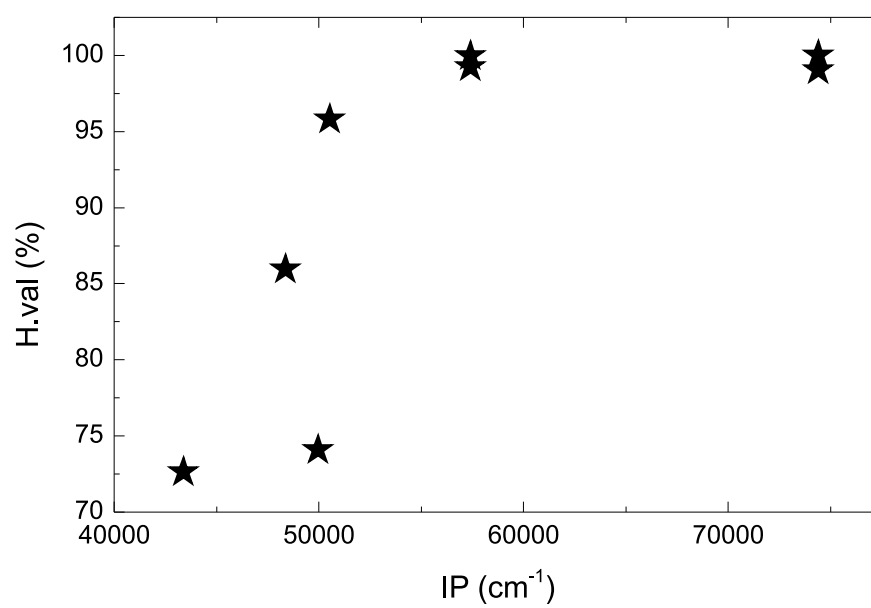


Figure C.3: Dependency of the H.val from the IP. (see text)

Appendix D

Laser scans of second excited states of astatine

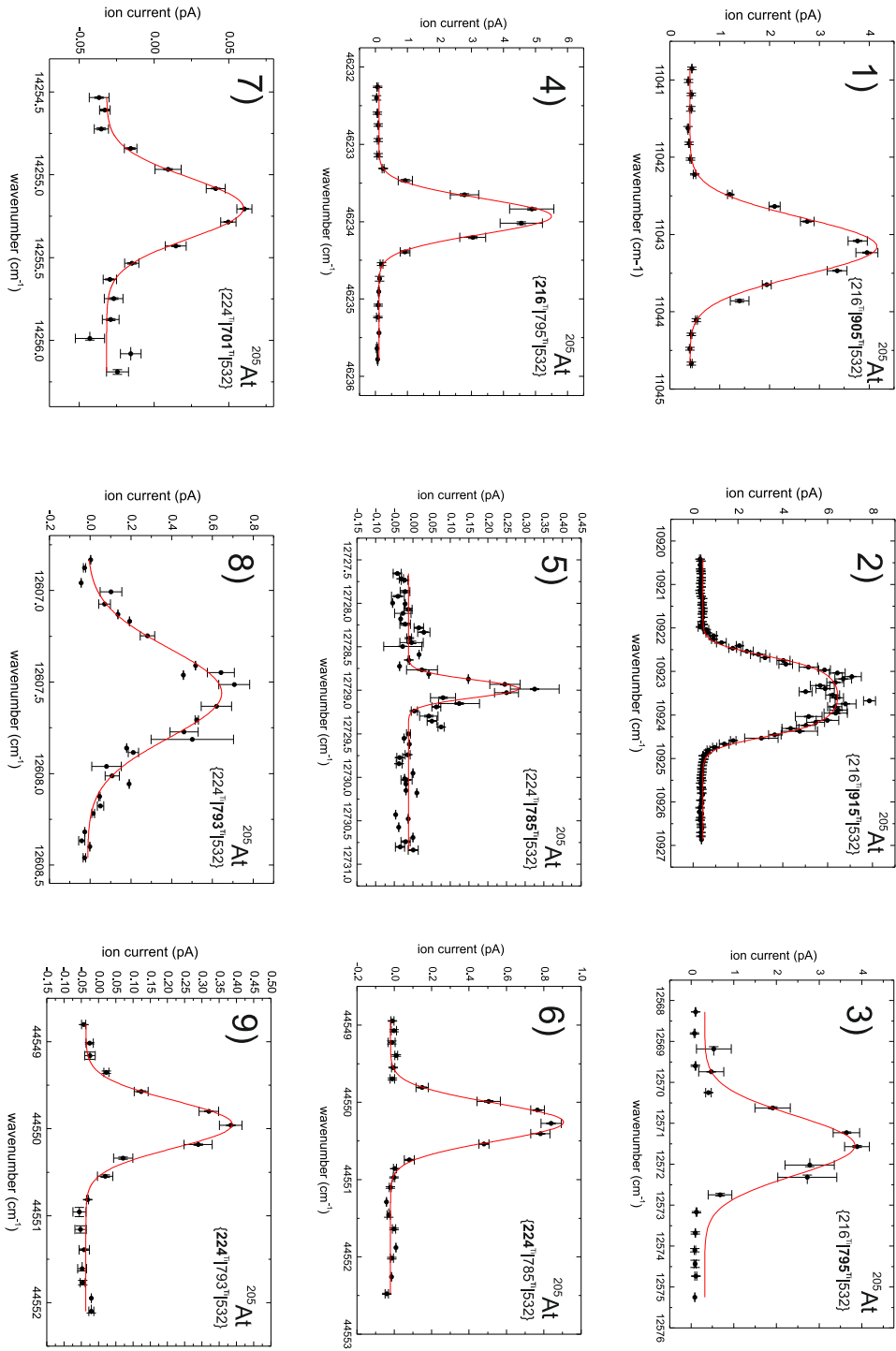


Figure D.1: Compilation 1 of astatine laser scans. Details are given in Table 10.4 and the text.

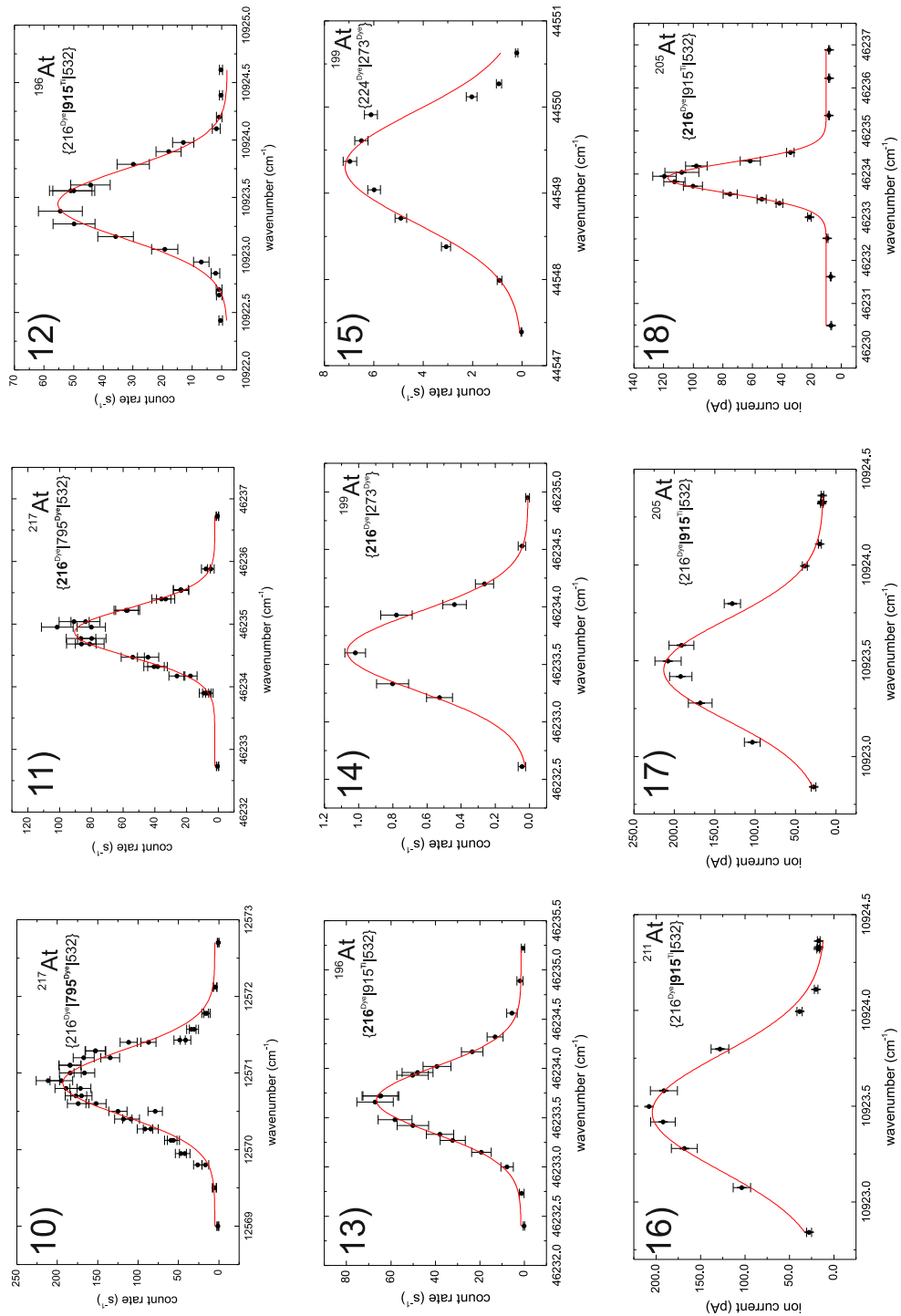


Figure D.2: Compilation 2 of astatine laser scans. Details are given in Table 10.4 and the text.

Appendix E

Targets and parameters used for astatine spectroscopy runs

Table E.1: Targets used for astatine spectroscopy runs

At isotope	1st	2nd	3rd	yield	p-current (μ)	where	Target	T#	time	Experiment
169	Ti:216	Ti:915	Yag:532	0.004 a/s		Windmill	HRS	UC447		
193	Ti:216	Ti:915	Yag:532	1.7 a/s		Windmill	HRS	ThO445	19.05.2011-07:03	IS466
194	Ti:216	Ti:915	Yag:532	4 a/s	1.7	Windmill	HRS	ThO445	19.05.2011-07:03	IS466
194	Ti:216	Ti:915	Yag:532	2.5 a/s		Windmill	HRS	UC453-W	26.07.2011-23:02	IS511
195	Ti:216	Ti:915	Yag:532	60 a/s		Windmill	HRS	ThO445	19.05.2011-07:03	IS466
196	Ti:216	Ti:915	Yag:532	220 a/s	1.7	Windmill	HRS	ThO445	19.05.2011-07:03	IS466
196	Ti:216	Ti:915	Yag:532	0.1 a/s	0.27	Windmill	HRS	UC453-W	26.07.2011-23:02	IS511
197	Dy:216	Dy:273.4		3.3 a/s	0.27	Windmill	HRS	HDUC440-W	12.11.2010-01:13	IS466
198	Dy:216	Dy:273.4			0.27	Windmill	HRS	HDUC440-W	12.11.2010-01:13	IS466
199	Dy:216	Dy:273.4		22 a/s	0.27	Windmill	HRS	ThO445	10.05.2011	IS466
199	Dy:224	Dy:273.4		3.3 a/s	0.1	Windmill	HRS	HDUC440-W	12.11.2010-01:13	IS466
199	Dy:224	Dy:273.4				Windmill	HRS	HDUC440-W	12.11.2010-04:51	IS466
200	Dy:216	Dy:273.4	-	33 a/s	0.27	Windmill	HRS	ThO445	12.11.2010-01:13	IS466
200	Dy:224	Dy:330		13 a/s	0.3	Windmill	HRS	HDUC440-W	12.11.2010-19:26	IS466
201	Dy:224	Dy:330		26.3 a/s	0.3	Windmill	HRS	ThO445	12.11.2010-19:26	IS466
202	Dy:216	Dy:273.4		11 a/s	0.27	Windmill	HRS	HDUC440-W	12.11.2010-04:30	IS466
202	Dy:224	Dy:330		7.33 a/s	0.3	Windmill	HRS	HDUC440-W	12.11.2010-19:26	IS466
204	Ti:216	Ti:915	Yag:532	108+-18pA	1.5	FC490, no slits	HRS	UC453-W	26.07.2011-14:29	IS466
204	Ti:216	Ti:795	Dy:Ryd	30pA	1.62	FC490	HRS	UC455-W	12.08.2011-20:50	IS466
205							HRS	UC457-Ta		
205							HRS	UC447		
205							HRS	ThO445		IS466
205	Ti:216	Dy:795	Yag:532	3-4 pA	1.5	HRS,FC490	HRS	ThO445	18.05.2011-13:28	IS466
205	Ti:216	Ti:915	Yag:532	0.4 pA	0.45	CAO,FC30	HRS	ThO445	18.05.2011-18:21	IS466
205	Ti:216	Ti:915	Yag:532	10pA	1.5	CAO,FC30	HRS	ThO445	19.05.2011-00:05	IS466
205	Ti:216	Ti:915	Yag:532	150pA	1.5	FC490, no slits	HRS	UC453-W	26.07.2011-16:08	IS511
205							HRS	UC457-Ta		
205							HRS	UC466		
217	Dy:216	Ti:795	Dy:Ryd	200pA	1.03	FC490, noslits	HRS	UC466	02.11.2011-03:08	IS466
218	Dy:216	Dy:795	Yag:532	190 a/s		Windmill	HRS	ThO445	19.05.2011-13:01	IS466
220							HRS	UC447		
222							HRS	UC447		

Appendix F

The PSB supercycle structure observed with the Faraday cup.

The section of the laser scan as shown in Fig. 10.16 (p.129) between 15600 cm^{-1} and 15900 cm^{-1} in which no resonances were observed, was analysed for the periodicity of the FC signal. Following function was applied to convert the time axis to the position in the super cycle.

$$n_{\text{SC}} = \frac{\text{Mod}(t, T_{\text{SC}})}{\Delta t_{\text{pulse}}} = \frac{\text{Mod}(t, 46.8\text{ s})}{1.2\text{ s}}$$

The so treated data were plot and are shown in Fig. F.1. The vertical breakdown of the ion current is explained by the switching of the extraction voltage to ground potential, while the proton pulse impinges on the target. The number of pulses per PSB supercycle was 39, of which 14 were sent onto the GPS target. These are visible as peaks in the plot, followed by a characteristic release curve. This curve is determined by the half-life and the release of the product from the target. In this case the time constant was about 2.2 s, determined from a fit single exponential curve to the pulse at position 27. The following pulse arrives at position 34. At this time most of the product was released already from the target and the peak ion current recorded is reduced.

For the second scan of the Rydberg series in astatine, the PSB operators were asked to give evenly distributed proton pulses over the supercycle. The resulting background ion current curve is shown in Fig. F.2. Two odd spaces for position 15 and 25 are visible, the peak intensities are all similar.

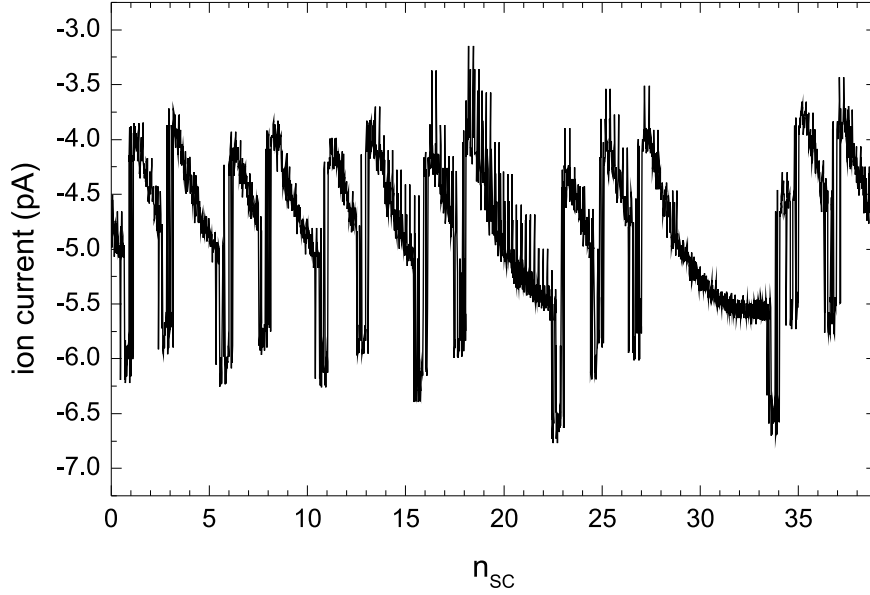


Figure F.1: Visualization of the structure of the PSB supercycle. The Faraday cup current is plotted against the position in the PSB supercycle. The positions have a spacing of 1.2 s. The proton pulses are visible as well as the release from the target.

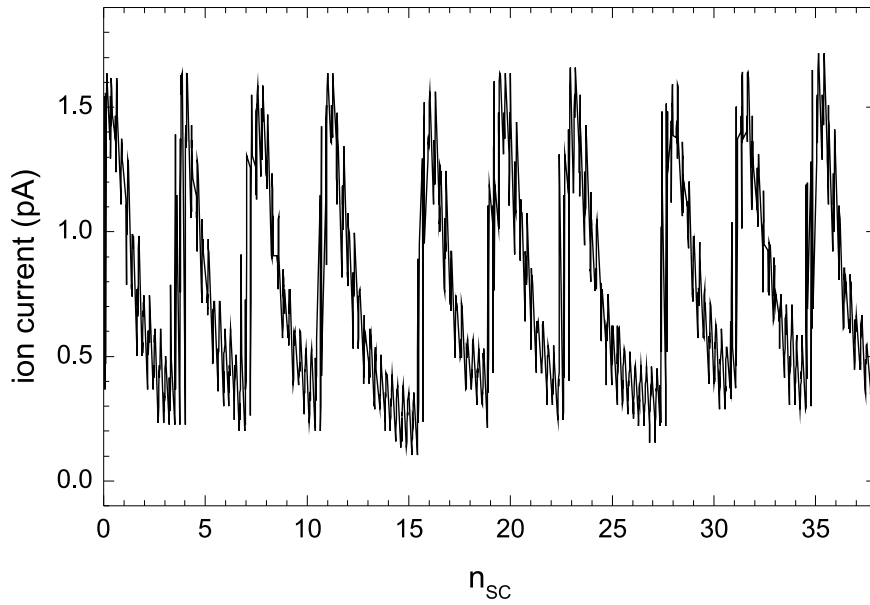


Figure F.2: Visualization of the PSB supercycle optimized for spectroscopy

Appendix G

Graphical analysis for other elements

Spectroscopic data on ^{197}Au that were obtained earlier [Mat10] were treated with the methods introduced in 10.3.3. At first the maximum-histogram method was used to determine the ionization potential of gold. Two data sets were available and the resulting max-histogram-plots (MaxH) are shown in Fig. G.1. The signal quality of the first measurement, shown in a) was not as good as in the second measurement b), resulting in a broader peak. The results of the Gaussian fit to the calculated MaxH spectrum and the Rydberg analysis performed in [Mat10] are compared in Tab. G.1. The errors given are only the statistical errors since the same datasets were used for the different analysis. While the MaxH result differs by 0.17 cm^{-1} for data set a) the results for data set b) match with a difference of 0.01 cm^{-1} within the errors. As already pointed out, the statistical error for the MaxH method depends strongly on the binning and is therefore underestimated.

Table G.1: Results of the MaxH fit and the conventional Rydberg analysis for gold

Data set	MaxH-Plot (cm^{-1})	FWHM (cm^{-1})	Rydberg analysis (cm^{-1})
a)	74409.44(3)	1.73(8)	74409.27(3) [Mat10]
b)	74409.00(1)	0.82(3)	74409.01(3) [Mat10]

The data set b) was converted to give the $\delta^* - n^*$ contour plot and the $\delta^* - E_{\text{set}}$ plot as shown in Fig. G.2. For the calculation, the central ionization limit was set to $E_{\text{set}} = 74409.0\text{ cm}^{-1}$. The observed series was assigned as an nf -series. The reported quantum defect was $\delta = 1.0$ this is also visible in the figures ($\delta^* = 0$).

The graphical method for visualization of Rydberg-spectra was applied for comparison also to data obtained for astatine (*dataset 2*), gallium and technetium. Data for other elements is credited to the Working group LARISSA. The plots are shown in Figs. G.2, G.3, G.4 and G.5.

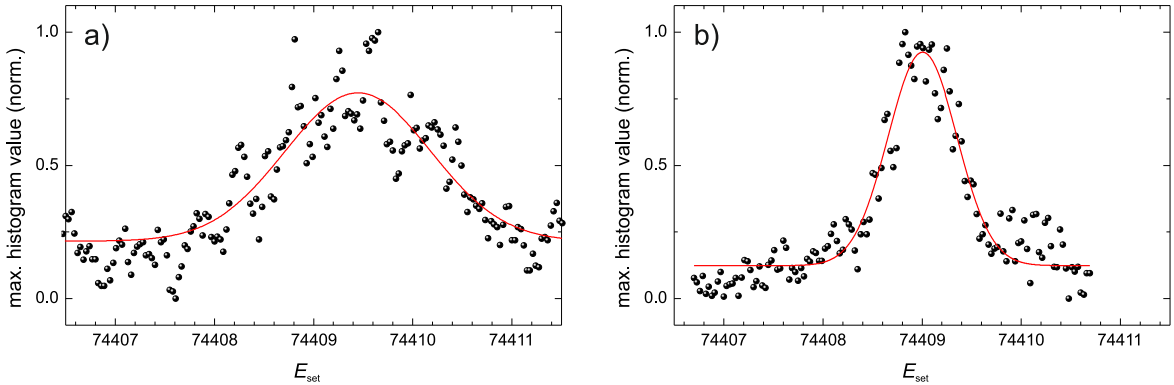


Figure G.1: Max histogram plots for gold data

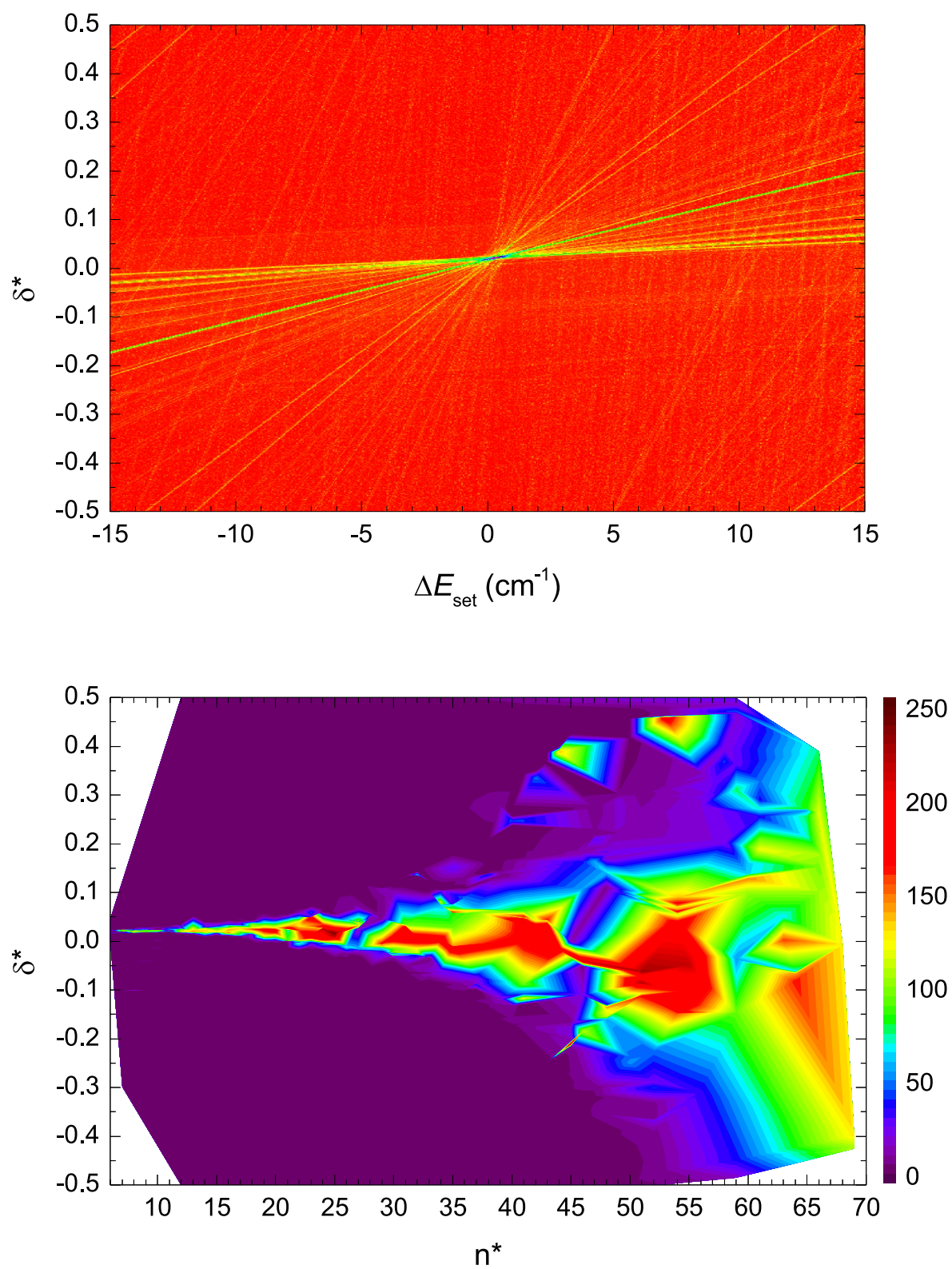
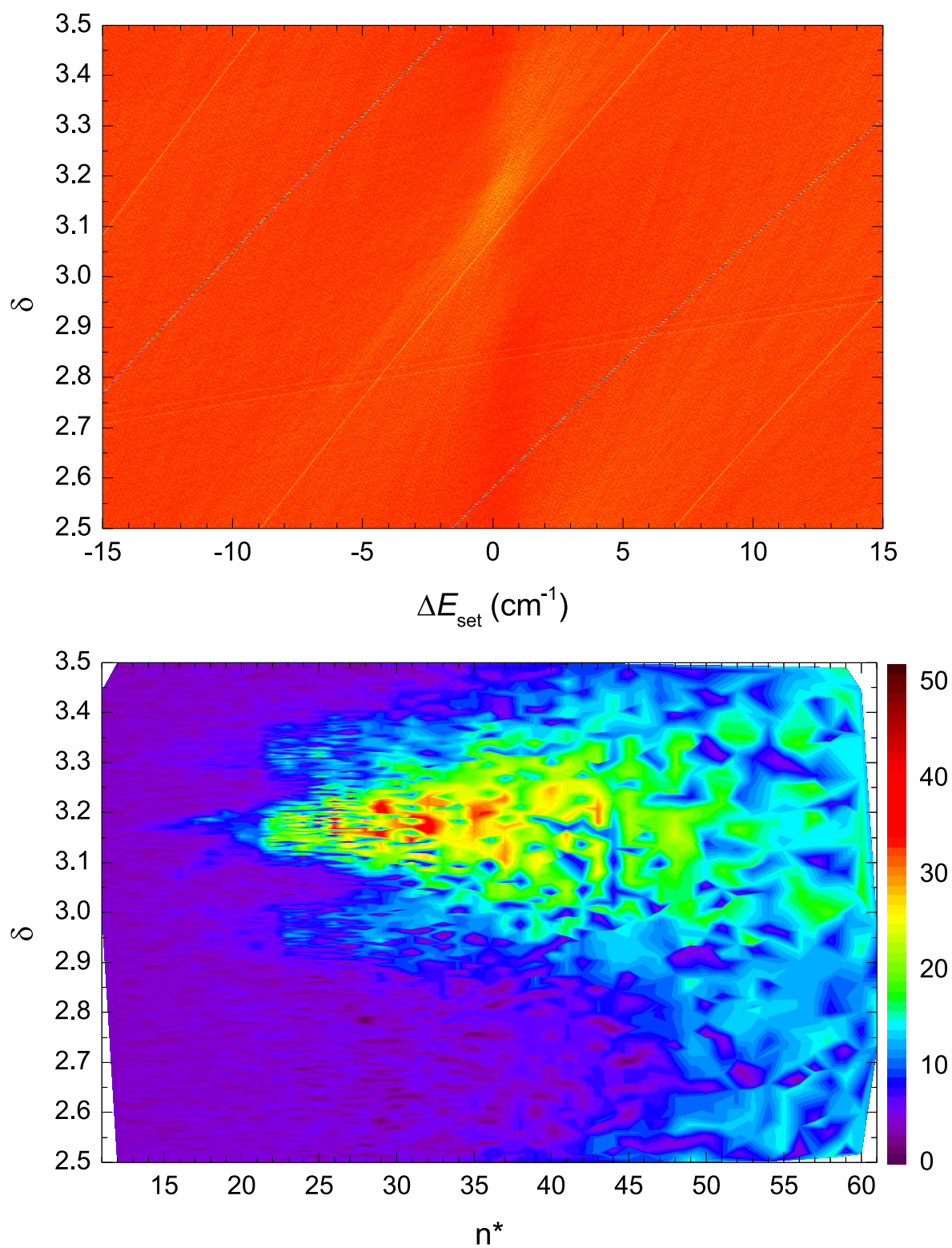


Figure G.2: Graphical visualization for gold.

Figure G.3: Graphical visualization for astatine *dataset 2*.

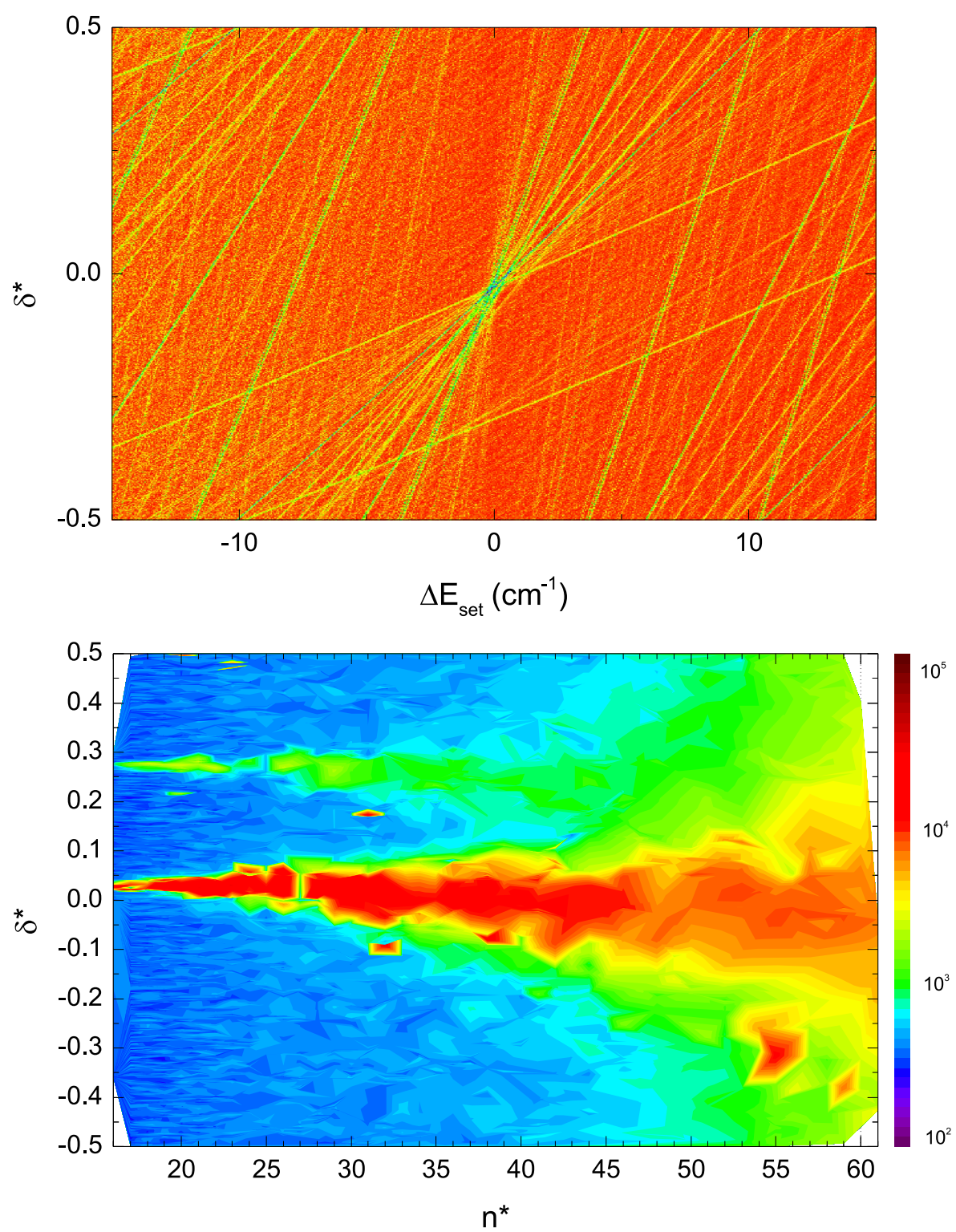


Figure G.4: Graphical visualization for gallium.

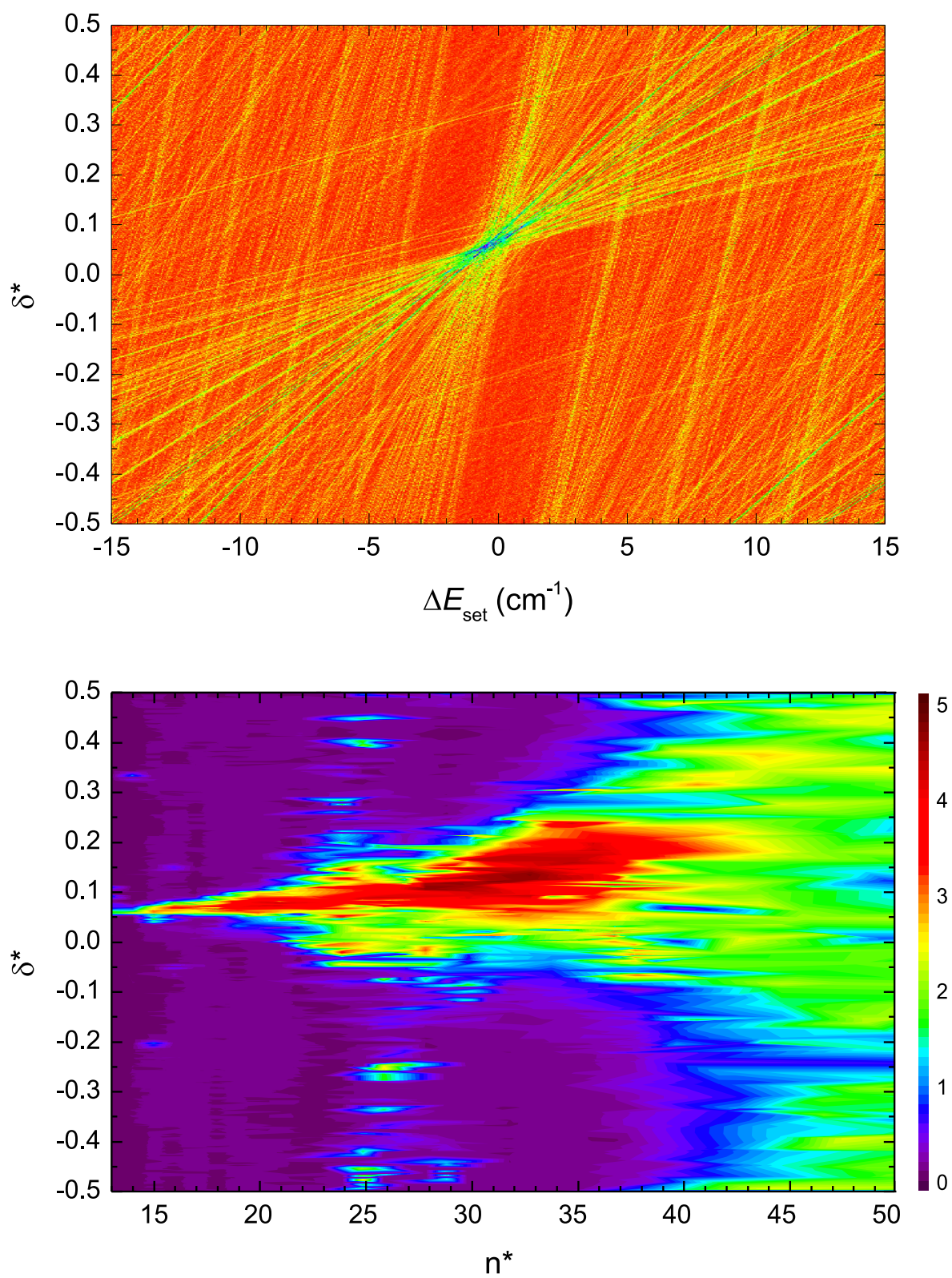


Figure G.5: Graphical visualization for technetium.

Appendix H

Tables of observed Rydberg resonances in astatine

Table H.1: Resonances observed in the Rydberg spectrum of astatine.

n	name	centroid (cm^{-1})	fit error (cm^{-1})	δ^*
12	δ	14917.26	0.03	0.23
12	ϵ	14914.47	0.00	0.24
12	ϵ	14901.66	0.03	0.28
12	ϕ	14951.25	0.01	0.13
12	η	14857.55	0.11	0.41
13	α	14997.11	0.02	0.98
13	β	15005.35	0.04	0.95
13	χ	15167.54	0.01	0.35
13	δ	15192.31	0.01	0.24
13	ϵ	15182.42	0.01	0.29
13	ϕ	15211.44	0.01	0.16
13	η	15148.13	0.02	0.43
14	α	15249.43	0.01	0.99
14	β	15258.79	0.01	0.95
14	χ	15374.95	0.01	0.37
14	δ	15394.51	0.00	0.26
14	ϵ	15388.87	0.01	0.29
14	ϕ	15410.42	0.00	0.17
14	η	15359.52	0.01	0.45
15	α	15439.20	0.01	1.00
15	β	15446.52	0.01	0.95
15	χ	15533.72	0.01	0.37

Continued on next page

n	name	centroid (cm^{-1})	fit error (cm^{-1})	δ^*
15	δ	15547.65	0.01	0.27
15	ϵ	15545.03	0.01	0.29
15	ϕ	15561.59	0.00	0.17
15	η	15517.05	0.01	0.49
16	α	15583.88	0.01	1.00
16	β	15589.45	0.01	0.95
16	χ	15656.85	0.02	0.38
16	ϵ	15666.18	0.00	0.29
16	ϕ	15678.85	0.00	0.17
16	η	15635.72	0.02	0.57
17	α	15696.45	0.01	1.00
17	β	15700.67	0.01	0.95
17	χ	15754.05	0.02	0.38
17	δ	15760.48	0.01	0.30
17	ϵ	15761.34	0.01	0.29
17	ϕ	15771.75	0.00	0.17
17	η	15726.47	0.02	0.68
18	α	15785.83	0.01	1.00
18	β	15788.73	0.01	0.96
18	χ	15832.08	0.04	0.38
18	δ	15836.50	0.01	0.32
18	ϵ	15838.03	0.01	0.29
18	ϕ	15846.39	0.00	0.17
18	η	15799.47	0.04	0.82
19	α	15857.86	0.01	1.00
19	β	15858.83	0.01	0.98
19	β	15914.95	0.01	0.03
19	χ	15895.62	0.04	0.38
19	δ	15898.85	0.01	0.32
19	ϵ	15900.48	0.01	0.30
19	ϕ	15907.47	0.00	0.17
19	η	15863.47	0.03	0.91
20	α	15916.89	0.01	1.00
20	β	15962.61	0.01	0.07
20	χ	15948.08	0.04	0.38
20	δ	15950.47	0.01	0.33
20	ϵ	15952.11	0.01	0.30

Continued on next page

n	name	centroid (cm ⁻¹)	fit error (cm ⁻¹)	δ^*
20	ϕ	15957.97	0.00	0.17
20	η	15920.27	0.01	0.93
21	α	15965.85	0.01	1.00
21	β	16003.17	0.01	0.09
21	χ	15991.90	0.04	0.38
21	δ	15993.72	0.01	0.34
21	ϵ	15995.34	0.01	0.30
21	ϕ	16000.21	0.00	0.17
21	η	15968.37	0.01	0.94
22	α	16006.83	0.01	1.00
22	β	16037.87	0.01	0.11
22	χ	16028.79	0.06	0.38
22	δ	16030.22	0.01	0.34
22	ϵ	16031.74	0.01	0.30
22	ϕ	16035.90	0.01	0.17
22	η	16008.92	0.01	0.94
23	α	16041.55	0.02	1.00
23	β	16067.68	0.01	0.12
23	χ	16060.22	0.08	0.38
23	δ	16061.44	0.01	0.34
23	ϵ	16062.77	0.01	0.30
23	ϕ	16066.28	0.01	0.17
23	η	16043.26	0.01	0.94
24	α	16071.15	0.02	1.00
24	β	16093.44	0.01	0.13
24	χ	16087.20	0.07	0.39
24	δ	16088.20	0.02	0.35
24	ϵ	16089.39	0.01	0.30
24	ϕ	16092.41	0.00	0.17
24	η	16072.63	0.01	0.94
25	α	16096.67	0.02	1.00
25	β	16115.86	0.01	0.14
25	χ	16110.53	0.06	0.39
25	δ	16111.35	0.01	0.35
25	ϵ	16112.45	0.01	0.30
25	ϕ	16115.08	0.00	0.17
25	η	16097.91	0.01	0.94

Continued on next page

n	name	centroid (cm^{-1})	fit error (cm^{-1})	δ^*
26	α	16118.74	0.01	1.00
26	β	16135.44	0.01	0.14
26	χ	16130.89	0.06	0.38
26	δ	16131.60	0.02	0.35
26	ϵ	16132.53	0.01	0.30
26	ϕ	16134.81	0.00	0.17
26	η	16119.83	0.01	0.94
27	α	16137.99	0.02	1.00
27	β	16152.67	0.01	0.14
27	β	16152.61	0.01	0.14
27	χ	16148.58	0.08	0.39
27	χ	16148.53	0.09	0.39
27	δ	16149.21	0.02	0.35
27	δ	16149.23	0.02	0.35
27	ϵ	16150.12	0.01	0.30
27	ϵ	16150.10	0.01	0.30
27	ϕ	16152.10	0.01	0.18
27	ϕ	16152.19	0.00	0.17
27	η	16138.96	0.01	0.95
28	α	16154.95	0.02	1.00
28	α	16154.96	0.02	1.00
28	β	16167.77	0.01	0.15
28	β	16167.82	0.01	0.14
28	χ	16164.45	0.18	0.38
28	χ	16164.20	0.09	0.39
28	δ	16164.88	0.05	0.35
28	δ	16164.83	0.01	0.35
28	ϵ	16165.56	0.02	0.30
28	ϵ	16165.56	0.01	0.30
28	ϕ	16167.35	0.01	0.18
28	ϕ	16167.36	0.00	0.17
28	η	16155.83	0.01	0.94
28	η	16155.80	0.01	0.94
29	α	16169.87	0.03	1.00
29	α	16169.85	0.01	1.00
29	β	16181.25	0.01	0.15
29	χ	16178.14	0.12	0.39

Continued on next page

n	name	centroid (cm ⁻¹)	fit error (cm ⁻¹)	δ^*
29	δ	16178.61	0.03	0.35
29	ϵ	16179.32	0.01	0.30
29	ϕ	16180.87	0.01	0.18
29	η	16170.62	0.01	0.94
29	η	16170.61	0.02	0.94
30	α	16183.09	0.01	1.00
30	β	16193.29	0.02	0.14
30	χ	16190.40	0.19	0.39
30	δ	16190.91	0.05	0.35
30	ϵ	16191.52	0.02	0.30
30	ϕ	16192.91	0.01	0.18
30	η	16183.76	0.01	0.95
31	α	16194.88	0.03	0.00
31	β	16204.01	0.01	0.14
31	δ	16201.73	0.02	0.37
31	ϵ	16202.31	0.02	0.31
31	ϵ	16202.67	0.03	0.27
31	ϕ	16203.64	0.01	0.18
31	η	16195.51	0.02	0.94
32	α	16205.45	0.02	0.00
32	α	16214.90	0.03	0.00
32	β	16213.58	0.01	0.15
32	δ	16211.59	0.04	0.37
32	ϵ	16211.99	0.07	0.32
32	ϵ	16212.34	0.02	0.28
32	ϕ	16213.28	0.01	0.18
32	η	16206.00	0.01	0.94
33	ϵ	16220.92	0.02	0.31
33	ϕ	16222.12	0.00	0.17
33	η	16215.40	0.01	0.95
34	ϵ	16228.91	0.01	0.31
34	ϕ	16229.96	0.00	0.17
34	η	16223.87	0.02	0.95
35	ϵ	16236.06	0.02	0.32
35	ϕ	16237.11	0.01	0.17
35	η	16231.47	0.02	0.97
36	ϵ	16242.63	0.02	0.33

Continued on next page

n	name	centroid (cm^{-1})	fit error (cm^{-1})	δ^*
36	ϕ	16243.65	0.00	0.16
36	η	16238.52	0.02	0.96
37	ϵ	16248.63	0.02	0.33
37	ϕ	16249.49	0.00	0.18
37	η	16244.86	0.02	0.97
38	ϵ	16254.16	0.02	0.32
38	ϕ	16254.98	0.01	0.17
38	η	16250.59	0.02	0.98
39	ϵ	16259.13	0.04	0.34
39	ϕ	16259.95	0.01	0.17
39	η	16256.01	0.02	0.97
40	ϵ	16263.78	0.02	0.34
40	ϕ	16264.44	0.01	0.19
40	η	16260.83	0.03	0.98
41	ϵ	16268.06	0.02	0.34
41	ϕ	16268.72	0.00	0.17
41	η	16265.32	0.02	0.99
42	ϵ	16271.97	0.01	0.35
42	ϕ	16272.60	0.00	0.18
42	η	16269.49	0.02	0.98
43	ϵ	16275.62	0.03	0.35
43	ϕ	16276.23	0.01	0.18
43	η	16273.36	0.01	0.98
44	ϵ	16279.11	0.04	0.32
44	ϕ	16279.63	0.01	0.16
44	η	16276.88	0.02	0.99
45	ϕ	16282.67	0.01	0.18
45	η	16280.18	0.04	0.99
46	ϕ	16285.57	0.01	0.18
47	ϕ	16288.27	0.01	0.18
48	ϕ	16290.83	0.01	0.17
49	ϕ	16293.20	0.02	0.16
50	ϕ	16295.36	0.02	0.18
51	ϕ	16297.43	0.02	0.18
52	ϕ	16299.43	0.02	0.15
53	ϕ	16301.26	0.02	0.15
54	ϕ	16302.93	0.02	0.18

Continued on next page

n	name	centroid (cm ⁻¹)	fit error (cm ⁻¹)	δ^*
55	ϕ	16304.57	0.02	0.17
56	ϕ	16306.13	0.02	0.15
57	ϕ	16307.59	0.02	0.14
58	ϕ	16308.87	0.02	0.21
59	ϕ	16310.16	0.03	0.21
60	ϕ	16311.41	0.02	0.20
61	ϕ	16312.68	0.03	0.11
62	ϕ	16313.70	0.04	0.18
63	ϕ	16314.71	0.03	0.22
64	ϕ	16315.79	0.04	0.15
65	ϕ	16316.77	0.04	0.11
67	ϕ	16317.77	0.04	1.00
68	ϕ	16318.77	0.04	0.83
69	ϕ	16319.85	0.03	0.49

Appendix I

Hyperfine structure of ^{205}At

During the on-line RILIS operation for the ISOLDE experiment IS534 (“Beta-delayed fission, laser spectroscopy and shape-coexistence studies with radioactive At beams”) the second step transition at 795 nm was provided by the Ti:Sa laser. As described in Section 6.2.1 the Ti:Sa laser was operated in narrow-band mode and manually scanned across the resonance. The two etalons were the standard 0.3 mm fused silica with a $R \approx 40\%$ coating on both sides and the ‘thick’ 6.35 mm optically polished YAG substrate¹. A dedicated *LabVIEW* program was used to record and average the Faraday cup current of YGPS.FC558 as a function of the laser wavelength over 10 subsequent proton pulses hitting the ISOLDE target. The mode structure of the Ti:Sa laser was observed in a 4 GHz scanning Fabry-Perot interferometer (FPI) and with the *WS7* wavemeter in fine mode and enabled line-width measurement. The line-width measured by the *WS7* was $0.02(1) \text{ cm}^{-1}$ corresponding to 0.6 GHz. A rather similar line-width of about 0.8 GHz was obtained from the analysis of the fringe pattern in the FPI. For each laser frequency, the thick etalon was tilted and the mode structure was checked both in the FPI and the *WS7*. If a multi-mode operation of the laser was observed, the thin etalon was tilted slightly to return to single-mode operation, then a measurement was started. The result of the scan is shown in figure I.1.

Although the GPS mass separator was set to ^{205}At , the neighbouring isotopes $^{204,206}\text{At}$ were not fully suppressed by the GPS dipole magnet, as reported by the users from their data of the α -decay spectroscopy setup at LA1. Therefore no attempt was made to further analyse the spectrum. This measurement will be repeated in a dedicated in-source spectroscopy campaign for IS534, scheduled for October 2012.

¹Purchased from LAYERTEC

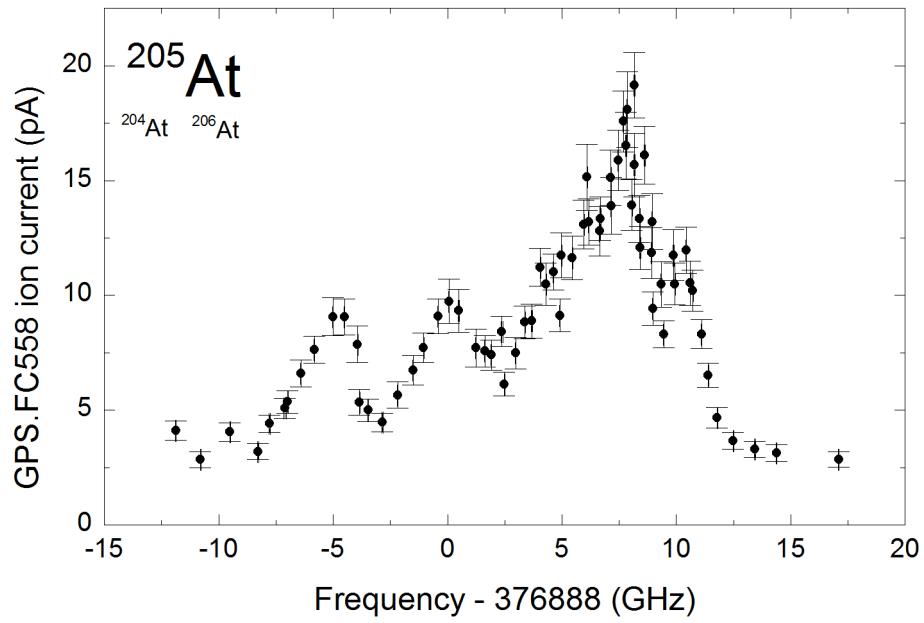


Figure I.1: Hyperfine structure of ^{205}At measured with the Ti:Sa laser in narrow-band mode.

References

- [AAB⁺10] A. Andreyev, S. Antalic, L. Berg, T. Cocolios, V. Fedosseev, T. Gottwald, M. Huyse, Y. Kudryavtsev, U. Köster, W. Kurcewicz, J. Lassen, H. Mach, B. Marsh, R. Page, D. Pauwels, S. Raeder, S. Rothe, A. Sjödin, T. Stora, P. Van Duppen and K. Wendt. *Letter of Intent to the ISOLDE and N-ToF Experiments Committee (INTC): Development of astatine ion beams with RILIS*. Tech. rep., CERN (2010).
URL <http://cdsweb.cern.ch/record/1232260>
- [AAB⁺12] A. Andreyev, S. Antalic, A. Barzakh, R. Chapman, T. E. Cocolios, X. Derkx, H. D. Witte, J. Elseviers, D. Fedorov, L. Ghys, M. Huyse, Z. Kalaninova, U. Köster, J. Lane, V. Liberati, P. Molkanov, K. Nishio, D. Pauwels, L. Popescu, R. Page, D. Radulov, E. Rapisarda, K. Sandhu, M. Seliverstov, J. F. Smith, K. Spohr, I. Tsekhanovich, V. Truesdale, P. Van, D. Bergh, C. V. Beveren, P. Van Duppen, M. Veselský, S. Fritzsche, K. Wendt, S. Raeder, V. Fedosseev, B. Marsh and S. Rothe. *A Proposal on “Beta-delayed fission, laser spectroscopy and shape-coexistence studies with radioactive At beams”*. Tech. rep., CERN, Geneva (2012).
URL <http://cdsweb.cern.ch/record/1410652/files/INTC-P-319.pdf>
- [ABB⁺91] G. Alkhazov, L. Batist, A. Bykov, V. Vitman, V. Letokhov, V. Mishin, V. Panteleyev, S. Sekatsky and V. Fedoseyev. , *Application of a high efficiency selective laser ion source at the IRIS facility*. Nuclear Instruments and Methods in Physics Research Section A: Accelerators, Spectrometers, Detectors and Associated Equipment 306 (1-2):400–402 (1991).
- [ABD⁺92] G. Alkhazov, A. Barzakh, V. Denisov, K. Mezilev, Y. Novikov, V. Panteleyev, A. Popov, E. Sudentas, V. Letokhov, V. Mishin, V. Fedoseyev, S. Andreyev, D. Vedeneyev and A. Zyuzikov. , *A new highly efficient method of atomic spectroscopy for nuclides far from stability*. Nuclear Instruments and Methods in Physics Research Section B: Beam Interactions with Materials and Atoms 69 (4):517–520 (1992).
- [AEH⁺10] A. Andreyev, J. Elseviers, M. Huyse, P. Van Duppen, S. Antalic, A. Barzakh, N. Bree, T. Cocolios, V. Comas, J. Diriken, D. Fedorov, V. Fedosseev, S. Franchoo,

- J. Heredia, O. Ivanov, U. Köster, B. Marsh, K. Nishio, R. Page, N. Patronis, M. Seliverstov, I. Tsekhanovich, P. Van den Bergh, J. Van De Walle, M. Venhart, S. Vermote, M. Veselsky, C. Wagemans, T. Ichikawa, A. Iwamoto, P. Möller and A. Sierk. , *New Type of Asymmetric Fission in Proton-Rich Nuclei*. Phys. Rev. Lett. 105 (25):1–5 (2010).
- [AL72] R. V. Ambartsumian and V. S. Letokhov. , *Selective Two-Step (STS) Photoionization of Atoms and Photodissociation of Molecules by Laser Radiation*. Applied Optics 11 (2):354 (1972).
- [And59] E. Anders. , *Technetium and Astatine Chemistry*. Annual Review of Nuclear Science 9 (1):203–220 (1959).
- [ASH86] P. Albers, E. Stark and G. Huber. , *Continuous-wave laser operation and quantum efficiency of titanium-doped sapphire*. Journal of the Optical Society of America B 3 (1):134 (1986).
- [Asi53] I. Asimov. , *The natural occurrence of short-lived radioisotopes*. Journal of Chemical Education 30 (12):616 (1953).
- [AW12] A. D. McNaught and A. Wilkinson. *IUPAC Compendium of Chemical Terminology - Gold Book*. IUPAC, Research Triangle Park, NC, 2.3.1 edn. (2012). ISBN 0-9678550-9-8.
URL <http://dx.doi.org/10.1351/goldbook>
- [Bar11] A. Barzakh. Private communication (2011).
- [BBB⁺11] M. L. Bissell, K. Blaum, I. Budincevic, N. Frömmgen, R. G. Ruiz, C. Geppert, M. Hammen, M. Kowalska, K. Kreim, P. Lievens, R. Neugart, G. Neyens, W. Nörtershäuser, J. Papuga, M. Rajabali and D. T. Yordanov. *Proposal to the ISOLDE and Neutron Time-of-Flight Committee: Spins, Moments and Charge Radii Beyond ⁴⁸Ca*. Tech. rep., CERN (2011).
URL <http://cdsweb.cern.ch/record/1387985/files/INTC-P-313.pdf>
- [BBG81] J. Berkowitz, C. Batson and G. Goodman. , *Photoionization of atomic iodine and atomic tellurium*. Physical Review A 24 (1) (1981).
- [BHH⁺86] T. Bjørnstad, E. Hagebø, P. Hoff, O. C. Jonsson, E. Kugler, H. L. Ravn, S. Sundell, B. Vosicki and t. I. Collaboration. , *Methods for Production of Intense Beams of Unstable Nuclei: New Developments at ISOLDE*. Physica Scripta 34 (6A):578–590 (1986).

- [BMN⁺81] W. Bloomer, W. McLaughlin, R. Neirinckx, S. Adelstein, P. Gordon, T. Ruth and A. Wolf. , *Astatine-211-tellurium radiocolloid cures experimental malignant ascites*. Science 212 (4492):340–341 (1981).
- [Boy68] G. D. Boyd. , *Parametric Interaction of Focused Gaussian Light Beams*. Journal of Applied Physics 39 (8):3597 (1968).
- [Bro86] I. Brown. , *Astatine-211: Its possible applications in cancer therapy*. International Journal of Radiation Applications and Instrumentation. Part A. Applied Radiation and Isotopes 37 (8):789–798 (1986).
- [Bro87] I. Brown. , *Astatine: its organonuclear chemistry and biomedical applications*. Advances in Inorganic Chemistry 31:43 – 88 (1987).
- [BV92] K. Berei and L. Vasaros. *Bibliography of astatine chemistry and biomedical applications* (1992).
- [CDS⁺11] T. Cocolios, W. Dexters, M. Seliverstov, A. Andreyev, S. Antalic, A. Barzakh, B. Bastin, J. Büscher, I. Darby, D. Fedorov, V. Fedosseyev, K. Flanagan, S. Franchoo, S. Fritzsche, G. Huber, M. Huyse, M. Keupers, U. Köster, Y. Kudryavtsev, E. Mané, B. Marsh, P. Molkanov, R. Page, A. Sjoedin, I. Stefan, J. Van de Walle, P. Van Duppen, M. Venhart, S. Zemlyanoy, M. Bender and P.-H. Heenen. , *Early Onset of Ground State Deformation in Neutron Deficient Polonium Isotopes*. Physical Review Letters 106 (5):1–4 (2011).
- [CF10] B. Cheal and K. T. Flanagan. , *Progress in laser spectroscopy at radioactive ion beam facilities*. Journal of Physics G: Nuclear and Particle Physics 37 (11):113101 (2010).
- [CG78] W. Cooke and T. Gallagher. , *Dependence of Rydberg-state field-ionization thresholds on $|m_l|$* . Physical Review A 17 (3):1226–1228 (1978).
- [CLD10] Z. Chang, J. Li and C. Dong. , *Ionization potentials, electron affinities, resonance excitation energies, oscillator strengths, and ionic radii of element Uus ($Z = 117$) and astatine*. The journal of physical chemistry. A 114 (51):13388–94 (2010).
- [CMF⁺08] T. E. Cocolios, B. A. Marsh, V. N. Fedosseev, S. Franchoo, G. Huber, M. Huyse, A. M. Ionan, K. Johnston, U. Köster, Y. Kudryavtsev, M. Seliverstov, E. Noah, T. Stora and P. Van Duppen. , *Resonant laser ionization of polonium at rillisolde for the study of ground- and isomer-state properties*. Nuclear Instruments and Methods in Physics Research Section B: Beam Interactions with Materials and Atoms 266 (19-20):4403–4406 (2008).

- [CMS40] D. Corson, K. MacKenzie and E. Segrè. , *Artificially Radioactive Element 85*. Physical Review 58 (8):672–678 (1940).
- [CMS47] D. R. CORSON, K. R. MACKENZIE and E. SEGRÈ. , *Astatine: The Element of Atomic Number 85*. Nature 159 (4027):24–24 (1947).
- [Con26] E. Condon. , *A Theory of Intensity Distribution in Band Systems*. Physical Review 28 (6):1182–1201 (1926).
- [CSSG⁺11] J. Champion, M. Seydou, A. Sabatié-Gogova, E. Renault, G. Montavon and N. Galland. , *Assessment of an effective quasirelativistic methodology designed to study astatine chemistry in aqueous solution*. Physical chemistry chemical physics : PCCP 13 (33):14984–92 (2011).
- [Dem07] W. Demtröder. *Laserspektroskopie*. Springer-Verlag, Heidelberg (2007).
- [Dem08] W. Demtröder. *Laser Spectroscopy*, vol. 2. Springer Berlin Heidelberg, Berlin, Heidelberg (2008). ISBN 978-3-540-74952-3.
URL <http://dx.doi.org/10.1007/978-3-540-74954-7>
- [Dem10] W. Demtröder. *Atoms, Molecules and Photons*. Graduate Texts in Physics. Springer Berlin Heidelberg, Berlin, Heidelberg (2010). ISBN 978-3-642-10297-4.
URL <http://dx.doi.org/10.1007/978-3-642-10298-1>
- [Dre68] M. J. Dresser. , *The Saha-Langmuir Equation and its Application*. Journal of Applied Physics 39 (1):338 (1968).
- [DS91] G. Drake and R. Swainson. , *Quantum defects and the $1/n$ dependence of Rydberg energies: Second-order polarization effects*. Physical Review A 44 (9):5448–5459 (1991).
- [EDK88] J. Eggleston, L. DeShazer and K. Kangas. , *Characteristics and kinetics of laser-pumped Ti:sapphire oscillators*. IEEE Journal of Quantum Electronics 24 (6):1009–1015 (1988).
- [FBF⁺12] V. N. Fedosseev, L.-E. Berg, D. V. Fedorov, D. Fink, O. J. Launila, R. Losito, B. a. Marsh, R. E. Rossel, S. Rothe, M. D. Seliverstov, a. M. Sjödin and K. D. a. Wendt. , *Upgrade of the resonance ionization laser ion source at ISOLDE on-line isotope separation facility: new lasers and new ion beams*. The Review of scientific instruments 83 (2):02A903 (2012).
- [FBL⁺08] V. Fedosseev, L.-E. Berg, N. Lebas, O. Launila, M. Lindroos, R. Losito, B. Marsh, F. Österdahl, T. Pauchard, G. Tranströmer and J. Vannesjö. , *ISOLDE RILIS: New beams, new facilities*. Nuclear Instruments and Methods in Physics Research

- Section B: Beam Interactions with Materials and Atoms 266 (19-20):4378–4382 (2008).
- [FD26] J. Franck and E. G. Dymond. , *Elementary processes of photochemical reactions*. Trans. Faraday Soc. 21:536–542 (1926).
- [FFF⁺12] V. Fedosseev, D. Fedorov, D. Fink, N. Imai, B. Marsh, R. Rossel, S. Rothe, M. Seliverstov, A. Sjödin and K. Wendt. *New development stage of the laser ion source at the ISOLDE on-line isotope separation facility: Dual dye - Ti:Sa RILIS*. submitted (2012).
- [FH55] W. Finkelburg and W. Humbach. , *Ionisierungsenergien von Atomen und Atomionen*. Die Naturwissenschaften 42 (2):35–37 (1955).
- [Fin] D. Fink. *Improving the selectivity and efficiency of the laser ion source RILIS*. Thesis, to be published.
- [FJJ⁺95] V. N. Fedoseyev, Y. Jading, O. C. Jonsson, R. Kirchner, K. L. Kratz, M. Krieg, E. Kugler, J. Lettry, T. Mehren, V. I. Mishin, H. L. Ravn, T. Rauscher, F. Scheerer, O. Tengblad, P. Duppen and A. Wüßler. , *Study of short-lived silver isotopes with a laser ion source*. Zeitschrift für Physik A Hadrons and Nuclei 353 (1):9–10 (1995).
- [FKM12] V. N. Fedosseev, Y. Kudryavtsev and V. I. Mishin. , *Resonance laser ionization of atoms for nuclear physics*. Physica Scripta 85 (5):058104 (2012).
- [Foc11] G. J. Focker. *PicoAmpereMeter (PAM)* (2011).
URL http://isolde.web.cern.ch/isolde/group/PG-minutes-2011/20110504_Mini-PicoAmpMeter-talk_Physicists.pdf
- [FPR60] G. Fricke, S. Penselin and E. Recknagel. , *Die Hyperfeinstrukturaufspaltung des $2S_{1/2}$ -Grundzustandes und das magnetische Kerndipolmoment von Au197*. Die Naturwissenschaften 47 (6):129–129 (1960).
- [FS50] W. Finkelburg and F. Stern. , *Electron Screening and Ionization Potentials of Neutral and Singly Ionized Atoms*. Physical Review 77 (2):303–303 (1950).
- [FT12] C. Fry and M. Thoennessen. , *Discovery of the astatine, radon, francium, and radium isotopes*. arXiv (2012). 1205.5841.
- [FWB00] D. Forkel-Wirth and G. Bollen. , *Preface*. Hyperfine Interactions 129 (1):– (2000).
- [Gal88] T. F. Gallagher. , *Rydberg atoms*. Reports on Progress in Physics 51 (2):143–188 (1988).

- [Gal12] N. Galland. Private communication (2012).
- [GBB⁺] A. B. Garnsworthy, G. C. Ball, P. C. Bender, R. Churchman, A. Close, J. Glistler, S. Ketelhut, R. Kruecken, S. Sjue, E. Tardiff, P. E. Garrett, G. A. Demand, R. Dunlop, P. Finlay, B. Hadinia, K. Leach, E. T. Rand, C. E. Svensson, C. Andreoiu, R. Ashley, A. Chester, D. Cross, K. Starosta, Z. Wang and E. F. Zganjar. *Beta-Decay Studies at TRIUMF And Future Opportunities with GRIFFIN*.
- [GC79] T. Gallagher and W. Cooke. , *Interactions of Blackbody Radiation with Atoms*. Physical Review Letters 42 (13):835–839 (1979).
- [GGS⁺08] T. Gottwald, C. Geppert, F. Schwellnus, K. Wies, K. Wendt, Y. Liu, C. Baktash, J. Beene, C. Havener and H. Krause. , *Optical spectroscopy and performance tests with a solid state laser ion source at HRIBF*. Nuclear Instruments and Methods in Physics Research Section B: Beam Interactions with Materials and Atoms 266 (19-20):4398–4402 (2008).
- [GHK⁺04] C. Grüning, G. Huber, P. Klopp, J. Kratz, P. Kunz, G. Passler, N. Trautmann, A. Waldek and K. Wendt. , *Resonance ionization mass spectrometry for ultratrace analysis of plutonium with a new solid state laser system*. International Journal of Mass Spectrometry 235 (2):171–178 (2004).
- [GJS⁺02] U. Georg, A. Junghans, H. Simon, U. Bergmann, R. Catherall, T. Giles, O. Jons-son, U. Köster, E. Kugler, J. Lettry, T. Nilsson, H. Ravn, K.-H. Schmidt and C. Tamburella. , *Isotope production comparison at ISOLDE with 1 and 1.4 GeV protons*. Nuclear Physics A 701 (1-4):137–143 (2002).
- [Got10] T. Gottwald. *Spektroskopie schwerster Elemente*. Ph.D. thesis, Johannes Gutenberg-Universität Mainz (2010).
- [Got12] A. Gottberg. Private communication (2012).
- [Hän72] T. W. Hänsch. , *Repetitively pulsed tunable dye laser for high resolution spectroscopy*. Applied optics 11 (4):895–8 (1972).
- [Her10] A. Herlert. *Minutes of the 36th meeting of the INTC*. Tech. rep., CERN (2010). URL <http://committees.web.cern.ch/committees/intc/minutes/intc36.pdf>
- [HG92] D. Hanstorp and M. Gustafsson. , *Determination of the electron affinity of iodine*. Journal of Physics B: Atomic, Molecular and Optical Physics 25 (8):1773–1783 (1992).

- [HH68] N. Hush and R. Hobbs. *Progress in Inorganic Chemistry Volume 10*. Interscience Publishers (1968).
- [HJKW85] W. R. H-J Kluge, F Ames and K. Wallmeroth. *Laser ion sources*. In *Proceedings of the Accelerated Radioactive Beams Workshop* (1985).
- [HL94] S. G. Hurst and V. S. Letokhov. , *Resonance Ionization Spectroscopy*. Physics Today 47 (10):38 (1994).
- [Hor03] R. Horn. *Aufbau eines Systems gepulster, abstimmbarer Festkörperlaser zum Einsatz in der Resonanzionisations-Massenspektrometrie*. Ph.D. thesis, University of Mainz (2003).
- [HP88] G. S. Hurst and M. G. Payne. *Principles and Applications of Resonance Ionisation Spectroscopy*,. Taylor & Francis (1988). ISBN 0852744609.
- [HPKY79] G. Hurst, M. Payne, S. Kramer and J. Young. , *Resonance ionization spectroscopy and one-atom detection*. Reviews of Modern Physics 51 (4):767–819 (1979).
- [Jab35] A. Jablonski. , *Über den Mechanismus der Photolumineszenz von Farbstoffphosphoren*. Zeitschrift für Physik 94 (1-2):38–46 (1935).
- [JLS49] G. L. Johnson, R. F. Leininger and E. Segrè. , *Chemical Properties of Astatine. I*. The Journal of Chemical Physics 17 (1):1 (1949).
- [JR00] B. Jonson and A. Richter. , *More than three decades of ISOLDE physics*. Hyperfine Interactions 129:1–22 (2000).
- [Kö1] U. Köster. , *How to produce intense and pure ISOL beams*. Progress in Particle and Nuclear Physics 46 (1):411–412 (2001).
- [Kö2] U. Köster. , *Intense radioactive-ion beams produced with the ISOL method*. The European Physical Journal A - Hadrons and Nuclei 15 (1-2):255–263 (2002).
- [KBB⁺11a] S. Kreim, D. Beck, K. Blaum, C. Böhm, C. Borgmann, M. Breitenfeldt, R. B. Cakirli, T. E. Cocolios, F. Herfurth, A. Herlert, M. Kowalska, D. Lunney, S. Naimi, M. R. A. L. Schweikhard, S. Schwarz, J. Stanja, T. Stora, F. Wienholtz, R. N. Wolf and K. Zuber. *Proposal to the ISOLDE and Neutron Time-of-Flight Committee: Extending and Refining the Mass Surface around ²⁰⁸Pb by High-Precision Penning-Trap Mass Spectrometry with ISOLTRAP*. Tech. rep., CERN (2011). URL <http://cdsweb.cern.ch/record/1319110/files/INTC-P-299.pdf>
- [KBB⁺11b] S. Kreim, D. Beck, K. Blaum, C. Böhm, C. Borgmann, M. Breitenfeldt, R. B. Cakirli, F. Herfurth, M. Kowalska, Y. Litvinov, D. Lunney, V. Manea, S. Naimi,

- D. Neidherr, M. Rosenbusch, L. Schweikhard, J. Stanja, T. Stora, F. Wienholtz, R. N. Wolf and Zuber. *Proposal to the ISOLDE and Neutron Time-of-Flight Committee: Seeking the Purported Magic Number $N = 32$ with High-Precision Mass Spectrometry*. Tech. rep., CERN (2011).
URL <http://cdsweb.cern.ch/record/1388237/files/INTC-P-317.pdf>
- [KBDH99] R. Keitel, D. Bishop, D. Dale and H. Hui. , *Design and Commissioning of the ISAC Control System at TRIUMF*. ICALEPCS99, 674–676 (1999).
- [KDSP91] W. Küchle, M. Dolg, H. Stoll and H. Preuss. , *Ab initio pseudopotentials for Hg through Rn*. Molecular Physics 74 (6):1245–1263 (1991).
- [Kes04] T. Kessler. *Optimierung eines Ti:Saphir-Lasersystems für den Einsatz an einer on-line-Ionenquelle*. Master's thesis, Universität Mainz (2004).
- [KFJ⁺92] E. Kugler, D. Fiander, B. Johnson, H. Haas, A. Przewloka, H. Ravn, D. Simon and K. Zimmer. , *The new CERN-ISOLDE on-line mass-separator facility at the PS-Booster*. Nucl. Instrum. Methods B 70 (1-4):41–49 (1992).
- [KFM03] U. Köster, V. Fedoseyev and V. Mishin. , *Resonant laser ionization of radioactive atoms*. Spectrochimica Acta Part B: Atomic Spectroscopy 58 (6):1047–1068 (2003).
- [Kir81] R. Kirchner. , *Progress in ion source development for on-line separators*. Nuclear Instruments and Methods in Physics Research 186 (1-2):275–293 (1981).
- [Kis60] R. W. Kiser. , *Estimation of the Ionization Potential and Dissociation Energy of Molecular Astatine*. The Journal of Chemical Physics 33 (4):1265 (1960).
- [Klu85] H. J. Kluge. , *Optical measurements of ground-state properties of short-lived nuclei in resonance cells*. Hyperfine Interactions 24 (1-4):69–93 (1985).
- [Koe76] W. Koechner. *Solid-State Laser Engineering (Springer Series in Optical Sciences; V. 1)*. Springer (1976). ISBN 0387901671.
- [KR⁺] M. Klein, S. Rothe *et al.* *Management of ionization schemes for laser ion sources*. To be published.
- [KR76] R. Kirchner and E. Roeckl. , *Investigation of gaseous discharge ion sources for isotope separation on-line*. Nuclear Instruments and Methods 133 (2):187–204 (1976).
- [KS92] S. Kobtsev and N. Svetsitskaya. , *Application of birefringent filters in continuous-wave tunable lasers: a review*. Optics and spectroscopy 73:114–123 (1992).

- [KTM⁺08] T. Kessler, H. Tomita, C. Mattolat, S. Raeder and K. Wendt. , *An injection-seeded high-repetition rate Ti:Sapphire laser for high-resolution spectroscopy and trace analysis of rare isotopes*. Laser Physics 18 (7):842–849 (2008).
- [L⁺] J. Lassen *et al.* *In-source laser spectroscopy of astatine at TRIUMF-ISAC*. To be published.
- [L⁺84] V. Letokhov *et al.* *in abstracts from the workshop on the isolve programme “on-line in 1985 and beyond”* (1984).
- [LACC⁺10] N. Lecesne, R. Alvès-Condé, E. Coterreau, F. De Oliveira, M. Dubois, J. L. Flambard, H. Franberg, T. Gottwald, P. Jardin, J. Lassen, F. Le Blanc, R. Leroy, C. Mattolat, A. Olivier, J. Y. Pacquet, A. Pichard, S. Rothe, M. G. Saint-Laurent and K. Wendt. , *GISELE: a resonant ionization laser ion source for the production of radioactive ions at GANIL*. The Review of scientific instruments 81 (2):02A910 (2010).
- [Las12] J. Lassen. *In-source laser spectroscopy of astatine@ONLINE* (2012). URL <http://mis.triumf.ca/science/experiment/view/560>
- [Lay11] Layertec GmbH. *Layertec Catalog 2011* (2011). URL http://www.layertec.de/en/downloads/files/Layertec_Katalog_2011_Gesamt.pdf
- [LBB⁺06] Y. Liu, C. Baktash, J. Beene, H. Bilheux, C. Havener, H. Krause, D. Schultz, D. Stracener, C. Vane, K. Brück, C. Geppert, T. Kessler and K. Wendt. , *Laser ion source tests at the HRIBF on stable Sn, Ge and Ni isotopes*. Nuclear Instruments and Methods in Physics Research Section B: Beam Interactions with Materials and Atoms 243 (2):442–452 (2006).
- [LBD⁺09] J. Lassen, P. Bricault, M. Dombisky, F. Izdebski, J. P. Lavoie, M. Gillner, T. Gottwald, F. Hellbusch, A. Teigelhöfer, A. Voss, K. D. a. Wendt, F. D. McDaniel and B. L. Doyle. *Solid-State Laser, Resonant Ionization Laser Ion Source (Rilis) and Laser Beam Transport at Radioactive Ion Beam Facilities*. In *AIP Conference Proceedings*, vol. 769, 769–773. AIP (2009). URL <http://dx.doi.org/10.1063/1.3120151>
- [Lee85] J. Lee. *Proposal for TRIUMF-ISOL, appendix to “the TRIUMF-ISOL Facility”* (1985).
- [Let87] V. S. Letokhov. *Laser Photoionization Spectroscopy*. Academic Pr (1987). ISBN 0124443206.

-
- [LF70] K. Lu and U. Fano. , *Graphic Analysis of Perturbed Rydberg Series*. Physical Review A 2 (1):81–86 (1970).
- [LGK⁺06] S. Lukić, F. Gevaert, A. Kelić, M. Ricciardi, K.-H. Schmidt and O. Yordanov. , *Systematic comparison of ISOLDE-SC yields with calculated in-target production rates*. Nuclear Instruments and Methods in Physics Research Section A: Accelerators, Spectrometers, Detectors and Associated Equipment 565 (2):784–800 (2006).
- [Lin03] M. Lindroos. , *Future plans at ISOLDE*. Nuclear Instruments and Methods in Physics Research Section B: Beam Interactions with Materials and Atoms 204:730–735 (2003).
- [Lit78] M. G. Littman. , *Single-mode operation of grazing-incidence pulsed dye laser*. Optics Letters 3 (4):138 (1978).
- [Liu12] Y. Liu. *Ti:sapphire laser system at HRIBF-ORNL*. Private communication (2012).
- [LPA⁺92] F. Le Blanc, J. Pinard, J. Arianer, J. Crawford, H. Dautet, H. Duong, P. Kilcher, J. Lee, J. Obert, J. Oms, J. Putaux, B. Roussière, J. Sauvage and G. Thekkadath. , *PILIS: Post-ISOCLE Laser Isobar Separation - a high efficiency apparatus for laser spectroscopy*. Nuclear Instruments and Methods in Physics Research Section B: Beam Interactions with Materials and Atoms 72 (1):111–118 (1992).
- [M⁺82] P. Moulton *et al.* , *Ti-doped sapphire: tunable solid-state laser*. Opt. News 8 (6):9 (1982).
- [Mat06] C. Mattolat. *Entwicklung der resonanzionisations- massenspektrometrie an 26aluminium mit einem geseedeten titan:saphir-lasersystem*. Diplomarbeit (2006).
- [Mat10] C. Mattolat. *Spektroskopische Untersuchungen an Technetium und Silizium - Ein Festkörperlasersystem für die Resonanzionisationsspektroskopie*. Ph.D. thesis, Johannes Gutenberg-Universität (2010).
- [MBF⁺10] B. A. Marsh, L.-E. Berg, D. V. Fedorov, V. N. Fedosseev, O. J. Launila, M. Lindroos, R. Losito, F. K. Österdahl, T. Pauchard, I. T. Pohjalainen, U. Sassenberg, M. D. Seliverstov, A. M. Sjödin and G. Tranströmer. , *The ISOLDE RILIS pump laser upgrade and the LARIS Laboratory*. Hyperfine Interactions 196 (1-3):129–141 (2010).
- [McL64] R. McLAUGHLIN. , *Absorption Spectrum of Astatine*. Journal of the Optical Society of America 54 (8):965 (1964).

- [Men69] D. Mendeleev. , *Über die beziehungen der eigenschaften zu den atomgewichten der elemente*. Zeitschrift für Chemie 5:405–406 (1869).
- [Men07] R. Menzel. *Photonics*. Springer Berlin Heidelberg, Berlin, Heidelberg (2007). ISBN 978-3-540-23160-8.
URL <http://dx.doi.org/10.1007/978-3-540-45158-7>
- [MFK⁺93] V. Mishin, V. Fedoseyev, H.-J. Kluge, V. Letokhov, H. Ravn, F. Scheerer, Y. Shirakabe, S. Sundell and O. Tengblad. , *Chemically selective laser ion-source for the CERN-ISOLDE on-line mass separator facility*. Nuclear Instruments and Methods in Physics Research Section B: Beam Interactions with Materials and Atoms 73 (4):550–560 (1993).
- [MGR⁺10] C. Mattolat, T. Gottwald, S. Raeder, S. Rothe, F. Schwellnus and K. Wendt. , *Determination of the first ionization potential of technetium*. Physical Review A 81 (5):2–6 (2010).
- [MNB⁺05] I. D. Moore, A. Nieminen, J. Billowes, P. Campbell, C. Geppert, A. Jokinen, T. Kessler, B. Marsh, H. Penttilä, S. Rinta-Antila, B. Tordoff, K. D. a. Wendt and J. Äystö. , *Development of a laser ion source at IGISOL*. Journal of Physics G: Nuclear and Particle Physics 31 (10):S1499–S1502 (2005).
- [Mou86] P. F. Moulton. , *Spectroscopic and laser characteristics of Ti : Al₂O₃*. Journal of the Optical Society of America B 3 (1):125 (1986).
- [MTN08] P. J. Mohr, B. N. Taylor and D. B. Newell. , *CODATA recommended values of the fundamental physical constants: 2006*. Reviews of Modern Physics 80 (2):633–730 (2008).
- [MvW06] A. V. Mitin and C. van Wüllen. , *Two-component relativistic density-functional calculations of the dimers of the halogens from bromine through element 117 using effective core potential and all-electron methods*. J. Chem. Phys. 124 (6):64305 (2006).
- [NNTK68] V. D. Nefedov, Y. V. Norseev, M. A. Toropova and V. A. Khalkin. , *Astatine*. Russian Chemical Reviews 37 (2):87–98 (1968).
- [OAB⁺10] Y. T. Oganessian, F. S. Abdullin, P. D. Bailey, D. E. Benker, M. E. Bennett, S. N. Dmitriev, J. G. Ezold, J. H. Hamilton, R. A. Henderson, M. G. Itkis, Y. V. Lobanov, A. N. Mezentsev, K. J. Moody, S. L. Nelson, A. N. Polyakov, C. E. Porter, a. V. Ramayya, F. D. Riley, J. B. Roberto, M. A. Ryabinin, K. P. Rykaczewski, R. N. Sagaidak, D. A. Shaughnessy, I. V. Shirokovsky, M. A. Stoyer, V. G. Subbotin, R. Sudowe, A. M. Sukhov, Y. S. Tsyganov, V. K. Utyonkov,

- A. A. Voinov, G. K. Vostokin and P. A. Wilk. , *Synthesis of a New Element with Atomic Number $Z=117$* . Physical Review Letters 104 (14):1–4 (2010).
- [Pho11] Photonics Industries. *Diode pumped Silid-State Lasers Tunable ns Ti:Sapphire* (2011).
URL <http://www.photonix.com/index10/img/Brochure/TU.pdf>
- [Pis12] E. Piselli. *Isolde gps vistars screen@ONLINE* (2012).
URL <http://op-webtools.web.cern.ch/op-webtools/vistar/vistars.php?usr=GPS>
- [PLA⁺07] E. J. Prime, J. Lassen, T. Achtzehn, D. Albers, P. Bricault, T. Cocolios, M. Domb-sky, F. Labrecque, J. P. Lavoie, M. R. Pearson, T. Stubbe, N. Lecesne, C. Geppert and K. D. a. Wendt. , *TRIUMF resonant ionization laser ion source*. Hyperfine Interactions 171 (1-3):127–134 (2007).
- [RAA⁺] S. Rothe, A. N. Andreyev, S. Antalic, A. E. Barzakh, A. Borschevsky, L. Capponi, T. E. Cocolios, H. D. Witte, E. Eliav, J. Elseviers, D. V. Fedorov, V. N. Fedosseev, S. Fritzsche, L. Ghys, N. Imai, U. Kaldor, Y. Kudryavtsev, J. Lane, J. Lassen, V. Liberati, B. A. Marsh, K. Nishio, D. Pauwels, V. Pershina, L. Popescu, T. J. Procter and M. Sjødin. *Measurement of the first ionization potential of astatine by laser ionization spectroscopy*. submitted.
- [RAA⁺06] W. T. Rhodes, A. Adibi, T. Asakura, T. W. Hänsch, T. Kamiya, F. Krausz, B. Monemar, H. Venghaus, H. Weber, H. Weinfurter and W. T. Rhodes. *Solid-State Laser Engineering*, vol. 1 of *Springer Series in Optical Sciences*. Springer New York, New York, NY (2006). ISBN 978-0-387-29094-2.
URL <http://dx.doi.org/10.1007/0-387-29338-8>
- [Rae10] S. Raeder. *Spurenanalyse von Aktiniden in der Umwelt mittels Resonanzionisations-Massenspektrometrie*. Ph.D. thesis, Johannes Gutenberg-Universität Mainz (2010).
URL <http://ubm.opus.hbz-nrw.de/volltexte/2011/2775/>
- [RBC⁺94] H. Ravn, P. Bricault, G. Ciavola, P. Drumm, B. Fogelberg, E. Hagebø, M. Huyse, R. Kirchner, W. Mittag, A. Mueller, H. Nifenecker and E. Roeckl. , *Comparison of radioactive ion-beam intensities produced by means of thick targets bombarded with neutrons, protons and heavy ions*. Nuclear Instruments and Methods in Physics Research Section B: Beam Interactions with Materials and Atoms 88 (4):441–461 (1994).

- [Ren12] K. F. Renk. *Basics of Laser Physics*. Graduate Texts in Physics. Springer Berlin Heidelberg, Berlin, Heidelberg (2012). ISBN 978-3-642-23564-1.
URL <http://dx.doi.org/10.1007/978-3-642-23565-8>
- [RFG⁺10] S. Raeder, S. Fies, T. Gottwald, C. Mattolat, S. Rothe and K. Wendt. , *In-source resonance ionization spectroscopy of high lying energy levels in atomic uranium*. Hyperfine Interactions 196 (1-3):71–79 (2010).
- [RFM12] S. Rothe, V. Fedosseyev and B. Marsh. *The Dual RILIS* (2012).
URL http://isolde.web.cern.ch/isolde/science/Newsletter_Spring2012.pdf
- [RGB84] B. Ruscic, J. P. Greene and J. Berkowitz. , *Photoionisation of atomic bromine*. Journal of Physics B: Atomic and Molecular Physics 17 (8):1503–1514 (1984).
- [RGH⁺04] C. Rauth, C. Geppert, R. Horn, J. Lassen, P. Bricault and K. Wendt. , *First laser ions at an off-line mass separator of the ISAC facility at TRIUMF*. Nuclear Instruments and Methods in Physics Research Section B: Beam Interactions with Materials and Atoms 215 (1-2):268–277 (2004).
- [Rit11] W. Ritz. *Gesammelte Werke Walter Ritz*. Paris: Gautier-Villars (1911).
URL ftp://ftp.bnf.fr/000/N0003382_PDF_1_-1DM.pdf
- [RK70] G. Rudstam and A. Kjelberg. *The ISOLDE isotope separator on-line facility at CERN*. CERN, Geneva (1970).
URL <http://cdsweb.cern.ch/record/274972/files/CERN-70-03.pdf>
- [RMK⁺12] M. Reponen, I. D. Moore, T. Kessler, I. Pohjalainen, S. Rothe and V. Sonnenschein. , *Laser developments and resonance ionization spectroscopy at IGISOL*. The European Physical Journal A 48 (4) (2012).
- [RMM⁺11] S. Rothe, B. A. Marsh, C. Mattolat, V. N. Fedosseev and K. Wendt. , *A complementary laser system for ISOLDE RILIS*. Journal of Physics: Conference Series 312 (5):052020 (2011).
- [Ros11] R. E. Rossel. *Programming of the Wavelength Stabilization for a Titanium:Sapphire Laser using LabVIEW and Implementation into the CERN ISOLDE RILIS Measurement System*. Bachelor’s thesis, Hochschule RhenMain (2011).
- [Rot09] S. Rothe. *Aufbau eines Chrom:Forsterit-Lasers und Resonanzionisationsspektroskopie an Strontium, Titan, Nickel, Scandium und Silicium*. Master’s thesis, Universität Mainz (2009).

- [RR⁺] R. E. Rossel, S. Rothe *et al.* *A labview based monitoring and control system for the isotope laser ion source RILIS*. To be published.
- [RR12] S. Rothe and RILIS. *Status of the RILIS@ONLINE* (2012).
URL <http://riliselements.web.cern.ch/riliselements/lasers/>
- [RRH⁺12] J. Roßnagel, S. Raeder, A. Hakimi, R. Ferrer, N. Trautmann and K. Wendt. , *Determination of the first ionization potential of actinium*. Physical Review A 85 (1):1–6 (2012).
- [RRM⁺12] R. E. Rossel, S. Rothe, B. Marsh, V. Fedosseev and K. Wendt. *Monitoring and control of the isotope resonance laser ion source RILIS*. Poster DPG (2012).
- [RSG⁺11] S. Raeder, V. Sonnenschein, T. Gottwald, I. D. Moore, M. Reponen, S. Rothe, N. Trautmann and K. Wendt. , *Resonance ionization spectroscopy of thorium isotopes towards a laser spectroscopic identification of the low-lying 7.6 eV isomer of ²²⁹Th*. Journal of Physics B: Atomic, Molecular and Optical Physics 44 (16):165005 (2011).
- [Sal90] E. Saloman. , *A resonance ionization spectroscopy/resonance ionization mass spectrometry data service. Data sheets for As, B, Cd, C, Ge, Au, Fe, Pb, Si and Zn*. Spectrochimica Acta Part B: Atomic Spectroscopy 45 (1-2):37–83 (1990).
- [Sch73] F. P. Schäfer. *Dye Lasers*, vol. 1 of *Topics in Applied Physics*. Springer Berlin Heidelberg, Berlin, Heidelberg (1973). ISBN 978-3-540-51558-6.
URL <http://dx.doi.org/10.1007/3-540-51558-5>
- [SD11] R. F. Stebbings and F. B. Dunning. *Rydberg States of Atoms and Molecules*. Cambridge University Press (2011). ISBN 052118973X.
- [Sea83] M. J. Seaton. , *Quantum defect theory*. Reports on Progress in Physics 46 (2):167–257 (1983).
- [Sen02] A. Sennaroglu. , *Broadly tunable Cr⁴⁺-doped solid-state lasers in the near infrared and visible*. Progress in Quantum Electronics 26 (6):287–352 (2002).
- [Sir04] S. Sirotzki. *Konzeption und aufbau einer frequenzverdreifachungseinheit für ein gepulstes titan-saphir lasersystem*. Staatsexamensarbeit (2004).
- [SJ83] V. N. Sarma and Y. N. Joshi. , *Absorption spectrum of atomic bromine (Br I) in the vacuum ultraviolet region*. Journal of Physics B: Atomic and Molecular Physics 16 (10):1671–1683 (1983).
- [SM05] J. E. Sansonetti and W. C. Martin. , *Handbook of basic atomic spectroscopic data*. Journal of Physical and Chemical Reference Data 34 (4):1559–2259 (2005).

- [Smi00] A. Smith. *How to select nonlinear crystals and model their performance using snlo software*. In *Proc. SPIE*, vol. 3928, 62–69 (2000).
URL <http://www.osti.gov/bridge/servlets/purl/752529-KJa8vz/webviewable/752529.pdf>
- [SR92] S. Sundell and H. Ravn. , *Ion source with combined cathode and transfer line heating*. Nuclear Instruments and Methods in Physics Research Section B: Beam Interactions with Materials and Atoms 70 (1-4):160–164 (1992).
- [ST07] B. E. A. Saleh and M. C. Teich. *Fundamentals of Photonics (Wiley Series in Pure and Applied Optics)*. Wiley-Interscience (2007). ISBN 0471358320.
- [Sto12] T. Stora. *Nuclear chart for isolate (online)* (2012).
URL https://oraweb.cern.ch/pls/isolde/nuc1_chart.nuclear_chart?scale=1
- [TBC⁺10] A. Teigelhöfer, P. Bricault, O. Chachkova, M. Gillner, J. Lassen, J. P. Lavoie, R. Li, J. Meißner, W. Neu and K. D. a. Wendt. , *Grating tuned Ti:Sa laser for in-source spectroscopy of Rydberg and autoionizing states*. Hyperfine Interactions 196 (1-3):161–168 (2010).
- [TSTG⁺03] J. Taïeb, K.-H. Schmidt, L. Tassan-Got, P. Armbruster, J. Benlliure, M. Bernas, A. Boudard, E. Casarejos, S. Czajkowski, T. Enqvist, R. Legrain, S. Leray, B. Mustapha, M. Pravikoff, F. Rejmund, C. Stéphan, C. Volant and W. Wlazlo. , *Evaporation residues produced in the spallation reaction at 1 AGeV*. Nuclear Physics A 724 (3-4):413–430 (2003).
- [Van97] P. Van Duppen. , *Laser ion sources for on-line isotope separators*. Nuclear Instruments and Methods in Physics Research Section B: Beam Interactions with Materials and Atoms 126 (1-4):66–72 (1997).
- [Var53] Y. P. Varshni. , *Die Schwingungsfrequenzen im Grundzustand befindlicher Moleküle vom Typ XX*. Zeitschrift für Physik 135 (5):512–515 (1953).
- [Wal74] H. Walther. , *Application of Tunable Dye Lasers to Atomic Spectroscopy*. Physica Scripta 9 (5):297–305 (1974).
- [WBB⁺12] R. Wolf, D. Beck, K. Blaum, C. Böhm, C. Borgmann, M. Breitenfeldt, F. Herfurth, a. Herlert, M. Kowalska, S. Kreim, D. Lunney, S. Naimi, D. Neidherr, M. Rosenbusch, L. Schweikhard, J. Stanja, F. Wienholtz and K. Zuber. , *On-line separation of short-lived nuclei by a multi-reflection time-of-flight device*. Nuclear Instruments and Methods in Physics Research Section A: Accelerators, Spectrometers, Detectors and Associated Equipment 686:82–90 (2012).

- [WBG⁺03] K. Wendt, K. Blaum, C. Geppert, R. Horn, G. Passler, N. Trautmann and B. Bushaw. , *Laser resonance ionization for efficient and selective ionization of rare species*. Nuclear Instruments and Methods in Physics Research Section B: Beam Interactions with Materials and Atoms 204:325–330 (2003).
- [ZRA⁺08] M. R. Zalutsky, D. a. Reardon, G. Akabani, R. E. Coleman, A. H. Friedman, H. S. Friedman, R. E. McLendon, T. Z. Wong and D. D. Bigner. , *Clinical experience with alpha-particle emitting ²¹¹At: treatment of recurrent brain tumor patients with ²¹¹At-labeled chimeric antitenascin monoclonal antibody 81C6*. Journal of nuclear medicine : official publication, Society of Nuclear Medicine 49 (1):30–8 (2008).

Acknowledgements

The three years of being a doctoral student at CERN have been very intense and rewarding as working in a professional environment amongst enthusiastic people was always a great pleasure. I would like to thank my supervisors for continuously supporting me, for all the valuable advice and for giving me the freedom to live out my creativity.

The BMBF is acknowledged for funding my Wolfgang Gentner Stipendium; the local support is greatly appreciated.

I would like to thank the members and former members of the working group LARISSA at the University of Mainz for the good collaboration.

The mechanical workshop of the Institute for Physics at the University of Mainz is acknowledged for the high precision work machining the laser cavities and the frequency conversion units and fighting through over 50 pages of technical drawings. I would like to thank the EN-STI group secretaries for organizing last minute trips and dealing with my travel claims, the operator team and physics group of ISOLDE for the support during the measurements and regular RILIS operation. The ISOLDE physics coordinator gets a big thanks! for allocating special last minute beam times.

Furthermore I want to thank the Furios Laser guys and IGISOL team for the good times in in Jyväskylä and the on-line training, the Astatine Collaboration for all the support and the TRILIS laser team and the TRIUMF/ISAC crew for the exciting states in astatine.

I appreciate the relaxed atmosphere in the RILIS team. The numerous support letters written by supervisors and professors allowed me participating in conferences around the globe and finally helped to have been given the opportunity to continue my work at the RILIS, to finalize and - more importantly - to start new projects.

I want to thank my family for accepting the lack of my physical presence.